



City Research Online

City, University of London Institutional Repository

Citation: Themistos, C. (1998). Characterization of loss/gain in optical waveguides. (Unpublished Doctoral thesis, City, University of London)

This is the accepted version of the paper.

This version of the publication may differ from the final published version.

Permanent repository link: <https://openaccess.city.ac.uk/id/eprint/31018/>

Link to published version:

Copyright: City Research Online aims to make research outputs of City, University of London available to a wider audience. Copyright and Moral Rights remain with the author(s) and/or copyright holders. URLs from City Research Online may be freely distributed and linked to.

Reuse: Copies of full items can be used for personal research or study, educational, or not-for-profit purposes without prior permission or charge. Provided that the authors, title and full bibliographic details are credited, a hyperlink and/or URL is given for the original metadata page and the content is not changed in any way.

**CHARACTERIZATION OF LOSS/GAIN
IN OPTICAL WAVEGUIDES**

by

Christos Themistos

A thesis submitted to
City University
in fulfilment of the requirement
for the Degree of Doctor of Philosophy

CITY UNIVERSITY

Measurement and Instrumentation Centre
Department of Electrical, Electronic and Information Engineering
Northampton Square, London EC1V 0HB

February 1998

*To my parents
and my wife*

Table of Contents

Table of Contents	ii
List of Tables	v
List of Figures	vi
Acknowledgements.....	xiii
Declaration	xiv
Abstract	xv
Symbols and Abbreviations	xvi
1 Introduction.....	1
1.1 Historical Development of Lightwave Technology.....	1
1.2 Optical waveguides	5
1.2.1 Guided modes in a planar slab optical waveguide	7
1.2.2 Guided modes for the 3-D optical waveguide	9
1.3 Solutions to optical waveguide problems	10
1.3.1 Analytical approximation solutions	11
1.3.1.1 Marcatili's Method	11
1.3.1.2 The effective index method.....	11
1.3.2 Numerical approximation solutions	12
1.3.2.1 Selection of the numerical method.....	13
1.3.2.2 The Variational method.....	14
1.3.2.3 The Finite Difference Method.....	15
1.3.2.4 Point matching method	16
1.3.2.5 The boundary element method	17
1.3.2.6 The mode matching or equivalent network method.....	18
1.3.2.7 The spectral index method.....	19
1.3.2.8 The method of lines	20
1.3.2.9 The finite element method	21
1.3.2.10 The beam propagation method	22
1.4 Loss and gain in optical waveguides	24
1.5 Aims and objectives of the thesis	25
1.6 Structure of the thesis	27
2 The Finite Element Method	31
2.1 Introduction	31
2.2 Basic equations	34
2.2.1 Maxwell's equations.....	35
2.2.2 Boundary Conditions	36
2.2.2.1 Natural and Forced Boundary Conditions	37
2.2.3 Wave equations.....	38
2.3 Variational Formulations.....	39
2.3.1 The scalar approximation	40
2.3.2 Vector formulations.....	40
2.4 Finite Element Method formulation	43
2.5 Elements and nodal values.....	45
2.6 Shape functions.....	47

2.7	Assembly of element matrices.....	50
2.8	Global matrices and sparsity	54
2.9	Infinite elements	57
2.10	Boundary Conditions	58
2.11	Spurious solutions	59
2.12	Summary.....	61
3	Loss/Gain Analysis and Perturbation Techniques.....	62
3.1	Introduction	62
3.2	Analytical solutions.....	63
3.2.1	Maxwell's equations for the planar waveguide	64
3.2.2	The transcendental equation	65
3.2.3	Solution of the complex transcendental equation.....	67
3.2.4	The Effective Index Method	69
3.2.5	Multilayer planar waveguides.....	71
3.3	Numerical solutions for gain/loss analysis	74
3.4	The perturbation technique.....	76
3.4.1	Finite Element Method with Perturbation	78
3.4.1.1	Scalar formulation for the TE and TM modes.....	79
3.4.1.2	Scalar FEM with perturbation.....	81
3.4.1.3	Full vector FEM with perturbation.....	84
3.5	Field Confinement Method.....	86
3.6	Summary.....	87
4	Gain/Loss Analysis of planar waveguides.....	88
4.1	Introduction	88
4.1.1	Surface plasmon polaritons	89
4.2	Single metal-dielectric interface.....	90
4.3	Three layer planar waveguides.....	93
4.3.1	Non-metal planar waveguides	93
4.3.2	Metal-clad planar waveguides.....	96
4.3.2.1	Graded-index metal-clad planar waveguides	98
4.3.3	Surface plasmon modes in planar waveguides.....	105
4.3.3.1	Thin metal film surrounded by dielectrics	105
4.3.3.2	Dielectric medium surrounded by thin metal films	115
4.4	Multilayer metal-clad planar optical waveguides	125
4.5	Summary.....	134
5	Two-dimensional modal gain/loss analysis of optical waveguides	135
5.1	Introduction	135
5.2	The Rectangular dielectric waveguide.....	136
5.3	The Rib Waveguide.....	144
5.3.1	The simple Rib waveguide.....	145
5.3.2	The Integrated laser Rib Waveguide	147

5.3.3	Dependence of refractive index, of active layer, on carrier concentration	152
5.3.4	Multiple Quantum Well Rib waveguide	157
5.4	Electro-optic directional coupler modulator	165
5.5	Summary	167

6 Surface plasmon modes in 2-D

gain/loss analysis of optical waveguides 168

6.1	Introduction	168
6.2	Composite coupled structure	169
6.3	TE/TM Polarization Mode splitters	178
6.4	Sub-Micron Metal-Clad Optical Fibers	189
6.4.1	Classification of propagating modes in metal-clad optical fibers ..	190
6.4.2	TM mode analysis.....	191
6.4.3	TE mode analysis	201
6.5	Summary.....	206

7 Discussion and Suggestions for further work 207

7.1	General Conclusions	207
7.2	Suggestions for future work.....	212

Appendix A: Evaluation of the element matrices..... 214

Appendix B: Calculations for a four-layer planar waveguide 217

Appendix C: Calculations for the scalar FEM with perturbation..... 219

Appendix D: Calculations for the full H-field vector FEM with perturbation..... 223

Appendix E List of Publications by the Author Relevant to the Thesis..... 228

References 230

List of Tables

Table 4.1: Comparison of the complex propagation constant for the TE_0 and TE_1 modes, for graded-index planar optical waveguide with graded-index film length $a=5\mu\text{m}$.

List of Figures

- Figure 1.1:** Reflection and refraction of a light ray in a planar slab optical waveguide.
- Figure 2.1:** Arbitrarily shaped optical waveguide, divided into arbitrary sub-domains, each having different type of material.
- Figure 2.2:** Boundary between two media of refractive indices n_1 and n_2 , where \mathbf{n} , is the unit vector normal to the interface.
- Figure 2.3:** Arbitrary cross section of an optical waveguide (shaded core region), Ω , enclosed by boundary Γ .
- Figure 2.4:** a) First-order and b) second-order triangular elements.
- Figure 2.5:** Coordinates and node numbers of a first-order triangular element.
- Figure 2.6:** Simple structure discretized in four, first-order triangular elements.
- Figure 2.7:** Node representation of a rectangular dielectric waveguide, discretized into finite and infinite elements (two-fold symmetry assumed).
- Figure 2.8:** Representation of the H_x^{11} mode across a rectangular dielectric waveguide.
- Figure 3.1:** Three-layer planar optical waveguide.
- Figure 3.2:** Flow-chart diagram for the solution of the complex transcendental equation.
- Figure 3.3:** Solution of the rectangular dielectric waveguide by the Effective Index Method.
- Figure 3.4:** Multilayer planar waveguide.
- Figure 4.1:** The dielectric slab or planar waveguide.
- Figure 4.2:** Variation of the normalized field profile, for the TM_0 mode with the transverse direction for several values of the refractive index of the dielectric.
- Figure 4.3:** Variation of the effective index and normalized attenuation constant with the refractive index of the dielectric material.
- Figure 4.4:** Variation of the normalised phase and attenuation constants with the imaginary part of the film refractive index, (n'_1) of a slab waveguide, using the analytical approach (AM) and the Finite Element Method (FEM).
- Figure 4.5:** Convergence of the normalized phase and attenuation constants by analytical approach, for two different values of the imaginary part of the film refractive index (n'_1) for a slab waveguide.
- Figure 4.6:** Variation of modal loss with guide thickness.
- Figure 4.7:** Variation of normalized loss with normalized film thickness for TE and TM modes.
- Figure 4.8:** Variation of the refractive index profile in a graded-index metal-clad planar optical waveguide.
- Figure 4.9:** Variation of the effective index, n_e , with the variation of the length, a , of the graded-index film with linear index profile, for TE and TM modes.

- Figure 4.10:** Variation of the attenuation constant, α , with the variation of the length, a , of the graded-index film with linear index profile, for the TE and TM modes.
- Figure 4.11:** Propagation characteristics for the exponential index profile.
- Figure 4.12:** Attenuation characteristics for the exponential index profile.
- Figure 4.13:** Variation of the effective indices for a symmetric surface plasmon structure.
- Figure 4.14:** H_x field profile for the Odd-like Supermode (A_b), for $t=0.03\mu\text{m}$.
- Figure 4.15:** H_x field profile for the Even-like Supermode (S_b), for $t=0.03\mu\text{m}$.
- Figure 4.16:** H_x field profile for the Odd-like Supermode (A_b), for $t=0.08\mu\text{m}$.
- Figure 4.17:** H_x field profile for the Even-like Supermode (S_b), for $t=0.08\mu\text{m}$.
- Figure 4.18:** Effective index versus metal thickness for each of the first two supermodes of non-symmetrical structures for different values of the lower-cladding refractive index.
- Figure 4.19:** Variation of normalized modal loss coefficient versus metal thickness for the first two supermodes for different values of the lower-cladding refractive index.
- Figure 4.20:** Comparison of the variation of the effective index with the metal thickness, for the first supermodes, of nonsymmetrical structure, by different approaches.
- Figure 4.21:** Comparison of the attenuation characteristics versus the metal thickness for the first two supermodes, by various approaches.
- Figure 4.22:** Comparison of the variation of the propagation characteristics with metal thickness for non symmetrical planar structure.
- Figure 4.23:** Variation of the effective index with the dielectric film thickness for a symmetrical surface plasmon structure.
- Figure 4.24:** Normalized field profile for the even supermode of a symmetrical structure, for a normalized film thickness, $k_0a=0.7$.
- Figure 4.25:** Normalized field profile for the even supermode of a symmetrical structure, for a normalized dielectric thickness, $k_0a=2.4$.
- Figure 4.26:** Normalized field profile for the odd supermode of a symmetrical structure, for a normalized dielectric thickness, $k_0a=0.7$.
- Figure 4.27:** Normalized field profile for the odd supermode of a symmetrical structure, for a normalized dielectric thickness, $k_0a=2.4$.
- Figure 4.28:** Attenuation characteristics of a symmetrical metal-clad surface plasmon structure.
- Figure 4.29:** Variation of the effective index with the dielectric film thickness for a non-symmetrical surface plasmon structure.
- Figure 4.30:** Normalized field profile for the even-like supermode of a non-symmetrical structure, for a normalized film thickness, $k_0a=0.7$.
- Figure 4.31:** Normalized field profile for the even-like supermode of a non-symmetrical structure, for a normalized film thickness, $k_0a = 1.6$.

- Figure 4.32:** Normalized field profile for the odd-like supermode of a non-symmetrical structure, for a normalized film thickness, $k_0a=0.7$.
- Figure 4.33:** Normalized field profile for the odd-like supermode of a non-symmetrical structure, for a normalized film thickness, $k_0a=1.6$.
- Figure 4.34:** Variation of the normalized attenuation constant with the dielectric film thickness for a non-symmetrical surface plasmon structure.
- Figure 4.35:** Attenuation characteristics for the metal-clad planar optical waveguide, for lower-index buffer layer thickness, $b=0.1\mu\text{m}$.
- Figure 4.36:** Variation of the phase constant (β), with the buffer layer thickness, of the TE and TM modes, for a multilayer metal-clad planar optical waveguide.
- Figure 4.37:** Variation of the normalized attenuation constant, with the buffer layer thickness, for the TE and TM modes, of a multilayer metal-clad planar optical waveguide.
- Figure 4.38:** H_x field distribution for the TM_0 and TM_1 modes for a buffer layer thickness, a) $b=0.001\mu\text{m}$, b) $b=0.1\mu\text{m}$.
- Figure 4.39:** H_x field distribution for the TM_2 and TM_3 modes for a buffer layer thickness: a) $b=0.001\mu\text{m}$, b) $b=0.1\mu\text{m}$.
- Figure 4.40:** H_y field distribution for the TE_0 and TE_1 mode, for a buffer layer thickness, $b=0.053\mu\text{m}$.
- Figure 4.41:** H_x field profile for the TM modes for the multilayer metal-clad planar waveguide for buffer layer thickness, $b=0.053\mu\text{m}$.
- Figure 5.1:** Three types of practical optical waveguides.
- Figure 5.2:** Variation of modal gain with the normalized dimension for the TE_{11} mode of an embedded channel waveguide.
- Figure 5.3:** Variation of the normalized modal gain (g/k_0) with the normalized dimension for the H_{11}^y mode of an embedded-channel waveguide, using the complex Effective Index Method (EIM) and the scalar and vector Finite Element Method.
- Figure 5.4:** Variation of the effective index (n_e) and the normalized attenuation constant (α/k_0) with the mesh division of an embedded channel waveguide, using the \mathbf{H}_t , the vector \mathbf{H} -field with perturbation (V+P) and the scalar \mathbf{H} -field with perturbation (S+P) finite element formulations and the complex effective index method (EIM).
- Figure 5.5:** Variation of the effective index and the attenuation constant with the imaginary part of the refractive index of the core of an embedded channel optical waveguide (Hayata *et al.*, 1986), using the \mathbf{H}_t formulation, the vector \mathbf{H} (V+P) formulation with perturbation and the Complex Effective index Method (EIM).
- Figure 5.6:** H_y , field distribution along the y -axis for different values of the imaginary part of the refractive index of the core (n_1'') of an embedded channel optical waveguide, using the \mathbf{H} vector formulation with perturbation and the \mathbf{H}_t formulation.

- Figure 5.7:** Accuracy of the approximate method using the field confinement factor, comparison of the scalar FEM with perturbation with the variation of the confinement factor Γ , for an embedded channel waveguide.
- Figure 5.8** Variation of the normalized propagation constant characteristics for a GaAlAs/GaAs rib waveguide with D , by the Effective index method (EIM) and the scalar (SFEM) and vector (VFEM) Finite Element Method.
- Figure 5.9:** Variation of the normalized phase (β/k_0) and the attenuation (α) constants with the imaginary part of the refractive index (n_1'').
- Figure 5.10:** Variation of the normalized gain constant with top confinement layer thickness, H , for the H_{11}^y mode of a semiconductor laser rib waveguide, by the vector, scalar and the H_t formulations in the Finite Element Method and the Spectral Index Method.
- Figure 5.11:** Variation of the effective index with the top confinement layer thickness, H , for the H_{11}^y mode, of a semiconductor laser rib waveguide by the scalar and the vector Finite Element Method and the Finite Difference Method (FDM).
- Figure 5.12:** Variation of the normalized modal gain with H , for the H_{11}^y mode, of a semiconductor laser rib, by the scalar and the vector FEM and the FDM.
- Figure 5.13:** Variation of the normalized modal gain with H , for the H_{11}^y mode, by the Vector Finite Element Method.
- Figure 5.14:** Comparison of the scalar FEM with perturbation and the approximate method using the field confinement, with the confinement factor, Γ , for different values of the imaginary part of the refractive index of the substrate of a rib waveguide, n_2'' , for constant imaginary part of the refractive index of the active layer $n_1''=0.001$.
- Figure 5.15:** Rib waveguide structure where the imaginary part of the refractive index in the active layer varies according to the carrier profile.
- Figure 5.16:** Carrier profile along the x-axis in the active layer of the rib semiconductor laser optical waveguide, for different values of the diffusion length L , of the carrier.
- Figure 5.17:** Variation of the modal gain constant for the rib semiconductor laser waveguide with the carrier concentration at threshold, N_0 , of the active layer for different values of the diffusion length of the carrier.
- Figure 5.18:** Multiple Quantum Well (MQW) Rib waveguide (Al% is given).
- Figure 5.19:** Variation of the normalized gain constant with the quantum well thickness for a single, two and three quantum well rib waveguide.
- Figure 5.20:** Normalized H_x field profile, along the y-axis of symmetry for a single Quantum Well (QW) structure, for the active layer thickness, $t=0.005\mu\text{m}$
- Figure 5.21:** Normalized H_x field profile, along the y-axis of symmetry for a Two Quantum Well (QW) structure, for each QW active layer thickness, $t=0.005\mu\text{m}$

- Figure 5.22:** Normalized H_x field profile, along the y -axis of symmetry for a three Quantum Well (QW) structure, for each QW active layer thickness, a) $t=0.005\mu\text{m}$, b) $t=0.01\mu\text{m}$
- Figure 5.23:** Variation of the normalized gain constant with the thickness of the active layer, t , for one, two and three active layers in a rib waveguide structure.
- Figure 5.24:** Comparison of the scalar FEM with perturbation and the Field Confinement method, with the variation of the active layer thickness for a one, two and three active layer system in a rib waveguide.
- Figure 5.25:** Attenuation characteristics for a directional coupler modulator with the variation of the SiO_2 buffer thickness, d , for aluminum and gold metal electrodes.
- Figure 6.1:** Composite waveguiding structure incorporating a dielectric structure with a metal strip coupled with a dielectric waveguide surrounded by dielectric material
- Figure 6.2:** Variation of the effective index with metal-strip thickness, t , for the first two supermodes of the coupled structure.
- Figure 6.3:** H_x field profile along symmetry y -axis for the first supermode, for metal film thickness a) $t=0.05\mu\text{m}$ b) $t=0.054\mu\text{m}$, c) $t=0.06\mu\text{m}$.
- Figure 6.4:** H_x field profile along symmetry y -axis for the second supermode, for metal film thickness a) $t=0.05\mu\text{m}$ b) $t=0.054\mu\text{m}$, c) $t=0.06\mu\text{m}$.
- Figure 6.5:** H_x field distribution for the first supermode for metal-strip thickness $t=0.054\mu\text{m}$ (only half the structure is shown because of one-fold symmetry along the y -axis).
- Figure 6.6:** Variation of the normalized loss coefficient with metal strip thickness, t , for the coupled structure.
- Figure 6.7:** Variation of the coupling length with the metal-strip thickness, t , for various aspect ratios (w/d) of the rectangular dielectric waveguide.
- Figure 6.8:** Variation of the metal-strip thickness at phase matching, t_p , with the (w/d) aspect ratio. The planar solution for $w/d=\infty$ is shown by the dashed line.
- Figure 6.9:** Cross section of the TE/TM mode polarization splitter.
- Figure 6.10:** Effective index variation of TE and TM modes, with the variation of the rib height, for a metal-clad rib optical waveguide.
- Figure 6.11:** Field profiles along the y -axis of symmetry, for the TE and TM modes of a metal-clad rib waveguide, for rib height a) $d=0.5\mu\text{m}$ and b) $d=1\mu\text{m}$.
- Figure 6.12:** Variation of the attenuation constant, with the increase of the rib height, for the TE and TM modes, of the metal-clad rib waveguide.
- Figure 6.13:** Variation of the effective index, with the increase of the rib height, for the TE and TM modes, of the polarization mode splitter, for different separations between the two ribs.
- Figure 6.14:** H_y field distribution of the TE_{00} mode for $d=0.8\mu\text{m}$ and $s=0.7\mu\text{m}$, of the mode polarization splitter.

- Figure 6.15:** H_y field profile, for the TE mode, along the x-axis, in the centre of the InGaAsP dielectric region for different values of the rib height.
- Figure 6.16:** H_x field distribution of the TM_{01} mode of the mode polarization splitter, for $d=0.8\mu\text{m}$ and $s=0.7\mu\text{m}$.
- Figure 6.17:** H_x field profile, for the TM_{01} mode, along the x-axis, in the centre of the InGaAsP region, for different values of the rib height, at a separation, $s=0.7\mu\text{m}$
- Figure 6.18:** H_x field distribution of the TM_{11} mode of the mode polarization splitter, for $d=0.8\mu\text{m}$ and $s=0.7\mu\text{m}$,
- Figure 6.19:** Variation of the attenuation constant for the TM modes, of the polarization mode splitter, with the increase of the rib height for different values of the separation, s .
- Figure 6.20:** Schematic representation of the cross section of a metal-clad optical fiber with core radius r_{co} . The dielectric core medium with dielectric constant $\epsilon_{co}=2.16$ is surrounded by an infinite metal medium (shaded area) with complex dielectric constant $\epsilon_{cl}=-34.5+j8.5$.
- Figure 6.21:** Variation of the effective indices with the dielectric core radius of the metal-clad optical fiber for the TM polarized modes.
- Figure 6.22:** Optical field distribution and axial field profile (insert) for the fundamental TM_{00} optical mode of the metal-clad optical fiber, $r_{co}=0.12\mu\text{m}$.
- Figure 6.23:** Variation of the ratio of the dielectric core to dielectric/metal interface field intensity for the TM_{00} optical mode and the ratio of the dielectric/metal interface to dielectric core field intensity of the TM_{01} optical mode, with the core radius, r_{co} .
- Figure 6.24:** Optical field distribution and axial field profile (insert) for the higher order TM_{01} optical mode of the metal-clad optical fiber.
- Figure 6.25:** Variation of the normalized attenuation constants for the TM polarized modes for the metal-clad optical fiber.
- Figure 6.26:** H_x field distribution for the a) TM_{10} and b) TM_{20} modes for the metal-clad optical fiber.
- Figure 6.27:** Variation of the effective indices of the two TM polarized modes with the mesh refinement for core radius, $r_{co}=0.2\mu\text{m}$.
- Figure 6.28:** Variation of the normalized attenuation constants of the two TM polarized modes with the mesh refinement, for core radius, $r_{co}=0.2\mu\text{m}$.
- Figure 6.29:** Variation of the effective index with the core radius, r_{co} , for the TE polarized modes of the metal-clad optical fiber.
- Figure 6.30:** Optical field distribution and axial field profile (insert) for the fundamental TE_{00} optical mode of the metal-clad optical fiber.
- Figure 6.31:** Optical field distribution and axial field profile (insert) for the higher order TE_{01} optical mode of the metal-clad optical fiber.

Figure 6.32: Variation of the attenuation constants for the TM polarized modes for the metal-clad optical fiber.

Figure 6.33: H_y optical field distribution for the a) TE_{10} and b) TE_{20} modes for the metal-clad optical fiber.

Acknowledgements

I would like to express my deepest gratitude to my two supervisors, Professor K.T.V. Grattan and Dr. B.M.A. Rahman, for their assistance, guidance and support throughout the project and the writing up of this thesis.

I am grateful to the Committee of Vice-Chancellors and Principals of the Universities of the UK, for the financial support of my studies by the "Overseas Research Awards Scheme".

I would also like to express my appreciation to my wife for her help and encouragement over the years.

Last but not least, my thanks are due to my family for their support, and my colleagues for the enjoyable atmosphere. Also, many thanks to the secretarial and technical staff of the Electrical, Electronic and Information Engineering Department who never denied to offer any help.

Declaration

I grant powers of discretion to the University Librarian to allow this thesis to be copied in whole or in part without further reference to the author. The permission covers only single copies made for study purposes, subject to normal conditions of acknowledgement.

Abstract

The recent advances in lightwave technology have revealed the need for the accurate modelling of a range of optoelectronic devices, via efficient computer algorithms. The characterization of optical waveguides, which are the key elements in integrated optics design, requires the accurate determination of the impact of various material parameters and fabrication tolerances, for example. During the early years of the development of the field, the estimation of loss and gain was not considered critical, since it was maintained at low levels, due to the simplicity of the structures and the properties of the materials. The loss and gain analysis is becoming of considerably greater importance nowadays, with the introduction of new laser technology and integrated optics design which has enabled the fabrication of complicated structures, where various metallic elements and active regions are combined in a large scale integration.

The finite element method, which is a very popular numerical approach for the solution of many engineering problems, is currently recognized as a very powerful tool for the analysis of several optical waveguide structures, particularly structures with arbitrary shapes, index profiles, nonlinearities and anisotropies. Most of the formulations used in the finite element method are restricted to structures without modal loss or gain. The H_t vector formulation, defined in terms of the transverse magnetic field components, which was recently introduced for such analysis though it is considered accurate, may result in an increase of the computing time, due to the involvement of complex matrices and the limitation of efficient solvers. Therefore, more efficient algorithms are required, especially in the cases where the optical waveguides suffer small loss or gain, which is common in most of the practical applications considered.

In this work, a finite element analysis employing the H-field formulation, with the aid of the perturbation technique, has been developed to calculate the modal loss or gain for several different types of optical waveguides. Further, a semi-analytical approach has also been developed and used to obtain the complex propagation constant of simple optical waveguides from the solution of the complex transcendental equation and the use of the effective index approach. The accuracy limit of the perturbation technique, which is limited to structures with low to medium loss or gain is also examined. An approximate approach for the calculation of the modal loss or gain, in terms of the mode confinement factor has also been employed for certain types of optical waveguides.

The above approaches are used for the solution of several planar optical waveguides and optical waveguides with two-dimensional mode confinement. The results obtained were compared with previous results for some of the structures examined, and found to be in good agreement. Finally, the finite element approach with the introduction of a perturbation technique has been used for the characterization and optimization of certain types of optical waveguides of practical interest, such as optical polarizers, electro-optic directional coupler modulators and metal clad fibers used in near-field scanning optical microscopy, which enhance surface-plasmon properties.

Symbols and Abbreviations

BEM	Boundary Element Method
BPM	Beam Propagation Method
CW	Continuous-Wave
DFB	Distributed Feedback
DH	Double Heterostructure
IEC	Integrated Electronic Circuits
EIM	Effective Index Method
ENM	Equivalent Network Method
FDM	Finite Difference Method
FEM	Finite Element Method
IOC	Integrated Optical Circuits
MAM	Multilayer Approximation Method
MM	Marcatili's Method
MMM	Mode Matching Method
MOL	Method of Lines
NFSOM	Near Field Scanning Optical Microscopy
PMM	Point Matching Method
RAM	Ray Approximation method
TE	Transverse Electric mode
TM	Transverse Magnetic mode
VM	Variational Method
WKB	Wentzel Krammers Brillouin method
α	Attenuation constant
β	Phase constant
γ	Propagation constant

ε	Permittivity
λ	Wavelength in μm
μ	Permeability
π	$\pi \cong 3.141593$
k_0	free space Wavenumber= $2\pi/\lambda$
n_e	effective index= β/k_0

(Throughout this work, an American spelling convention is used, for consistency with published material by the author).

1

Introduction

1.1 Historical Development of Lightwave Technology

The phenomenon of the guidance of light along transparent cylinders by multiple total internal reflections had been observed and used in the ancient world by Greek and later by Venetian glassblowers, in fabricating their decorative glassware. In fact, the basic techniques used then form an important aspect of present-day fiber optic technology. The earliest recorded scientific demonstration of light confinement, was given by John Tyndall at the Royal Society in England in 1870, where he used an illuminated vessel of water and showed that, when a stream of water was allowed to flow through a hole in the side of the vessel, light was conducted along the curved path of the stream (Kapany, 1967). Ten years later, in 1880, Alexander Graham Bell invented the “photophone”, a device that varied the intensity of sunlight incident upon it in response to the amplitude of speech vibrations. The light variations were reconverted into electrical signal and then into sound, at the receiver end, via a selenium detector. Although the photophone was impractical due to propagation losses, it provided the idea for transmission of signals over a specified distance by

modulation of an optical wave: in other words, the concept of optical communication. This brought new ideas in the early years of this century, and in 1910 Hondros and Debye presented the first form of an optical waveguide, the dielectric circular rod, in an attempt to guide electromagnetic waves through a dielectric medium. The dielectric losses of the non-radiative modes propagating along the dielectric circular rod, were computed much later, by Elsasser (1949).

The development of glass fibers of high refractive index surrounded by air or glass of lower refractive index, in the mid-50s, led Kapany to first apply the term “fiber optic”, which he defined as *the art of the active and passive guidance of light (rays and waveguide modes), in the ultraviolet, visible, and infrared regions of the spectrum, along transparent fibers through predetermined paths* (Kapany, 1967). A few years later, Snitzer and Osterberg (1961) recorded dielectric waveguide modes in the visible region of the spectrum of various optical fibers and Kapany and Burke (1961) investigated the coupling phenomenon in adjacent optical fibers. These observations were followed by further work in the field, which established the use of optical fibers in long distance telecommunications (Kao and Hockham, 1966).

Along with the research for higher transmission capacity, larger bandwidth and lower losses in optical fibers, some other major developments were achieved in the 1960s, which revolutionized lightwave technology and telecommunication industry. In 1960, T.H. Maiman first demonstrated laser action in ruby, by applying Einstein’s ideas for stimulated emission, dated back to 1917. This invention had given birth to the laser technology, a science dealing with the generation of coherent light in small but powerful beams, which are extremely directional. Soon afterwards, some other groups (Hall *et al.*, 1962; Nathan *et al.*, 1962; Holonyak and Bevacqua, 1962; Quist *et al.*, 1962), obtained laser action in GaAs p-n junctions. That development, which was then associated with the observation of a dielectric waveguide mode of light propagation in p-n junctions (Yariv and Leite, 1963; Bond *et al.*, 1963), initiated new research activity for understanding the laser phenomenon, achieving it in new semiconductor materials, such as $\text{InP}_x\text{As}_{1-x}$ (Alexander *et al.*, 1964) and IV-VI compounds (Butler *et al.*, 1964), and applying it in the design of various devices. These first lasers, which comprised a single semiconductor and are referred to as homostructure injection lasers (Casey and Panish, 1978), had a common discouraging feature, that the usual threshold current density was very high at room temperature. This diminished the interest in such work in the field by 1965, since considerable reduction of the threshold current density had not

been achieved until then. The achievement of low-threshold room-temperature lasers (Hayashi *et al.*, 1969; Panish *et al.*, 1969), in a structure where a layer of semiconductor with a relatively narrow energy gap is sandwiched between two layers of a wider energy gap semiconductor, called a heterojunction, boosted the research interest. It was followed by the development of more interesting heterostructure laser structures, such as Double-Heterostructure (DH) lasers, in which continuous-wave (CW) lasing operation had been achieved at room temperature with much lower threshold current intensity (Alferov *et al.*, 1970; Hayashi *et al.*, 1970). The implementation of low-loss silica fibers (Miya *et al.*, 1979), and the use of lasers as a CW coherent source of light at optical frequencies, in the range 1.3-1.55 μm , where such fibers exhibit minimum dispersion, had given a new dimension in the field of optical communication.

The invention of the laser gave an enormous stimulus to the entire field of optics. The requirement for more compact and more economical optical transmission systems, less vulnerable to environmental changes, in order to replace the existing laser beam transit in a system via mirrors and lenses, then emerged. These requirements stimulated the development of improved thin-film fabrication techniques and studies on new materials for both active and passive function (Osterberg and Smith, 1964; Shubert and Harris, 1968), and led eventually to the idea of *integrated optics*. As a concept, it was first visualized by Miller (1969), that *the new art that would facilitate isolating the laser circuitry assembly from thermal, mechanical, and acoustic ambient changes through small overall size, and would result in economy*. Integrated optics is based on the guiding of electromagnetic energy at optical frequencies by thin films, which can be placed one next to the other on a single substrate, forming an optical system meeting the requirements mentioned above. Semiconductors had played an important role in the effort to develop monolithic integrated optical circuits (IOC), that would serve as miniature optical counterparts of microwave devices and networks. The pioneering days of integrated optics, in the early 1970s were characterized by successive efforts in developing devices that were compatible with the technology of integrated optics. The problem of coupling laser beams into planar guides was solved by Tien *et al.* (1969), by the prism-coupler, while active components in integrated optics had also been studied with developments in acousto-optic (Kuhn *et al.*, 1971), magneto-optic (Tien *et al.*, 1972) and electro-optic (Martin, 1973) techniques, and the invention of the distributed feedback laser (DFB) principle (Kogelnik and Shank, 1972).

The period that followed initiated new activities, which aimed as an ultimate goal for the replacement of the existing integrated electronic circuits (IEC) by integrated optical circuits (IOC), in order to benefit from the advantages of larger bandwidth and negligible sensitivity to interference by natural or man-made electromagnetic fields of lower frequencies, that optical communication systems can offer.

Recent advances in integrated optics demonstrated a rich variety of optical components and devices, such as directional couplers, Y-branches, waveguide crossings, Bragg gratings, transmission gratings, acousto optical filters, optical filters modulators, optical amplifiers and others (Tamir, 1979). Also, recent technological achievements such as laser copiers, laser printers, laser bar-code readers, CD players and other, have entered our households and have become part of everyday life.

The development of more sophisticated integrated optical communications systems requires a knowledge of the properties of the basic elements, such as the optical waveguides. This can more conveniently be achieved by the implementation of accurate analytical or numerical approaches for the determination of the propagation characteristics of such structures, via the solution of the Maxwell's equations. In the present work, several approaches have been developed, for the determination of the propagation characteristics of different types of optical waveguides and optoelectronic devices, with a focus on their loss or gain properties. Throughout the work, uniform optical waveguide structure along the direction of propagation has been assumed.

1.2 Optical waveguides

Optical waveguides are the structures used to trap the light locally and guide it in waveguides such as optical fibers or in optical integrated circuits, in other words, the “wires” which carry optical signals in the interconnections between various optoelectronic devices. They can be classified approximately into optical waveguides for optical integrated circuits and optical fibers (optical waveguides, with a circular cross-section), which are mostly used for optical communication.

The simplest type of optical waveguide, is the asymmetric planar slab waveguide, shown in Fig.1.1, where a thin film is loaded with dielectric material with higher refractive index, n_f , than the substrate, n_s , and the upper cladding, n_c , which is usually air, having the lowest refractive index. Under these conditions, and depending on the angle of incidence, a light beam is confined by total internal reflection at the film-substrate and film-cladding interfaces, and therefore guidance is achieved in the z -direction.

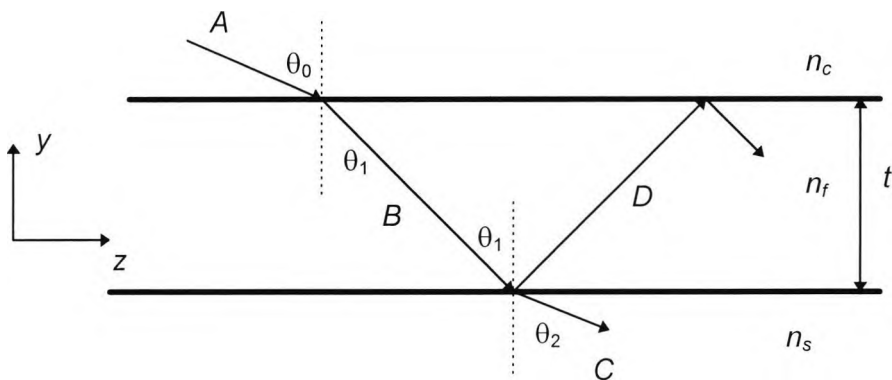


Fig.1.1 Reflection and refraction of a light ray in a planar slab optical waveguide

A planar slab optical waveguide may support a finite number of guided modes, which is supplemented by an infinite continuum of unguided radiation modes. The solution for both the modes can be obtained via Maxwell's equations, which are discussed in detail in Sections 2.2 and 3.2.1, where the problem is considered as a boundary value problem and the solution matches the boundary conditions at the film-substrate and film-cladding interfaces. The guided modes can also be considered from the geometrical (or ray) optics point of view, where the propagation of the light fields is described by defining rays as the lines that cross the surfaces of constant phase of the

light field at right angles (Marcuse, 1991). For the planar slab optical waveguide it may be assumed that a light ray in a homogeneous medium follows a straight path.

By considering the cladding-film interface of the planar slab optical waveguide, and a light ray, A , incident at an angle θ_0 , between the light field normal and the normal to the interface, as shown in Fig.1.1, Snell's law of refraction can be expressed as (Tien, 1971):

$$\frac{\sin \theta_0}{\sin \theta_1} = \frac{n_f}{n_c} \quad (1.1)$$

where, θ_1 , is the angle of the refracted light ray, B , with the normal to the interface.

For the film-substrate interface, Snell's law can then be expressed as:

$$\frac{\sin \theta_1}{\sin \theta_2} = \frac{n_s}{n_f} \quad (1.2)$$

where θ_2 , is the angle of the refracted in the substrate region, light ray C , with the normal to the interface.

Under the above conditions, since $n_f > n_c$, an incident light ray A , is refracted into the film region following the path of ray B as shown in Fig.1.1. The route of the light ray B which is then incident by an angle θ_1 on the film-substrate interface, is determined by a *critical angle*, θ_c , expressed as (Adams, 1981):

$$\theta_c = \sin^{-1} \left(\frac{n_s}{n_f} \right) \quad (1.3)$$

If $\theta_1 < \theta_c$, then the light ray B is refracted at an angle θ_2 , given by Snell's law (1.2), following the ray path C , and *radiation modes* of the light wave are observed. When the incident angle θ_1 is greater than the critical angle θ_c , then total reflection occurs and the light ray follows the path D , which in turn is either reflected or refracted, depending again on the analogous critical angle of incidence on the film-cladding interface. When continuous total reflections occur inside the film region between the two interfaces, the light is trapped in the film and propagates in a *zig-zag* path. This

case corresponds to a *guided mode* of propagation of the light wave along the z -direction.

1.2.1 Guided modes in a planar slab optical waveguide

When guided modes occur in a planar slab optical waveguide, the light energy is trapped in the film as the wave is totally reflected back and forth between the two film boundaries. The zig-zag wave motion, shown in Fig.1.1, can be described by a picture of two superimposed uniform plane waves with wave normals following the zig-zag path. The light wave in the waveguide mode can be defined as TE or TM wave, depending whether the Electric or Magnetic field, respectively, is perpendicular to the plane of incidence. The two repeated (incident and reflected) wave vectors of the light wave can be decomposed into vertical and horizontal components, where the horizontal components determine the wave velocity parallel to the film and the vertical components determine the field distribution across the thickness of the film. The wave propagation constant, β , and the related phase velocity, v_p , of the light wave can be expressed as (Kogelnik, 1990):

$$\beta = \frac{\omega}{v_p} = kn_f \sin \theta_1 \quad (1.4)$$

where, ω , k and θ_1 are the angular frequency, the wavenumber and the reflection angle of the wave respectively.

The condition for all the multiple reflected waves to add in phase is that the total phase change experienced by the plane wave for it to travel one round trip, up and down across the film, should be equal to $2m\pi$, where m is an integer. The phase change for the plane wave to cross the thickness, t , of the film twice (up and down) is then $2kn_f t \cos \theta_1$. Additionally, the wave suffers phase shifts, due to total reflection, of $-2\Phi_c$ and $-2\Phi_s$ at the upper film-cladding and lower film-substrate interfaces, respectively (Tien, 1971).

From the above relationships, the self-consistency condition for a guided mode in a planar slab optical waveguide can be expressed as:

$$2kn_f t \cos \theta_1 - 2\Phi_c - 2\Phi_s = 2m\pi \quad (1.5)$$

Equation (1.5) is also known as the eigenvalue or the transcendental equation and it is being analysed in the present work, in terms of Electromagnetic Theory, via Maxwell's equations, described in detail in Section 3.2.2.

It should be noted that in a total reflection condition, the incident wave is related linearly to the reflected wave by a reflection coefficient R , which depends on the angle of incidence and the polarization of light, and can be defined in terms of the Fresnel formulas (Kogelnik, 1990). By considering the film-cladding interface the Fresnel formulas for each polarization can be expressed as:

$$R_{TE} = \frac{n_f \cos \theta_1 - \sqrt{n_c^2 - n_f^2 \sin^2 \theta_1}}{n_f \cos \theta_1 + \sqrt{n_c^2 - n_f^2 \sin^2 \theta_1}} \quad (1.6)$$

$$R_{TM} = \frac{n_c^2 \cos \theta_1 - n_f \sqrt{n_c^2 - n_f^2 \sin^2 \theta_1}}{n_c^2 \cos \theta_1 + n_f \sqrt{n_c^2 - n_f^2 \sin^2 \theta_1}} \quad (1.7)$$

Similar expressions can also be derived for the film-substrate interface, where the refractive index of the cladding n_c is substituted by the refractive index of the substrate, n_s .

As long as the angle of incidence, θ_1 , is less than the critical angle, θ_c , partial reflection occurs and the reflection coefficient is real. As soon as the critical angle is exceeded, then $|R|=1$, and total reflection of the light occurs. The reflection coefficient becomes complex and can be expressed as (Kogelnik, 1990):

$$R = \exp(2j\Phi) \quad (1.8)$$

where Φ is the phase-shift imposed on the reflected light, defined in the total reflection condition (1.5). By considering again the film-cladding, by using Fresnel's formulas for each polarization, the phase shift can be expressed as:

$$\Phi_{c(TE)} = \frac{\sqrt{n_f^2 \sin^2 \theta_1 - n_c^2}}{n_f \cos \theta_1} \quad (1.9)$$

$$R_{TM} = \frac{n_f^2 \sqrt{n_f^2 \sin^2 \theta_i - n_c^2}}{n_c^2 n_f \cos \theta_i} \quad (1.10)$$

Similar expressions can also be derived for the film-substrate interface, by substituting the refractive index of the cladding, n_c , with the refractive index of the substrate, n_s .

1.2.2 Guided modes for the 3-D optical waveguide

In the previous section, the guided modes for a planar slab optical waveguide were examined, they being purely TE or TM. In 3-D optical waveguides the guided modes can be described as hybrid modes, which are normally a combination of a TE ($E_z=0$) and a TM mode ($H_z=0$). Generally these are divided into the E_{pq}^x mode (in which the main components of the electromagnetic field are E_x and H_y) and the E_{pq}^y mode (in which the main components of the electromagnetic field are E_y and H_x), depending on whether the main component of the electric field is in the x direction or in the y direction. The subscripts p and q denote the total number of extrema that appear in the distribution of the dominant electric fields in the x and y directions respectively.

1.3 Solutions to optical waveguide problems

The propagation characteristics of optical waveguides can be calculated by solving Maxwell's equations, which is not an easy task. Some optical waveguides have complex structures, anisotropic or nonlinear optical materials, or materials with complex refractive index such as semiconductors and metals, or arbitrary refractive index distribution. The above problems can be solved with the development of various methods for the analysis of optical waveguides, which can be classified into analytical approximation solutions and numerical solutions using computers.

Analytical solutions can only be obtained for stepped 2-D optical waveguides and stepped optical fibers, where the refractive index changes gradually in the thickness and the radial direction respectively. Such solutions use the Ray Approximation Method (RAM) (Qiao and Wang, 1992), and the Wentzel, Kramers Brillouin (WKB) method (Srivastava *et al.*, 1987).

For 3-D optical waveguides, which are widely used in optical integrated circuits (OIC), and non-axisymmetrical optical fibers, the above solutions do not satisfy the boundary conditions, even for homogeneous media, and therefore, hybrid-modes analysis is required. However, the analytical approximation solutions do not treat the above waveguides as hybrid modes, but more often as purely TE or TM modes. For the above reason, their accuracy deteriorates near the cut-off frequency.

The numerical solutions obtained can be classified into two groups. These are the domain solutions, also known as differential solutions, in which the whole domain of the optical waveguide is considered as the operational area, and the boundary solutions, also known as integral solutions, which include only the boundaries as the operational area. The Variational Method (VM), the Finite Element Method (FEM), the Finite Difference Method (FDM), and the Multilayer Approximation Method (MAM) are some of the most commonly used domain solutions, while, the Boundary Element Method (BEM), the Point Matching Method (PMM) and the Mode Matching Method (MMM), are typical boundary solutions (Koshiya, 1992a).

1.3.1 Analytical approximation solutions

Analytical approximation solutions are very widely used in many applications for the determination of the propagation characteristics of various types of optical waveguides, with relatively simple geometry. Such solutions are the Marcatili Method (MM), the Effective Index Method (EIM), and the Equivalent Network Method (ENM).

1.3.1.1 Marcatili's Method

In the Marcatili's method (MM), (Marcatili, 1969), the field in a rectangular dielectric waveguide (a dielectric rod with rectangular cross-section, surrounded by four different dielectrics of lower refractive indices), is approximated to the fields in two slab waveguides, obtained by extending the width and the height of the rectangular core to infinity. The rectangular dielectric waveguide is assumed to support a well-confined mode, therefore, only the regions on each side of the dielectric rod are considered to carry appreciable amount of field, and the problem is then decoupled in two slab waveguides, one at each transverse direction. The field in the centre region is assumed to vary sinusoidally, while that in the substrates is considered to decay exponentially. Transcendental equations (Tamir, 1990), shown in Section 3.2.2, are then derived for each transverse direction, each of them giving a transverse propagation constant. The axial propagation constant of the waveguide is then calculated from the transverse propagation constants, obtained by solving simultaneously the two transcendental equations. In a similar way, the MM can also be applied to the solution of the directional coupler problem. The above approach works well in the far-from cut-off region but gives poor results in the near-cut-off region (Chiang, 1994). Kumar *et al.* (1983) reported an exact scalar formulation for a rectangular-core structure, with similar modal fields as those used by Marcatili, and by using perturbation techniques, they obtained propagation characteristics of practical integrated-optical structures, with greater accuracy than Marcatili.

1.3.1.2 The effective index method

The Effective Index Method (EIM), is an improvement of the Marcatili's method, proposed by Knox and Toullos (1970). In this approach, the core of a rectangular

dielectric waveguide is replaced by a an equivalent slab with an effective index obtained from another slab. The dielectric core is decoupled into two slab waveguides, one at each transverse direction, and the transcendental equation is first solved in one direction, by applying the appropriate boundary conditions. The effective index calculated is then used as the refractive index of the centre region in the solution of the transcendental equation in the other transverse direction, which is obtained by applying boundary conditions in that direction. The new effective index obtained corresponds to the overall effective index of the waveguide. The EIM and the Complex EIM, which is applied to waveguides incorporating loss or gain, are discussed in detail, in Chapter 3.

The above approach does not give satisfactory results near the cut-off region, therefore, several techniques have been proposed to improve the accuracy of the method. Zhou and Itoh (1982) used the approach for a trapped image guide, where they replaced the original waveguide by an equivalent structure. Then they imposed the transverse resonance at the dielectric-air interface, to include the free-space regions of the guide and solved the problem in terms of the surface impedances in an approximate manner, with an improved accuracy at low frequencies. Chiang (1996) derived an expression for the error in the propagation constant of a rectangular waveguide, which occurs by using the conventional EIM, and proposed a new effective-index approach with a built-in perturbation correction of the above error, suitable for rectangular dielectric waveguides, channel waveguides, strip waveguides and arrays of such waveguide structures. Chiang *et al.* (1996), proposed a dual effective index approach, in which, by combining two solutions, corresponding to two different ways of applying the EIM to the waveguide, they achieved the elimination of the errors occurring by applying each solution separately.

1.3.2 Numerical approximation solutions

Most of the numerical solutions are concerned with methods of finding numerical solution to the Helmholtz's wave equation which can be derived directly from Maxwell's equations, and can be expressed as (Koshiba, 1990):

$$\nabla^2 \Phi + k^2 \Phi = 0 \quad (1.11)$$

The above equation is valid over the cross section, Ω , of an arbitrarily shaped optical waveguide, bounded by the closed curve, C , and is subject to the boundary conditions (described in detail in Section 2.2.2.1), which can be of Dirichlet type:

$$\Phi = 0 \quad (1.12)$$

on C , or Neumann type:

$$\frac{\partial \Phi}{\partial \mathbf{n}} = 0 \quad (1.13)$$

on C , or can even be the complex type, where Φ is the corresponding field (\mathbf{E} or \mathbf{H}), k is the wavenumber, and \mathbf{n} is the normal unit vector.

The above had been a central problem in boundary-value theory for many years, but the possibility of a numerical solution had received attention only after the availability of fast computers with large memory capacity. It is a very practical problem in the microwave regime, which leads to the determination of the cut-off frequencies and field distribution of one or more waveguide modes. Like all the boundary problems, it is of the classic eigenvalue type, and most of the approaches yield standard forms of matrix-eigenvalue problems, which can be solved by using well established matrix algorithms (Davies, 1972).

1.3.2.1 Selection of the numerical method

The selection of the numerical technique, for the solution of a particular optical waveguide problem, should be made according to the requirements of the structure under investigation. Some factors that should be taken into consideration, based on reviews by Davies (1972), Ng (1974), Saad (1985) and Chiang (1994), are the following:

a) the shape of the cross section, Ω , whether it is curved or polygonal or whether it is convex or non-convex.

b) whether the method can be realized as a computer program, suitable for the solution of a wide range of geometries or whether it has to be written specifically for each region.

- c) whether the dominant mode or the other higher order modes are required.
- d) whether the field distribution is required as well as the cut-off frequency.
- e) whether the method can deal with more than two homogeneous dielectric layers
- f) the accuracy of the method in modelling the dielectric boundaries and regions.
- g) the accuracy of the method for specific frequency ranges, especially near cut-off frequencies.
- h) whether the accuracy of the method is sufficient to distinguish optical modes which are very close together.
- i) the ability of the method to identify and eliminate spurious solutions.
- j) the limitations and assumptions of the approach, for particular cases.
- k) the degree and understanding and involvement required from the user.
- l) the computational efficiency and storage requirements of the method.

1.3.2.2 The Variational method

In the variational approach, a field solution of the optical waveguide problem, usually based on the wave equation (1.1) is assumed, where the unknown parameters are chosen to match the assumed field to the actual field solution. The above solution is then expressed in integral form, in terms of a functional satisfying the boundary conditions of the problem. By minimizing the expression, the stationarity of the functional about the correct solution, with respect to small variation of the field values, is achieved. Then by using trial functions to represent the field solutions, the integral equations are reduced to a set of linear equations which can be solved by standard numerical techniques. The accuracy of the results depends on the choice of the trial functions (Goyal *et al.*, 1993), which must be sufficiently differentiable and satisfy the boundary conditions (Wexler, 1969). Several types of trial functions have been proposed, such as Gaussian and Hermite-Gaussian functions (Austin, 1984; Erteza and Goodman, 1995), or Airy functions (Goyal *et al.*, 1993). The variational method forms the basis of other fundamental numerical techniques, such as the Finite-Element and the Finite-Difference methods, which are discussed in the following sections. Mao and Huang (1992) have proposed an efficient scalar variational approach, with vector correction using the perturbation technique.

1.3.2.3 The Finite Difference Method

The finite difference method (FDM) (Wexler, 1969), is one of the oldest and perhaps the most commonly used numerical techniques for the solution of boundary value problems. In the above approach, a finite cross-section is defined by enclosing the optical waveguide under investigation in a rectangular box, where the side walls may be either electric or magnetic walls, in order to include coupled structures. At the boundaries of the enclosing rectangular box, the fields are assumed to be negligibly small, therefore infinite elements with an associated decay factor can be introduced, to approximate the infinite exterior region. The cross-section of any non-homogeneous optical waveguide is implemented by a rectangular grid, where it is essential that all the dielectric boundaries must lie on points of the above grid. By considering any arbitrary nodal point of the rectangular grid, the corresponding nodal field value can be expressed in terms of the neighbouring nodes, in the two transverse directions, by the five-point formula (Davies, 1989) of finite differences, which is based on the Taylor series expansion. The Helmholtz wave equation, or a variational expression, can be arranged into a set of two coupled wave equations, one for each transverse direction H_x and H_y , which can be then discretized in the five-point finite difference form. By imposing the correct continuity conditions of the fields between the adjacent cells of the grid, an eigenvalue matrix equation, of the type $Ax - \lambda x = 0$, can be formed, which can be solved by using sparse matrix techniques.

The solution of the wave equation, in terms of the longitudinal components, E_z - H_z , by the FDM, has also been demonstrated in the past (Hornsby and Gopinath, 1969), but such solution yields non-physical spurious modes, because it does not satisfy Maxwell's divergence condition. Therefore, solutions in terms of the transverse field components (Schweig and Bridges, 1984; Lusse *et al.*, 1994), which automatically satisfy the above condition, are preferred nowadays.

In some cases, (Bierwirth *et al.*, 1986) the FDM analysis includes modes which are below cut-off. These non-propagating modes can be modelled as complex waves (Clarricoats and Slinn, 1965) with an imaginary propagation constant (Strube and Arndt, 1985). The decay factor modelling of the exterior region of the waveguide, at the above frequency range, becomes difficult to apply, and therefore in such cases it is

preferred to increase the size of the rectangular box, enclosing the structure, in order to reduce the influence of the above modes (Bierwirth *et al.*, 1986).

Recently, Benson *et al.* (1994), extended the FDM to the study of structures with regions having optical loss or gain, like semiconductor lasers, by using perturbation techniques to evaluate the complex propagation constant and field profiles.

1.3.2.4 Point matching method

The point matching method (PMM) can be classified as a typical boundary solution of the optical waveguide problem, and as an approach in which the electromagnetic field is expanded in a series of orthonormal functions (basis functions). It was first proposed by Goell (1969) for the solution of the rectangular optical waveguide, where the radial variation of the longitudinal electromagnetic fields of the modes can be represented by a series of circular harmonics. In the above approach the electromagnetic fields inside the waveguide core are expressed by a sum of Bessel functions and their derivatives, with the fields outside the core by a sum of modified Bessel functions and their derivatives, both multiplied by trigonometric functions. Solutions can be obtained by imposing boundary conditions of the above fields at a finite number of points, named matching points, placed symmetrically along the boundary of the waveguide core. The matching of the tangential electromagnetic fields leads to continuity equations, arranged into matrix form, from which the eigenvalues and the expansion coefficients can be determined.

The above approach can be applied to dielectric waveguides having arbitrary cross sections, composite dielectric waveguides having multiple dielectric materials and coupled dielectric waveguides composed of multiple waveguides. The number of matching points lies only on the boundaries of the structures, and therefore, less computational time and memory capacity are required for the solution of the problem, compared to the use of other numerical approaches, such as the FEM and the FDM, where nodal points are required, not only for the boundaries, but for the whole waveguide cross section, as well. However, it is difficult to apply the method to structures with three-dimensional boundary surface, or to structures with an index

distribution within the waveguides, such as graded index fibers (Yamashita and Atsuki, 1990).

Cullen *et al.* (1971) improved the approach, by rotating the grid of equi-angularly-spaced matching points, in order to place matching points at the corner of a rectangular dielectric waveguide, to reduce the overall mismatch at the boundary. Bates *et al.* (1973), in a review of the method, examined the validity of the expansions in the approach, the accuracy and the convergence as the number of matching points increases.

1.3.2.5 The boundary element method

The boundary element method (BEM) (Morita, 1990) is a computer technique, where the basic equations are boundary integral equations, which are solved numerically, by dividing the integration domain into a set of elements. The approach has similar features with the FEM, but instead of taking unknown nodal field values throughout the waveguide region, as in the FEM, in the BEM the unknowns are taken only along the boundary.

The solution of the problem, is accomplished by first deriving integral equations with respect to unknowns taken on the boundaries. The integral equations are then discretized to linear equations, to obtain numerical solutions, which are again expressed in integral forms in order to represent the values of various physical quantities. Integral representations play a key role throughout the process, not only in the derivation of integral but also in the evaluation of the physical quantities. Various integral representations can be used, depending on the particular case, with the Green's formula being the most popular for many applications.

The BEM offers the ability to deal with odd-shaped boundaries, as the FEM, but with far less number of unknowns, since unknown values are considered only along the boundary, while in the FEM, these are considered for the whole waveguide cross-section, less memory storage and less computational time are required. Unlike the FEM, the BEM incorporates automatically the boundary conditions at infinity and no infinite elements are required. Additionally, both approaches may have the same discretization schemes, thus enabling the FEM to be used for the each case. The BEM is limited though to homogeneous structures, while some unphysical solutions, known

as resonant solutions, may be involved. Another drawback of the BEM is that it may require some analytical treatment and more programming, in some cases where the Green's function has some singularities with respect to the integral equations. Also the BEM formulation yields to dense matrices, while in the FEM they remain sparse, therefore offering a more efficient matrix solution.

Zhu and Zhang (1988) reported a modified BEM for the solution of waveguide problems, named the eigenweighted boundary integral equation method, in which a fictitious boundary and a set of eigenfunctions satisfying the boundary conditions were introduced, but they reduced the weighting of eigenfunction in only one term, rather than an infinite series in modified Green's functions, thus increasing the computational efficiency. Nallo *et al.* (1995) developed a BEM formulation, for cylindrical dielectric structures, by expressing the fields inside and outside the cylinder by means of free space dyadic Green's functions, enabling a great flexibility in the choice of basis functions for the unknowns, thus enlarging significantly the class of algorithms for the numerical solution of the integral equations.

1.3.2.6 The mode matching or equivalent network method

The mode matching method (MMM) (Pen and Oliner, 1981), which is also known as the equivalent network method (ENM), is an approximate analysis used for the determination of the propagation characteristics of an open dielectric waveguide. In the above approach, the open waveguide structure is considered artificially bounded, therefore the TE-TM coupling and the continuous spectrum distribution at the sides of the waveguide are neglected (Koshiba *et al.*, 1982). The waveguide cross section is viewed in terms of its constituent parts or building blocks, which are usually portions of uniform dielectric layered structures interfaced by dielectric step discontinuities. The fields in the various regions are then expanded in terms of transverse modal expansions over each region, thus resulting in an microwave equivalent circuit representation of the waveguide. The uniform dielectric regions are then represented by uniform transmission lines with their characteristic impedances, and the various step discontinuities are modelled by a set of transformers, where equivalent network admittances take into account the effects of the outer region. Therefore, it is possible to model the whole spectrum of open waveguide structures as a cascade of uniform regions and step discontinuities. By applying boundary conditions to the above modes

and a transverse-resonance condition, which requires that, for a particular mode, the total admittance seen at any of the ports is zero, the dispersion relation for the propagation constant can be obtained.

For more accurate analysis of open waveguide structures, which exhibit continuous and discrete modal spectra, the continuous spectrum should be discretised by suitable basis function expansions, rather than by artificially bounding the structure (Dagli and Fonstad, 1987). Additionally, the effects of TE-TM coupling at the sides of such structures, must be taken into account. Koshiba and Suzuki (1985) reported a vectorial wave analysis of optical waveguides with a rectangular structure by the ENM, where by taking into consideration the discrete-continuous spectrum coupling and the TE-TM coupling, they calculated the propagation characteristics. Dagli and Fonstad (1987) extended the ENM to GaAs Rib waveguides, directional and three guide couplers, by cascading the models of single waveguide structures.

1.3.2.7 The spectral index method

The spectral index method (SIM), is a relatively fast and accurate approach, in which the wave equation is expressed in terms of Fourier transforms and Fourier series. It has been applied in the solution of the simple semiconductor rib waveguide (Kendall *et al.*, 1989; Stern *et al.*, 1990) and the strip loaded directional coupler (Burke, 1990). Recently, Pola *et al.* (1996) have extended the approach to multiple rib waveguides.

By considering a simple semiconductor rib waveguide, the SIM replaces the original rib structure by an effective structure, by displacing the actual physical dimensions to new ones on which the optical field is zero, in order to model the penetration of the optical field into the cladding. The method consists of expanding the fields in terms of local modes and matching the fields along the base of the rib. The **E**- or **H**-field (depending on the polarization) inside the rib region, is expressed in terms of trial functions, such as cosine and sine Fourier series, representing the symmetric and antisymmetric modes respectively. In the region below the rib, the wave equation is expressed in terms of its Fourier Transform and the problem is reduced to a 1-D slab problem, where the refractive indices of the layers below the rib are represented by their corresponding spectral indices. The equations for the two regions are then linked

via a transfer relation and a transcendental equation is formed, which determines the propagation constant of the waveguide. In order to overcome the field discontinuities in the rib region, an effective width is introduced, while in the Fourier transform for the region below the rib, the evanescent regions are expressed by imaginary spectral indices.

Although the method requires much less computational time than other numerical methods, such as the FDM and the FEM, in the presence of dielectric corners the electric field exhibits a singular behaviour produced by its transverse components. This makes the design of rapidly converging numerical algorithms for vector mode field computations difficult (Sudbo, 1992).

1.3.2.8 The method of lines

The method of lines (MOL) is a semi-analytical approach, suitable for the analysis of the hybrid modes of optical waveguide structures. The method was first applied to microwave devices by Schulz and Pregla (1981), for the analysis of the dispersion characteristics of isotropic planar waveguides and microstrips. Sherrill and Alexopoulos (1987), proposed a modified version of the method to treat cases having uniaxially anisotropic regions, such as finline/strip configurations on an anisotropic substrate. Rogge and Pregla (1991) applied the method for the analysis of strip-loaded film waveguides and rib waveguides, and Gerdes *et al.* (1991) to optimize broad-band electro-optic modulators with asymmetric co-planar strip electrodes. Also, Pregla (1993) used the approach for the analysis of multilayered gyrotropic waveguide structures, where a complex permittivity and susceptibility were considered for the magnetised gyromagnetic and gyroelectric media, respectively. Recently, Berini and Wu (1996) reported the application of the MOL, in modeling optical waveguides with lossy inhomogeneous anisotropic media.

In the MOL, the optical waveguide is enclosed in a rectangular box, with electric or magnetic walls at the sides, satisfying the boundary conditions of the required polarization. The waveguide cross section is then divided into a set of equidistant lines along the one transverse direction, resulting to the discretization of the electromagnetic fields, which are calculated on the lines along the other transverse direction. By substituting difference operators for the second derivatives of the electromagnetic

wave equations, a system of coupled ordinary differential equations, for each dielectric layer, is obtained. By suitable matrix transformations, the above system is uncoupled and the equations can be solved analytically. Further application of boundary conditions at waveguide discontinuities leads to a matrix equation, from which the eigenvalues can be determined.

The above approach is related to a discrete Fourier transformation, therefore the calculation of the fields on the discretization lines is very accurate. Since the interface conditions on dielectric steps are included, discontinuous field curves can be described accurately (Pregla, 1993). Nevertheless, it is difficult to apply for waveguides with curved boundaries and the accuracy in the near cut-off region is limited to the finite size of the rectangular box, as in the finite-difference method (Chiang, 1994).

1.3.2.9 The finite element method

The finite element method (FEM), (Zienkiewicz and Taylor, 1989; Silvester and Ferrari, 1991) is a relatively new and a very powerful numerical technique, in the analysis of optical waveguide problems, with a wide range of applications in other engineering areas as well. In the above approach, any optical waveguide cross-section can be divided in a patchwork of triangular elements, where the appropriated field components are approximated by polynomial expressions over these elements. Each element can have different dielectric material, which may be, anisotropic, non-linear or lossy. The FEM, which is based on the Ritz-Galerkin approach, converts a continuous system into a discretized model. By applying the variational principle (Davies, 1989) to the functional of the system, the problem reduces to a standard eigenvalue matrix equation, $Ax - \lambda Bx = 0$, which can be solved by applying standard matrix algorithms.

For solutions near the cut-off region, where there field decays slowly and there might be an appreciable field component outside the guide region, infinite elements (Rahman and Davies, 1984a) can be introduced along the outer boundary of the structure, to extend the domain of explicit field representation to infinity. Some vector formulations yield non-physical spurious solutions, because the numerical solution does not automatically satisfy the Maxwell's divergence condition. These spurious solutions can be reduced by the penalty function method (Rahman and Davies, 1984b), or completely eliminated by using the **H**-field formulation in terms of the

transverse magnetic field formulation, known as the H_z formulation (Koshiba *et al.*, 1985a).

The FEM can be used effectively for the analysis of various optical waveguides, with any shape, including 2D and 3D optical waveguides, axisymmetrical and non-axisymmetrical optical fiber, and non-linear optical waveguides. A detailed description of the several variational formulations and the development of the H -field vector formulation is presented in the present work, in Chapter 2.

The FEM is based on the same principles as the FDM, therefore a comparison of the two methods can be attempted. Although in the FDM simpler matrix eigenvalue equations are formed, which are formulated with less computer programming, less computer memory storage and execution time, and the solution is free of spurious modes ($H_x - H_y$ formulation), the above approach cannot be easily applied to structures with odd-shaped boundaries. The triangular elements used in the FEM can give a better fit to such structures and also the change of the density or the order of the elements, in regions where there is more rapid field variation, is performed more easily with the FEM. Additionally, in the FEM, the field is defined explicitly everywhere and this makes for easier manipulation, such as when evaluating spatial derivatives to give related fields (Davies, 1989).

1.3.2.10 The beam propagation method

The research on integrated optical circuits (IOC) and optical planar devices, has emerged from the necessity of calculating the propagation of a light wave in an optical circuit having an arbitrary refractive index distribution. This type of field propagation can be simulated numerically by the beam propagation method (BPM), an approach that was developed in underwater acoustics and seismology before it was adapted to optical waveguide problems by Feit and Fleck (1980). Since then, it has been widely used for analyzing the performance of a light beam propagated in an optical planar circuit that has a nearly stripelike waveguiding structure and in which the refractive index varies smoothly compared with the wavelength. The main features of the BPM are that the electromagnetic fields are Fourier transformed with respect to the direction normal to that of light propagation and that a stepwise method is used for

successively calculating the electromagnetic field along the axial direction (Okoshi and Kitazawa, 1990).

In the BPM, the optical field is transported within one propagation step, from the transverse plane at the longitudinal coordinate z , to the transverse plane at $z+\Delta z$. Calculations are performed, to relate the optical fields at the input and output planes, which are based on the assumption that the dielectric profile within one step, Δz , remains unchanged (Marz, 1994). As the optical field propagates through a medium, it is subject to diffraction due to its wave nature, and the light rays of the wave experience a certain amount of phase shift, depending on their x,y positions. The above influences can be applied one at a time, provided that the space along the path is subdivided into very small sections, Δz . By doing so, the continuous medium can then be realized as a series of lenses separated by short sections of homogeneous space, where the contribution of the lenses in the phase shift is expressed in the solution of the wave equation. For computational purposes, the wave between the lenses can be decomposed into its spectrum of plane waves by applying a Fast Fourier Transform (FFT) algorithm, and then it is reconstructed halfway, $(\Delta z/2)$, before the next lens, by applying the inverse FFT. The above process is repeated for each section along the whole propagation path. The propagation step size Δz , which must be at most one wavelength of the light beam, must ensure that the contribution of evanescent waves, which are part of the plane wave, is negligible, and that the rays associated to the wave, travel parallel to the z -axis, with minimum phase shift (Marcuse, 1991).

The BPM is widely accepted as the most powerful method for the analysis of non-uniform structures but it is not as efficient as the methods specifically developed for the analysis of uniform structures, where discretizations in both the transverse and the longitudinal plane are required (Chiang, 1994). To handle the discretization in the transverse plane, two-dimensional methods can be employed, such as the FDM (Yevick and Hermansson, 1990) and the FEM (Buah *et al.*, 1997). The latter can be used in many devices, such as directional couplers, optical fibers, bent optical waveguides, Bragg and diffraction gratings, tapered optical waveguides and optical Y-junctions. It can also be used in conjunction with other numerical techniques such as the Fresnel approximation (Yevick and Hermansson, 1989).

1.4 Loss and gain in optical waveguides

Several methods for the analysis of optical waveguide problems were being discussed in the previous section, the majority of them dealing with loss-free structures. This has been the case in the early days of the development of integrated optics technology, where dielectric materials used in the fabrication of optical waveguides, regarded as loss-less at the optical frequencies. Recent advances in material science and fabrication technology introduced more complicated waveguide structures and several new integrated optic devices, such as power dividers, optical filters, optical sensors, optical switches, amplifiers, modulators etc. In order to establish a more realistic and accurate model of such devices, the effect of the loss and the gain in the optical waveguides due to the dielectric materials, which becomes more significant with the increase of the complexity of the structures, should be taken into consideration.

As it was mentioned in Section 1.2, an optical waveguide can support a finite number of guided wave modes, where each mode can propagate with a different propagation constant. If the optical waveguide under investigation incorporates lossy media, the wave motion is accompanied by certain attenuation, and can be represented by a complex propagation constant, γ , which can be expressed as:

$$\gamma = \alpha + j\beta \quad (1.14)$$

where, β (rad/m) and α (Np/m) are the phase constant and the attenuation constant, per unit length, respectively.

Lossy media, such as metals or certain types of semiconductor materials (Deri and Kapon, 1991), can be expressed by complex refractive indices, where the imaginary part, n'' , which is negative and also termed as the extinction coefficient (Adams, 1981), represents the amount of loss in the above materials. There is a wide range of optical waveguide applications, where the loss estimation plays important role in the determination of the propagation characteristics, such as, metal-clad optical waveguides (Reisinger, 1973, Kaminow *et al.*, 1974; Yamamoto *et al.*, 1975), surface plasmon-polariton waves guided by thin metal films (Stegeman *et al.* 1983; Zervas, 1991), metal-clad waveguide polarizers (Sun and Yip, 1994; Saini *et al.*, 1995), TE/TM polarization splitters (Albrecht *et al.*, 1990; Soldano *et al.* 1994), metal-clad optical

fibers for near-field scanning optical microscopy (Novotny and Hafner, 1994), optical waveguides chemical or biological sensors (Qing *et al.*, 1996) and other.

In certain applications, such as semiconductor lasers, optical waveguides incorporate active regions, exhibiting gain properties. These can be modelled by complex refractive indices with positive imaginary parts. When the above optical waveguides do not contain any lossy regions, a negative attenuation constant ($-\alpha$) is obtained for the propagating modes, implying gain, therefore, the above negative attenuation constant can also be termed as the gain constant, g . In optical waveguide applications with purely gain properties, such as, semiconductor rib lasers (Benson *et al.*, 1994), ridge waveguide laser amplifiers (Goano *et al.*, 1992), quantum well lasers (Yariv, 1989; Hunziker *et al.*, 1994), erbium doped waveguide amplifiers (Giles and Desurvire, 1991; Di Pasquale and Zoboli, 1993; Torres and Guzman, 1997), and other, the calculation of the gain constant is critical in the determination of the propagation characteristics.

In some optical waveguide applications such as, buried heterostructure laser diodes (Hayata *et al.*, 1986a) and metal-clad ridge waveguide distributed feedback laser diodes (Borchert and Stegmuller, 1990; Wolf *et al.*, 1990), the structures contain both active and lossy media. In the above types of optical waveguides, several design parameters must be taken into consideration, in order to achieve the required overall net gain, such as, the size and the contribution of each active or lossy region.

In the present work, several optical waveguide structures incorporating small loss or gain, as in the most practical applications, have been examined. The propagation and attenuation characteristics of such structures were calculated, by using the finite-element method in conjunction with the perturbation technique and other numerical or semi-analytical approaches described in Chapter 3.

1.5 Aims and objectives of the thesis

The information given so far has provided a background to the work reported in this thesis. The following presents the primary aims of the research undertaken in this field.

1. To investigate established work on the several approaches for the solution of optical waveguide problems, and to justify the use of the finite element method, in the analysis of optical waveguide structures.
2. To investigate the accuracy of an existing finite element package, based on the vector \mathbf{H} -field and the scalar approximation variational formulation, for the analysis of different types of loss-free optical waveguide structures. This has been carried out by applying the above program to the solution of lossless planar, dielectric and rib optical waveguides and comparing the obtained propagation characteristics with previous published work.
3. To develop an accurate and efficient approach for the analysis of optical waveguides incorporating small loss or gain, which are properties exhibited in the most practical applications. A perturbational approach, in conjunction with the scalar finite element method, was considered suitable to accomplish this task, for three main reasons. First, the propagation characteristics of an optical waveguide under the influence of small loss or gain, are a small perturbation of the propagation characteristics of a loss-free structure. Second, the above approach benefits from all the advantages of the finite element method, such as the ability to handle optical waveguides with any cross-section, anisotropy or non-linearity. Thirdly, the solution can be obtained, as it is shown in Chapter 3, by simple matrix multiplication, without solving any complex eigenvalue equation.
4. To extend the perturbation method, to be used with the \mathbf{H} -field vector finite element program, in order to model more accurately, optical waveguides with 2-D confinement and to compare the obtained results with the scalar version of the approach and other previous published work.
5. To develop a semi-analytical approach for the analysis of optical waveguides with simple geometry, incorporating loss or gain, in order to investigate the accuracy and the limit of the perturbation method, for the above structures. A complex effective index approach was implemented, suitable for handling any value of the imaginary part of the refractive index, but applicable only to structures with simple geometry, such planar, rectangular and simple rib waveguides. The two approaches were compared in order to obtain the level of the gain or the attenuation constant, which is the value where

their characteristics begin to diverge and which determines the limit of the perturbation technique.

6. To extend the approach based on finite element method and the perturbation technique, in order to investigate the propagation characteristics of various optoelectronic and integrated optics device applications, such as surface plasmon-polariton devices, semiconductor laser structures, optical polarizers, directional coupler modulators and metal-clad fibers for scanning microscopy.

1.6 Structure of the thesis

The thesis is comprised of work carried out by the author in the use of the finite element method in conjunction with the perturbation technique, and other approaches, such as the complex effective index and the confinement factor method, in the analysis of certain types of interesting optically guiding devices, incorporating loss or gain. The subsequent discussion gives an outline of the carefully structured thesis, beginning with an Introduction to the subject, which is presented in this first chapter.

In the Introduction a brief review of the historical development of the lightwave technology is presented, followed by a general description of the optical waveguide structure in terms of the ray optics theory, a review of the several semi-analytical and numerical approaches for the solution of optical waveguide problems, and a discussion on the importance of the loss and gain consideration in the modelling of certain optoelectronic devices.

In Chapter 2, the relevant theoretical background on the finite element method and its development as a powerful tool dealing with the solution of major engineering applications, are presented. The fundamental mathematical relations, derived from the Maxwell's equations, for the application of the approach in the solution of optical waveguide problems are defined and several variational formulations of a finite element analysis, based on the variational principle, are examined. A detailed analysis of the vector \mathbf{H} -field finite element variational formulation is attempted, where the use of triangular coordinates and shape functions to calculate the eigenvectors and the propagation constants, in uniform, isotropic optical waveguide structures, is considered. Finally, the various problems arising from the application of the approach in open waveguide structures and the generation of non-physical (spurious) solutions

are encountered, and various techniques for the elimination of the above problems, such as the use of infinite elements and the penalty coefficient method, are suggested.

In Chapter 3, the development of various semi-analytical and numerical approaches, for the analysis of optical waveguide structures, incorporating loss or gain, is examined. Firstly, the lossy planar optical waveguide with one-dimensional mode confinement is considered, where, the solution in terms of the complex transcendental equation, arising from the scalar form of the Maxwell's equations, is suggested. The extension of the above approach to the analysis of lossy optical waveguides with two-dimensional confinement, by means of the complex effective index method, is then considered. The development of the solution of multilayer planar structures with loss or gain, in terms of a generalized algorithm, which formulates the repeated application the boundary conditions at the interfaces of the various layers, is also presented. The several published numerical approaches, for the determination of loss or gain in optical waveguides are reviewed and the application of perturbation theory in the solution of optical waveguides incorporating small loss or gain is then examined.

The development of a numerical approach, where the accurate finite element results obtained from the solution of loss-free optical waveguide structures are utilised in the perturbation technique, to determine the characteristics of optical waveguides incorporating small amount of loss or gain, is analysed. The implementation of the above approach is presented, for both the **H**-field vector variational formulation and the scalar approximation of the finite element method. Further, an approximate numerical approach, based on the relation between the mode confinement and the loss or gain properties of the dielectric materials in an optical waveguide, for the determination of the complex propagation characteristics, is also examined.

Chapters 4, 5 and 6 are devoted to the use of the finite element method and the perturbation technique, along with the other approaches described in Chapter 3, in the solution of certain types of optical waveguides and other optoelectronic device applications, incorporating loss or gain. The limit of the perturbational approach, is also investigated, by comparing the calculated attenuation or gain characteristics, with the results obtained from the solution of the transcendental equation and the complex effective index method, for planar waveguides and simple optical waveguide structures with two-dimensional mode confinement, respectively.

In Chapter 4 certain types of planar waveguide structures, such as the three layer non-metal slab, the metal-clad, the graded-index metal clad optical waveguides, are examined. In some of the above structures, which exhibit loss due to the metal-cladding, the propagation and attenuation characteristics are determined, by using the scalar approximation of the finite element method in conjunction with the perturbation technique and by solving the complex transcendental equation. The limit of the perturbation technique is then defined from the value of the attenuation constant, where the two approaches are diverging. Planar structures composed of thin metal layers, which exhibit surface plasmon modes and loss properties due to interaction of the metal/dielectric interfaces are then considered and their attenuation characteristics are calculated and compared with previously published results for the same structures. Finally, the propagation and the attenuation characteristics of a multilayer metal-clad planar optical waveguide with a low-index dielectric buffer, which has some important features used in the design of an absorption modulator, are presented.

Optical waveguides with two-dimensional mode confinement, such as the rectangular dielectric and certain types of the rib optical waveguide, are analysed in Chapter 5. First, a rectangular dielectric waveguide, used for the modelling of buried heterostructure diode lasers is examined. The gain characteristics of the above structure are calculated, by the \mathbf{H} -field vector and the scalar approximation variational formulation of the finite element method in conjunction with the perturbation technique, and compared with those obtained by the confinement factor method and the \mathbf{H}_t formulation. A comparison with the results obtained by the complex effective index method is also attempted, in order to determine the limit of the perturbational approach. An air-clad GaAs/GaAlAs simple rib waveguide, in which small loss was introduced, in order to determine the attenuation characteristics by the \mathbf{H} -field vector and the scalar approximation variational formulation of the finite element method in conjunction with the perturbation technique, is then examined. The complex effective index method is then employed for the above structure, in order to investigate the limit of the perturbational approach. Next, an integrated laser rib waveguide, exhibiting gain due to the active region, is considered, and the calculated propagation characteristics are presented and compared with published results obtained by other approaches, such as the finite difference method and the spectral index method. The effect on the overall gain of the waveguide, by introducing a small amount of loss in the cladding regions, is then examined. Further, the gain characteristics of the above optical

waveguide, by introducing an active region with a varying imaginary part of the refractive index according to the carrier concentration, are also presented. Next the gain characteristics of a multiple quantum well rib waveguide, where the effect on the overall gain, by increasing the number of quantum layers, are investigated. The effect in the gain properties, of the increase of the quantum layers' thickness beyond typical values, is then examined and the accuracy of the approximate confinement factor method for different number of quantum layers, is also presented. Finally, the last section of this chapter is devoted to the study of the effect of the lossy metal electrodes on the optical properties of a Ti:LiNbO₃ directional coupler modulator.

Chapter 6 is devoted to the application of the finite element method and the perturbation technique to optical waveguide structures, with two-dimensional confinement, incorporating metallic elements, and therefore exhibiting surface plasmon and attenuation properties. A composite coupled structure, consisting of an aluminum surface plasmon guide and an InGaAs rectangular dielectric waveguide, both surrounded by InP substrate, is first examined. The field distributions, and the propagation and attenuation characteristics of the above structure, are presented and the coupling length for the phase-matching of the two coupled supermodes, is determined. A two parallel rib structure with metal-cladding on the top of the one rib, suitable for TE-TM mode polarisation splitter design, is then investigated. The attenuation characteristics of the two TE and TM polarizations, with the variation of certain dimensions of the structure, and the field distributions, are then presented. The importance of the above calculations and the various other parameters, determining the design of an optical polarizer, are also discussed. Sub-micron metal-clad optical fibers, suitable for near-field optical scanning microscopy, are then considered in the last section of this section. The above structures are analysed by the perturbational finite-element approach and their fundamental TE and TM modes are classified and their attenuation characteristics are determined. The applicability in optical scanning microscopy, of some of the above modes, is also discussed.

Finally, general conclusions arising from the work carried out in this research are summarised and explored in Chapter 7. Possible extension of the present work, to suit the future needs of the fast advancing technology in this area, is also suggested. The work ends with a list of all references to relevant published work, cited throughout the thesis.

2

The Finite Element Method

2.1 Introduction

Typical Engineering problems involve the derivation of differential equations, relating the variables of interest, which are based on physics and engineering principles. The principles used to describe the behaviour of the engineering problem are seen in the concepts of equilibrium, a state defined in Newton's ideas regarding force acting on a mass, in potential energy, in strain energy, in thermodynamics, in conservation of total energy, in Maxwell's equations and in many other application areas. Solution of the differential equations (sometimes non-linear), arising from the formulation of a problem based on the above principles, is only possible for simple geometry problems, with the most simple boundary conditions. In the finite-element method (FEM), the differential equations defining a system under consideration, can be replaced by variational expressions to which a variational principle (Davies, 1989) is applied, and the region of interest is divided into discrete elements. Thus, an equivalent discretized model for each element is constructed and all the elemental contributions to the system may be assembled. In other words, the FEM is an approximation of a continuous system by a discretized model, where, as the number of

the discrete variables increases, the solution approaches the true continuum solution (Zienkiewicz and Taylor, 1989). Therefore, in the FEM, a differential equation approach is transformed into an algebraic problem, where the building blocks, or finite elements have all the complex equations solved for their simple shape (say triangle, rod, beam, etc.).

From historical point of view, the idea originated, in the last part of the 19th century, where Lord Rayleigh applied Castigliano's energy principles and the theory of equilibrium in structural mechanics, to solve many practical problems by assuming a shape of, say, the lateral displacement of a column or a shaft and then obtaining answers, through minimization of the energy, by using a function. Great skill was required to select the function in order to satisfy the boundary conditions and real problems emerged when the geometrical shape of many members, made them impossible to handle. In 1909, Ritz extended Rayleigh's principles by using multiple independent functions allowing more than one frequency of a shaft to be computed. The disadvantage of that approach was the need to solve an increasingly large number of simultaneous algebraic equations. Three decades later, Courant (1943) extended Ritz's method by using different geometric regions (triangles), establishing separate approximate functions and then linking them together. Courant's idea had to wait for few more decades to be implemented, until modern digital computers could handle the large number of algebraic equations. The method was first established by Turner *et al.* (1956) at the Boeing Aircraft Company, where it was used to calculate the stress-strain relations for complicated aircraft structures. In 1960, Clough introduced the term "finite-elements" to describe the new technique for plane stress analysis, and since then the name was kept and the approach found wider applicability in areas like structural and fluid mechanics, heat transfer, electromagnetic theory, acoustics and biomedical engineering.

Mathematically, the FEM is a numerical technique for obtaining approximate solutions to boundary-value problems, and it is the extension of two classical methods, the Raleigh-Ritz variational method, and the Galerkin method of weighted residuals. A boundary value problem can be defined by a governing differential equation in a domain, together with the boundary conditions on the boundary that encloses the domain. In the variational approach the boundary-problem is formulated in terms of variational expressions, referred to as functionals, whose minimum corresponds to the governing differential equation. The approximate solution is obtained by minimising the

functional with respect to its variables (Jin, 1993). The Galerkin method is based on the method of weighted residuals (Davies, 1989), in which the domain of the differential equation is discretized, and the solution is approximated by the summation of the unknown solutions for each subdomain weighted by known functions, relating them to the domain. The overall solution is obtained by minimising the error residual of the differential equation.

Research on the application of the FEM to electromagnetic-wave engineering began during the last years of the 1960's and since then, with the availability of larger and faster computers, it has been established as a very powerful tool dealing with the analysis of optical waveguides, particularly structures with arbitrary shapes, index profiles nonlinearities and anisotropies.

A cross section of an arbitrarily shaped optical waveguide, Ω , in the x - y transverse plane, as shown in Fig.2.1, is considered, divided into a number of subdomains, called elements, being composed of several different materials, each of which can be described by arbitrary permittivity and permeability tensors, $\hat{\epsilon}(x,y)$ and $\hat{\mu}(x,y)$ respectively. A uniform shape of the waveguide along the longitudinal z -axis, is assumed and time and axial dependencies are given by $\exp(j\omega t)$ and $\exp(-\gamma z)$, where, ω is the angular frequency and the complex propagation constant, γ , given by:

$$\gamma = \alpha + j\beta \quad (2.1)$$

where α (Np/m) is the attenuation constant and β (rad/m) is the phase constant.

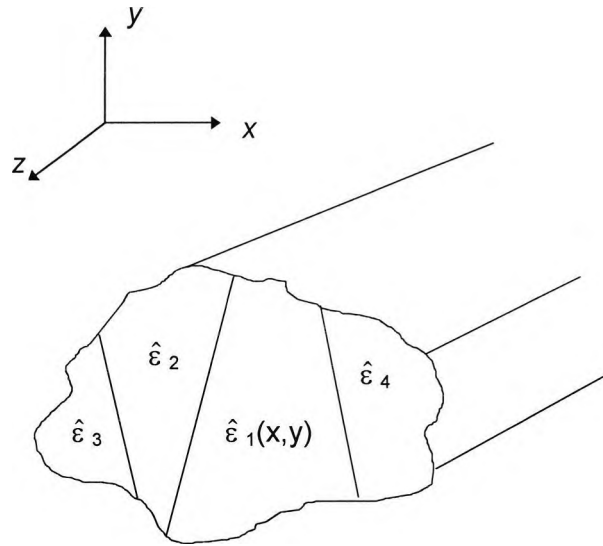


Fig.2.1 Arbitrarily shaped optical waveguide, divided into arbitrary sub-domains, each having different type of material.

For the loss-free case the propagation constant is considered to be equal to the phase constant, $j\beta$. The electric, $\mathbf{E}(x,y,z,t)$, and the magnetic, $\mathbf{H}(x,y,z,t)$ fields over the region of the waveguide can be expressed by:

$$\mathbf{E}(x,y,z,t) = \mathbf{E}(x,y) [\exp j(\omega t - \beta z)] \quad (2.2)$$

$$\mathbf{H}(x,y,z,t) = \mathbf{H}(x,y) [\exp j(\omega t - \beta z)] \quad (2.3)$$

where $\mathbf{H}(x,y)$ and $\mathbf{E}(x,y)$, are the spatial time-independent electric and magnetic fields respectively.

2.2. Basic equations

For the application of the FEM in the analysis of optical waveguide problems, some fundamental electromagnetic field equations should be considered, such as the Maxwell's equations, the boundary conditions and the Helmholtz's wave equations.

2.2.1 Maxwell's Equations

Maxwell's equations comprise a set of four electromagnetic field vectors, which represent the governing laws of the electromagnetic wave phenomena. The four vectors are: the electric field intensity \mathbf{E} (Volts/meter), the magnetic field intensity \mathbf{H} (Amperes/meter), the electric flux density \mathbf{D} (Coulomb/meter²) and the magnetic flux density \mathbf{B} (Tesla). For source-free, time dependent fields they can be written in differential or integral form. Since, the FEM is a boundary-value problem which is defined by differential equations, Maxwell's equations are presented in differential form as follows:

$$\nabla \times \mathbf{E} + \frac{\partial \mathbf{B}}{\partial t} = 0 \quad (\text{Faraday's law}) \quad (2.4)$$

$$\nabla \times \mathbf{H} - \frac{\partial \mathbf{D}}{\partial t} = 0 \quad (\text{Maxwell-Ampere law}) \quad (2.5)$$

$$\nabla \cdot \mathbf{D} = \rho \quad (\text{Gauss's law}) \quad (2.6)$$

$$\nabla \cdot \mathbf{B} = 0 \quad (\text{Gauss's law-magnetic}) \quad (2.7)$$

where ρ , is the (scalar) electric charge density (Coulomb/meter³).

The associated constitutive equations for the medium can be written as:

$$\mathbf{D} = \epsilon \mathbf{E} \quad (2.8)$$

$$\mathbf{B} = \mu \mathbf{H} \quad (2.9)$$

where ϵ , is the permittivity and μ the permeability of the medium and can be defined by:

$$\epsilon = \epsilon_0 \epsilon_r \quad (2.10)$$

$$\mu = \mu_0 \mu_r \quad (2.11)$$

where ϵ_0 , ϵ_r , μ_0 , μ_r are the permittivity of the vacuum (8.854×10^{-12} Farad/meter), the relative permittivity of the medium, the permeability of the vacuum ($4\pi \times 10^{-7}$ Henry/meter) and the relative permeability of the medium respectively.

Additionally, the flow of energy carried by an electromagnetic field, is expressed by the Poynting vector \mathbf{S} (W/m^2) and can be expressed by:

$$\mathbf{S} = \mathbf{E} \times \mathbf{H} \quad (2.12)$$

2.2.2 Boundary Conditions

Boundary conditions are conditions that must be met at the boundary surface when two different media 1 and 2 come into contact. If the unit normal vector \mathbf{n} , is directed from medium 1 to medium 2, as shown in Fig.2.2., in the absence of any surface currents ($\mathbf{J}=0$) and surface charges ($\rho=0$), the following boundary conditions apply:

- 1) The tangential component of the electric field must be continuous

$$\mathbf{n} \times (\mathbf{E}_1 - \mathbf{E}_2) = 0 \quad (2.13)$$

- 2) The tangential component of the magnetic field must be continuous

$$\mathbf{n} \times (\mathbf{H}_1 - \mathbf{H}_2) = 0 \quad (2.14)$$

- 3) The normal component of the electric flux must be continuous

$$\mathbf{n} \cdot (\mathbf{D}_1 - \mathbf{D}_2) = 0 \quad (2.15)$$

- 4) The normal component of the magnetic flux density must be continuous

$$\mathbf{n} \cdot (\mathbf{B}_1 - \mathbf{B}_2) = 0 \quad (2.16)$$

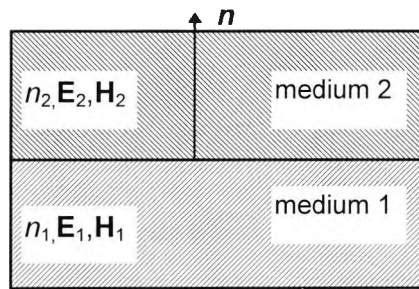


Fig.2.2 Boundary between two media of refractive indices n_1 and n_2 , where \mathbf{n} , is the unit vector normal to the interface.

In certain cases, one of the two media can be considered, either as a perfect electric conductor or a perfect magnetic conductor. When one of the two media becomes a perfect electric conductor, an *electric wall* boundary condition is imposed as:

$$\mathbf{n} \times \mathbf{E} = 0 \quad \text{or} \quad \mathbf{n} \cdot \mathbf{H} = 0 \quad (2.17)$$

Such condition ensures the continuity of the normal component of the electric field vector, \mathbf{E} , and vanishes the magnetic field vector, \mathbf{H} , at the boundary. When one of the two media becomes a perfect magnetic conductor, a magnetic wall boundary condition is imposed as:

$$\mathbf{n} \times \mathbf{H} = 0 \quad \text{or} \quad \mathbf{n} \cdot \mathbf{E} = 0 \quad (2.18)$$

The above condition, vanishes the electric field vector, \mathbf{E} , and ensures the continuity of the normal component of the magnetic field at the boundary.

2.2.2.1 Natural and Forced Boundary Conditions

In the case of a closed surface, such as the boundary of an optical waveguide, additional boundary conditions are considered. These boundary conditions can be *natural*, in cases where the field decays at the boundary, therefore they can be left free. In some other cases they can be *forced*, in order to take advantage of the symmetry of a waveguide, to reduce the number of elements in FEM (and the order of the matrices), or to impose complementary symmetry to the waveguide, in order to

achieve the required polarization. The above boundary conditions can be classified as follows (Davies, 1989):

$$\varphi=0 \quad (\text{Homogeneous Dirichlet}) \quad (2.19)$$

$$\varphi=k \quad (\text{Inhomogeneous Dirichlet}) \quad (2.20)$$

where φ can be the Electric (E), or Magnetic (H) field, and k is a prescribed constant value.

$$\partial\varphi/\partial\mathbf{n}=0 \quad (\text{Homogeneous Neumann}) \quad (2.21)$$

where \mathbf{n} is the unit vector normal to the surface.

The Neumann boundary conditions represents the rate of change of the field when is directed out of the surface, and it can be used in the FEM to impose the field decay along finite-elements, adjacent to the boundary elements of a waveguide structure.

2.2.3 Wave equations

In an isotropic lossless medium with no wave source ($J=0$, $\rho=0$), with uniform permeability $\mu=\mu_0$, and uniform and constant permittivity, by eliminating the magnetic flux density in and the electric flux density components from Maxwell's equations, (2.4) and (2.5) respectively, these can be written as (Koshiba, 1990):

$$\nabla^2 E + k^2 E = 0 \quad (2.22)$$

$$\nabla^2 H + k^2 H = 0 \quad (2.23)$$

where the wavenumber, k (rad/m) is

$$k=\omega\sqrt{\epsilon\mu_0} \quad (2.24)$$

If $\varepsilon=\varepsilon_0$, then the wavenumber k_0 , is called free space wavenumber and is defined by:

$$k_0 = \omega\sqrt{\varepsilon_0\mu_0} \quad (2.25)$$

Equations (2.22) and (2.23) are known as vector Helmholtz wave equations (Marz, 1994) for homogeneous media, and in addition to the physical solutions, they also support non-physical, spurious solutions, since the condition $\nabla\cdot\mathbf{H}=0$, is not satisfied.

In a rectangular coordinate system, if only one component of the electric or magnetic field is considered, suppose E_x , vector Helmholtz wave equation can lead to the scalar Helmholtz wave equation as (Koshiba, 1990):

$$\nabla^2 E_x + k^2 E_x = 0 \quad (2.26)$$

2.3 Variational Formulations

As it was discussed in section 2.1, the finite-element formulation is based on the variational or Raleigh-Ritz approach, therefore, several variational formulations have been proposed for the analysis of the optical waveguide problem. These can be in a scalar form (Mabaya *et al.*, 1981), where the Electric or Magnetic field is expressed only in terms of one component, according to the predominant field component, or, can be in vector form, where the Electric or Magnetic field is expressed in terms of at least two of the constituent field components.

It should be noted that most of the formulations applied in the finite element method, yield to a standard eigenvalue problem (Rahman and Davies, 1984a):

$$[A] \{x\} - \lambda [B] \{x\} = 0 \quad (2.27)$$

where A and B are real symmetric sparse matrices, and B is also positive definite. The eigenvalue λ , can be chosen as β^2 or k^2 , depending on the formulation, and the

eigenvalues represent the nodal field values of the finite-elements. It is desirable for the above matrix equation to be of this canonical form, to allow an efficient solution. Details of the constituent components of the eigenvalue equation and solution methods are discussed in Section 2.7.

2.3.1 The scalar approximation

The scalar approximation can be applied in situations where the field can be described as predominantly TE or TM and it can be expressed in terms of the longitudinal components of the above modes. It has been used for the solution of homogeneous waveguide problems (Daly, 1984), open boundary problems (Wu and Chen 1986), and for the analysis of anisotropic waveguides (Koshiya *et al.*, 1984).

For the quasi-TE modes over a region Ω , where the dominant field component is E_x , the formulation can be written as (Mabaya *et al.* 1981):

$$L = \iint_{\Omega} \left[\left(\frac{\partial E_x}{\partial x} \right)^2 + \left(\frac{\partial E_x}{\partial y} \right)^2 - k_0 n^2 E_x^2 + \beta^2 E_x^2 \right] d\Omega \quad (2.28)$$

where, β is the propagation constant and n is the refractive index.

For the quasi-TM modes, where H_x is the dominant field component, the formulation can be written as (Mabaya *et al.*, 1981):

$$L = \iint_{\Omega} \left[\frac{1}{n^2} \left(\frac{\partial H_x}{\partial x} \right)^2 + \frac{1}{n^2} \left(\frac{\partial H_x}{\partial y} \right)^2 - k_0 H_x^2 + \frac{1}{n^2} \beta^2 H_x^2 \right] d\Omega \quad (2.29)$$

2.3.2 Vector formulations

The scalar formulation is inadequate to handle general anisotropic or inhomogeneous problems and it can be used only as an approximation in such cases. For a more accurate representation of general waveguide fields, a vector formulation, with at least two components is essential. Several vector formulations dealing with optical waveguide problems have been proposed by many authors. However, some of

them are affected by non-physical spurious solutions, which appear mixed with the correct ones in the computations, and therefore several methods have also been proposed to overcome such problems.

The E_z - H_z formulation which is one of the first formulations used in finite-element analysis (Csendes and Silvester, 1970; Mabaya *et al.* 1981; Yeh *et al.* 1975; Yeh *et al.*, 1979), cannot treat general anisotropic problems without destroying the canonical form of the eigenvalue equation (2.27), and also some problems arise in enforcing boundary conditions for a waveguide with an arbitrary dielectric distribution. Additionally, this approach is based on the axial field components which are the least important of the \mathbf{E} and \mathbf{H} fields.

A vector \mathbf{E} -field formulation (English and Young, 1971; Hano, 1984; Koshiba *et al.* 1985b), which can handle general anisotropy, but loss-less problems, has also been applied to the solution of several types of optical waveguides. For such a formulation, the natural boundary conditions correspond to a magnetic wall, and therefore it is essential to enforce the electric wall ($\mathbf{n} \times \mathbf{E} = 0$) as a boundary condition, which is difficult to implement for irregular shaped structures.

The vector \mathbf{H} -field formulation is more suitable for dielectric waveguide problems, because the magnetic field is continuous everywhere, and the natural boundary conditions correspond to those of the electric wall, therefore no forced boundary conditions at the boundaries are required.

This formulation can be written as (Berk, 1956; Rahman and Davies, 1984a):

$$\omega^2 = \frac{\int (\nabla \times \mathbf{H})^* \cdot \hat{\epsilon}^{-1} \cdot (\nabla \times \mathbf{H}) d\Omega}{\int \mathbf{H}^* \cdot \hat{\mu} \cdot \mathbf{H} d\Omega} \quad (2.30)$$

where ω , is the natural frequency, Ω is the waveguide cross-section and $\hat{\epsilon}$ and $\hat{\mu}$ are the permittivity and permeability tensors respectively.

However, the above formulation (as well as the \mathbf{E} -field), yields spurious solutions, because the divergence condition, $\nabla \cdot \mathbf{H} = 0$ is not satisfied, therefore alternative approaches, such as the penalty coefficient method (Rahman and Davies,

1984b; Koshiba *et al.*, 1985a) have been proposed to eliminate those non-physical solutions. This method will be discussed in a later section.

Most recently a variational formulation in terms of the transverse **E**-field or **H**-field components has been proposed for the solution of optical waveguide problems (Hayata *et al.*, 1986b; Lu and Fernandez 1993a; Silveira and Gopinath, 1995). In this approach the minimum number of field components (two) are used, and the divergence condition, $\nabla \cdot \mathbf{H} = 0$, is satisfied. It can handle accurately lossy structures (Lu and Fernandez, 1993b; Cheung *et al.*, 1995), but it can lead to large sparse, complex, non-symmetric matrices in the eigenvalue equation, which increase computation time, therefore effort has been made to develop efficient sparse matrix solvers (Fernandez *et al.*, 1991) in order to solve such problems.

2.4 Finite Element Method formulation

In order to explain the application of the variational principle in the FEM, based on the Ritz-Galerkin approach, a cross section of an arbitrarily shaped waveguide, as shown in Fig.2.3, divided into a patchwork of elements, is considered, where Ω , is the cross-sectional area of the waveguide and Γ , is the boundary that encloses Ω . The boundary, Γ , can consist of an electric wall, Γ_e , where the tangential electric field is 0, and a magnetic wall, Γ_m , where the tangential magnetic field is also 0. By assuming that the core and cladding of the above structure consist of random anisotropic media, the wave equation for the magnetic \mathbf{H} -field (2.23), based on Maxwell's equations, (2.4-2.7), can be represented as (Koshiya, 1992b):

$$\nabla \times ([\epsilon_r]^{-1} \nabla \times \mathbf{H}) - k_0^2 \mathbf{H} = 0 \quad (2.31)$$

where $[\epsilon_r]$, is the relative permittivity tensor.

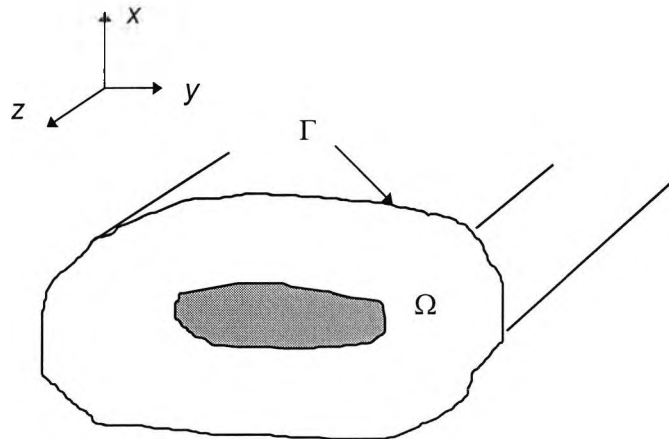


Fig. 2.3 Arbitrary cross section of an optical waveguide (shaded core region), Ω , enclosed by boundary Γ .

In the Rayleigh-Ritz method, the boundary value problem, defined by the differential wave equation and the boundary conditions, can be expressed in terms of a scalar quantity, referred as the functional, F . This functional, F , can be defined by an integral form, where the differential equation and the boundary conditions are represented. In the case of the optical waveguide, the functional, F , of the wave equation (2.31) can be expressed as (Koshiya, 1992b):

$$F = \iint_{\Omega} (\nabla \times \mathbf{H})^* \left([\epsilon_r]^{-1} \nabla \times \mathbf{H} \right) d\Omega - k_0^2 \iint_{\Omega} \mathbf{H}^* \cdot \mathbf{H} d\Omega \quad (2.32)$$

In the above equation, the unknown function is the magnetic field, \mathbf{H} , and the solution of the problem is a function \mathbf{H} , which makes the functional, F , stationary with respect to small changes, δH . This can be expressed by the Euler's equation (Koshiba, 1990) as:

$$\delta F = 0 \quad (2.33)$$

By taking the first variation δF (Davies, 1989) and applying Gauss' divergence theorem, Euler's equation (2.33) can be expressed as (Koshiba, 1992a):

$$\delta F = \iint_{\Omega} \delta \mathbf{H}^* \cdot \left[\nabla \times \left([\epsilon_r]^{-1} \nabla \times \mathbf{H} \right) - k_0^2 \mathbf{H} \right] d\Omega - \int_{\Gamma} \delta \mathbf{H}^* \cdot \left[\mathbf{n} \times \left([\epsilon_r]^{-1} \nabla \times \mathbf{H} \right) \right] \delta \Gamma \quad (2.34)$$

where, \mathbf{n} is the unit normal vector to boundary Γ and the expression, $\mathbf{n} \times \left([\epsilon_r]^{-1} \nabla \times \mathbf{H} \right)$, corresponds to the tangential electric field on the boundary Γ .

It can be seen from the above equation (2.34), that by applying the variational principle to equation (2.32), Euler's equation (2.33) coincides with the wave equation (2.31). The integral \iint_{Ω} should be satisfied in the cross-section, Ω , and the integral \int_{Γ} along the boundary, Γ . Since the boundary condition $\mathbf{n} \times \left([\epsilon_r]^{-1} \nabla \times \mathbf{H} \right)$, is automatically satisfied along the boundary Γ_e , it can be considered as the natural boundary condition. Equation (2.34) does not satisfy the boundary condition on the magnetic wall boundary, Γ_m , and therefore a forced boundary condition, $\mathbf{n} \times \mathbf{H} = 0$, should be imposed, if necessary.

By subdividing the cross section Ω , into a number of elements, e , the solution \mathbf{H} , for each element can be approximated by:

$$\mathbf{H} = \sum_{i=1}^m N_i H_i \quad (2.35)$$

where, m is the number of nodes, H_i is the nodal \mathbf{H} -field for each node of the elements, and N_i is a set of known basis functions (Davies, 1989), named *shape functions*, which will be discussed in Section 2.6.

Equation (2.35) can be also expressed in matrix notation as:

$$\mathbf{H} = [\mathbf{N}]^T \{H\}_e \quad (2.36)$$

where, T denotes transpose and $[\mathbf{N}]^T$ and $\{H\}_e$ are the matrix of the shape functions and the column vector of the nodal field values for each element respectively.

The expression for \mathbf{H} in (2.36) can be then substituted in eqn. (2.32) and by applying the variational principle, Euler's equation (2.33) can be obtained. By using the term related to the cross-section, Ω , from the Euler's equation, the solution to the optical waveguide problem can be obtained from:

$$\iint_{\Omega} \left(\nabla \times [\mathbf{N}]^T \{H\}_e^* [\epsilon_r]^{-1} \nabla \times [\mathbf{N}]^T \{H\}_e - k_0^2 [\mathbf{N}]^T \{H\}_e^* [\mathbf{N}]^T \{H\}_e \right) d\Omega = 0 \quad (2.37)$$

Since the problem is discretized into a finite number of elements, the integral can be evaluated by summing over the whole region, Ω . By rearranging equation (2.36) and transforming it into a matrix form, the problem can be formulated as a standard eigenvalue problem as (Rahman and Davies, 1984a; Koshiya, 1992b):

$$[\mathbf{A}]\{H\} - k_0^2 [\mathbf{B}]\{H\} = 0 \quad (2.38)$$

where, k_0^2 is the eigenvalue and $\{H\}$ the eigenvector for each eigenvalue. Matrix \mathbf{A} is a complex Hermitian, which can be reduced to a real symmetric, for the loss-less case, and matrix \mathbf{B} is real symmetric and positive definite. Both matrices are discussed in Section 2.7.

2.5 Elements and nodal values

Different types of elements can be used in the discretization of a continuum problem, such as triangles, rectangles, *etc.* Triangular elements are often preferred

due to the simplicity of their shape and their ability to represent more complicated structures. Such elements can be also of first or second order, as shown in Fig.2.4, or even higher order, depending on the number of nodes, or nodal points assigned on their vertices and their sides. All the elements in a discretized cross-section of an optical waveguide are considered to be interconnected at a discrete number of nodal points on their boundaries.

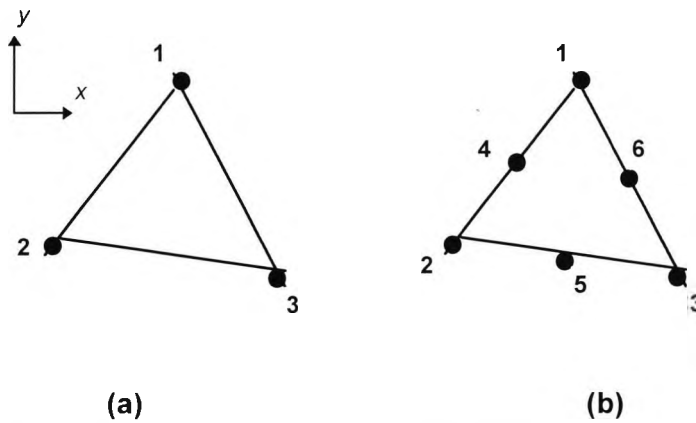


Fig.2.4 a) First-order and b) second-order triangular elements

In the finite-element approach different expansions are used over each element, such as polynomials or sinusoids, which must have the same form over all the elements, but different coefficients. These functions must satisfy some conditions between elements, such as continuity. Throughout this work, first-order triangular elements have been used, which are assigned three nodal points, one at each vertex, as shown in Fig.2.4.a. For each of the above elements a first-degree polynomial ($a+bx+cy$) can be used, which is continuous across adjacent triangles. Therefore, if the **H** or **E** field, in the case of the optical waveguide, is interpreted like a third dimension, it can be viewed as a surface with many triangular facets.

The electromagnetic field for each first-order element can be expressed in terms of first-order polynomials as:

$$\phi_e(x,y) = a_e + b_e x + c_e y \quad (2.39)$$

where $\phi_e(x,y)$, is the electric, **E**, or magnetic, **H**, field, and a_e , b_e , and c_e are the coefficients of the polynomial expression, over each element respectively.

The overall field for each element can also be defined in terms of the components, ϕ_1, ϕ_2, ϕ_3 , which are known (Davies, 1989) as the *nodal field values*, and correspond to the unknown but wanted **E** or **H** field values at the element vertices.

These can be expressed in matrix notation as:

$$\begin{Bmatrix} \phi_1 \\ \phi_2 \\ \phi_3 \end{Bmatrix} = \begin{bmatrix} 1 & x_1 & y_1 \\ 1 & x_2 & y_2 \\ 1 & x_3 & y_3 \end{bmatrix} \begin{Bmatrix} a_e \\ b_e \\ c_e \end{Bmatrix} \quad (2.40)$$

By rearranging eqn.(2.40) as:

$$\begin{Bmatrix} a_e \\ b_e \\ c_e \end{Bmatrix} = \begin{bmatrix} 1 & x_1 & y_1 \\ 1 & x_2 & y_2 \\ 1 & x_3 & y_3 \end{bmatrix}^{-1} \begin{Bmatrix} \phi_1 \\ \phi_2 \\ \phi_3 \end{Bmatrix} \quad (2.41)$$

and substituting the coefficients a_e, b_e and c_e in eqn. (2.39), this can be transformed to:

$$\phi_e(x, y) = \begin{bmatrix} N_1 & N_2 & N_3 \end{bmatrix} \begin{Bmatrix} \phi_1 \\ \phi_2 \\ \phi_3 \end{Bmatrix} \quad (2.42)$$

where, N_1, N_2, N_3 are known as the *shape functions*, and can be defined by:

$$N_1(x, y) = \{(x_2 y_3 - x_3 y_2) + (y_2 - y_3)x + (x_3 - x_2)y\} / \det \quad (2.43)$$

where, \det , is the determinant of the 3x3 matrix in eqn. (2.40) and the other two shape functions, and N_2 and N_3 , are obtained by cyclic exchange of 1→2→3 in eqn. (2.43).

2.6 Shape functions

The expressions N_1, N_2 and N_3 in eqn. (2.42) and (2.43), defined in the previous sections as the shape functions, are a set of interpolation functions, in terms of complete polynomials which are normalized over each triangle. They are chosen

uniquely to define the field within each finite element under consideration and they are linearly dependent on the values of fields assigned to the vertices of the element. Each of them has a value 1 on the vertex defined by its subscript and 0 value on the other vertices. Shape functions can be normalized further, in terms of x and y coordinates and by doing so, the same function can be applied to any triangular element. This can be achieved by introducing local (or area) coordinates (Davies, 1989) which can normalize all triangles to one prototype. Primarily, a first-order triangular element is considered, as shown in Fig.2.5, where 1, 2 and 3 are the three nodal, one at each vertex, (x_1, y_1) , (x_2, y_2) , (x_3, y_3) are the coordinates of each vertex and point P is any arbitrarily chosen point at the surface of the triangle.

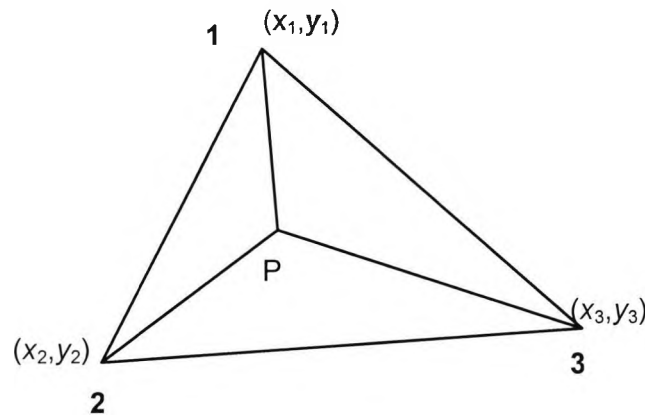


Fig. 2.5 Coordinates and node numbers of a first-order triangular element.

Local coordinate L_1 can be expressed by the ratio (Davies, 1989):

$$L_1 = \frac{\text{area of triangle (P - 2 - 3)}}{\text{area of triangle (1 - 2 - 3)}} \quad (2.44)$$

where (P-2-3) denotes the triangle with vertices, the nodes defined as P, 2 and 3.

L_1 , is proportional to the perpendicular distance of P from side (2-3) and can also be defined into matrix form as:

$$L_1 = \frac{\begin{vmatrix} 1 & x & y \\ 1 & x_2 & y_2 \\ 1 & x_3 & y_3 \end{vmatrix}}{\begin{vmatrix} 1 & x_1 & y_1 \\ 1 & x_2 & y_2 \\ 1 & x_3 & y_3 \end{vmatrix}} = \frac{\begin{vmatrix} x_2 & y_2 \\ x_3 & y_3 \end{vmatrix} + (y_2 - y_3)x + (x_3 - x_2)y}{2A_e} = \frac{a_1 + a_2x + a_3y}{2A_e} \quad (2.45)$$

where the notation, $\begin{vmatrix} \dots \\ \dots \\ \dots \end{vmatrix}$, denotes determinant, and A_e , is the area of the triangular element.

From Fig.2.4, it is obvious that L_1 , takes the value 1 at vertex 1 and the value 0 at any other vertex and therefore it is the unique interpolating first degree polynomial for node 1. The other local coordinates, L_2 and L_3 can be expressed by cyclic exchange of $1 \rightarrow 2 \rightarrow 3$ in the x , and y , coordinates, in eqn. (2.45). These can be then expressed as:

$$L_2 = \frac{a_4 + a_5x + a_6y}{2A_e}, \quad L_3 = \frac{a_7 + a_8x + a_9y}{2A_e} \quad (2.46)$$

From the area definition, it can also be seen that:

$$L_1 + L_2 + L_3 = 1 \quad (2.47)$$

For the first order triangular elements the three shape functions N_1 , N_2 , N_3 , correspond to the three local coordinates, defined in (2.45) and (2.46) and as:

$$N_1 = L_1 \quad N_2 = L_2 \quad N_3 = L_3 \quad (2.48)$$

The above definition of the shape functions for the first-order triangular element coincides also with equation (2.43).

In order to generalize to higher order elements, the shape functions have to be calculated in terms of higher order-interpolation polynomials, depending on the degree of the finite-elements used, and the local coordinates of the triangle. For a second order triangular element, shown in Fig.2.4.b, the shape functions can be defined as (Koshiba, 1992a):

$$\begin{array}{lll} N_1 = L_1(2L_1 - 1) & N_2 = L_2(2L_2 - 1) & N_3 = L_3(2L_3 - 1) \\ N_4 = 4L_1L_2 & N_5 = 4L_2L_3 & N_6 = 4L_3L_1 \end{array} \quad (2.49)$$

2.7 Assembly of element matrices

As was mentioned in Section 2.4, the solution of the optical waveguide problem by the FEM can be transformed to a standard eigenvalue problem as in eqn. (2.38). Matrices A and B in (2.38), are known as *global matrices* and consist of the summation of the element matrices for each triangular element of the discretised cross-section of the optical waveguide. In this section, the assembly of the element matrices is shown, with respect to the shape functions and the nodal field values of each triangular element, based on the variational formulation. Throughout the procedure, the full \mathbf{H} -field formulation in terms of the three axial components is assumed and first-order triangular elements are being used.

By considering eqn. (2.36) where the magnetic field vector, \mathbf{H} , is expressed in terms of the shape functions, the nodal magnetic field vector $\{H\}_e$ over the cross section of a triangular element can be defined with respect to its axial components as:

$$\{H\}_e = [\{H_x\}_e \quad \{H_y\}_e \quad \{H_z\}_e]^T \quad (2.50)$$

where $\{H_x\}$, $\{H_y\}$, $\{H_z\}$ are the nodal field vectors along each axis.

Also, the shape function matrix, $[N]^T$, can be analysed as:

$$[N]^T = \begin{bmatrix} \{N\} & \{0\} & \{0\} \\ \{0\} & \{N\} & \{0\} \\ \{0\} & \{0\} & j\{N\} \end{bmatrix} \quad (2.51)$$

where $\{N\}$ is the shape function vector:

$$\{N\} = [N_1 \quad N_2 \quad N_3]^T \quad (2.52)$$

and $\{0\}$, is the null vector. The term j arises, as for lossless cases H_z component is 90° out of phase with the transverse components.

Equation (2.36) can then be re-written as:

$$\{H\}_e = \begin{bmatrix} N_1 & N_2 & N_3 & 0 & 0 & 0 & 0 & 0 & 0 \\ 0 & 0 & 0 & N_1 & N_2 & N_3 & 0 & 0 & 0 \\ 0 & 0 & 0 & 0 & 0 & 0 & jN_1 & jN_2 & jN_3 \end{bmatrix} \begin{bmatrix} H_{x1} \\ H_{x2} \\ H_{x3} \\ H_{y1} \\ H_{y2} \\ H_{y3} \\ H_{z1} \\ H_{z2} \\ H_{z3} \end{bmatrix} \quad (2.53)$$

Similarly, the expression $(\nabla \times \mathbf{H})_e$, within the element can be defined as:

$$(\nabla \times \mathbf{H})_e = [\nabla \times] [N]^T \{H\}_e = \begin{bmatrix} 0 & -\partial / \partial z & \partial / \partial y \\ \partial / \partial z & 0 & -\partial / \partial x \\ -\partial / \partial y & \partial / \partial x & 0 \end{bmatrix} [N]^T \{H\}_e \quad (2.54)$$

which can also be written as:

$$(\nabla \times \mathbf{H})_e = [Q]^T \{H\}_e \quad (2.55)$$

where, the matrix $[Q]$ is defined by:

$$[Q] = \begin{bmatrix} \{0\} & -j\beta\{N\} & -\partial\{N\} / \partial y \\ j\beta\{N\} & \{0\} & \partial\{N\} / \partial x \\ j\partial\{N\} / \partial y & -j\partial\{N\} / \partial x & \{0\} \end{bmatrix} \quad (2.56)$$

and by using the shape functions coefficients in (2.45) and (2.46):

$$\partial\{N\} / \partial x = [a_2 \quad a_5 \quad a_8] \quad (2.57)$$

$$\partial\{N\} / \partial y = [a_3 \quad a_6 \quad a_9] \quad (2.58)$$

It has been shown in Section 2.4, that the solution to the optical waveguide problem can be obtained from Euler's equation, which can be transformed to a discretized form as in eqn. (2.37). By assuming isotropic media ($[\epsilon_r] = \epsilon_r$) and substituting equation (2.55) in (2.37), the resulting element equation will become:

$$\frac{1}{\epsilon_r} \iint_{\Omega} (\{H\}_e^T [Q]^* [Q]^T \{H\}_e) d\Omega - k_0^2 \iint_{\Omega} (\{H\}_e^T [N]^* [N]^T \{H\}_e) = 0 \quad (2.59)$$

By summing all the elements over the cross-section of the guide, the above equation can be expressed in matrix form as:

$$[A]\{H\} - k_0^2 [B]\{H\} = 0 \quad (2.60)$$

where,

$$[A] = \sum_e [A]_e = \sum_e \iint_{\epsilon_e} \frac{1}{\epsilon_e} [Q]^* [Q]^T dx dy \quad (2.61)$$

$$[B] = \sum_e [B]_e = \sum_e \iint_e [N]^* [N]^T dx dy \quad (2.62)$$

[A] and [B] are the global matrices of the eigenvalue equation, $\frac{1}{\epsilon_e}$ is the relative dielectric permittivity of the element, and $[A]_e$ and $[B]_e$ are the element matrices which may be evaluated as follows:

For matrix $[A]_e$:

$$[A]_e = \frac{1}{\epsilon_e} \iint_e \begin{bmatrix} \{0\} & j\beta\{N\} & -\partial\{N\}/\partial y \\ -j\beta\{N\} & \{0\} & \partial\{N\}/\partial x \\ -j\partial\{N\}/\partial y & j\partial\{N\}/\partial x & \{0\} \end{bmatrix} \begin{bmatrix} \{0\} & j\beta\{N\}^T & j\partial\{N\}^T/\partial y \\ -j\beta\{N\}^T & \{0\} & -j\partial\{N\}^T/\partial x \\ -\partial\{N\}^T/\partial y & \partial\{N\}^T/\partial x & \{0\} \end{bmatrix} dx dy = \quad (2.63)$$

$$= \frac{1}{\epsilon_e} \iint_e \begin{bmatrix} \beta^2 \{N\}\{N\}^T + \frac{\partial\{N\}}{\partial y} \frac{\partial\{N\}^T}{\partial y} & -\frac{\partial\{N\}}{\partial y} \frac{\partial\{N\}^T}{\partial x} & \beta\{N\} \frac{\partial\{N\}^T}{\partial x} \\ \frac{\partial\{N\}}{\partial y} \frac{\partial\{N\}^T}{\partial x} & \beta^2 \{N\}\{N\}^T + \frac{\partial\{N\}}{\partial x} \frac{\partial\{N\}^T}{\partial x} & \beta\{N\} \frac{\partial\{N\}^T}{\partial y} \\ \beta\{N\} \frac{\partial\{N\}^T}{\partial x} & \beta\{N\} \frac{\partial\{N\}^T}{\partial y} & \frac{\partial\{N\}}{\partial y} \frac{\partial\{N\}^T}{\partial y} + \frac{\partial\{N\}}{\partial x} \frac{\partial\{N\}^T}{\partial x} \end{bmatrix} dx dy$$

The resulting matrix is a 9x9 real symmetric matrix and by using the shape function coefficients and the relation for a triangular element (Davies, 1989):

$$\iint_e N_1^i N_2^j N_3^k dx dy = \frac{i! j! k!}{(i+j+k+2)!} (2 \times \text{Area}) \quad (2.64)$$

the various terms can be determined.

For the element matrix $[B]_e$:

$$\begin{aligned}
 [B]_e &= \iint_e [N]^* [N]^T dx dy = \iint_e \begin{bmatrix} \{N\} & \{0\} & \{0\} \\ \{0\} & \{N\} & \{0\} \\ \{0\} & \{0\} & -j\{N\} \end{bmatrix} \begin{bmatrix} \{N\}^T & \{0\}^T & \{0\}^T \\ \{0\}^T & \{N\}^T & \{0\}^T \\ \{0\}^T & \{0\}^T & j\{N\}^T \end{bmatrix} dx dy = \\
 &= \iint_e \begin{bmatrix} \{N\}\{N\}^T & \{0\}\{0\}^T & \{0\}\{0\}^T \\ \{0\}\{0\}^T & \{N\}\{N\}^T & \{0\}\{0\}^T \\ \{0\}\{0\}^T & \{0\}\{0\}^T & \{N\}\{N\}^T \end{bmatrix} dx dy
 \end{aligned} \tag{2.65}$$

where the various terms can be evaluated by using again (2.64).

Typical calculations for the evaluation of several terms of both the element matrices $[A]_e$ and $[B]_e$, are shown in detail in Appendix A.

2.8 Global matrices and sparsity

The eigenvalue problem (2.60) can be solved by constructing the global matrices $[A]$ and $[B]$ from the summation of the element matrices, $[A]_e$ and $[B]_e$ respectively, and using the appropriate matrix solver to obtain the eigenvalues and eigenvectors of the equation.

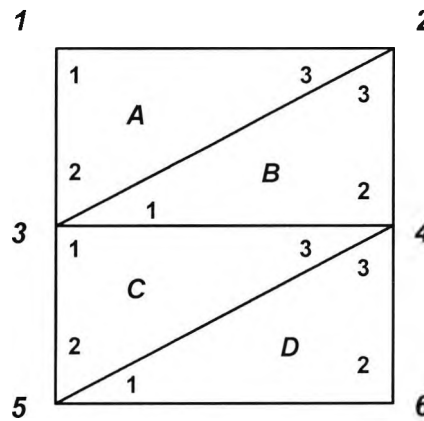


Fig.2.6 Simple structure discretized in four, first-order triangular elements.

The assembly of the global matrix is performed with respect to the nodal points of the structure and attention should be given when some nodes are common to two or more elements. In such a case, the contribution of each adjacent element should be added to the global matrix when a common node is calculated.

A simple structure consisting of four first-order triangular elements (A-D), is considered, as shown in Fig.2.6. The node numbers **1-6**, are the global numbers for the structure, referring to the global matrices and the nodal points inside each triangle 1, 2, 3, are the local node numbers for each element. In the above structure the global matrix, G , is formed by addition of the element matrices A, B, C and D.

As it has been shown in the previous section, for every element in the discretized variational formulation there is an expression of the form:

$$\{H\}[L]\{H\}^T = \{H_1 \quad \dots \quad H_9\} \begin{bmatrix} L_{1,1} & \dots & L_{1,9} \\ \cdot & & \cdot \\ \cdot & \cdot & \cdot \\ \cdot & & \cdot \\ L_{9,1} & \dots & L_{9,9} \end{bmatrix} \begin{Bmatrix} H_1 \\ \cdot \\ \cdot \\ \cdot \\ H_9 \end{Bmatrix} \quad (2.66)$$

Each term in the matrix, $L_{i,j}$, relates two nodal field values, where the indices i and j , correspond to the nodal field values of vectors $\{H\}$ and $\{H\}^T$, respectively, according to the local numbering an element. By considering scalar formulation, where only one field component is considered, say H_x , the expression can be reduced to:

$$\{H_{x1} \quad H_{x2} \quad H_{x3}\} \begin{bmatrix} L_{1,1} & L_{1,2} & L_{1,3} \\ L_{2,1} & L_{2,2} & L_{2,3} \\ L_{3,1} & L_{3,2} & L_{3,3} \end{bmatrix} \begin{Bmatrix} H_{x1} \\ H_{x2} \\ H_{x3} \end{Bmatrix} \quad (2.67)$$

where H_{xi} , denotes the nodal field of node i , according to the local numbering.

For the particular structure, shown in Fig.2.6, the global matrix $G_{p,q}$, may be defined as:

$$G = \begin{bmatrix} G_{1,1} & \dots & G_{1,6} \\ \cdot & & \cdot \\ \cdot & \cdot & \cdot \\ \cdot & & \cdot \\ G_{6,1} & \dots & G_{6,6} \end{bmatrix} \quad (2.68)$$

The size of the above global matrix is of the order $NP \times NP$, where NP is the total number of the nodal points of the structure. The terms of the global matrix, $G_{p,q}$, denote the (global) field contribution of two nodes, p and q , according to the global numbering. Each term of the global matrix $G_{p,q}$, consists of a (local) contribution from only one element, unless the nodes lie on a boundary shared by other elements. For example, the terms of the global matrix, $G_{1,1}$, for node 1 with respect to itself, is defined by:

$$G_{1,1} = L_{1,1}^A \quad (2.69)$$

where $L_{1,1}^A$, is the term of the element matrix, for the element A .

In the same way, the terms of the global matrix, for some other nodes which do not lie on a shared boundary, can be given by: $G_{1,2}=L^A_{1,3}$, $G_{2,4}=L^B_{3,2}$, $G_{3,5}=L^C_{1,2}$, etc. When the nodes are shared by more than one element, then the contributions from each element are added as shown below:

$$G_{22}=L^A_{3,3}+L^B_{3,3}, \quad G_{3,4}=L^B_{1,2}+L^C_{1,3}, \quad G_{3,3}=L^A_{2,2}+L^B_{1,1}+L^C_{1,1} \quad (2.70)$$

One of the most important features of the global matrix is that a term will have zero value when the corresponding nodes are not connected. For example:

$$G_{1,4}=G_{4,1}=G_{1,6}=G_{6,1}=G_{5,2}=G_{2,5}=0 \quad (2.71)$$

The above feature of the global matrix, known as *sparsity*, is a very crucial aspect of finite elements and leads to the use of special algorithms for the matrix solution, which reduce computational time and matrix size. Special storage schemes are used, and sometimes elements are recalculated whenever needed, rather than being stored, to allow for the solution of very large order matrices (Davies, 1989).

In this project, a very efficient matrix solver has been used, which exploits the sparsity (number of zero elements) of the matrices and uses a one-dimensional storage scheme for the global matrix. The above matrix, $G(k)$, is generated as a one-dimensional array, where the subscript k , denotes the index of two other one-dimensional arrays, $Ro(k)$, $Co(k)$ which hold the row and column number of an $n \times n$ matrix, respectively.

2.9 Infinite Elements

One common problem of the open-type optical waveguide is that finite field value exists in the region outside the guide and sometimes its decay extends to infinity. The modelling of such structures, may cause problem for solutions near cut-off, where the field decays slowly and the region of significant field value can be arbitrarily large. In the orthodox finite-element discretization the cross-section of the waveguide cannot be extended to infinity. Rahman and Davies (1984a), have developed an approach in which infinite elements are added along the outer boundary of the orthodox finite elements, as shown in Fig.2.7, where for a typical rectangular dielectric waveguide problem, a quarter of the structure is discretized into orthodox and infinite elements, by assuming two fold symmetry. These infinite elements extend the domain of explicit field representation to infinity, without increasing the matrix order, so that the computational time is virtually unchanged.

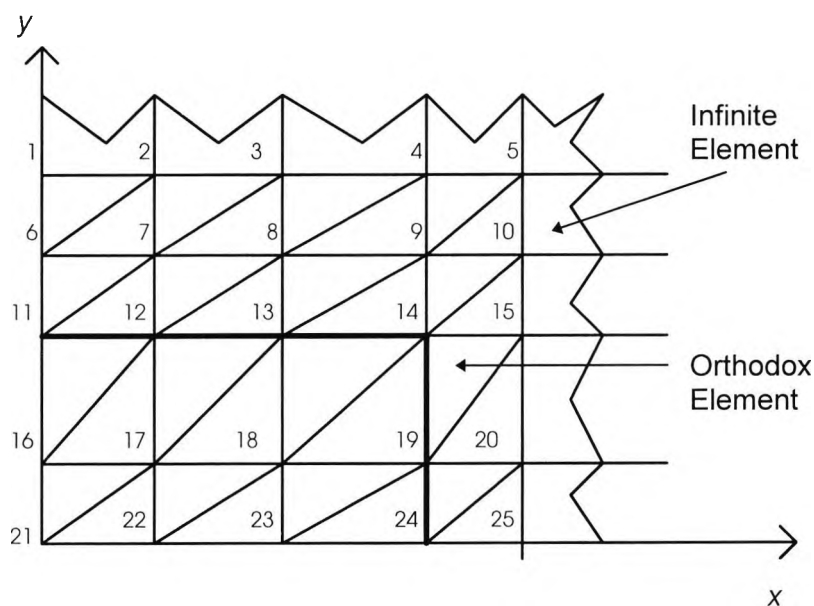


Fig. 2.7 Node representation of a rectangular dielectric waveguide, discretized into finite and infinite elements (two-fold symmetry assumed).

The shape functions of the infinite elements, which substitute the shape functions of the outer boundary of the orthodox elements, should decay exponentially in the direction where the field extends to infinity. For an infinite element extending towards infinity in the x -direction, an exponential decay in x and a conventional shape

function dependence in the y -direction can be assumed, given as (Rahman and Davies, 1984a):

$$N_i(x, y) = f_i(y) \exp(-x / L) \quad (2.72)$$

where $f_i(y)$ is a function of y depending on the dimensions of the infinite element and L is the decay length.

In a similar way shape functions can be obtained for infinite elements that extend to infinity along the y or both the x and y directions. The decay length depends on the structure under consideration and it can only be assumed any reasonable value during the first iteration. When a first solution to the problem is obtained, the decay parameters along each direction are calculated, and the values obtained are substituted in the shape function during the next iteration, in order to achieve the field decay along the required boundary of the structure.

2.10 Boundary conditions

It has been shown in Section 2.4 that the \mathbf{H} -field variational formulation (2.31) automatically satisfies the boundary conditions along the electric wall, Γ_e , but forced boundary conditions, of the type $n \times \mathbf{H} = 0$, can be imposed along any magnetic wall, Γ_m , particularly to exploit any symmetry.

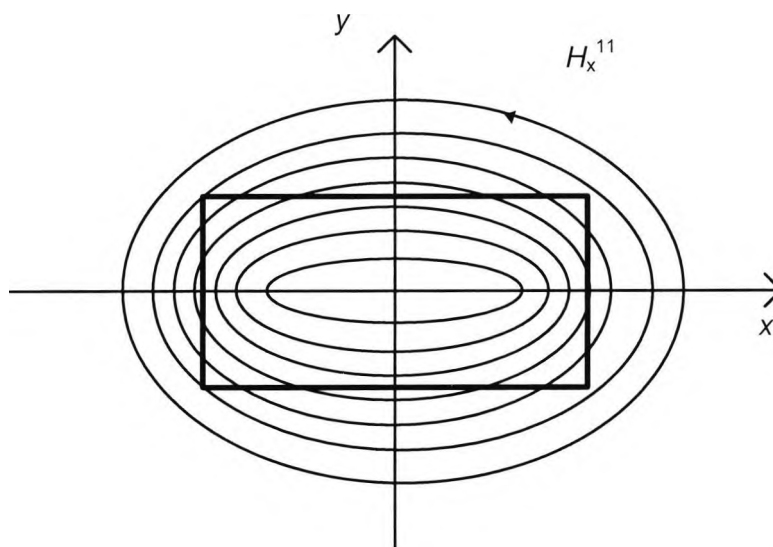


Fig.2.8 Representation of the H_x^{11} mode across a rectangular dielectric waveguide.

In the analysis of the optical waveguide problem, it is often convenient to take advantage of the symmetry of the structure, and therefore different boundary conditions must be applied. In the case of the rectangular dielectric waveguide, shown in Fig.2.7, where symmetry along the x and y -axis is assumed, different types of boundary conditions are considered, in order to achieve either a TE or TM solution. By considering a TM solution, the H_x^{11} mode, shown in Fig.2.8, must be continuous along the axis of symmetry. The continuity of the H_x^{11} mode along the y -axis is established by imposing a magnetic wall boundary condition (2.18), $n \times \mathbf{H} = 0$, to eliminate only the transverse components, H_y and H_z , along that boundary. On the other hand, the electric wall boundary condition (2.17), $n \cdot \mathbf{H} = 0$, should be imposed along the x -axis, to eliminate only the H_y component along that boundary, therefore to allow the continuity of the H_x and H_z components of the magnetic field. In a similar way, boundary conditions can be applied for the TE modes and further boundary conditions can also be applied when even or odd modes are required.

In the FEM analysis of the above problem, boundary conditions are imposed, by setting the boundary nodal field values as either known or unknown quantity. When the nodal field values along a boundary are set to zero (known via the boundary condition), then automatically the size of the global matrices reduces by a row or a column, thus, reducing storage requirements and computational time.

2.11 Spurious modes

The use of vector formulations, for the analysis of optical waveguides, results in the presence of some non-physical, spurious solutions along with the physical solutions of the system. The reason of the appearance of such spurious modes has not been fully resolved, but it could be due to various factors, such as enforcement of boundary conditions, or due to the nonzero divergence of the trial fields (Rahman and Davies, 1984a). In the \mathbf{H} -field formulation, the associated Euler equation is consistent with the two curl Maxwell's equations (2.4, 2.5), but does not imply the $\nabla \cdot \mathbf{B} = 0$, relation (2.7), which may be the cause of the spurious modes.

The identification of the spurious modes amongst the physical modes can be difficult, when a set of eigenmodes is computed. Sometimes spurious modes can be

spotted, from their dispersion curves, or by their eigenvectors, where the field varies in an unreasonable, sometimes in a random way along the cross section of the waveguide. Rahman and Davies (1984a) have developed a procedure which gives a reasonable identification of the spurious modes. In the above approach, the divergence of the magnetic field, $\nabla \cdot \mathbf{H}$, is calculated for each eigenvector, and when the value obtained is high, it is assumed that the eigenmode does not satisfy the divergence condition, and therefore it is a spurious mode.

Several approaches have been used, most of them aiming to force the condition $\nabla \cdot \mathbf{H} = 0$, which is considered the main cause of spurious modes. Rahman and Davies (1984b) have developed a penalty function method, in which an integral is added to the \mathbf{H} -field formulation, so that the resulting Euler equation is the Helmholtz equation, plus the $\nabla \cdot \mathbf{B} = 0$ condition. The variational formulation then becomes as (Rahman and Davies, 1984b):

$$\omega^2 = \frac{\int_{\Omega} (\nabla \times \mathbf{H})^* \hat{\epsilon}^{-1} (\nabla \times \mathbf{H}) d\Omega + \frac{\alpha}{\hat{\epsilon}_0} \int_{\Omega} (\nabla \cdot \mathbf{H})^* \cdot (\nabla \cdot \mathbf{H}) d\Omega}{\int_{\Omega} \mathbf{H}^* \hat{\mu} \mathbf{H} d\Omega} \quad (2.73)$$

where, α is the penalty coefficient.

The value of the penalty coefficient, α , can be estimated to be around $1/\epsilon_g$, where ϵ_g is the dielectric constant of the core of the optical waveguide. By introducing a higher penalty coefficient, further reduction of the spurious modes is achieved, but this results in the slight deterioration of the effective index of the optical waveguide, and therefore trade off should be considered in order to obtain the best solution. The method can be used more effectively, in conjunction with the infinite elements, resulting in the reduction of some unwanted field values along the boundaries by using appropriate decay parameters.

Another approach for the complete elimination of spurious modes is the use of the \mathbf{H} -field formulation in terms of the transverse field components, known as the \mathbf{H}_t formulation (Hayata et al., 1986b; Lu and Fernandez, 1993b). In this method, the magnetic field along the direction of propagation, H_z , is represented in terms of the other two transverse components of the magnetic field, H_x and H_y as:

$$H_z = \frac{1}{j\beta} \left(\frac{\partial H_x}{\partial x} + \frac{\partial H_y}{\partial y} \right) \quad (2.74)$$

Equation (2.74) corresponds to $\nabla \cdot \mathbf{H} = 0$, therefore the divergence condition is automatically satisfied in the variational formulation and no further action dealing with the spurious modes is required.

2.12 Summary

In this chapter, the application of the Finite Element Method, based on the variational principle, in the solution of the optical waveguide problem, has been examined. The properties of the various formulations have been presented and the development of the approach, by using the vector \mathbf{H} -field formulation has been analysed. Various aspects of the use of the method, such as boundary conditions, shape functions and infinite elements for open-boundary waveguides, have also been considered. Common problems, such as the existence of spurious modes and methods of eliminating them have been presented.

This chapter forms the basis for the work described in the subsequent Chapters, where the application of the Finite Element Method in conjunction with the perturbation technique is considered for the gain/loss analysis of several different types of optical waveguide.

3

Loss/Gain Analysis and Perturbation Technique

3.1 Introduction

Many optoelectronic devices, such as semiconductor lasers, optical amplifiers, and metal-clad TE-TM mode splitters, for example, contain materials with complex refractive indices, introducing modal gain or loss. As lightwave technology continues to advance, integrated optical circuits are becoming more complicated, the number of metal layers and the line-to-line spacing increases, mutual inductances and coupling capacitances are becoming more important, and therefore the effective modelling of loss and gain in such devices is considered critical (Lee, 1994). The design of metal clad TE-TM mode splitters (Soldano *et al.*, 1994), which are required in many optical communications applications, such as polarization shift keying and polarization diversity multiplexing, is based on the control of the absorption performance of the device. Laser gain in semiconductor integrated optics devices, in contrast with the loss due to absorption, scattering or leakage, of the semiconductors materials (Deri *et al.*, 1991), is another area where gain and loss investigation is important. Also, the development of high gain Er⁺ doped fiber amplifiers (Giles and Desurvire, 1991), which has increased the efficiency and capacity of optical telecommunication systems, is

another factor that emerged wider investigation of the gain properties of optoelectronic devices.

All the above advances in lightwave technology during the last decade have encouraged the development of various techniques, dealing with the solution of gain and loss problems encountered in the modelling of optoelectronic devices. The typical lossy waveguide problem can be solved, as in the lossless case, by two different approaches. For simple structures, like the planar waveguide, analytical or semi-analytical methods can be used, but when the geometry of the optical waveguide becomes more complicated, numerical techniques are preferred. In this Chapter, the various approaches for the solution of optical waveguide problems, by using both analytical and numerical techniques, are discussed, with the main focus given to the finite-element approach in conjunction with the perturbation technique, which has been widely used in this work for many applications.

3.2 Analytical solutions

Dielectric slabs, which are three-layer planar waveguides, are considered as the most basic optical waveguide structures, and their propagation characteristics can be described by simple mathematical expressions, which can be solved by an analytical approach. Guided waves propagating in such structures are considered only in one dimension and can be represented by the transcendental equation (Reisinger, 1973), where the propagation constant has to be evaluated. By introducing a metallic element for one or two of their layers of the above structures, metal-clad planar waveguides are formed and the transcendental equation becomes complex, due to the lossy nature of the metal layer, which is represented by a complex dielectric constant with negative real part.

Multilayer planar waveguides are employed in many applications, such as the use of buffer layers to separate electrodes from a guide, and the use of metal layers in TE/TM polarization splitters and in semiconductor lasers to achieve separate confinement for the charge carriers and the photons (Tamir, 1990). The solution of the above waveguides can be obtained by considering the wave equations of the dominant electromagnetic fields of each layer, for TE or TM polarizations and by applying repeatedly boundary conditions for each layer interface. For the loss analysis of the

above structures complex refractive indices for the lossy elements are considered, and therefore all the equations become complex.

3.2.1 Maxwell's equations for the planar waveguide

In planar optical waveguides, the light is confined in one dimension only, therefore, Maxwell's equations (2.4-2.7) can be simplified into their scalar form for the determination of the guided TE or TM modes in the above structures.

By choosing the light confinement to be in the y -direction, the partial derivative along the x -direction can be assumed to be $\partial/\partial x=0$. For the TE modes, where there is no longitudinal component of the electric field ($E_z=0$), by using the Maxwell's curl equations (2.4 and 2.5) the only non-vanishing fields obtained are H_y , H_z and E_x , which can be defined as:

$$H_y = \frac{\beta}{\omega\mu} E_x \quad (3.1)$$

$$H_z = \frac{1}{j\omega\mu} \frac{\partial E_x}{\partial y} \quad (3.2)$$

$$E_x = \frac{\beta}{\omega\epsilon} H_y + \frac{1}{j\omega\epsilon} \frac{\partial H_z}{\partial y} \quad (3.3)$$

where β is the phase constant, ω is the angular frequency and μ and ϵ are the permeability and permittivity, respectively.

For the TM modes, where there is no magnetic field along the direction of propagation ($H_z=0$), by using again Maxwell's curl equations (2.4 and 2.5) the only non vanishing fields obtained are E_y , E_z and H_x , which can be expressed as:

$$E_y = -\frac{\beta}{\omega\epsilon_0} H_x \quad (3.4)$$

$$E_z = -\frac{1}{j\omega\epsilon} \frac{\partial H_x}{\partial y} \quad (3.5)$$

$$H_x = -\frac{\beta}{\omega\mu} E_y - \frac{1}{j\omega\mu} \frac{\partial E_z}{\partial y} \quad (3.6)$$

3.2.2 The transcendental equation

By combining the equations (3.1-3.3) and (3.4-3.6) defined in the previous section, for each of the TE and TM modes, the scalar wave equation for the isotropic, three-layer, planar optical waveguide can be obtained, which can be expressed as (Koshiba, 1992a):

$$\frac{\partial^2 \phi}{\partial y^2} + (k_0^2 n^2 - \beta^2) \phi = 0 \quad (3.7)$$

where, k_0 is the wavenumber and ϕ is the dominant field component for each polarization *i.e.* E_x for the TE mode and H_x for the TM mode.

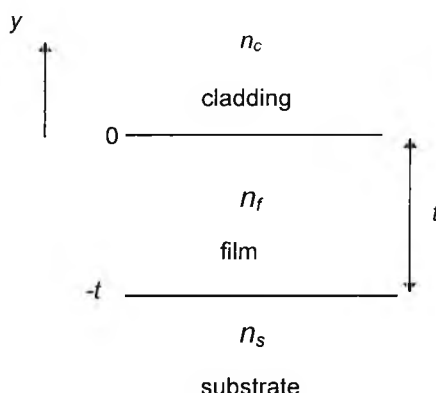


Fig.3.1 Three-layer planar optical waveguide.

In a three-layer planar optical waveguide, shown in Fig.3.1, provided that $n_f > n_s > n_c$ a guided mode satisfies the condition, $k_0 n_s \leq \beta \leq k_0 n_f$, where n_f , n_s and n_c are the refractive indices of the core, the substrate and the cladding of the guide, respectively. Then the solution to the wave equation can be expressed as (Koshiba, 1992a):

$$\Phi = \begin{cases} A_c \exp(-\alpha_c y) & 0 \leq y \\ A_f \cos(k_f y) + B_f \sin(k_f y) & -t \leq y \leq 0 \\ A_s \exp[\alpha_s (y + t)] & y \leq -t \end{cases} \quad (3.8)$$

where, A_c , A_f , A_s and B_f are arbitrary constants and α_c , α_s and k_f , can be defined by:

$$\alpha_c = \sqrt{\beta^2 - k_0^2 n_c^2} \quad (3.9)$$

$$\alpha_s = \sqrt{\beta^2 - k_0^2 n_s^2} \quad (3.10)$$

$$k_f = \sqrt{k_0^2 n_f^2 - \beta^2} \quad (3.11)$$

By applying the boundary conditions for continuity of the tangential components of the electric and magnetic fields (2.13 and 2.14), which are E_x and H_z for the TE mode and E_y and E_z for the TM mode, the phase shift relations can be obtained, which may be expressed as (Koshiba, 1992a):

$$\Phi_s = \tan^{-1}(m_s \alpha_s / m_f k_f) \quad (3.12)$$

$$\Phi_c = \tan^{-1}(m_c \alpha_c / m_f k_f) \quad (3.13)$$

where m_c , m_s and m_f can be defined by (Koshiba, 1992a):

$$m_c = m_s = m_f = 1 \quad (3.14)$$

for the TE mode and,

$$m_c = 1/n_c, \quad m_s = 1/n_s, \quad m_f = 1/n_f \quad (3.15)$$

for the TM mode.

Then, the condition for the existence of a guided mode is the total phase shift in the y direction during one cycle and it must be an integral multiple of 2π . This can be expressed by the transcendental, or eigenvalue equation as (Koshiba 1992a; Tamir 1990):

$$k_f t - \Phi_c - \Phi_s - q\pi = 0 \quad (3.16)$$

where, $q = 0, 1, 2, \dots$

3.2.3 Solution of the complex transcendental equation

In the case of a planar optical waveguide incorporating loss or gain, the refractive indices of the layers with loss or gain are considered complex, and therefore, the transcendental equation becomes complex. This can be achieved by substituting the complex refractive indices and by replacing the phase constant β , by the complex propagation constant, γ , which is defined by:

$$\gamma = \alpha + j\beta \quad (3.17)$$

where α is the attenuation constant.

The solution of the complex transcendental equation can be obtained by using an incremental search method, as shown schematically in the flow chart diagram in Fig.3.2. In the above approach, the dominant parameter, the phase constant, β , is firstly calculated as for a loss-less case by neglecting the imaginary part of the complex refractive indices. The attenuation constant, α , is then estimated by using the loss-free phase constant and the imaginary part of the refractive index. Further, the two constants are iterated until the solutions become stable and converge to their final values.

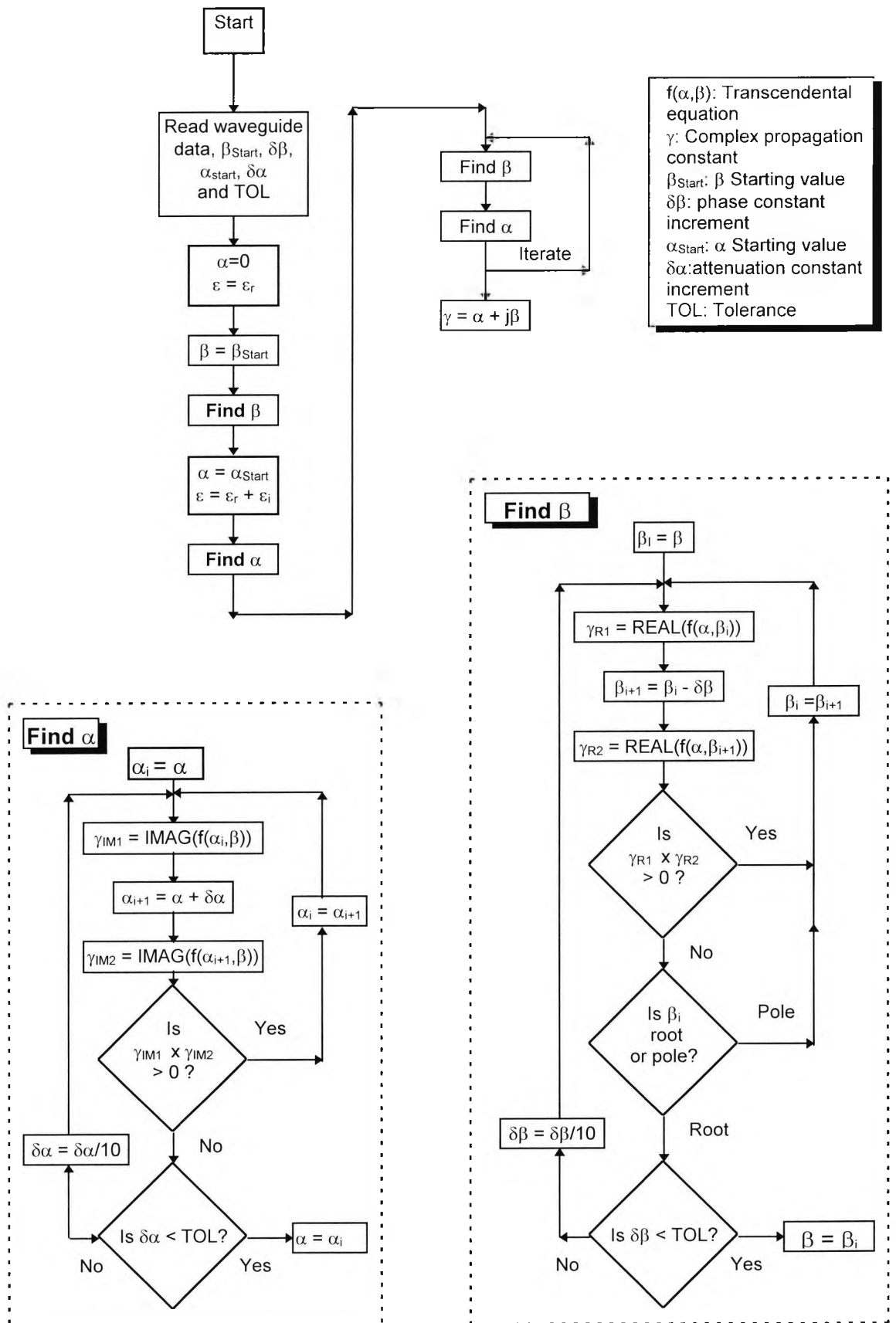


Fig.3.2 Flow-chart diagram for the solution of the complex transcendental equation.

3.2.4 The Effective Index Method

In 1969 Marcatili introduced a simple method for the solution of optical waveguides, in which a rectangular dielectric waveguide was approximated by two slab waveguides, one in each transverse direction, and the wave equations for the two directions were solved simultaneously. In 1970, Knox and Toullos introduced the effective index method (EIM), an improvement of the Marcatili's method, by incorporating an effective dielectric constant which served to couple the two slab guides and applied it to the solution of the dielectric image guide and directional coupler. The method is based on the assumption that the modes are far from cut-off, resulting in the confinement of the field exclusively in the core region, thus leaving little field energy carried by the surrounding media (Marcuse, 1991).

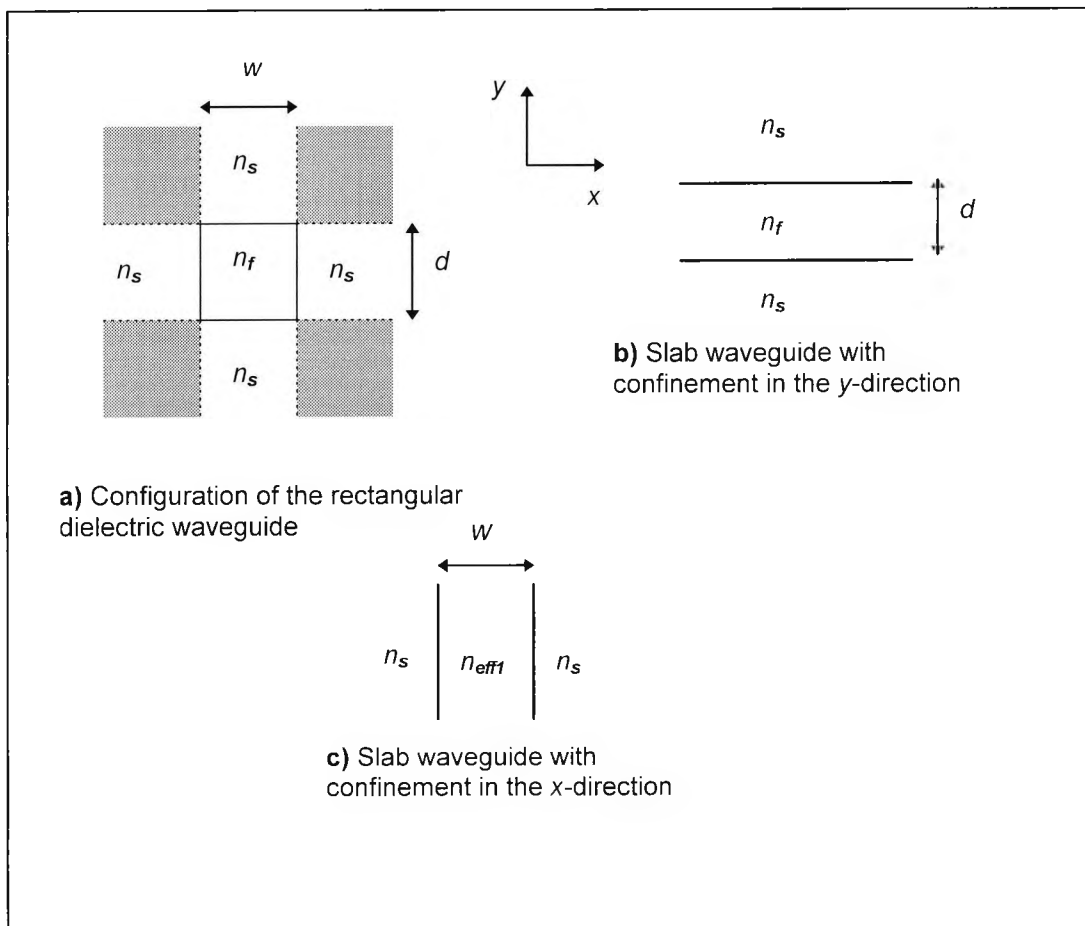


Fig.3.3 Solution of the rectangular dielectric waveguide by the Effective Index Method.

The EIM can be applied to the solution of the rectangular dielectric waveguide, as shown in Fig.3.3. The cross section of the structure can be divided into different

dielectric regions, as shown in Fig.3.3.a, where n_f and n_s , are the refractive indices of the core and the substrate respectively. For a well-confined mode, the field intensity in the shaded areas of the above structure is assumed negligible, and therefore these regions are not considered in the solution. The waveguide can then be approximated by two planar slabs, where the light is confined in either the y - or the x -direction, as shown in Fig.3.3.b and Fig.3.3.c, respectively. Firstly, the effective index of the first slab, shown in Fig.3.3b, is calculated by solving the transcendental equation (3.16) for a planar optical waveguide along the y -direction, and the value obtained is then used as the refractive index of the core of the second slab, as shown in Fig.3.3.c. The effective index, which is then calculated by solving the transcendental equation along the x -direction, approximates the effective index of the original rectangular dielectric waveguide. The rectangular dielectric optical waveguide can support either the TE or TM modes, and therefore, the type of solution of the transcendental equation along each direction depends on the mode requirements.

For the TE guided mode of the rectangular dielectric optical waveguide, the H_y and E_x are the dominant field components. After imposing the tangential field continuity boundary conditions along the y -direction, for the planar slab shown in Fig.3.3.b, the E_x field component can be obtained, via a TE solution of the transcendental equation, along that direction. Then by considering the second planar slab, shown in Fig.3.3.c, the H_y field component can be obtained by applying a TM solution to the transcendental equation, along the x -direction.

In the same way, for the TM guided mode of the rectangular waveguide, where the H_x and E_y are the dominant field components, a TM and a TE solution of the transcendental equation can be applied along the y - and the x -direction, respectively for the above two planar waveguides.

When one or more layers incorporates loss or gain, the corresponding refractive indices becomes complex, therefore, all the equations are transformed into complex by introducing the complex propagation constant, γ , and the solution for each polarization is obtained by the approach described in the previous section.

3.2.5 Multilayer planar waveguides

As the number of layers in a planar optical waveguide increases, the transcendental equation become more complicated, therefore, a more generalized algorithm is necessary for the solution of multilayer structures, which can be applied for any number of dielectric layers. The analysis of the above waveguides is based on the same principles used in the analysis of simple three-layer planar structures, with the only difference being the repeated application of boundary conditions at each layer interface. In this approach, the various coefficients of the solutions of the wave equations for each interface are assembled in a matrix form and the propagation characteristics of the waveguide are determined by the evaluation of the determinant of the above matrix.

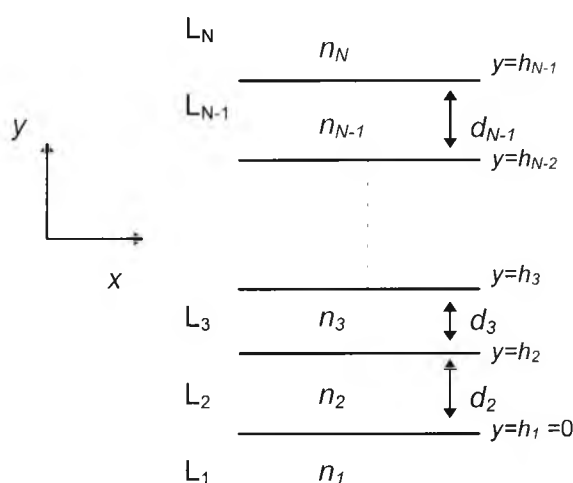


Fig.3.4 Multilayer planar waveguide

A multilayer planar optical waveguide is being considered, with N number of layers, as shown in Fig.3.4., where n_k and d_k denote the refractive index and the thickness of the k th inner layer, L_k , respectively, and h_k , the height of each interface with respect to the x -axis. It should be noted that the thickness of the two semi-infinite cover layers are not required. In the analysis a TE solution is being considered and complex refractive indices are being introduced in order to handle optical waveguides with loss or gain. By using the complex propagation constant, γ , the wave equation (3.7) for the E_x component of the electric field for the k th layer, L_k , can be expressed as:

$$\frac{\partial^2 E_{x,k}}{\partial y^2} - (\gamma^2 - k_0^2 n_k^2) E_{x,k} = 0 \quad (3.18)$$

where $E_{x,k}$ and n_k are the E_x component of the electric field and the complex refractive index for layer the k th layer, L_k , respectively.

The general solution of the above differential equation is given by (Schlereth and Tacke, 1990):

$$E_{x,k} = A_k \exp(p_k(y - h_k)) + B_k \exp(-p_k(y - h_k)) \quad (3.19)$$

where A_k and B_k are arbitrary constants for the k th layer and p_k is defined by:

$$p_k = \sqrt{\gamma^2 - k_0^2 n_k^2} \quad (3.20)$$

Also, from Maxwell's equations for the TE modes of a planar optical waveguide (3.2), the H_z component of the magnetic field at the k th layer can be expressed as

$$H_{z,k} = \frac{p_k}{j\omega\mu} (A_k \exp(p_k(y - h_k)) - B_k \exp(-p_k(y - h_k))) \quad (3.21)$$

By applying boundary conditions (2.13 and 2.14), at the interface, $y=h_k$, between the layers L_k and L_{k+1} , the continuity of the transverse components of the electromagnetic field (E_x and H_z for TE mode) for each layer, with respect to the boundary of the top layer, h_{k+1} , can be established by:

$$E_{x,k}(h_{k+1}) - E_{x,k+1}(h_{k+1}) = 0 \quad (3.22)$$

$$H_{z,k}(h_{k+1}) - H_{z,k+1}(h_{k+1}) = 0 \quad (3.23)$$

By using (3.19) and (3.21) the above equations can be evaluated as:

$$A_k \exp(\delta_k) + B_k \exp(-\delta_k) - A_{k+1} - B_{k+1} = 0 \quad (3.24)$$

$$A_k p_k \exp(\delta_k) - B_k p_k \exp(-\delta_k) - A_{k+1} p_{k+1} + B_{k+1} p_{k+1} = 0 \quad (3.25)$$

where

$$\delta_k = \rho_k d_k \quad (3.26)$$

By applying similar boundary conditions for each interface, a set of $2x(N-1)$ homogeneous algebraic equations, corresponding to the $N-1$ interfaces, is obtained, which can be arranged in a matrix form as:

$$[D] [A_1 \ B_1 \ A_2 \ B_2 \ \dots \ A_N \ B_N]^T = [0] \quad (3.27)$$

where $[D]$ is a $2(N-1) \times 2N$ complex matrix of band-diagonal form and contains the coefficients of the constants A_k and B_k , which can be evaluated in terms of the complex refractive indices, n_k , and thickness, d_k , for each layer and the complex propagation constant, γ .

It should be noted that the bottom layer axial distance (y) is assumed zero, and therefore equations (3.24) and (3.25) at the first interface, are converted to:

$$A_1 + B_1 - A_2 - B_2 = 0 \quad (3.28)$$

$$\rho_1 A_1 + \rho_1 B_1 - \rho_2 A_2 + \rho_2 B_2 = 0 \quad (3.29)$$

As it is well known, a homogeneous system admits a non-zero solution if and only if the determinant of the system is zero. Therefore, the value of the complex propagation constant, γ , that makes the determinant of matrix D equal to zero, is the solution to the multilayer planar optical waveguide problem. To obtain the above solution, the incremental search method, described in section 3.2.3 by the flowchart in Fig.3.2, has been used. For the three-layer planar optical waveguide the transcendental equation is evaluated in terms of the real and imaginary part of the complex propagation constant, γ . In the multilayer planar structure, the attenuation constant, α , and the phase constant, β , are substituted in matrix D for each increment, until the determinant becomes zero and the required tolerance is achieved. Detailed calculations for a typical example of a four-layer planar optical waveguide are shown in Appendix B.

For the analysis of the TM modes, similar analysis has been performed, but with H_x and E_z being the components of the electromagnetic field for which the continuity conditions were enforced.

3.3 Numerical solutions for gain/loss analysis

Analytical or semi-analytical approximations can be useful in the analysis of 2D, planar optical waveguides, or some simple 3D structures, such as the rectangular dielectric and the simple rib waveguide. As the shapes of the structures are becoming more complicated, the order and the complexity of the equations increases, therefore numerical techniques are preferable for the solution of optical waveguides with complex geometry.

The Finite Element Method (FEM), which is one of the most powerful numerical techniques in the analysis of optical waveguides with an arbitrary cross section, has been mainly focussed on a loss-free system. From the recent advances in lightwave technology emerged the development of various techniques which may be used in conjunction with the FEM or other numerical approaches, capable of handling optoelectronic devices incorporating loss or gain.

Among the several methods, a FEM formulation in terms of the longitudinal components, E_z - H_z has been applied on waveguides containing dissipative materials (McAulay, 1977) and on microstrip lines (Aubourg *et al.*, 1983). The main drawback of the above approach is the appearance of non-physical, spurious solutions, which couple with the physical solutions and make the distinction a difficult task, besides the E_z - H_z formulation is not suitable for optical waveguides.

A complex full-vector FEM formulation has also been used in the analysis of lossy microstrip lines (Lee, 1994) and for computing electromagnetic fields inside lossy dielectric objects (Paulsen *et al.*, 1988), with application to hypothermia research. Apart from the presence of spurious solutions in the above approach, which can be treated partially by the use of the penalty method (Rahman and Davies, 1984b) and other techniques, the main disadvantage of such a complex full-vector approach, is the generation of large size complex matrices, which require the availability of efficient solvers and computers with fast processors and large memory.

One of the most accurate methods for the solution of optical waveguides with loss or gain is a FEM approach based on the transverse magnetic field components (Hayata *et al.*, 1988; Lu and Fernandez, 1993a; Cheung *et al.*, 1995), known also as the \mathbf{H}_t formulation. In this approach the divergence condition, $\nabla \cdot \mathbf{H} = 0$, is expressed in terms of H_z as:

$$H_z = \frac{1}{\gamma} \left(\frac{\partial H_x}{\partial x} + \frac{\partial H_y}{\partial y} \right) \quad (3.30)$$

By using the above equation for the H_z component, in the vectorial wave equation (2.30), the magnetic field is expressed in only two-components, and therefore the size of the matrices is reduced by two-thirds. Additionally, since the divergence condition is satisfied all the spurious solutions are eliminated. In most of the formulations based on the \mathbf{H}_t approach, the generated global matrices are in a dense form, and require dense complex matrix solvers which are inefficient. Recently Lu and Fernandez (1993b), developed an \mathbf{H}_t formulation, which yields sparse matrices and used an efficient complex sparse matrix solver for the solution of lossy dielectric waveguides, which improved the computational time required for such problems. Further, Cheung *et al.* (1995), developed an \mathbf{H}_t formulation based on the Finite Difference Method and applied that approach in the analysis of rib semiconductor laser waveguides and multiple quantum well structures.

Other techniques developed for loss/gain analysis are based on the scalar approximation of the FEM, which is free of spurious solutions and has less computational time and memory requirements. Such an approach has been used in conjunction with the perturbation technique, for the TE solution of Buried Heterostructure diode lasers (Hayata *et al.*, 1986a) and for the quasi-TEM analysis of microwave transmission lines, where the conductor and dielectric losses were estimated (Pantic and Mittra, 1986).

In the present work, scalar and vector formulations of the FEM element method, in conjunction with the perturbation technique have been developed and used extensively for the estimation of the complex propagation characteristics of several types of optical waveguides, incorporating small amounts of loss or gain, a feature that most practical optoelectronic devices possess.

3.4 The perturbation technique

Perturbation theory is a widely used powerful technique that gives an (approximate) answer to a problem that is a small perturbation from some other problem to which a solution is available. For example, fibers that are slightly anisotropic or absorptive are perturbations of the circular loss-less fiber with an isotropic refractive-index profile. By taking advantage of the smallness of the perturbation, approximation techniques can be used to derive satisfactory expressions for the modes of the perturbed fiber, in terms of the known modes of the unperturbed fiber (Snyder and Love, 1991).

Perturbation formulae can be derived:

a) by approximating the answer with a series expansion, like Taylor series, in terms of the small perturbation parameter.

or b) directly from the variational expression. If there exists a variational expression this is quicker and is a more powerful approach.

A perturbation formula will automatically emerge if the known solution to the unperturbed problem is substituted as a trial function into a variational expression valid for the perturbed problem. The known solution must be an admissible function, and either it is an essential boundary condition, or the natural boundary conditions corresponds to the physical problem (Davies, 1989).

Perturbation theory can be applied in the gain and loss analysis of the optical waveguide problem, by approximating the perturbed phase constant, β , and field profiles \mathbf{H} and \mathbf{E} due to loss or gain, with the unperturbed values $\bar{\beta}$, $\bar{\mathbf{E}}$ and $\bar{\mathbf{H}}$, which are the solutions to the loss-free optical waveguide problem. The above approximation is valid for optical waveguides with *small* amounts of loss or gain. In the present work, the term *small*, which cannot be easily defined, is being investigated by calculating the amount of loss or gain in the dielectric material, at which the perturbation method fails. This is being achieved by comparing the results obtained in the analysis of simple optical waveguide structures with similar results calculated by using analytical approximation methods. The loss or gain of a dielectric material is defined by the imaginary part, n'' of the complex refractive index, \bar{n} , and therefore the value of n'' , at which the solution obtained by the perturbation approach diverges from the analytical

approximation can be considered as the limit of the perturbation technique. The loss or gain of the optical waveguide cannot be characterised as *small*, for values of the imaginary part of the refractive index, beyond the above limit.

In a dielectric medium, the attenuation constant, α , due to dielectric losses, can be expressed as (Pantic and Mittra, 1986):

$$\alpha = \frac{P_d}{2P_0} \quad (3.31)$$

where P_d , is the power dissipation in the dielectric material and P_0 , is the time-averaged power flow.

By considering a cross section, Ω , of a dielectric optical waveguide, with any number of subregions, Ω_k , incorporating loss or gain, expressed as a complex dielectric constant, $\bar{\epsilon}_k$, for each subregion, the perturbation method can be applied by evaluating the attenuation constant for the whole guide, in terms of the electromagnetic field as (Pantic and Mittra, 1986; Mirshekar-Syahkal and Davies, 1982):

$$\alpha = \frac{\omega \sum_k \epsilon_k \tan \delta_k \int_{\Omega_k} |\mathbf{E}_0|^2 d\Omega}{2 \operatorname{Re} \int_{\Omega} (\mathbf{E}_0 \times \mathbf{H}_0^*) \cdot \hat{z} d\Omega} \quad (3.32)$$

where ω , is the angular frequency, \hat{z} is the unit vector along the z-axis, \mathbf{E}_0 and \mathbf{H}_0 are the unperturbed electric and magnetic field vectors for the loss-less condition respectively and $\tan \delta_k$ is the loss tangent of each subregion defined by:

$$\tan \delta_k = \frac{\epsilon'_k}{\epsilon_k} \quad (3.33)$$

where ϵ'_k and ϵ_k is the imaginary and real part respectively, for the complex refractive index of each subregion, and the summation is carried out over all subregions.

The perturbation equation (3.32), is based on the assumption that the unperturbed electric, \mathbf{E}_0 , and magnetic, \mathbf{H}_0 , field components remain unchanged in the presence of loss and that the value of the loss tangent is very small, i.e. $\epsilon_i \ll \epsilon_r$. It can be extended to any optical waveguide structure which has a number of subregions that

incorporate loss or gain. Throughout this work, the sign of the attenuation constant defines whether an optical waveguide has loss or gain. A negative sign of α indicates loss, while a positive denotes gain. In some cases, where the optical waveguide exhibits gain, the attenuation constant is referred as the gain constant, g .

3.4.1 Finite Element Method with Perturbation

The perturbation method, described in the previous section, can be used in conjunction with the FEM, to determine the loss/gain characteristics of an optical waveguide. As was shown in Section 2.4, a loss-free optical waveguide problem can be formulated to a standard eigenvalue problem (2.38), where the eigenvalue corresponds to the square of the free space wavenumber, k_0^2 , and the eigenvectors to the magnetic field \mathbf{H} . By assuming that the above eigenvalue of the discretised model of the loss-free optical waveguide is perturbed by a small amount in the presence of a small loss, this can be directly substituted in a discretized form of the perturbation equation (3.32) in order to estimate the attenuation constant.

In the present work, discretized perturbation equations have been developed, based on the scalar formulation for the TE and TM modes and the full vector \mathbf{H} -field formulation, to determine the attenuation characteristics of the optical waveguide problem.

3.4.1.1 Scalar formulation for the TE and TM modes

In the scalar approximation of the FEM, where the field is predominantly TE or TM, variational formulations can be expressed in terms of the dominant transverse component of the above modes, for the general 3D optical waveguide structure.

By considering E_x as the dominant field component in the TE mode analysis ($E_z=0$) of a loss-free isotropic optical waveguide, E_y can be assumed negligible, and therefore, the scalar wave equation obtained from the Maxwell's equations (2.4-2.6) can be expressed as (Mabaya *et al.*, 1981):

$$\frac{\partial^2 E_x}{\partial x^2} + \frac{\partial^2 E_x}{\partial y^2} - k_0^2 n^2 E_x + \beta^2 E_x = 0 \quad (3.34)$$

By applying the FEM approach described in Section 2.4, the above equation can be expressed in integral form as:

$$\iint_{\Omega} \left(\frac{\partial E_x^*}{\partial x} \frac{\partial E_x}{\partial x} + \frac{\partial E_x^*}{\partial y} \frac{\partial E_x}{\partial y} + (\beta^2 - k_0^2 n^2) E_x^* E_x \right) d\Omega = 0 \quad (3.35)$$

By discretizing the waveguide region in triangular elements, E_x can be expressed in terms of the shape functions as:

$$E_x = [N]^T \{E_x\} \quad (3.36)$$

Then, the waveguide problem can be formulated in a matrix form to a standard eigenvalue problem as (Hayata *et al.*, 1986a):

$$[A]\{E_x\} - \beta^2 [B]\{E_x\} = \{0\} \quad (3.37)$$

where matrices A and B are defined by:

$$[A] = \sum_e \iint_{\Delta} \left(k_0^2 n^2 \{N\}^T \{N\} - \frac{\partial \{N\}^T}{\partial x} \frac{\partial \{N\}}{\partial x} - \frac{\partial \{N\}^T}{\partial y} \frac{\partial \{N\}}{\partial y} \right) dx dy \quad (3.38)$$

$$[B] = \sum_e \iint_{\Delta} \{N\}^T \{N\} dx dy \quad (3.39)$$

In the above equations, \sum_e stands for the summation over all the elements and \iint_{Δ} is the integration over each triangle.

By using a similar approach, for the TM modes ($H_z=0$), where H_x is considered to be the dominant field component and H_y is assumed negligible ($H_y=0$), the scalar wave equation can be expressed as:

$$\frac{1}{n^2} \frac{\partial^2 H_x}{\partial x^2} + \frac{1}{n^2} \frac{\partial^2 H_x}{\partial y^2} + \frac{\beta^2}{n^2} H_x^2 - k_0^2 H_x^2 = 0 \quad (3.40)$$

By applying the FEM approach, similar as for the TE modes, the problem can be expressed in matrix form as:

$$[A']\{H_x\} - \beta^2 [B']\{H_x\} = \{0\} \quad (3.41)$$

where for this case matrices $[A']$ and $[B']$ are defined by

$$[A'] = \sum_e \iint_{\Delta} \frac{1}{n^2} \left(k_0^2 n^2 \{N\}^T \{N\} - \frac{\partial \{N\}^T}{\partial x} \frac{\partial \{N\}}{\partial x} - \frac{\partial \{N\}^T}{\partial y} \frac{\partial \{N\}}{\partial y} \right) dx dy \quad (3.42)$$

$$[B'] = \sum_e \iint_{\Delta} \frac{1}{n^2} \{N\}^T \{N\} dx dy \quad (3.43)$$

The global matrices of the above eigenvalue equations (3.37) and (3.41) can be assembled in a one-dimensional storage scheme, as described in Section 2.8, in order to take advantage of the available efficient, real symmetric sparse solver, which exploits the sparsity (number of zero elements) of the matrices. The eigenvalue obtained by the solver of the FEM package, for the above equations, is β^2 , in contrast to the scalar formulation, presented by Mabaya *et al.* (1981), where the eigenvalue is k_0^2 . For the solution with a β^2 eigenvalue, the input parameters are, k_0 , and a trial solution for β which is an approximation to the phase constant of the required optical

mode. The eigenvalue and the associated eigenvector obtained, correspond to the phase constant, β , and the nodal field values of the required optical mode respectively. If the solutions for more than one optical modes are required, the eigenvalues are then calculated in ascending order, the last being the solution of the lowest order mode having a phase constant, β , closer to the trial input solution. Although the solution obtained by using the above formulation is not different from that obtained by the Mabaya *et al.* (1981) formulation, where the eigenvalue obtained is k_0^2 , the convergence of the latter approach is slower, because the trial solution has to be a very close approximation to the required phase constant, β , otherwise iterations are needed until convergence is achieved. It should be also noted that when more than one optical mode is needed, the solutions obtained by using the Mabaya *et al.* formulation are the eigenvalues which are closer to the trial input solution in the k_0^2 spectrum, and they appear in a descending order.

For a waveguide with a complex refractive index, \bar{n} , the eigenvalue equations (3.37) and (3.41) become complex and their solutions can be obtained by using a complex solver. This solver needs double the memory space within the computer and the available complex routines may be based on inefficient dense matrix algorithms with slow execution times. Moreover, in those formulations where the eigenvalue is related to the wavenumber, k_0 , rather than β , then complicated iteration techniques need to be used to find the real wavenumber by varying the complex eigenvalue of β . On the other hand, if the loss-free situation is considered initially, then the real eigenvalue equations (3.37) or (3.41) can be solved by using an efficient, real symmetric sparse solver, and the perturbation technique can be applied directly as soon as the unperturbed nodal field and phase constant values for the loss-free case are obtained.

3.4.1.2 Scalar FEM with perturbation

The scalar FEM formulation described in the previous section has been used in the present work, in conjunction with perturbation technique for the TE or TM solution of optical waveguide problems, with small-loss or gain. By assuming that the loss tangent (3.33) is small, the perturbed fields \mathbf{E} and \mathbf{H} were approximated by the fields obtained by solving (3.37) and (3.41), depending whether the field is TE or TM, using only the real part of the complex dielectric constant. The attenuation constant was then

calculated by using the perturbation formula, by performing simple matrix multiplication, directly from the results obtained for the loss-free system.

For the quasi-TE modes of an optical waveguide, the perturbation equation (3.32) has been expanded in terms of E_x , which is the dominant field component of the electric field for the above mode as:

$$\alpha = \frac{k_0^2 \sum_k \epsilon'_k \int_{\Omega_k} |E_x|^2 d\Omega}{2\beta \int_{\Omega} |E_x|^2 d\Omega} \quad (3.44)$$

By using the finite element discretization in terms of the shape functions to implement the integrations, equation (3.44) can then be expressed as:

$$\alpha = \frac{1}{2\beta} \frac{\{E_x\}^T [K] \{E_x\}}{\{E_x\}^T [B] \{E_x\}} \quad (3.45)$$

where the matrix $[B]$ is the same as in (3.39) and $[K]$ is defined by

$$[K] = \sum_e k_0^2 \epsilon'_e \iint_{\Delta} \{N\}^T \{N\} dx dy \quad (3.46)$$

It can be observed that equation (3.45) in this work is similar to equation (9) in the work of Hayata *et al.* (1986a), except that those authors had an additional term, k_0 , in their equation. It can be shown that $[K]$ has the same value as that of $\text{Im}[A]$ when a complex ϵ is considered and then on both sides of equation (3.45) the units are equal. Comparison of the results obtained by both the equations are discussed in section 5.2.

Detailed calculations for the derivation of equation (3.45) are shown in Appendix C.

For the quasi-TM modes, the perturbation equation (3.32) can be evaluated in terms of H_x which is the dominant magnetic field component, by using Maxwell's equations, as:

$$\alpha = \frac{\sum_k \frac{\epsilon'_k}{\epsilon_k^2} \int_{\Omega_k} \beta^2 |H_x|^2 + \left| \frac{\partial H_x}{\partial y} \right|^2 d\Omega}{2\beta \int_{\Omega} \frac{1}{\epsilon_k} |H_x|^2 d\Omega} \quad (3.47)$$

By using again the finite element discretization in terms of the shape functions to implement the integrations, equation (3.44) can then be expressed as:

$$\alpha = - \frac{1}{2} \frac{\{H_x\}^T [L] \{H_x\}}{\{H_x\}^T [B'] \{H_x\}} \quad (3.48)$$

where

$$[L] = (\beta[M] + \frac{1}{\beta}[Q]) \quad (3.49)$$

$$[M] = \sum_e \iint_{\Delta} \frac{\epsilon'_e}{\epsilon_e^2} \{N\}^T \{N\} dx dy \quad (3.50)$$

$$[Q] = \sum_e \iint_{\Delta} \frac{\epsilon'_e}{\epsilon_e^2} \{N_y\}^T \{N_y\} dx dy \quad (3.51)$$

$$\{N_y\} = \frac{\partial \{N\}}{\partial y} \quad (3.52)$$

Detailed calculations for the derivation of the above equations are also shown in Appendix C.

3.4.1.3 Full vector FEM with perturbation

The use of the scalar approximation of the FEM with the perturbation technique provides a quite accurate and time efficient computational tool for the determination of the propagation characteristics, in simple optical waveguide structures where the optical fields can be described as predominantly TE or TM. For a more accurate representation of the electromagnetic field, in optical waveguides a vector formulation is required, where all the field components are taken into account. Therefore, a perturbation formula has been developed, which has been used in conjunction with the full vector **H**-field formulation (2.30), for the estimation of the gain/loss properties of several optical waveguide structures, with small gain or loss. In the above approach, the contribution of all the three magnetic field components is considered in the calculation of the attenuation constant, α . By using Maxwell's equations to express the electric field, **E**, in terms of the magnetic field components, H_x , H_y and H_z , the perturbation formula (3.32) can be written as:

$$\alpha = \frac{\frac{1}{\omega} \sum_e \frac{\epsilon_e'}{\epsilon_e^2} \iint_{\Delta} \left\{ \left(\beta H_y - j \frac{\partial H_z}{\partial y} \right)^2 + \left(j \frac{\partial H_z}{\partial x} - \beta H_x \right)^2 + \left(j \frac{\partial H_x}{\partial y} - j \frac{\partial H_y}{\partial x} \right)^2 \right\} dx dy}{2 \sum_e \frac{1}{\epsilon_e} \iint_{\Delta} \left\{ \beta H_y H_y + \beta H_x H_x - \frac{\partial H_z}{\partial y} H_y - \frac{\partial H_z}{\partial x} H_x \right\} dx dy} \quad (3.53)$$

The components of the **H**-field for each element can be defined in terms of the shape function matrix (2.51) as:

$$\begin{Bmatrix} H_x \\ H_y \\ H_z \end{Bmatrix}_e = [N]^T \begin{Bmatrix} \{H_x\}_e \\ \{H_y\}_e \\ \{H_z\}_e \end{Bmatrix} \quad (3.54)$$

As it is shown in Appendix D, by using the above transformation, the components can be arranged in a matrix form, and the perturbation formula can be expressed as:

$$\alpha = \frac{\sum_e \frac{\epsilon_e'}{\epsilon_e^2} \{\mathbf{H}\}_e^T [C] \{\mathbf{H}\}_e}{2 \sum_e \frac{1}{\epsilon_e} \{\mathbf{H}\}_e^T [D] \{\mathbf{H}_t\}_e} \quad (3.55)$$

where the full $\{\mathbf{H}\}_e$ and transverse $\{\mathbf{H}_t\}_e$ element field vectors are

$$\{\mathbf{H}\}_e = \begin{Bmatrix} \{H_x\}_e \\ \{H_x\}_e \\ \{H_z\}_e \end{Bmatrix}, \quad \{\mathbf{H}_t\}_e = \begin{Bmatrix} \{H_x\}_e \\ \{H_y\}_e \end{Bmatrix} \quad (3.56)$$

Here, n_e and n_e' are the real and imaginary parts of the refractive indices in each element.

The element matrix $[C]$ is given by

$$[C] = [Q][Q]^T \quad (3.57)$$

where

$$[Q] = \iint_{\Delta} \begin{Bmatrix} \{0\} & -\beta\{N\} & j\{N_y\} \\ \beta\{N\} & \{0\} & -j\{N_x\} \\ -\{N_y\} & \{N_x\} & \{0\} \end{Bmatrix} dx dy \quad (3.58)$$

Similarly, the element matrix $[D]$ is given by:

$$[D] = \iint_{\Delta} \begin{Bmatrix} \beta[G] & [0] \\ [0] & \beta[G] \\ -[X] & -[Y] \end{Bmatrix} dx dy \quad (3.59)$$

where

$$[G] = \{N\}\{N\}^T \quad (3.60)$$

$$[X] = \{N_x\}\{N\}^T \quad (3.61)$$

$$[Y] = \{N_y\} \{N_x\}^T \quad (3.62)$$

where

$$\{N_x\} = \frac{\partial \{N\}}{\partial x} \quad (3.63)$$

A detailed derivation and evaluation of the perturbation formula (3.55) is also shown in Appendix D.

3.5 Field Confinement Method

It can be shown that the modal gain, g_m , of a well-confined mode, in a simple optical waveguide structure incorporating an active region, can be approximated by:

$$g_m = n' k_0 \Gamma \quad (3.64)$$

where n' is the imaginary part of the refractive index in the active region, k_0 is the wavenumber, and Γ is the power confinement factor given by:

$$\Gamma = P_{\text{active layer}} / P_{\text{guide}} \quad (3.65)$$

and P is the power in a given region, Ω , defined by:

$$P = \text{Re} \int_{\Omega} (\mathbf{E}_0 \times \mathbf{H}_0^*) \cdot \hat{z} d\Omega \quad (3.66)$$

where \mathbf{E}_0 , \mathbf{H}_0^* and Ω , are the electric and the conjugate of the magnetic field and the cross-section of the guide region, respectively.

Equation (3.64) provides a relatively easy way of estimating the gain/loss properties of a waveguide, in terms of the confinement factor. It can also be extended to structures with many active or lossy regions, each having a different imaginary part of the refractive index, as follows:

$$g_m = k_0 * \sum_{i=1}^L n_i' \Gamma_i \quad (3.67)$$

where, L is the number of active and lossy layers, n_i' is the imaginary part of the refractive index, which can take positive or negative values depending on whether there is gain or loss and Γ_i is the confinement factor of each layer.

3.6 Summary

In this chapter the several analytical and numerical approaches for the analysis of loss and gain in optical waveguides have been examined. An incremental search algorithm has been implemented for the solution of the complex transcendental equation, in planar optical waveguides, incorporating loss or gain. The above approach has been extended to the solution of simple optical waveguide structures with 2D mode confinement and loss/gain properties, via a complex effective index approach. A generalized algorithm for the solution of multilayer planar structures, with layers exhibiting loss/gain characteristics, has also been proposed. Further, a vector and a scalar finite element approach in conjunction with the perturbation approach has been developed, for the determination of the complex propagation characteristics of the arbitrarily shaped optical waveguide with dielectric regions incorporating small to medium loss or gain. Finally, an approximate approach for the loss/gain estimation in optical waveguides, in terms of the mode confinement factor, is suggested.

The above approaches are used in the subsequent chapters for the solution of several types of optical waveguides with loss/gain properties, and the details of the implementation described therein.

4

Gain/Loss analysis of planar waveguides

4.1 Introduction

The dielectric slab planar waveguide, shown in Fig.4.1, where a planar film of refractive index n_f is sandwiched between a substrate and a cladding material of lower refractive indices n_s and n_c respectively, is the simplest optical waveguide. By loading the film with a higher refractive index than either the substrate or the upper cladding on the substrate surface, the light can be trapped inside this film and as the thickness of the film increases, the effective refractive index sensed by the light increases. Therefore, the light is confined in the central area inside the thin film, resulting in the propagation of the light in the z direction. If $n_c=n_s$, then the slab waveguide is considered symmetric, otherwise it is asymmetric.

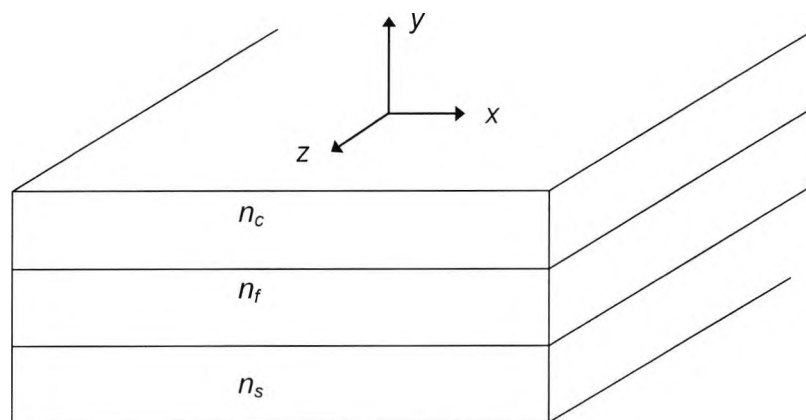


Fig.4.1 The dielectric slab or planar waveguide

The study of slab waveguides and their properties is very useful in understanding the basic concepts and waveguiding properties of more complicated dielectric waveguides, since, due to their simple geometry, guided and radiation modes can be described by simple mathematical expressions. However, slab waveguides are not only useful as models for more general types of optical waveguides, they are actually employed for light guidance in integrated optical circuits.

4.1.1 Surface plasmon polaritons

An electromagnetic wave travelling through a polarizable medium is modified by the polarization it induces and becomes coupled to it. This coupled mode of excitation is called a polariton and if the polarizable medium is identified, then the polariton is qualified. In the case of an electron plasma, the coupled modes are often called plasmon-polaritons (Boardman, 1982). Bulk polaritons propagate in an unbounded medium, while surface polaritons can be defined as the coupling of electromagnetic radiation to surface dipole excitation, which propagates in a wave-like manner along the interface between the two media. Surface plasmons exist in the boundary of a solid metal or semiconductor whose electrons behave like those of a quasi-free electron gas. These plasmons represent the quanta of the oscillations of surface charges, which are produced by exterior electric fields in the boundary (Raether, 1977). The Electromagnetic fields of the surface polariton can be either evanescent away from the interface (non-radiative surface polariton) or they can be oscillatory fields away from the interface (radiative surface polariton). In the first case, the amplitude of the field is maximum at the interface and decays exponentially away from it in a non-oscillatory

manner in a direction perpendicular to the propagation, while in the second, the field modes are unbound but maintained by balancing the energy radiating away from the surface with energy radiating to the surface. The surface plasmon-polaritons or surface plasma waves occur at the interface of a dielectric with a positive dielectric constant and a metal with a negative real part of the dielectric constant. In 1941 Fano pointed out that for non-magnetic media evanescent surface waves could exist for TM polarization only (Kovacs, 1982).

The properties of these waves are based on the solution of Maxwell's equations for an interface between two semi-infinite and isotropic dielectric media. They can be classified in four categories according to their dielectric function, $\epsilon(\omega)$, which are the 'Fano', 'Brewster', 'Evanescent' and the 'Zenneck modes'. The 'Fano modes' are the only surface normal modes since the existence of the other three modes depends in an essential way of damping and they are usually associated with $\epsilon(\omega) < 0$ (Halevi, 1982). In this project surface plasmon modes have been examined for different types of optical waveguide structures, like planar metal-clad waveguides, two-dimensional metal-clad waveguides, TE-TM optical polarizers and metal-clad optical fibers.

4.2 Single metal-dielectric interface

Firstly, a single metal-dielectric interface, which is the most basic structure that can support a guided wave, was examined. The waveguide consisted of an aluminum layer with a complex dielectric constant ϵ_m , attached to a dielectric layer with a refractive index, n_g , at an operating wavelength $\lambda = 1.3 \mu\text{m}$. By solving the problem using the scalar approximation of the Finite Element Method (FEM) with perturbation, only the lowest TM mode, (TM_0), could propagate along the interface. This is mode, which can be classified as a non-radiative surface plasmon mode and has a maximum amplitude at the interface and decays away from it. All the TE and the higher TM modes, were unbounded, *i.e.* they did not decay in the dielectric material region.

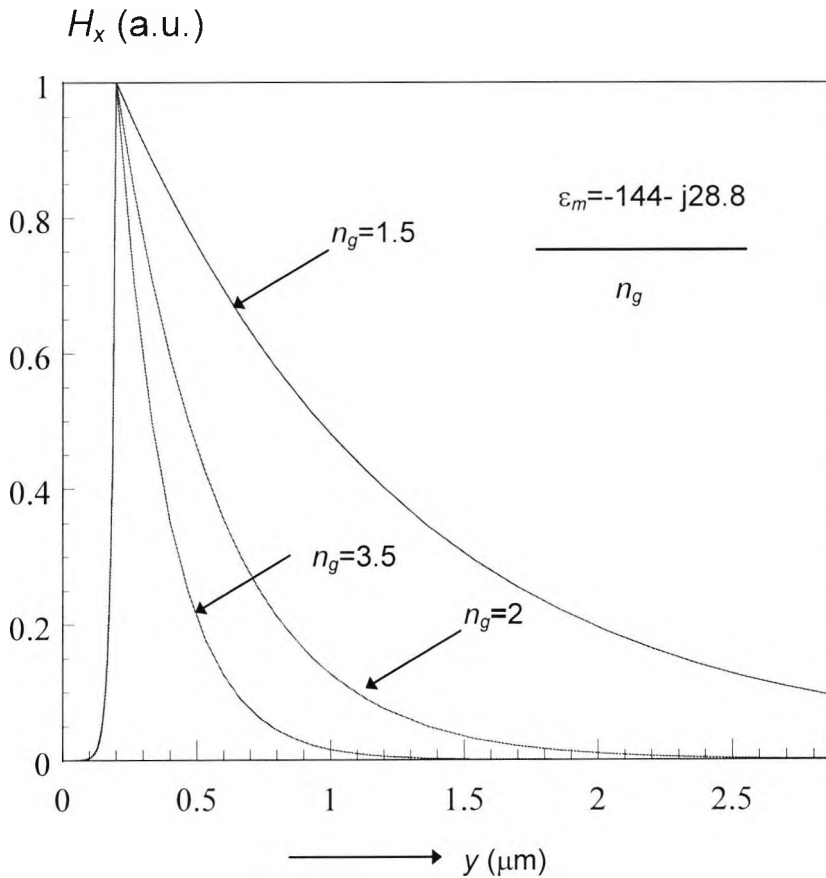


Fig. 4.2 Variation of the normalized field profile, for the TM_0 mode with the transverse direction for several values of the refractive index of the dielectric.

Fig. 4.2. shows the normalized magnetic field profile in the transverse direction to the propagation, (y), of the TM_0 optical mode, for different values of the refractive index of the dielectric material. In the metal region the field decays very rapidly, while in the dielectric region the decay depends on the value of the refractive index, n_g , of the dielectric material. As the refractive index, n_g , increases, the mode becomes more confined, with a faster decay of the field in the dielectric region, while the rapid decay in the metal region remains unchanged.

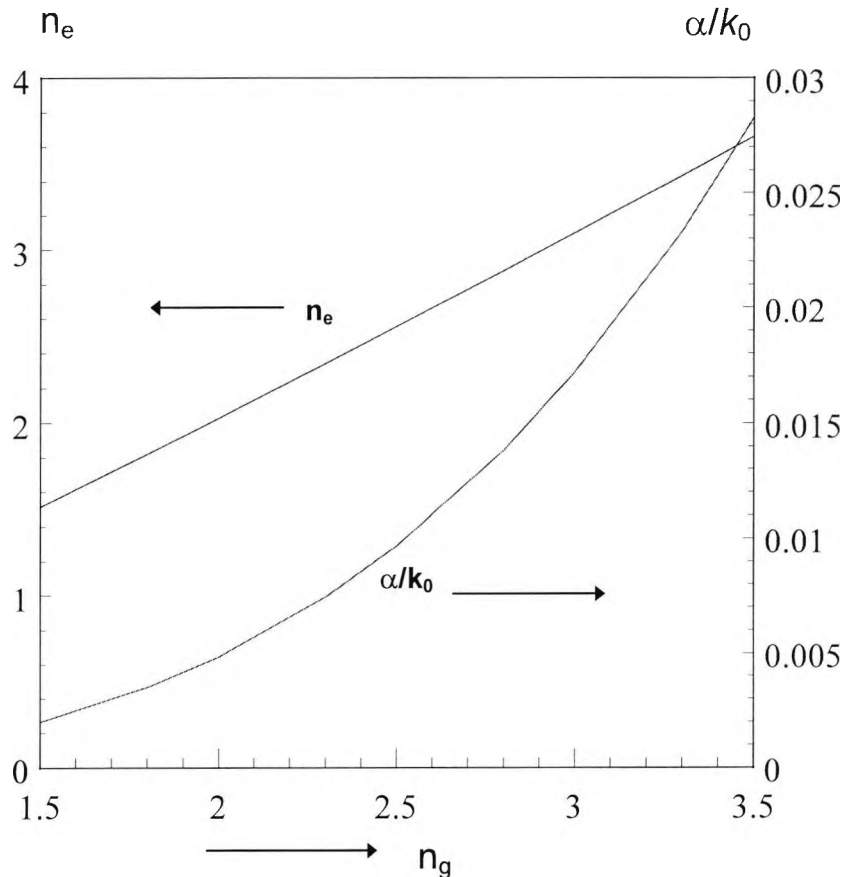


Fig. 4.3 Variation of the effective index and normalized attenuation constant with the refractive index of the dielectric material.

The propagation characteristics of the simple metal/dielectric optical waveguide have also been examined and the variation of the effective index, n_e , and the normalized attenuation constant α/k_0 , with the variation of the refractive index of the dielectric material are presented in Fig.4.3. The TM_0 mode propagates with an effective index, β/k_0 , very close to the refractive index of the dielectric material, n_g , so therefore, any increase of the refractive index, n_g , is followed by a linear increase of the effective index of the mode.

The optical field of the TM_0 mode is concentrated at the metal/dielectric interface, where the proportion of the optical power in the lossy metal region gives rise to the attenuation characteristics. As the refractive index of the dielectric material increases, the mode becomes more confined and the maximum field is higher at the metal/dielectric interface, so therefore, the proportion of the optical power in the metal region increases, resulting in an increase of the modal loss. The normalized attenuation constant, α/k_0 , of the TM_0 optical mode increases with the increase of the

refractive index, n_g , of the dielectric material, in a square law manner, because it is more dependent on the power confinement in the region than the refractive index variation.

4.3 Three layer planar waveguides

The propagation characteristics and field profiles, for different types of three layer planar waveguides are examined in this section, for TE and TM polarized modes. The interaction of metallic films with dielectric materials in order to accommodate guided optical waves is also examined, since, such structures play an important role in many optoelectronic applications. Practical metallic elements are not perfect conductors, but suffer a small amount of loss, and therefore, in the analysis of optical waveguides incorporating metal films, the attenuation characteristics should be taken into consideration. In optical waveguide analysis metallic elements are represented by a complex dielectric constant, ϵ_m , with a negative real part.

4.3.1 Non-metal planar waveguides

These structures, which were described in Section 4.1, have been extensively analyzed during the last decades and their study is fundamental in understanding the basic concepts of optical waveguides. In the majority of the cases examined, these types of waveguides are considered lossless, but in this work a small amount of loss was introduced in order to compare the various approaches developed for the gain/loss analysis of optical waveguides.

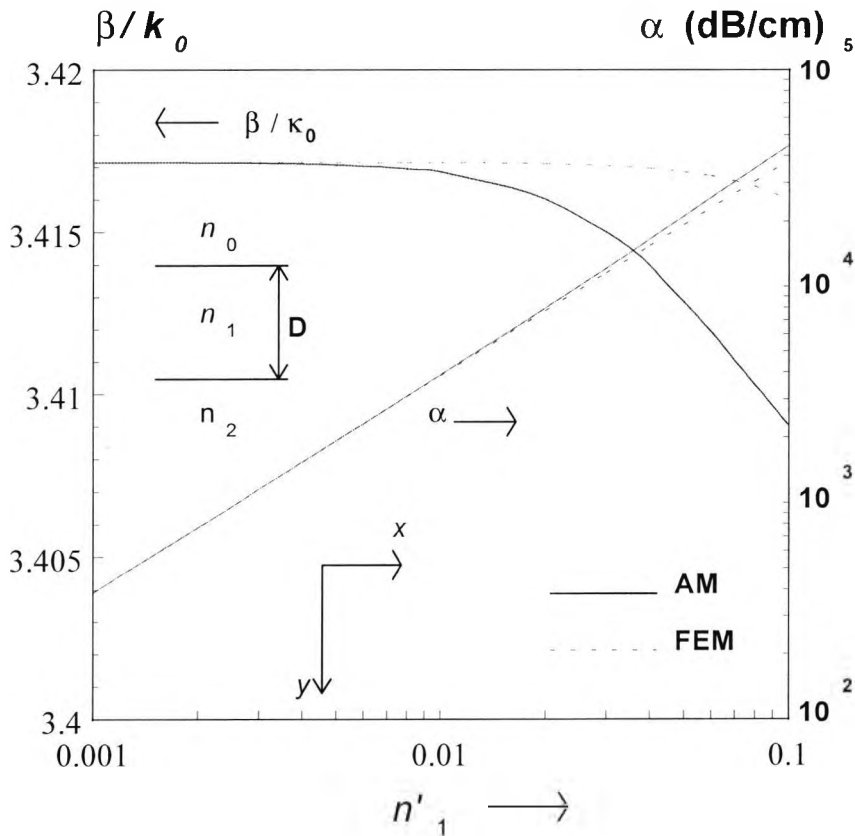


Fig.4.4 Variation of the normalized phase and attenuation constants with the imaginary part of the film refractive index, (n'_1) of a slab waveguide, using the analytical approach (AM) and the Finite Element Method (FEM).

A planar optical waveguide has been examined, as shown in Fig.4.4, with refractive indices $n_0=1.0$, $n_1=3.44 +jn'_1$, $n_2=3.4$ and film thickness $D=1.0\mu\text{m}$. The variation of the normalized propagation constant, β/k_0 , is shown for the TE_0 mode for the operating wavelength $\lambda=1.15\mu\text{m}$. The analytical result (AM), obtained from the solution of the complex transcendental equation, is compared with that from the scalar FEM with perturbation for different values of the imaginary part (n'_1) of the refractive index of n_1 . The finite element results (FEM) show good agreement with the analytical results, except when n'_1 is quite high. The attenuation constant, α , for the two methods is in excellent agreement for n'_1 being as large as 0.01. However, it can be noted that for most of the passive or active optical waveguides with significant loss or gain values, their modal loss/gain values are still lower than the limit of the perturbation approach, and in this example, for $n'_1=0.01$, the modal loss is about 4000 dB/cm and the difference between the analytical and finite element solutions is only about 0.72%. As n'_1 increases, the normalized phase constant (β/k_0) for the FEM solution does not vary

much compared to that obtained from the analytical solution (AM), where a rapid decrease is observed when n_1' is more than 0.01. This results, as does the FEM solution in the imaginary part of the propagation constant being based on a loss-free waveguide, where the effect of the imaginary part of the refractive index is quite small on the real part of the dielectric constant, ϵ_r .

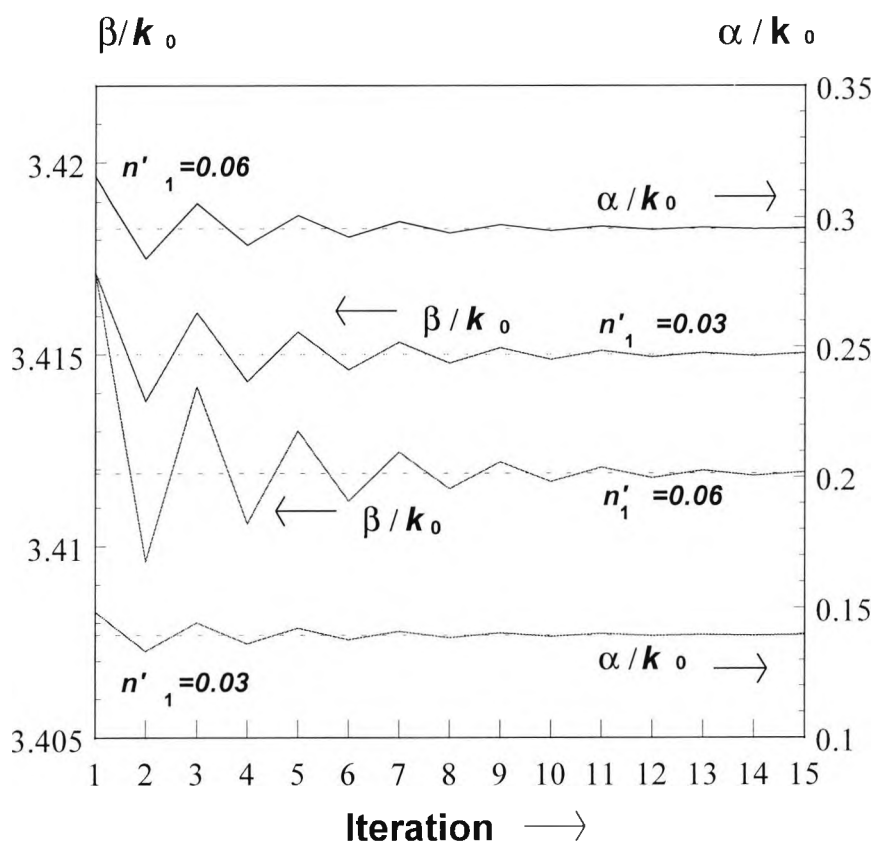


Fig.4.5 Convergence of the normalized phase and attenuation constants by analytical approach, for two different values of the imaginary part of the film refractive index (n_1') for a slab waveguide.

The convergence of the complex slab solution is shown in Fig.4.5. for two different values of n_1' , the imaginary part of n_1 . It can be noted that both the imaginary (β) and real (α) parts of the complex propagation constants vary with the iteration, but settle quickly to constant values. When n_1' increases from 0.03 to 0.06, the normalized final value of α also increases nearly two times whereas the normalized value of β is slightly decreased. As n_1' increases, the solution for both the normalised phase and attenuation constants requires further iterations to converge and the difference between the initial and final values also increases.

4.3.2 Metal-clad planar waveguides

Metal-clad planar optical waveguides are suitable for electrooptic or magneto-optic devices because the metal cladding can be used for a component of electric circuits (Yamamoto *et al.*, 1975). One of their most important features is that the mode attenuation is larger for the TM mode than that for the TE mode, and therefore they are also useful for mode filtering and the knowledge of their propagation and attenuation characteristics is essential. In this section, the scalar approximation of the finite element method with perturbation was used to calculate the attenuation characteristics of three layer metal-clad optical waveguides, for the TE and TM optical modes.

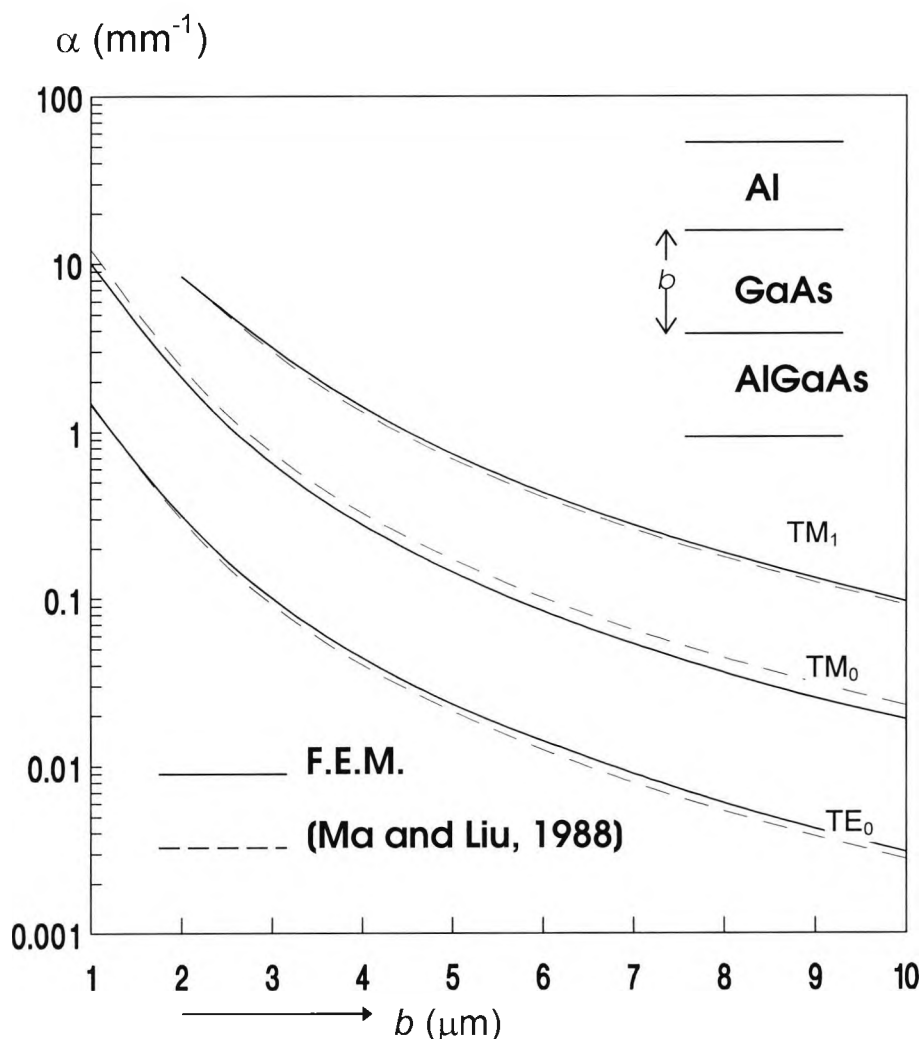


Fig. 4.6 Variation of modal loss with guide thickness

The above formulation has been tested for a metal-clad asymmetrical optical waveguide consisting of Al/GaAs/AlGaAs, for both the TE and TM modes. In this

example, the refractive indices of the aluminium, GaAs, AlGaAs are $1.75-j8.5$, 3.48 and 3.42 respectively at the operating wavelength of $1.06 \mu\text{m}$. Figure 4.6. shows the variation of loss with waveguide height for different modes by using the finite element method and an approximate analytical method. Our results agree well with those results obtained by using the approximate equations (22) and (24) of Ma and Liu (1988).

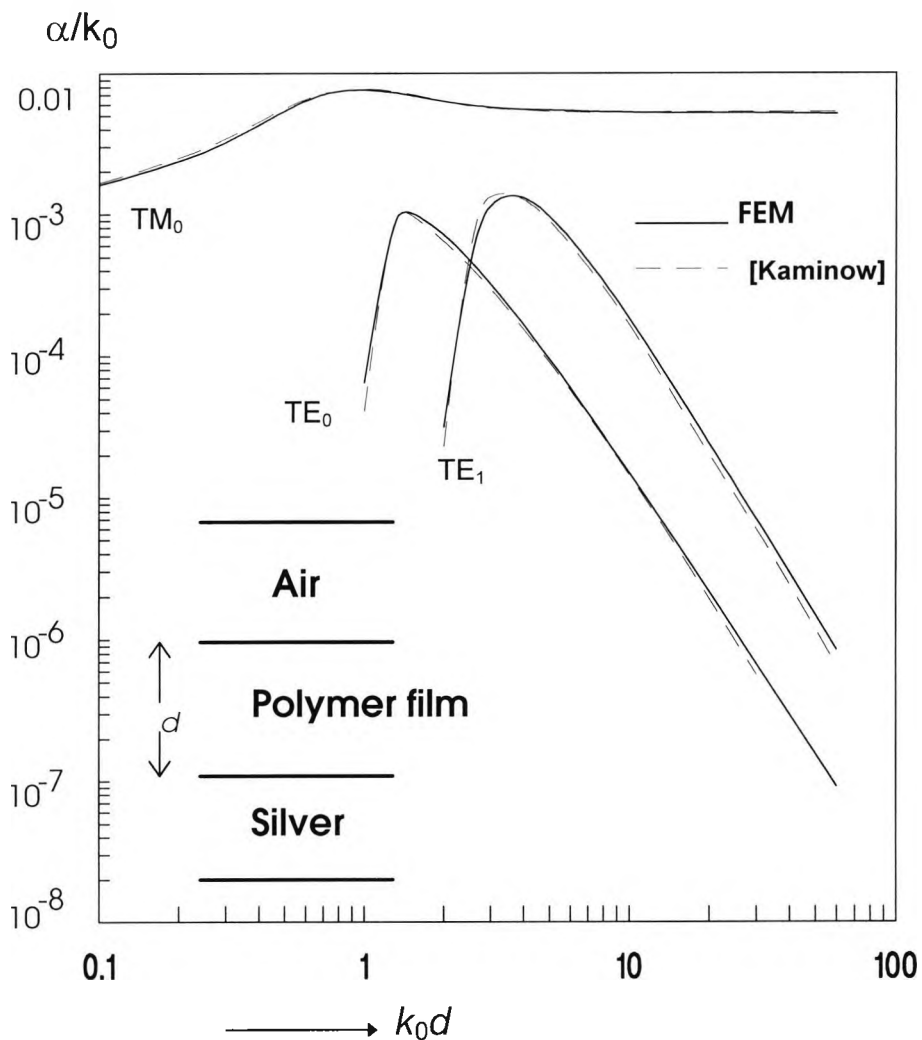


Fig.4.7 Variation of normalized loss with normalized film thickness for TE and TM modes.

An asymmetric metal-clad optical waveguide with air/polymer/silver layers has also been examined including the surface plasmon modes. In this type of waveguide, most of the energy for the TM_0 mode is concentrated at the metal-dielectric boundary and modes with such behaviour are described as surface plasma waves. The relative permittivities of the air, polymer and silver layers are 1, 2.523 and $-16.32-j0.5414$

respectively. The results obtained are compared with those for a normalized attenuation constant, as discussed by Kaminow *et al.* (1974) for the TE and TM modes. Figure 4.7 shows the variation of the normalized attenuation constant, α/k_0 , with the normalized film thickness, k_0d , and good agreement can be seen when compared with the results also reproduced from Kaminow *et al.* (1974). It can be observed that the two results disagree at a very low values of the attenuation, and this may be either due to the matrix evaluation error for modes with very high confinement or due to the approximation of the analytical procedure when many modes are present.

4.3.2.1 Graded-index metal-clad planar waveguides

Graded-index metal-clad planar optical waveguides serve as models of more complicated two-dimensional diffused waveguides. It is important to investigate the influence of the metallic films on their propagation and attenuation characteristics, since these features are useful in some applications, such as mode and polarization filtering.

A three-layer graded-index metal-clad optical waveguide has been examined, with a metal cladding of dielectric constant, ϵ_m , that occupies the region $x < 0$. For $x > 0$ the index profile is represented by the function $n^2(x)$, which extends from $x=0$ to $x=a$, where a is the length of the graded-index film, and to the substrate. Fig.4.8. shows the index variation in the graded-index film and the substrate for a linear and an exponential index profile.

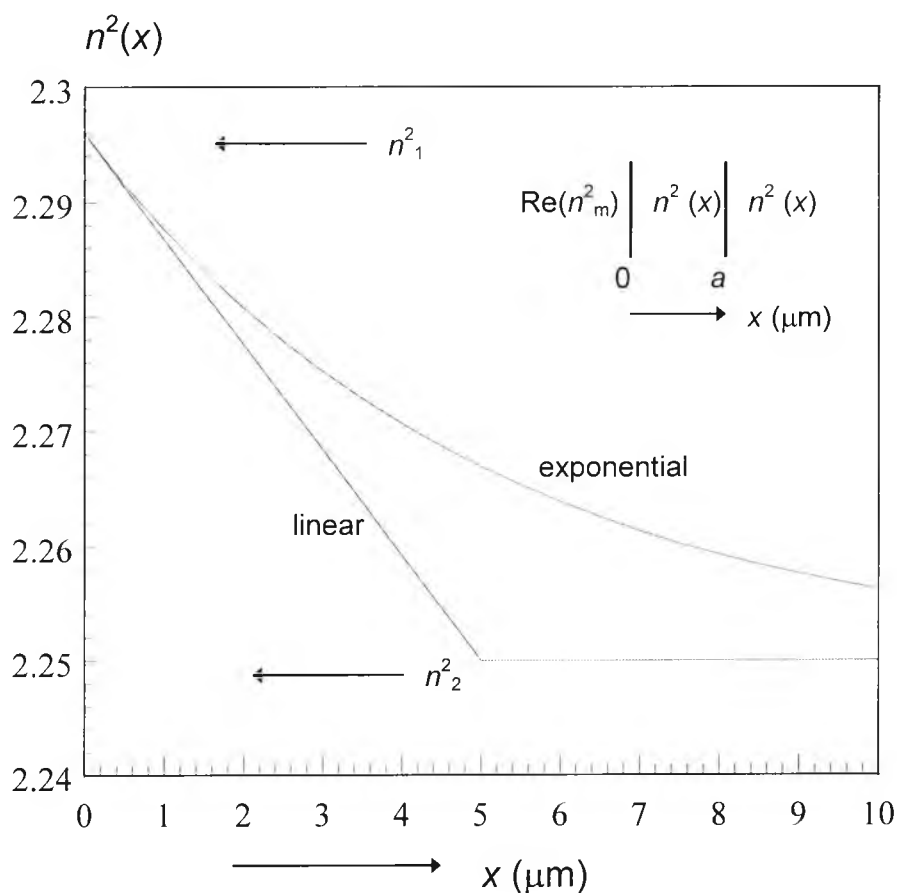


Fig.4.8 Variation of the refractive index profile in a graded-index metal-clad planar optical waveguide.

The refractive index profiles along the x -direction are given by (Lee and Wang, 1995):

a) Linear profile

$$n^2(x) = n_1^2 \left[1 - 2\Delta \left(\frac{x}{a} \right) \right] \quad 0 \leq x \leq a$$

$$= n_1^2 [1 - 2\Delta] = n_2^2 \quad x \geq a \quad (4.1)$$

b) Exponential profile

$$n^2(x) = n_1^2 [1 - 2\Delta(\exp(-x/a))] \quad x \geq 0 \quad (4.2)$$

where Δ is the normalized dielectric constant difference between the boundaries of the graded index film.

By using the scalar approximation of the FEM with perturbation, the propagation constant, β , and the attenuation constant, α , of the waveguide were calculated, for the TE and TM modes. The results obtained for the two low-order TE modes, TE_0 and TE_1 , for both the index profiles, were compared with the results obtained by Lee and Wang (1995) and found to be in very good agreement, as shown in Table 4.1.

a=5 μm		β		$-j\alpha \cdot 10^{-3}$	
Mode	profile	FEM	[Lee]	FEM	[Lee]
TE_0	linear	14.97295	14.9729	0.03404	0.03421
TE_1	linear	14.91859	14.9181	0.03275	0.03336
TE_0	exponential	14.98196	14.982	0.02395	0.02449
TE_1	exponential	14.94587	14.9459	0.01721	0.0176

Table 4.1 Comparison of the complex propagation constant for the TE_0 and TE_1 modes, for graded-index planar optical waveguide with graded-index film length $a=5\mu\text{m}$.

Further, the propagation characteristics for the TE and TM modes, with the variation of the length, a , of the graded index film, for this type of optical waveguide, were calculated, for both the linear and the exponential index profiles.

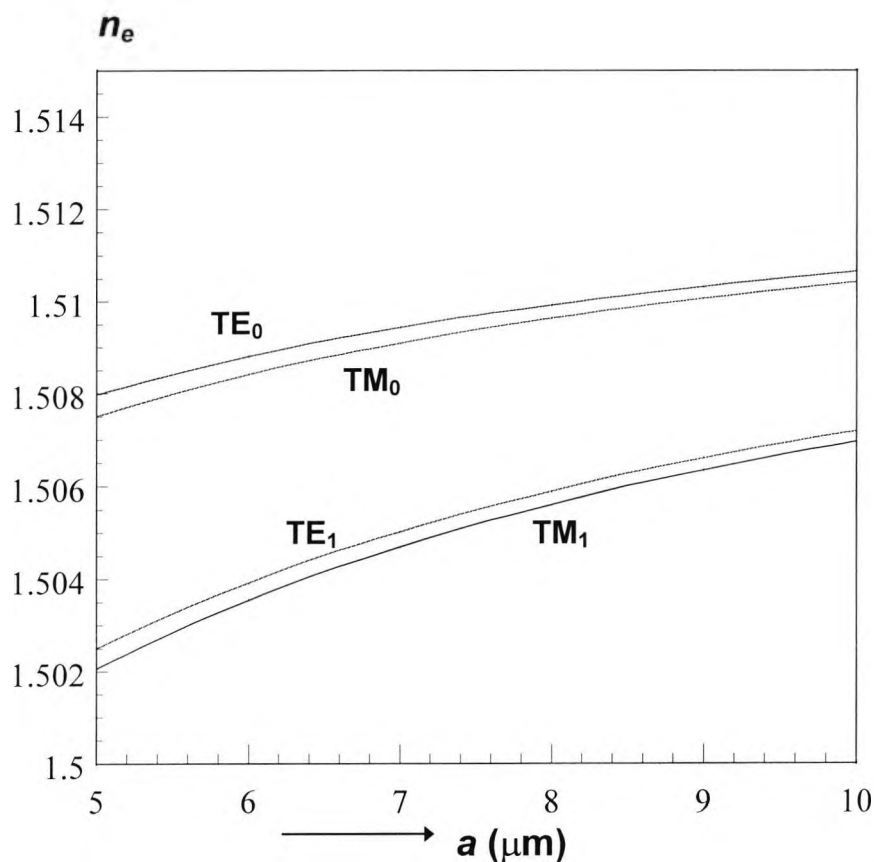


Fig.4.9 Variation of the effective index, n_e , with the variation of the length, a , of the graded-index film with linear index profile, for TE and TM modes.

Figure 4.9 shows the variation of the effective index of the waveguide with the variation of the graded-index film length, a , for a linear index profile for the two lower TE and TM modes. As the length of the film increases, the effective index increases for all the modes. The lower order TE_0 and TM_0 modes have a higher refractive index than those of the higher order and in both cases the TE mode is always slightly higher than the TM modes. It is well known that for all metal-clad planar waveguides, the metal cladding has no effect on the TE optical mode, whereas for the TM mode there is a change of sign of the field profile at the metal/dielectric interface, but the field intensity is not too high at the interface. For this reason, the TE mode is more confined in the dielectric film centre region, therefore the refractive index is higher than that of the TM mode.

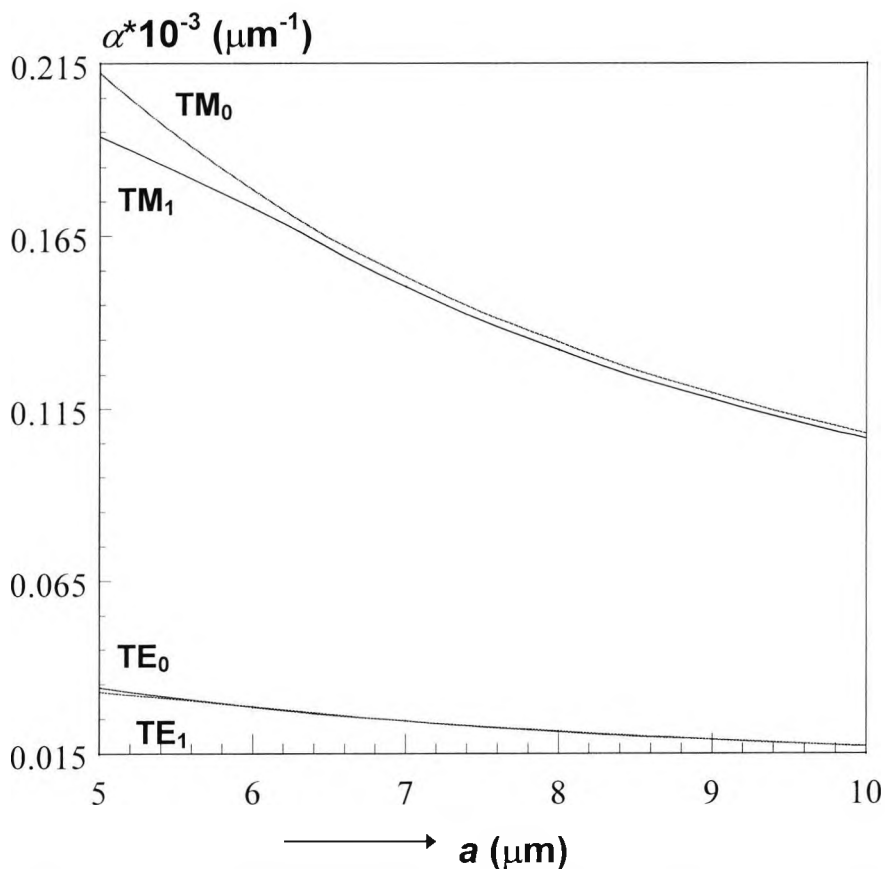


Fig.4.10 Variation of the attenuation constant, α , with the variation of the length, a , of the graded-index film with linear index profile, for the TE and TM modes.

The attenuation characteristics of the above case, for the TE and TM modes, were also calculated and presented in Fig. 4.10. From the curves obtained, it can be seen that the attenuation constant, α , decreases as the length of the film increases. The reason for this is that as the waveguide becomes larger, the mode becomes more confined in the graded-index film region. Thus the field intensity in the metal-cladding, which is the lossy area, becomes weaker, and therefore, the attenuation of the waveguide decreases. One of the most important features of the attenuation characteristics is that the attenuation constant for the TM modes is about ten times larger than that for the TE modes. This is due to the property of the TE mode to remain unaffected by the metal-cladding which is the lossy area of the waveguide. Since there is no appreciable field intensity in this region, the attenuation in the waveguide is less for this type of mode. The consideration of the attenuation constant difference between the TE and TM modes in this type of optical waveguide is an important design parameter in mode filtering applications.

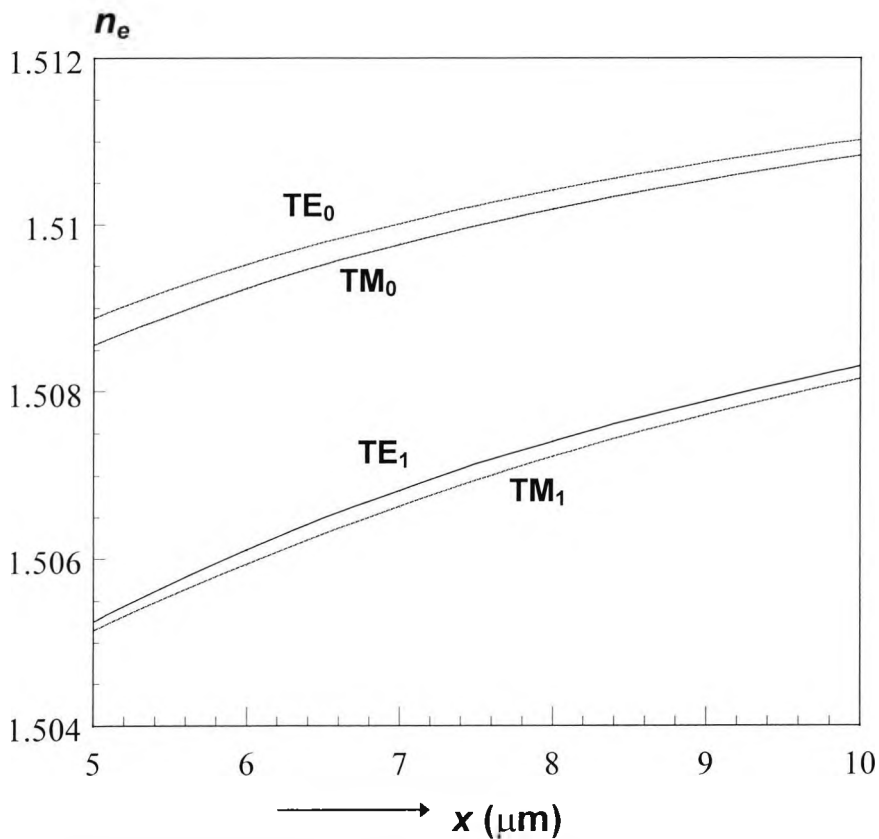


Fig.4.11 Propagation characteristics for the exponential index profile

Next, the variation of the effective index, n_e , with the variation of the film thickness, a , for an exponential index profile, was calculated for the TE and TM modes, as shown in Fig.4.11. The features are similar those of the linear index profile for all the modes considered, but in this case the effective index values are higher. This can be explained from the index profile curves in Fig.4.8, where the exponential index profile is higher than the linear profile for the whole region of the graded-index film and the substrate.

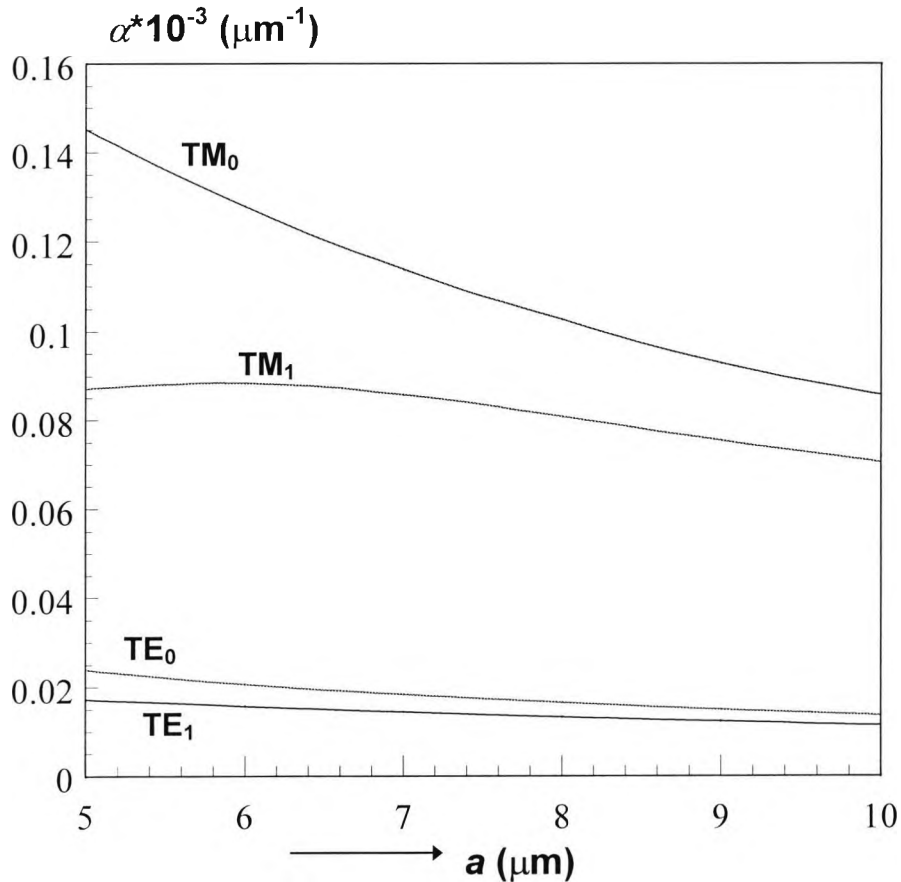


Fig.4.12 Attenuation characteristics for the exponential index profile

Additionally, the attenuation characteristics for the exponential index profile were obtained, as shown in Fig.4.12. Again, similar features are obtained to those of the linear index profile with the only difference the fact that the attenuation constant is lower for all the modes than that of the linear index profile. The reason for this is the higher refractive index in the graded-index film region which produces more field confinement in this area and less in the lossy metal-cladding, and therefore the attenuation of the waveguide reduces.

4.3.3 Surface-plasmon modes in planar waveguides

Surface-plasmon waves are TM-polarized, guided electromagnetic waves supported by a single or multiple metal/dielectric interface, where the refractive index of the metal film is considered to have an almost purely imaginary part at the operating wavelength, thus giving a high negative dielectric constant. Surface-plasmon mode properties are used in a wide range of device applications, such as in optical polarizers or highly sensitive evanescent optical sensors.

In this section, two different types of planar structures that support surface plasmon modes are examined. These are firstly, when a thin film is sandwiched between two dielectric materials, and secondly, when metallic films are deposited on each side of a normal dielectric. As was shown in Section 4.2, a single metal/dielectric interface can support only one TM-polarized mode, which is a surface-plasmon mode, where the field intensity is high at the interface and it decays exponentially away from it. When two such interfaces are placed together to form a composite structure, the two surface waves are coupled to form supermodes. These types of waveguides can support two fundamental guided modes, an even-like and an odd-like supermode and their properties depend on the arrangement of the dielectric and metallic films and the separation between the two metal/dielectric interfaces.

Since metallic films are lossy materials, an investigation of the attenuation characteristics is important. A scalar approximation of the FEM has been used in conjunction with the perturbation technique to calculate the complex propagation constant of the above structures and in some cases the complex solution of the transcendental equation has been employed to compare the results.

4.3.3.1 Thin metal film surrounded by dielectrics

The 3-layer structure under consideration consists of a thin metal film with a dielectric constant $\epsilon_m = \epsilon_r + j\epsilon_i$, bounded at $y=0$ and $y=t$, by two semi-infinite lossless dielectric materials, with refractive indices, n_1 for $y > t$ and n_3 for $y < 0$. The first example considered is a symmetrical waveguide with $n_1 = n_3$, and $n_m = -1.2 - j12$, representing a thin aluminum film at wavelength $\lambda = 1.3 \mu\text{m}$. Figure 4.13 shows the effective index variations with the metal thickness (t) and with inset modal field profiles, for different

values of the cladding refractive index. Two bounded modes are examined, the first corresponding to the anti-symmetrical (odd) mode (Ab) and the second to the symmetrical (even) mode (Sb).

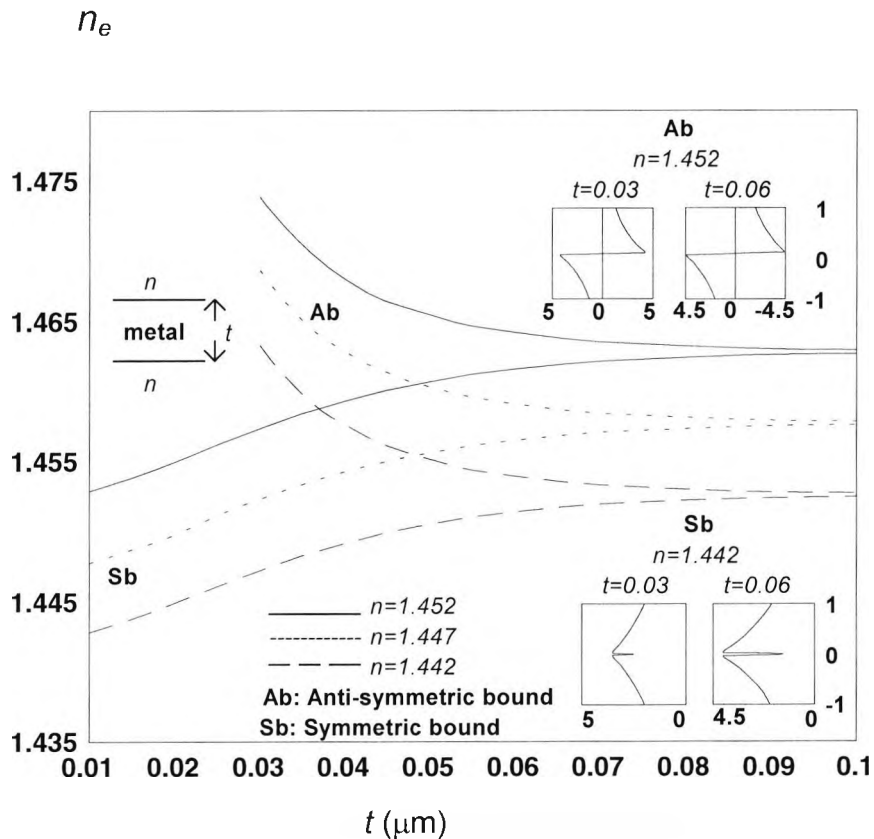


Fig.4.13 Variation of the effective indices for a symmetric surface plasmon structure.

Both the modes have a higher effective index than the common cladding refractive index ($n=n_1=n_3$) of the two (top and bottom) cladding regions. The effective index of the symmetrical mode reduces and approaches the cladding refractive index value, as the metal thickness decreases and the mode becomes more weakly bounded. As the film thickness increases, the effective index, (β/k_0) , increases and the symmetrical mode becomes more confined, showing a larger central dip as the two metal/dielectric interfaces move apart, (shown as second lower insert of Figure 4.13). However, as the film thickness increases, the anti-symmetrical mode becomes less confined, since the effective index decreases and the field spreads further into the cladding, (shown as second upper insert of the Figure 4.13). When the film thickness becomes wide enough, the two supermodes behave like two weakly coupled surface modes, one at each metal/dielectric interface, propagating with almost identical propagation constants. As the metal thickness, t , increases further, the two effective indices tend to

reach the effective index of the mode supported by a single metal dielectric interface. As the (identical) refractive index of both the cladding regions is increased, the effective index of each mode is shifted upwards by an amount equal to that increase. The finite element results agree very well (the curves would be visually indistinguishable) with the analytical solution which has been also obtained by solving the transcendental equation, and this structure has also been studied by Johnstone *et al.* (1988).

In most of the practical guiding structures incorporating a thin metal layer, the guides may not be symmetrical and in that case the mode properties are quite different from those of the symmetrical structures. Here, a non-symmetrical structure is examined, where this time the refractive index of the upper cladding is kept constant at $n_1=1.447$, while the refractive index of the lower one (substrate) is varied from $n_3=1.442$ to $n_3=1.457$. The variation of the propagation characteristics, the effective index and the normalized attenuation constant are investigated, with the metal thickness, for different lower cladding indices.

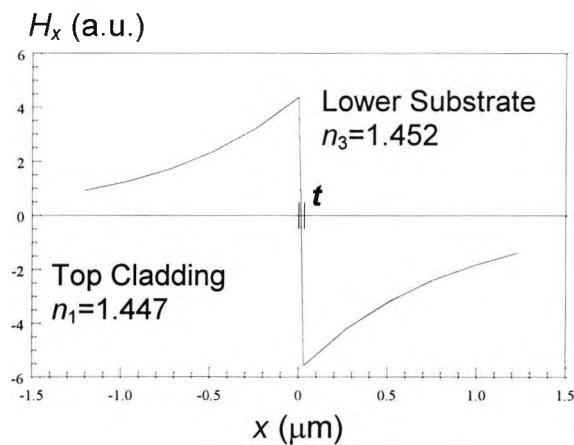


Fig.4.14 H_x field profile for the Odd-like Supermode (A_b), for $t=0.03\mu\text{m}$.

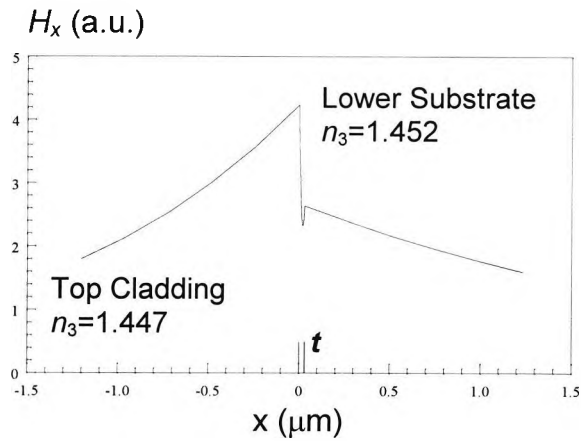


Fig.4.15 H_x field profile for the Even-like Supermode (S_b), for $t=0.03\mu\text{m}$.

Figure 4.14 to 4.17 show the field profiles for two values of the metal thickness, t , with $n_3=1.452$. When the metal film thickness $t=0.03\mu\text{m}$, the first supermode (A_b), the odd-like mode, is no longer antisymmetric. The field is more concentrated in the substrate region, as shown in Fig.4.14, which has a higher refractive index value. The first supermode has a higher effective index than the second supermode and so this mode is confined more in the region with the higher refractive index. Exactly the opposite phenomenon is observed for the second supermode, which is even-like. The even-like supermode, S_b , is also no longer symmetric and in this case the field is more concentrated in the top cladding region which has a lower refractive index value. It can also be noted that the field decreases very slowly in the substrate region as the modal effective index is very close to the substrate refractive index (n_3).

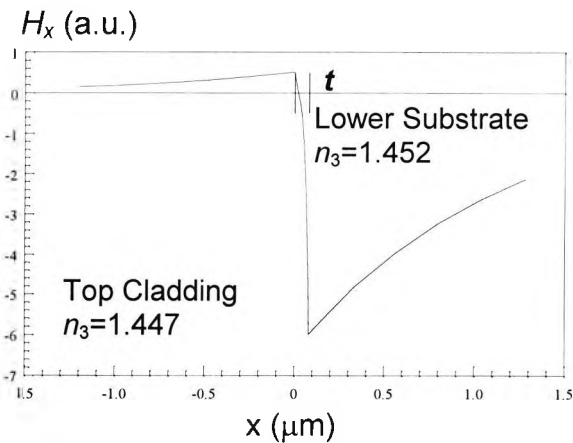


Fig.4.16 H_x field profile for the Odd-like Supermode (A_b), for $t=0.08\mu\text{m}$.

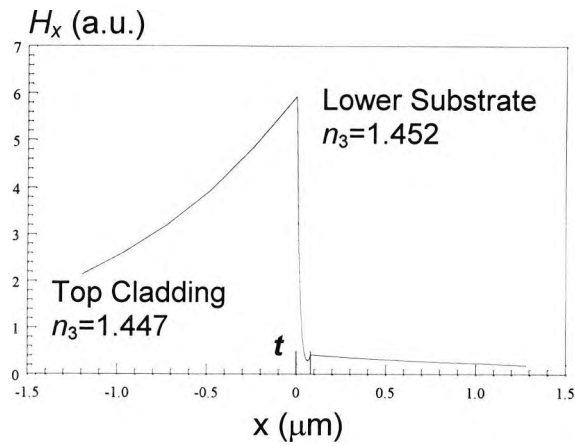


Fig.4.17 H_x field profile for the Even-like Supermode (S_b), for $t=0.08\mu\text{m}$.

When the metal thickness, t , is increased, the asymmetry increases further and most of the power is confined either in the cladding or in the substrate region, as is seen in Figures 4.16 and 4.17, for the odd-like (A_b) and the even-like (S_b) modes respectively. This can be explained, as at a larger separation distance (t) between the two dielectric/metal interfaces, the two surface modes are weakly coupled with very small modal field overlaps, and each of them can be approximated by only one of the two individual surface modes at the two nonidentical metal/dielectric interfaces. The asymmetry is also prominent when the difference between the two boundary refractive indices (n_3-n_1) increases. These types of behaviour can be studied in more detail as a nonsynchronous directional coupler problem.

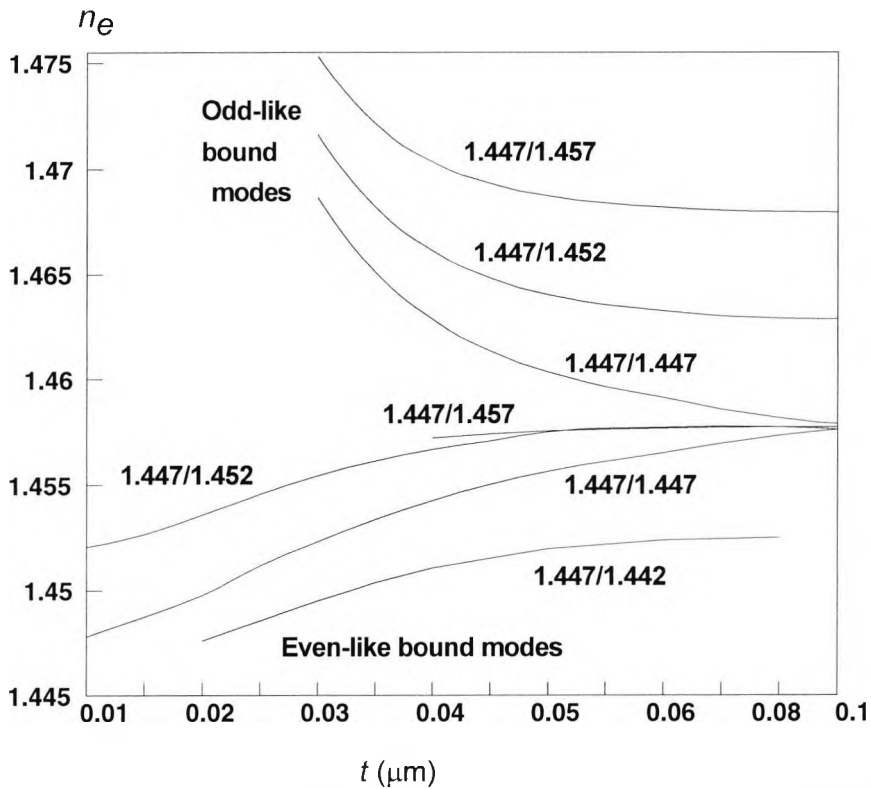


Fig.4.18 Effective index versus metal thickness for each of the first two supermodes of non-symmetrical structures for different values of the lower-cladding refractive index.

Figure 4.18 shows the variation of the effective index with the metal thickness, (t), for different $n_1:n_3$ combinations. The effective index of the first supermode (odd-like) converges to that of the mode supported by the metal and the higher dielectric of the two bounding sides, when the metal thickness, (t), increases. The effective index of the second supermode (the even-like), converges to that of the mode supported by the metal and lower valued bounding dielectric when t is increased. As the metal thickness, (t) decreases, the effective index increases monotonically for the first odd-like mode. However as the metal thickness, (t) decreases, the effective index for the second even-like supermode approaches n_3 or n_1 , depending on which is higher, until it reaches a cut-off thickness.

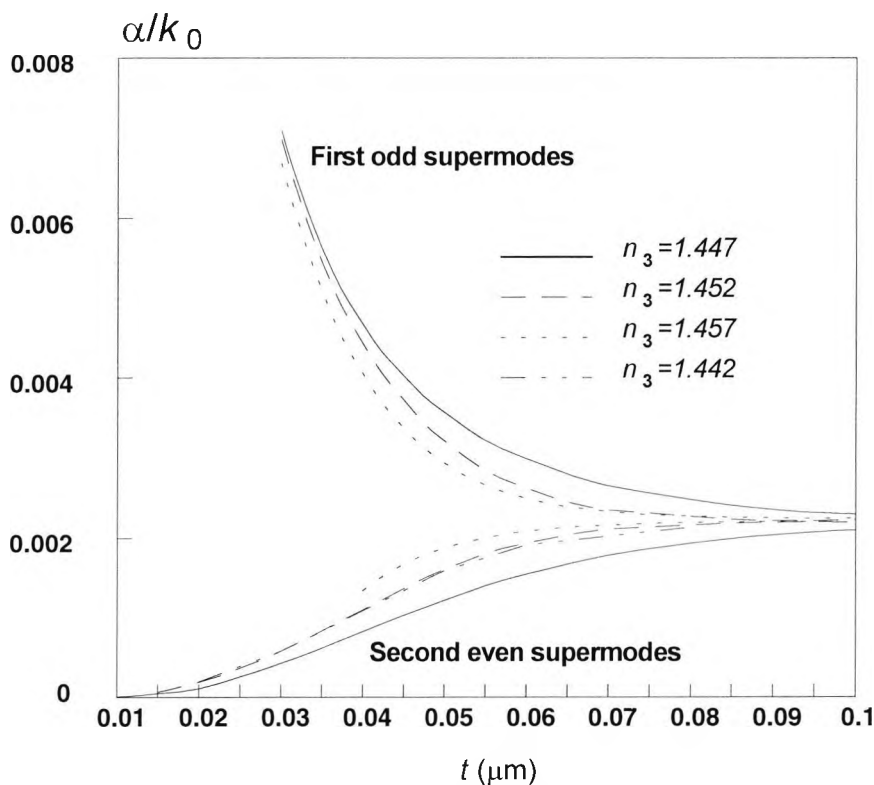


Fig.4.19 Variation of normalized modal loss coefficient versus metal thickness for the first two supermodes for different values of the lower-cladding refractive index.

Next, attenuation constants for such structures are also calculated by using the scalar approximation of the FEM with perturbation. In Figure 4.19, the solid lines represent the attenuation curves for the symmetrical and antisymmetrical modes in the symmetrical structure, which very much resemble the effective index curves shown earlier in Fig.4.13, where $n_1=n_3=1.447$. The attenuation constant decreases monotonically for the antisymmetric bound mode, with the metal thickness, whereas for the even mode, it increases. Broken lines represent the attenuation curves for the even-like and odd-like modes when the structure is not symmetrical. The modal loss for the even or even-like modes is less than for the odd or odd-like modes, which are also known as long range modes. Similarly the odd or the odd-like supermodes are known as short range modes. The attenuation constant values reach that of the surface mode supported by a single metal/dielectric interface when t is large. Modal losses for the odd-like and even-like modes are nearly independent of the individual refractive index values.

The FEM results for the attenuation characteristics, of the above structures were compared with analytical results obtained by the solution of the complex transcendental equation and found to be in very good agreement. Since previously published results were not available for these cases some other structures were examined for which attenuation characteristics, obtained by different approaches, were presented in other publications.

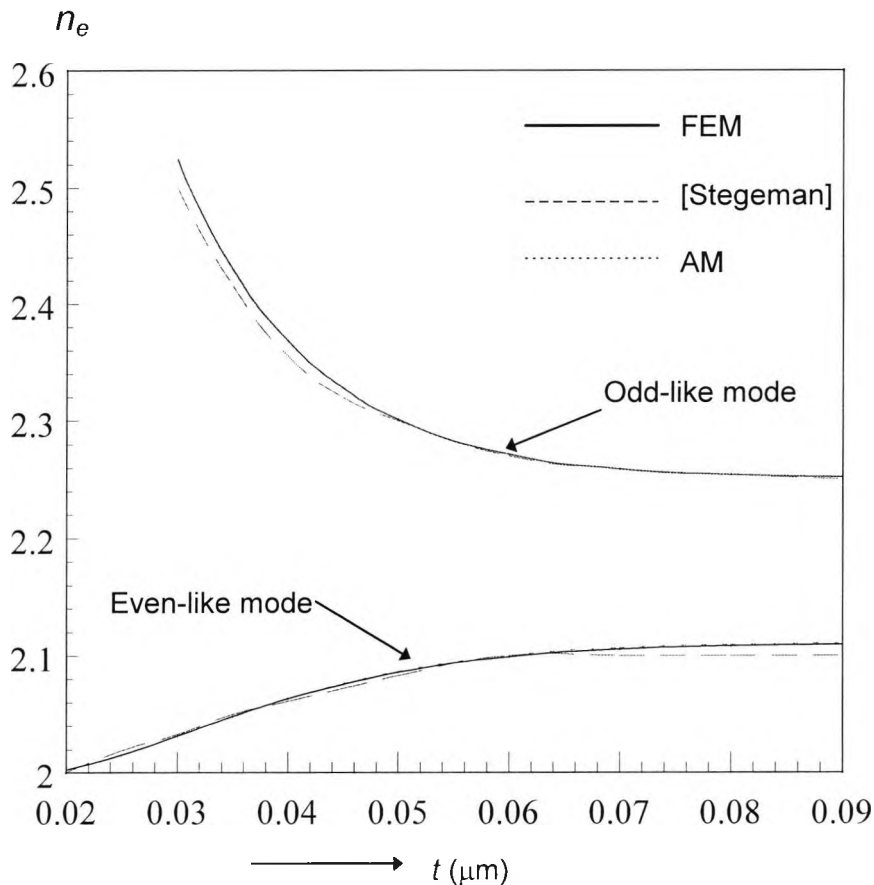


Fig.4.20 Comparison of the variation of the effective index with the metal thickness, for the first supermodes, of nonsymmetrical structure, by different approaches.

Results were obtained for both the propagation and attenuation constants, for a nonsymmetrical structure described by Stegeman *et al.* (1983), by using the scalar FEM with perturbation and the Analytical Method (AM), which involves the solution of the complex transcendental equation. The planar waveguide consists of a metal film with a dielectric constant, $\epsilon_m = -19 - j0.53$, a top cladding, $\epsilon_1 = 4$, and a lower substrate, $\epsilon_2 = 3.61$ at an operating wavelength $\lambda = 0.633 \mu\text{m}$. A comparison of the two methods the results obtained by Stegeman *et al.*, for the variation of the effective index with the metal thickness, is shown in Fig.4.20 and are in a very good agreement.

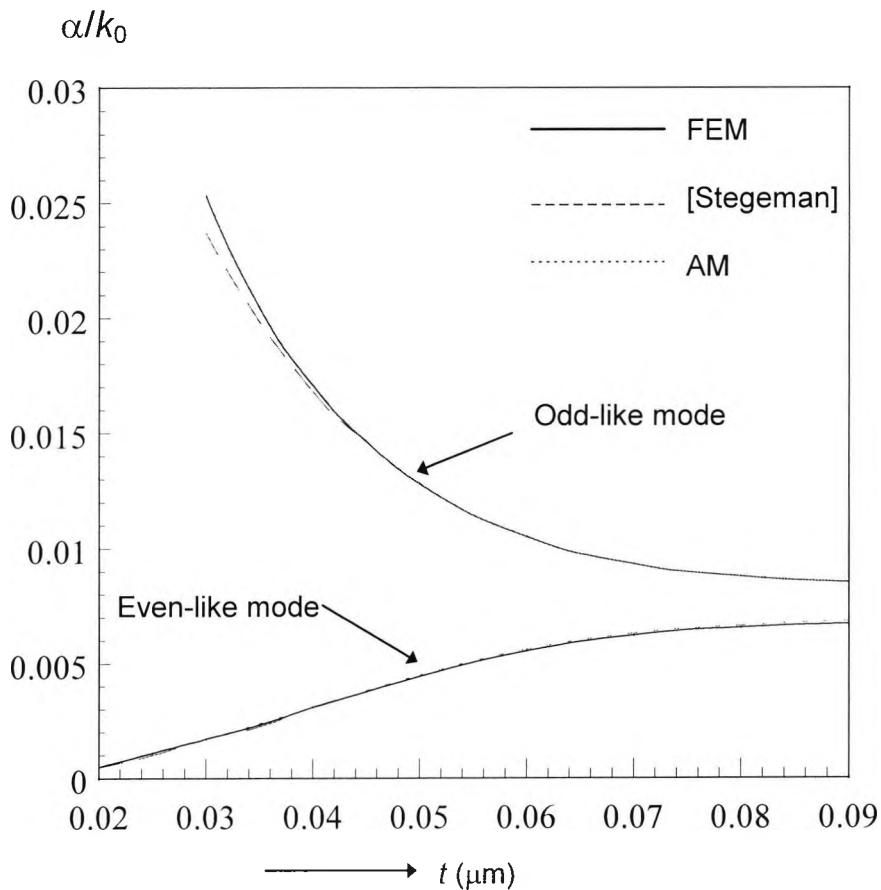


Fig.4.21 Comparison of the attenuation characteristics versus the metal thickness for the first two supermodes, by various approaches.

The attenuation characteristics, shown in Fig.4.21, for the above structure, compare the results obtained by various approaches and show very fine agreement, where in the case between the AM and the FEM, any differences are not distinguishable. The variation of the normalized attenuation constant with the metal thickness, is similar to the variation of the effective index, as in the previous cases of nonsymmetrical structures. For large metal thickness, each mode converges to the normalized attenuation constant of the single metal/dielectric interface where the field intensity is high.

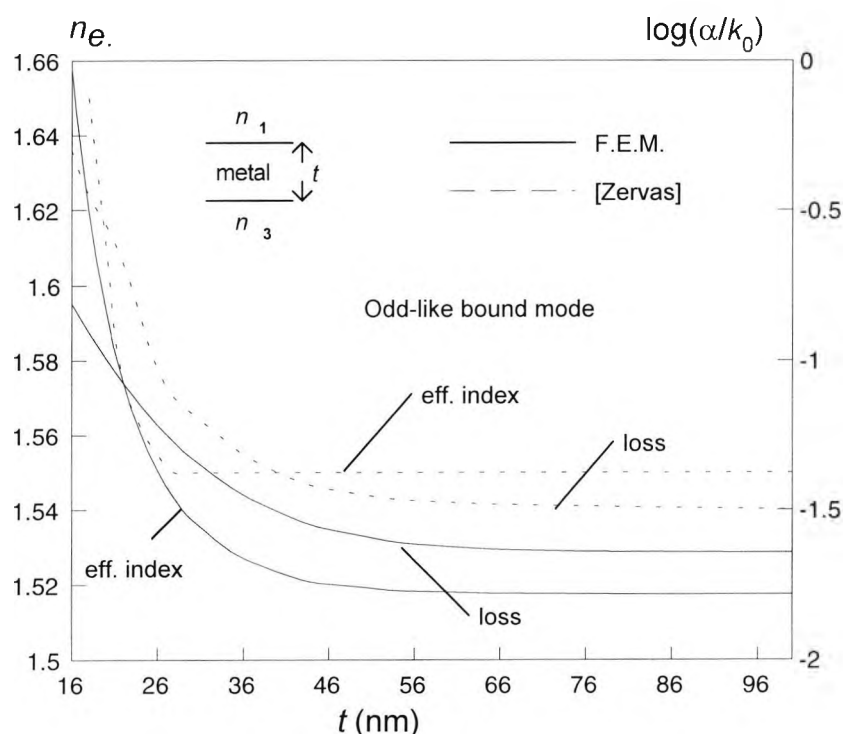


Fig.4.22 Comparison of the variation of the propagation characteristics with metal thickness for non symmetrical planar structure.

Finally, another nonsymmetrical structure was examined, for both the effective index and the attenuation constant and the results are compared with the work of Zervas (1991). In this case, the refractive indices of the 3 layers are $n_1=1.462$, $\epsilon_m=-29.8-j11.6$ and $n_3=1.3$ at a wavelength $\lambda=0.633\mu\text{m}$. In this type of nonsymmetrical structure, the refractive indices of the two bounding layers have a greater difference than in the previous cases studied. The dominant mode, the odd-like surface mode, is confined at the interface with the high refractive index. For this reason only the odd-like bound mode is examined and the results are compared with those obtained by Zervas (1991), as shown in Fig.4.22. It should be noted that curves given by Zervas have some strange features, when compared with the previously published work for similar structures. For low film thickness, their effective index curve increases very sharply, while our curve varies more smoothly, in a similar way to all other cases previously examined. Their attenuation characteristics, again for the same range, indicate a small deflection, which, to the best of our knowledge, has not been reported before and disagrees with the results obtained by the finite element method. These differences could be have been caused by the dispersion relation they used, which shows some minor alterations when compared with similar relations used for this particular structure.

4.3.3.2 Dielectric medium surrounded by thin metal films

Apart from the structure discussed in the previous section, where a thin metal film was embedded between two normal dielectrics, surface-plasmon waves can also propagate in waveguides with opposite arrangement, *i.e.* where a normal planar dielectric medium is sandwiched between two thin metallic films. In both cases the optical guided modes propagate along the metal/dielectric interfaces, where the field intensity is high and decays exponentially away from them. These modes are coupled to form a supermode and the coupling depends on the thickness of the dielectric film. Since metal layers are lossy materials and the modes suffer from small attenuation, this loss analysis is important, and therefore the scalar approximation of the FEM with perturbation was used again, for this type of structure, in order to calculate the propagation and attenuation characteristics.

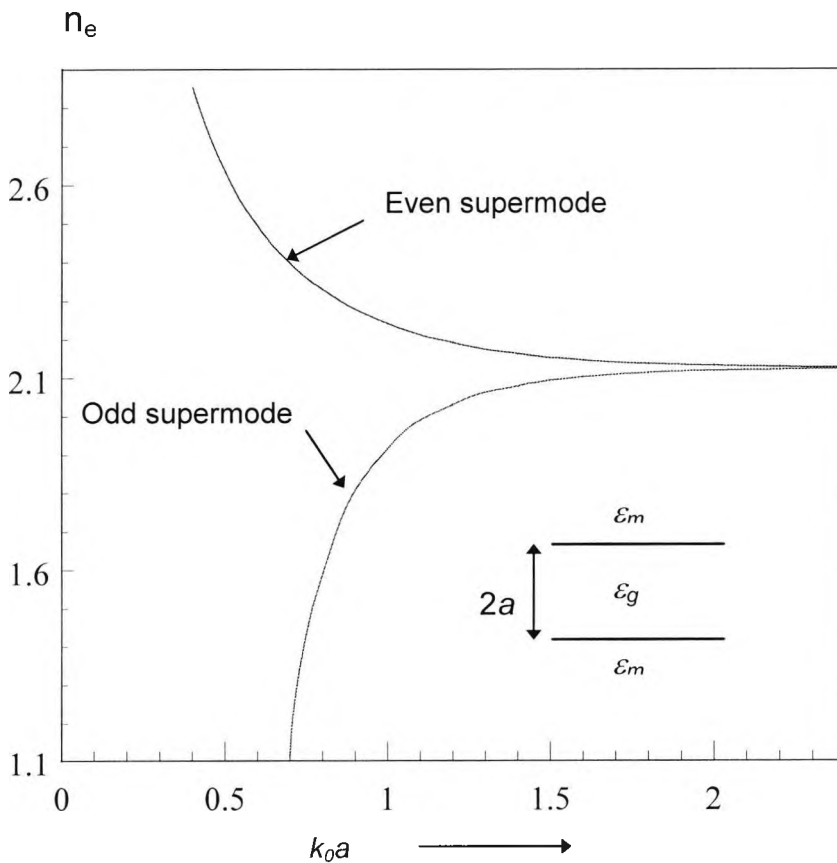


Fig.4.23 Variation of the effective index with the dielectric film thickness for a symmetrical surface plasmon structure.

The first structure under consideration is a symmetrical 3-layer planar waveguide, where a normal dielectric film of dielectric constant $\epsilon_g=2.12285$, is bounded

by two identical metal films of dielectric constant $\epsilon_m = -4 - j0.5414$, at an operating wavelength $\lambda = 0.6328 \mu\text{m}$.

Firstly, the variation of the effective index with the normalized dielectric film thickness was examined, for the first two bounded supermodes and results obtained are presented in Fig.4.23. As it can be seen from the graph, the supermode with the highest effective index is an even-like mode whereas in Section 4.3.3.1, for the opposite structure, the first supermode was an odd-like one. For small dielectric film thickness, $2a$, the effective index, n_e , is very high, but as the film thickness increases, the effective index, n_e , reduces to the value $n_e = 2.1289$. The second supermode in this type of structure is an odd-like mode, whereas in the opposite case, in the Section 4.3.3.1, it was an even-like mode. For small values of the dielectric film thickness, $2a$, the mode is in the cut-off region and as the film thickness increases, the effective index increases to a value very close to that encountered for the first supermode, which in this case is $n_e = 2.1252$.

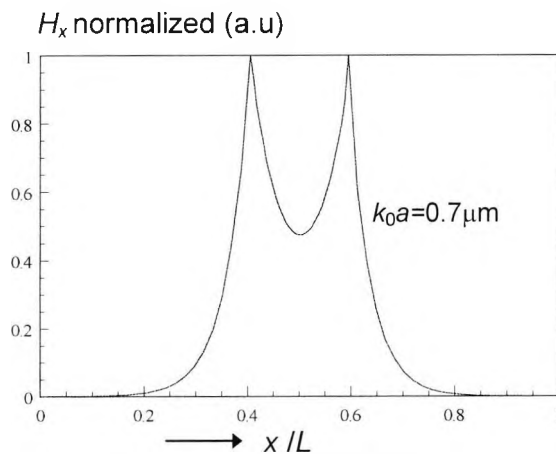


Fig.4.24 Normalized field profile for the even supermode of a symmetrical structure, for a normalized film thickness, $k_0 a = 0.7$.

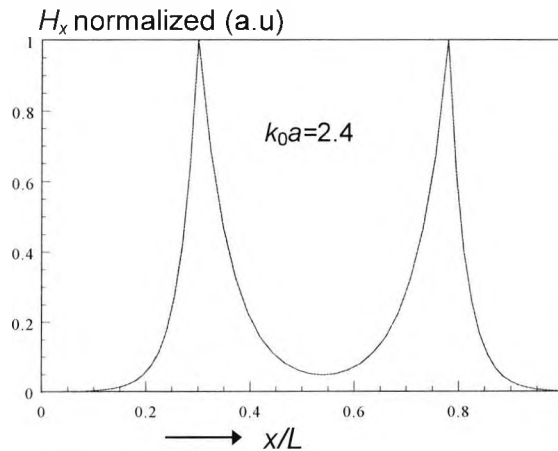


Fig.4.25 Normalized field profile for the even supermode of a symmetrical structure, for a normalized dielectric thickness, $k_0a=2.4$.

The propagation characteristics shown in Fig.4.23 can be explained from the observation of the field profiles of the first two supermodes, for different values of the dielectric thickness. The normalized field profile of the even supermode, for a small normalized film thickness, $k_0a=0.7$, is shown in Fig. 4.24, where it can be seen that the field intensity is equally high at the two metal/dielectric interfaces and quite strong in the center of the dielectric film as well. The supermode behaves like two strongly coupled surface plasmon modes which propagate at the two metal/dielectric interfaces. For a larger film thickness, $k_0a=2.4$, the field intensity at the centre of the even supermode reduces, as shown in Fig.4.25. As the two metal/dielectric interfaces are moved apart, the supermode decouples into two independent surface modes. These modes then propagate with an identical effective index, due to symmetry. This effective index corresponds to the effective index of a single metal dielectric interface, which was calculated, $n_e=2.12695$. This value corresponds to the value at which the effective index of the supermode converges, at a large film thickness, as shown in Fig.4.23.

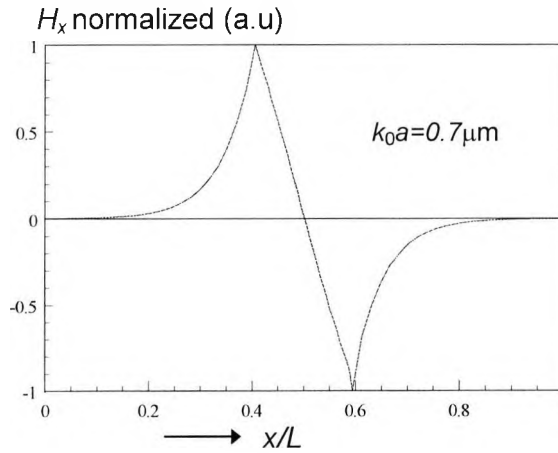


Fig.4.26 Normalized field profile for the odd supermode of a symmetrical structure, for a normalized dielectric thickness, $k_0a=0.7$.

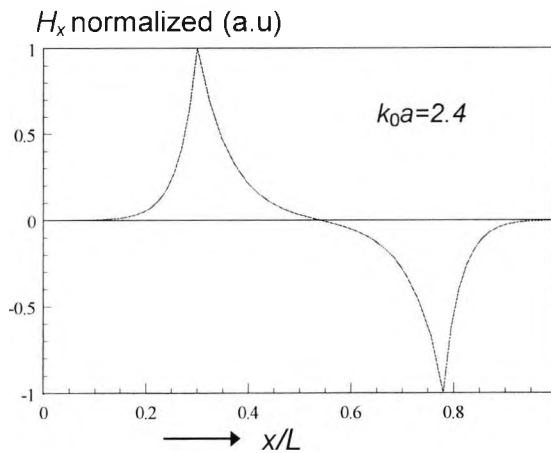


Fig.4.27 Normalized field profile for the odd supermode of a symmetrical structure, for a normalized dielectric thickness, $k_0a=2.4$.

Similar features can also be observed from the normalized field profiles of the odd-like supermode, for different values of dielectric thickness, $2a$. For a small normalized dielectric thickness, $k_0a=0.7$, as shown in Fig.4.26, there is an appreciable amount of field intensity in the dielectric region and the transition of the field intensity from positive to negative, from the two opposite peaks at the metal/dielectric interfaces, or *vice versa*, is nearly linear. For a larger normalized film thickness, $k_0a=2.4$, as shown in Fig.4.27., the supermode is more confined at each of the two interfaces, and the field intensity in the core of the waveguide flattens. The supermode decouples to two surface plasmon modes, which propagate at each metal/dielectric interface, but at opposite polarity, with an effective index equal to that of a single metal/dielectric interface, $n_e=2.12695$. The effective indices of the odd and the even

supermodes, converge to that value, as shown in Fig.4.23, one from below and the other from above, respectively.

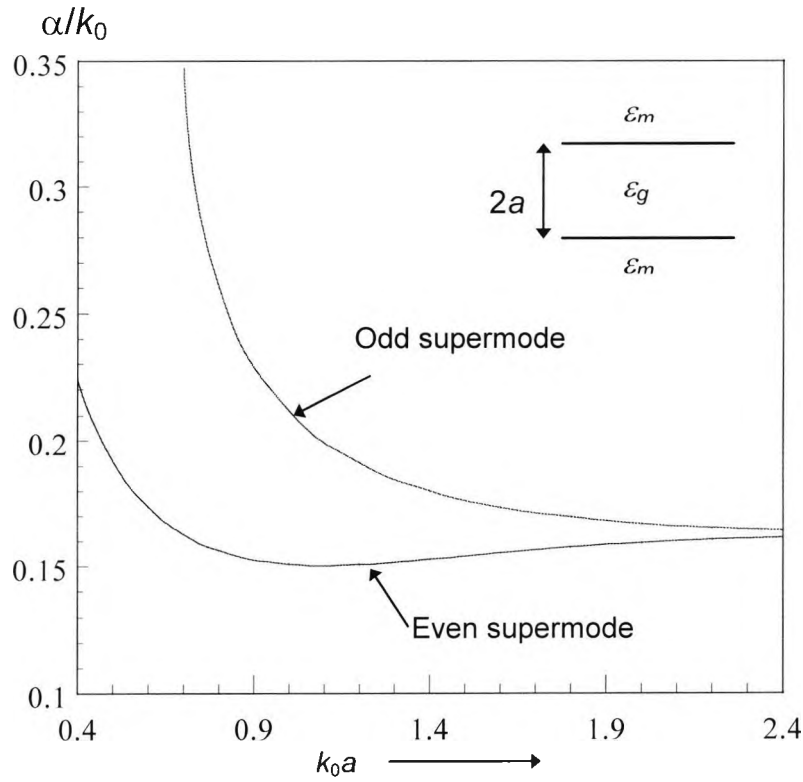


Fig.4.28. Attenuation characteristics of a symmetrical metal-clad surface plasmon structure.

Next, the attenuation characteristics of the first two supermodes, shown in Fig.4.28, are considered. Both the attenuation constants for the two supermodes decrease as the normalized film thickness, k_0a , increases, unlike the opposite structure in the previous section, where the attenuation constant was seen to be increasing for the even-like mode and decreasing for the odd-like one. In this type of structure the thickness of the two metal-claddings, which are the lossy regions, does not change, and therefore the attenuation constants depend mostly on the optical field intensity at the metal/dielectric interfaces. For the first supermode, the even supermode, the attenuation constant is lower than that for the second, the odd supermode. As the dielectric film thickness increases, the two normalized attenuation constants converge to a certain value which corresponds to the attenuation constant of a single metal/dielectric interface, as in the propagation characteristics, and this was calculated as $\alpha/k_0=0.16281$. This can be explained, again, from the field profiles of the two supermodes, which are decoupled to two independent surface plasmon modes, which propagate at the two interfaces, for large dielectric film thickness.

Next, a similar but a non-symmetrical structure was examined, where a normal dielectric film, $\epsilon_g=2.25$, is bounded by two thin metal film claddings and the dielectric constant of the top cladding, $\epsilon_{m1}=-4-j0.5414$, is higher than that of the lower, $\epsilon_{m2}=-3.24-j0.5414$, at an operating wavelength, $\lambda=0.6328\mu\text{m}$.

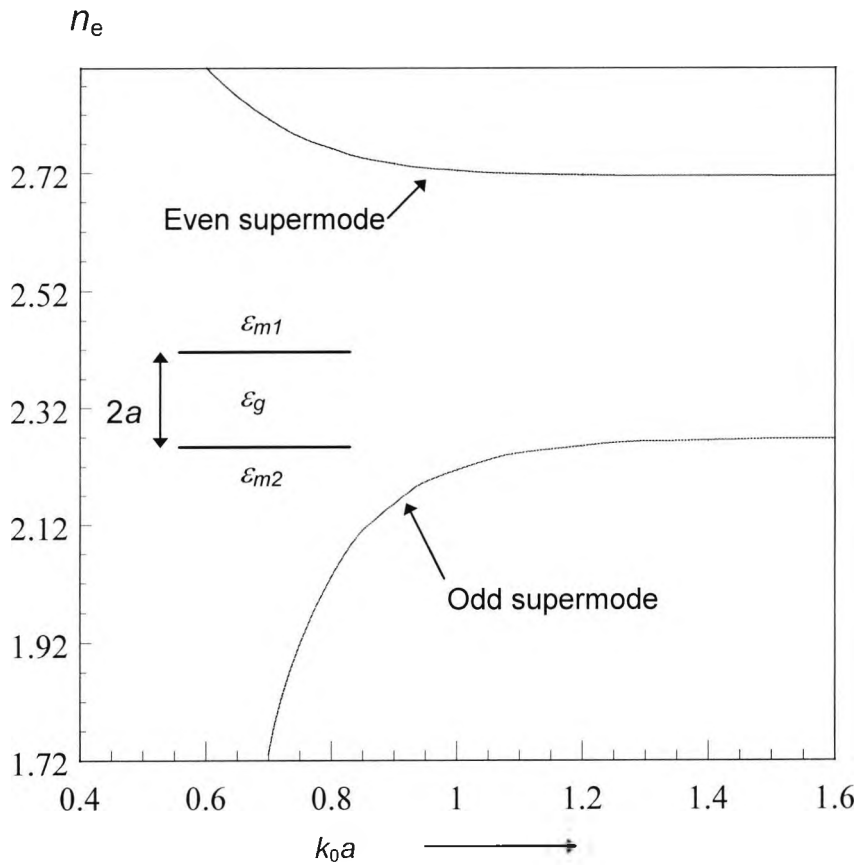


Fig.4.29 Variation of the effective index with the dielectric film thickness for a non-symmetrical surface plasmon structure.

From propagation characteristics, shown in Fig.4.29, it can be seen that the effective index variation, with the metal thickness, for the first two bound supermodes, has similar shape with that of the symmetrical structure. The only difference in this case is the value at which the two supermodes converge at a large metal thickness. The effective index of the even supermode, which decreases with the increase of the metal thickness, is again higher than that of the odd supermode and also converges at a higher value, $n_e=2.71458$, than that of the odd supermode, $n_e=2.2672$.

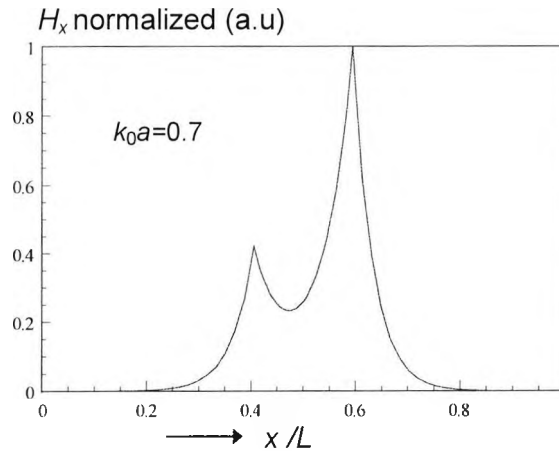


Fig.4.30 Normalized field profile for the even-like supermode of a non-symmetrical structure, for a normalized film thickness, $k_0a=0.7$.

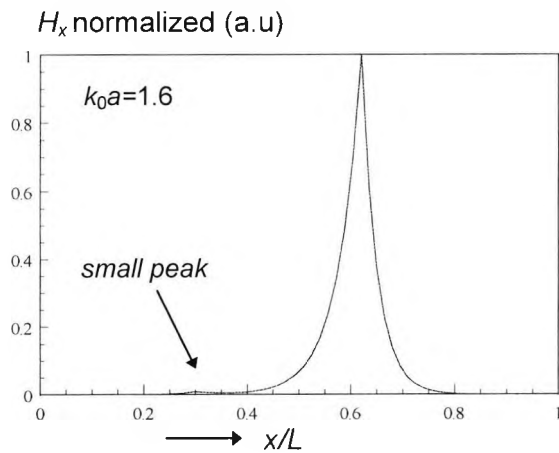


Fig.4.31 Normalized field profile for the even-like supermode of a non-symmetrical structure, for a normalized film thickness, $k_0a = 1.6$.

From the normalized field profile of the even supermode, for a dielectric film thickness $k_0a=0.7$, shown in Fig.4.30, it can be seen that there is higher field intensity in the right interface, which corresponds to the interface between the dielectric and the metal with the lower dielectric constant, $\epsilon_{m2}=-3.24$. When the normalized film thickness is increased to $k_0a=1.6$, as shown in Fig.4.31, the field intensity at the left interface becomes negligible and the supermode propagates almost entirely at the interface between the dielectric film and the metal with the lower dielectric constant. The coupled supermode then becomes a single surface plasmon mode and the overall effective index for such large film thickness converges to the effective index of a single metal/dielectric interface, which was calculated as $n_e=2.714$.

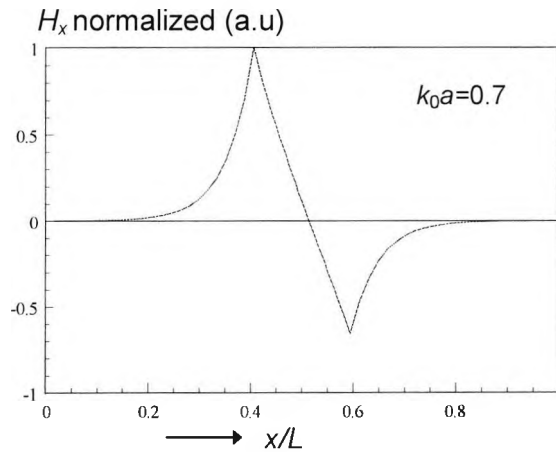


Fig.4.32 Normalized field profile for the odd-like supermode of a non-symmetrical structure, for a normalized film thickness, $k_0a=0.7$.

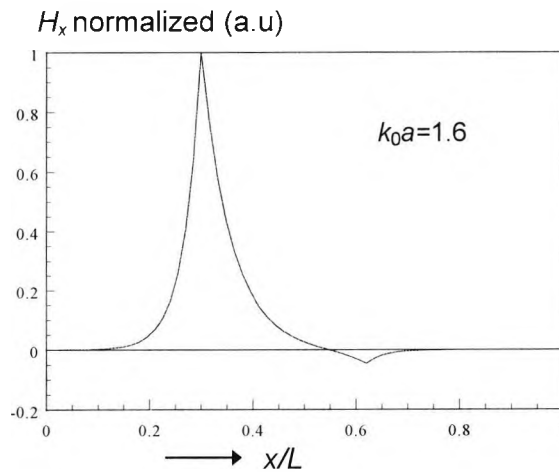


Fig.4.33 Normalized field profile for the odd-like supermode of a non-symmetrical structure, for a normalized film thickness, $k_0a=1.6$.

Figure 4.32, shows the normalized field profile of the odd supermode, for a normalized film thickness, $k_0a=0.7$, where the most of the field is concentrated at the left metal/dielectric interface, which is the interface of the metal with the higher dielectric constant $\epsilon_{m1}=-4$. When the film thickness is increased further to $k_0a=1.6$, as shown in Fig.4.33, the supermode propagates almost entirely so as to be confined near to that interface, and the effective index converges to the effective index of a single metal/dielectric interface, which for this case was calculated to be $n_e=2.2679$.

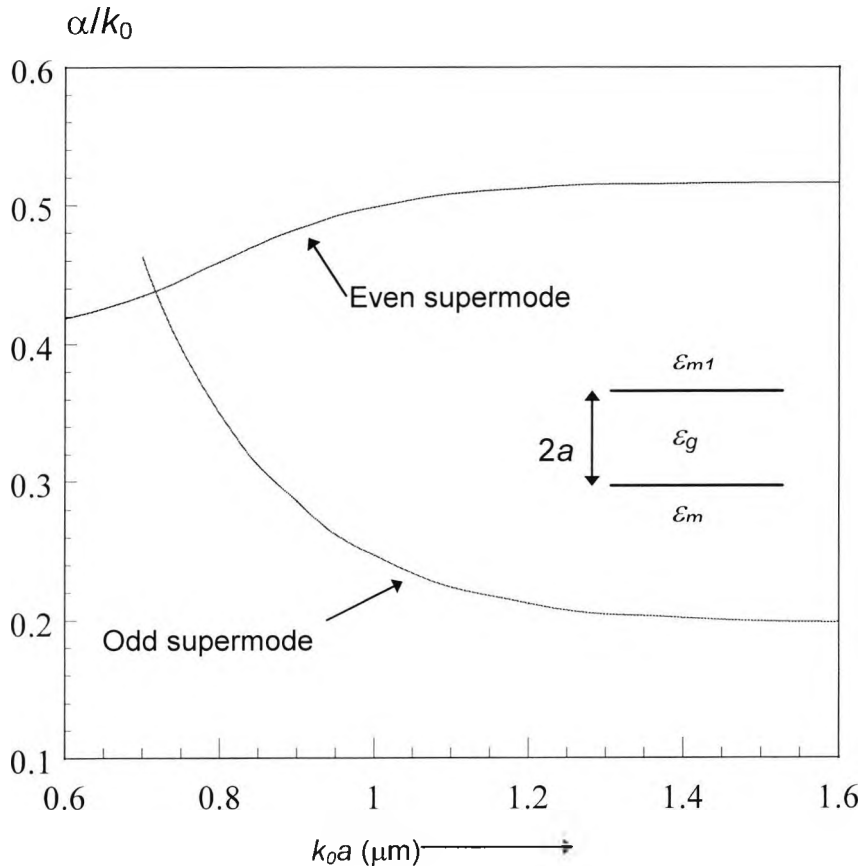


Fig.4.34 Variation of the normalized attenuation constant with the dielectric film thickness for a non-symmetrical surface plasmon structure.

Next, the attenuation characteristics, for the non-symmetrical waveguide, shown in Fig.4.34 were examined for the first two supermodes. From the two curves it can be seen that the normalized attenuation constant, α/k_0 , for the even supermode, increases with the increase of the normalized dielectric film thickness, k_0a , and converges to a limiting value. As was observed before, for large film thickness, the supermode propagates only at the interface between the dielectric and the metal with the lower dielectric constant, and therefore, the limiting value of the normalized attenuation constant approaches the normalized attenuation constant of a single metal/dielectric interface, which was calculated as $\alpha/k_0=0.51597$. Since the odd supermode, for large film thickness, propagates mainly at the interface of the dielectric and the metal with the higher dielectric constant, the normalized attenuation constant of that supermode converges to the value of the normalized attenuation constant of a single interface, consisting of the above two materials only, which was calculated to be $\alpha/k_0=0.19738$.

The two metal claddings in the non-symmetrical structure above have the same imaginary part of the dielectric constant, so, the most lossy material can be considered to be the material with the lowest real part of the dielectric constant, which in this case is ϵ_{m1} . Therefore, as the film thickness increases, the attenuation constant of the even supermode is higher than that of the odd, because the mode propagates mostly at the interface with the metal which has the lower real part of the dielectric constant, *i.e.*, the most lossy one. The odd mode has lower attenuation constant, for a large film thickness, because it propagates mostly at the interface with the less lossy metal film, that with the higher dielectric constant.

4.4 Multilayer metal-clad planar optical waveguides

The multilayer metal-clad planar optical waveguide, with a low-index dielectric buffer (shown as an insert in Fig.4.35), has some very important features, which are used in the design of many integrated optics circuit applications. In this type of structure, the attenuation constant of the TM mode is much larger than that of the TE, therefore it can be used as an integrated optics polarizer. This property can also be used in the design of a mode filter, where it is desirable to achieve high extinction ratio (α_{TM}/α_{TE}), without introducing significant loss to the transmitted light (Yamamoto *et al.*, 1975). Polky and Mitchel (1974), showed that in such structure, the TM guided modes exhibit an absorption peak, which is caused by the resonant coupling to the lossy surface mode and can be controlled by the thickness of the low-index buffer layer. This feature, combined with the steep slope of the TM loss curve, is desirable in the design of an absorption modulator. This structure was also proposed by Reisinger (1973), in order to reduce ohmic losses, which are caused by the build up of electromagnetic energy at the metal/dielectric boundaries in the TM guided modes, due to surface plasmon waves. Reisinger also claimed that as the buffer thickness increases, a TM_0 mode goes under continuous transformation to become the next TM_{n+1} , higher order mode.

A four layer metal-clad planar optical waveguide has been examined, in order to investigate the above properties, which consists of an aluminum metal-cladding with a complex refractive index, $n_m=1.2-j7$, a glass buffer layer, $n_2=1.544$, a core Al_2O_3 core, $n_3=1.758$, and a SiO_2 substrate, $n_4=1.457$, at an operating wavelength of $\lambda=0.633\mu m$.

The complex propagation characteristics of the above structure were calculated by using the scalar FEM with the perturbation technique, and the attenuation characteristics were compared with those obtained by Yamamoto *et al.* (1975), for the same structure, as shown in Fig.4.35. From the comparison of the variation of the normalized attenuation constant, $2a\alpha$, with the core normalized thickness, $2a/\lambda$, for a fixed buffer layer thickness, $b=0.1\mu m$, the attenuation curves presented are found to be in good agreement, for both the TE and TM modes.

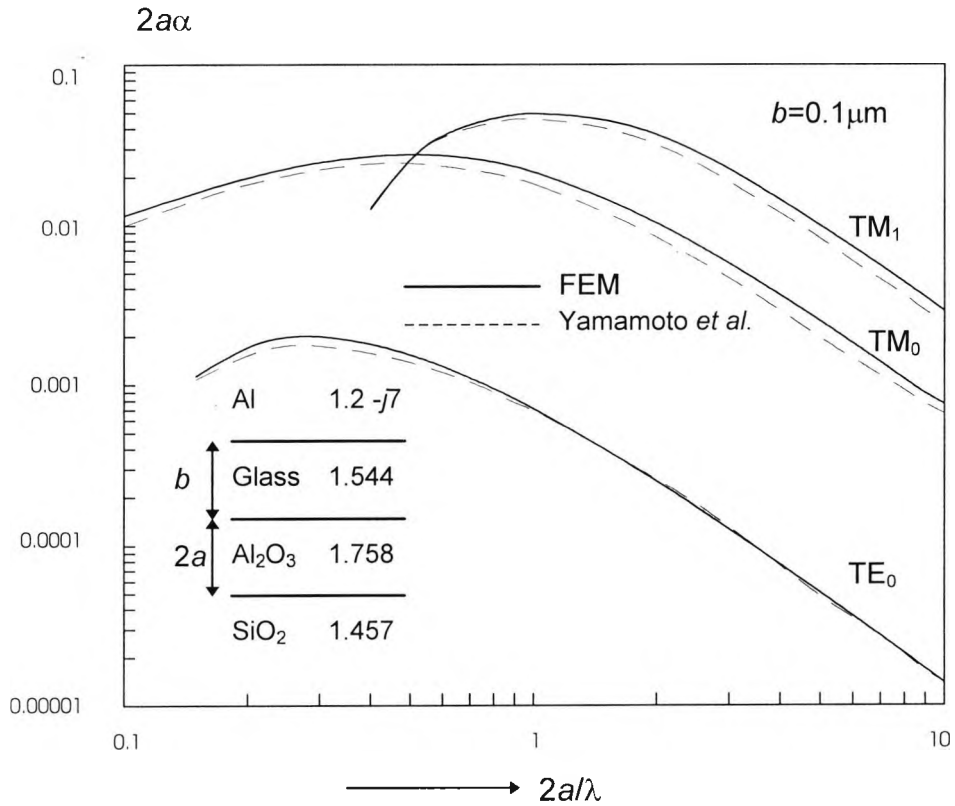


Fig.4.35. Attenuation characteristics for the metal-clad planar optical waveguide, for lower-index buffer layer thickness, $b=0.1\mu\text{m}$

From the attenuation characteristics in Fig.4.35, it can also be seen that the normalized attenuation constant, $2a\alpha$, for all the TM modes, is about 10 times larger than that of the corresponding TE mode, thus giving a high extinction ratio ($\alpha_{\text{TM}}/\alpha_{\text{TE}}$), suitable for the design of a mode filter, at certain attenuation levels. When the normalized film thickness, $2a/\lambda$, increases the normalized attenuation constants for all the modes decreases, because the mode becomes more confined in the film region and there is not much field intensity in the metal-clad region, which is the lossy region of the waveguide.

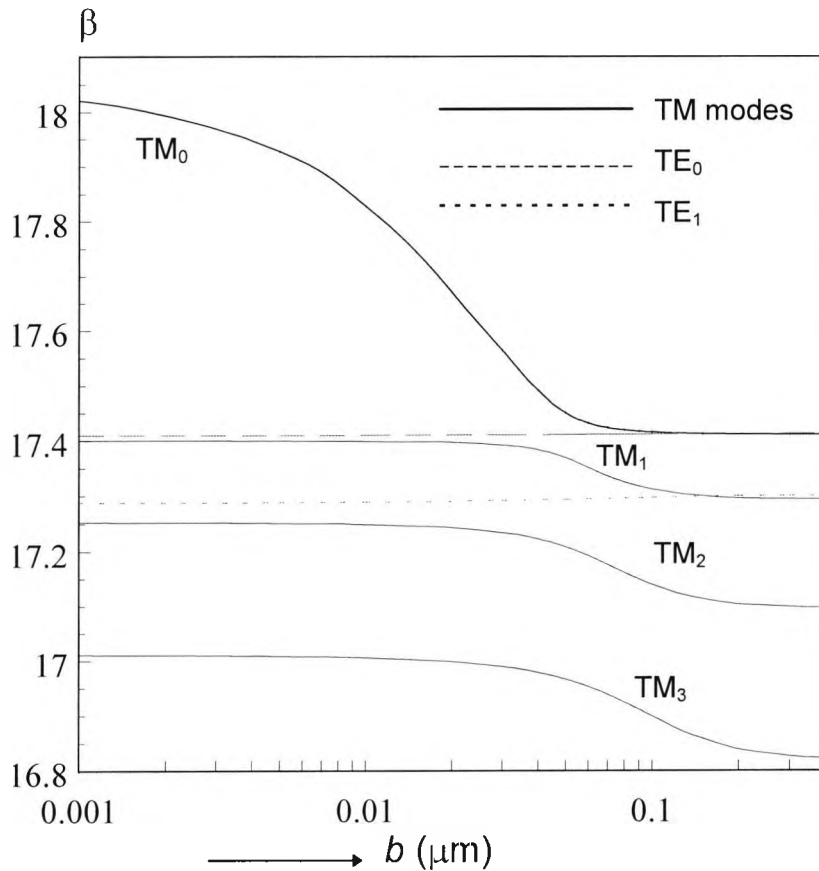


Fig.4.36 Variation of the phase constant (β), with the buffer layer thickness, of the TE and TM modes, for a multilayer metal-clad planar optical waveguide.

Further, the attenuation properties of the guide, with the variation of the low-index buffer layer thickness, b , were examined, for a fixed normalized core thickness, $2a/\lambda=4$. From the propagation characteristics, shown in Fig.4.36, it can be seen that initially the phase constant, β , decreases quickly for all the TM modes, as the buffer layer thickness increases, and then remains almost constant with a slight increase for the TE modes. The TM_0 mode has the highest phase constant for small buffer thickness and as the thickness increases, the phase constant reduces rapidly and after a buffer thickness of about $b=0.053 \mu\text{m}$, it remains almost constant and the mode propagates with a phase constant close to that of the TE_0 mode. The TM_1 mode which has a much smaller phase constant exhibits similar behaviour, and as the buffer thickness increases, it settles to a value close to that of the TE_1 mode.

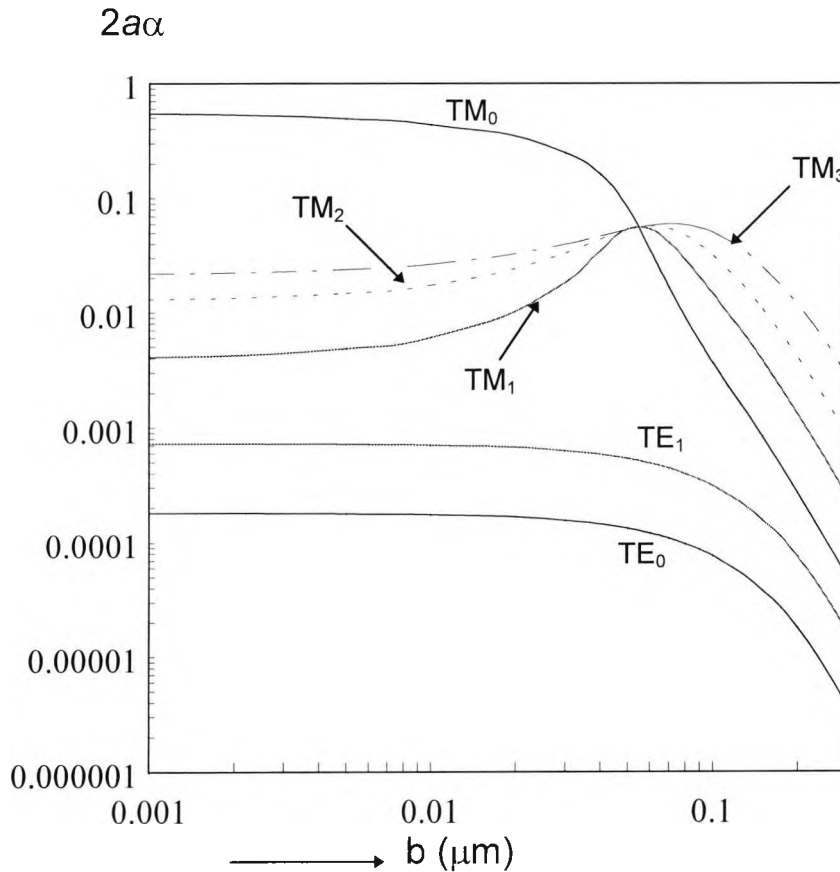


Fig.4.37 Variation of the normalized attenuation constant, with the buffer layer thickness, for the TE and TM modes, of a multilayer metal-clad planar optical waveguide.

Next, the effect of the variation of the buffer layer thickness on the modal loss of the above structure, is studied. From the attenuation characteristics, shown in Fig. 4.37, it can be seen that the TM modes have a higher normalized attenuation constant than their counterpart TE modes, particularly the lower order TM_0 having a magnitude about 3 orders greater than that of the TE_0 mode, for a small buffer layer thickness, b . These curves agree well with those obtained by Yamamoto *et al.* (1975), for the same structure. As the buffer layer thickness increases, the attenuation constant of the TM_0 mode decreases, while for the other higher order TM modes it increases, reaching a peak value. This point was defined by Polky and Mitchel (1974) as the *absorption peak*, for the TM_1 mode, but here it is shown that this peak value occurs for all the other higher order modes, and additionally, that as the mode order is higher the corresponding peak value of the attenuation constant, for each mode, is higher. The attenuation constants of all the TM modes intersect, at a buffer thickness of about $b=0.053 \mu\text{m}$, just before the absorption peak of the higher order modes, and after that they all decrease rapidly. The attenuation constant for the TE modes is much lower

than that of the TM modes and remains constant for small buffer layer thickness values. When the thickness reaches the point where the TM modes have an absorption peak, the attenuation constants for all the TE modes decrease rapidly like the TM modes.

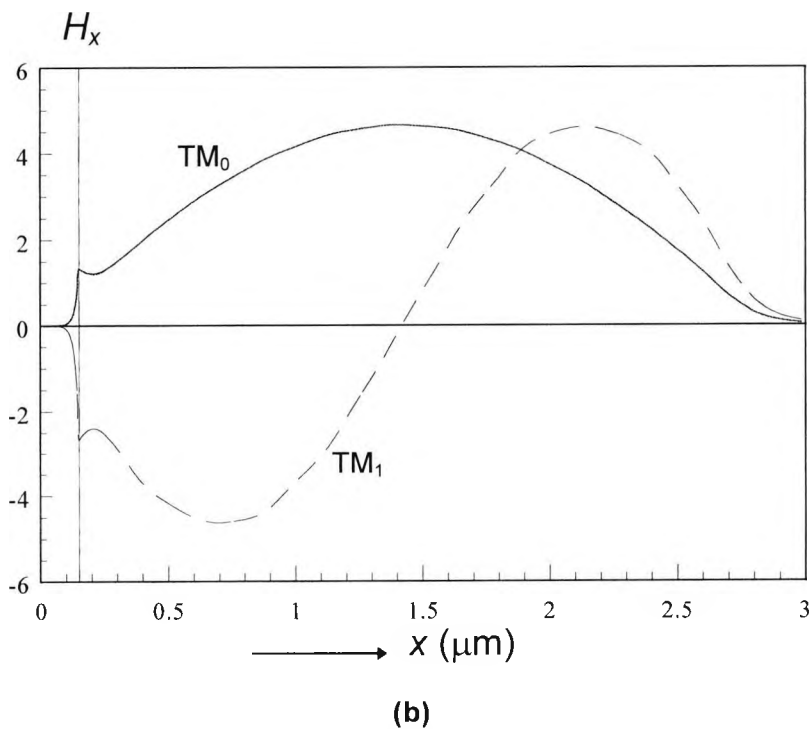
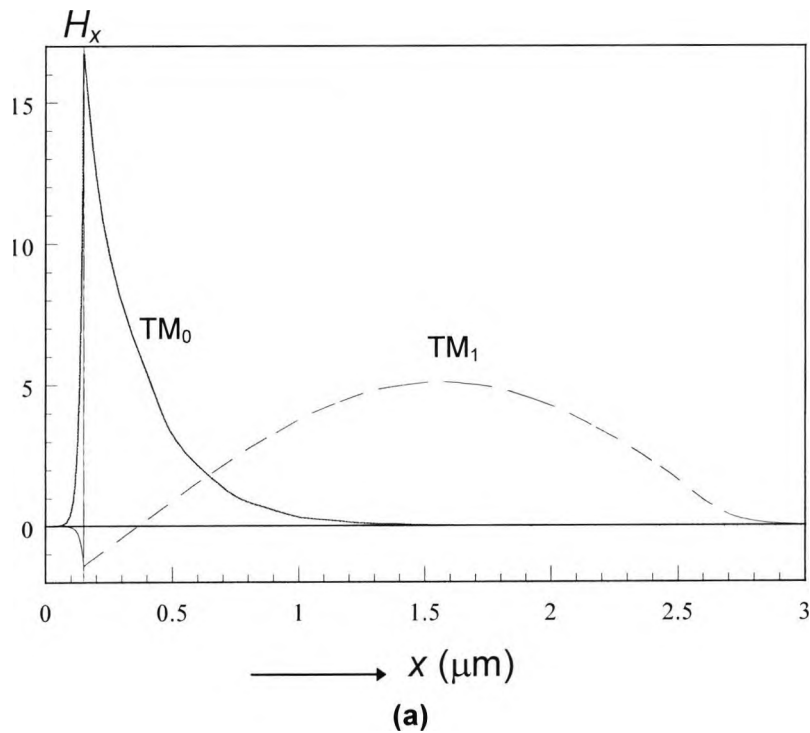


Fig. 4.38 H_x field distribution for the TM_0 and TM_1 modes for a buffer layer thickness, a) $b=0.001\mu\text{m}$, b) $b=0.1\mu\text{m}$.

In order to examine the loss mechanism of the above structure it is essential to observe the field profiles of the various modes for the different values of the buffer layer thickness. Figure 4.38 shows the H_x field profile for the TM_0 and TM_1 modes for two different values of the buffer layer thickness, b , where the subscripts of the modes used, denote the zero crossings of the field distribution. For $b=0.001\mu\text{m}$, the TM_0 mode is a pure surface plasmon mode, located at the boundary of the metal and the low index layer (shown as a vertical axis-line at $x=0.15\mu\text{m}$), and the TM_1 mode is a normal (fiber) guided mode, with some minor interference at the metal/dielectric interface. On the other hand, for a large value of the buffer thickness, $b=0.1\mu\text{m}$, the TM_0 mode undergoes transformation from a surface plasmon mode to a guided film mode and the TM_1 mode to a higher order (odd) guided mode. For small buffer thickness, the TM_0 mode has higher attenuation constant, because there is a high field intensity in the metal layer which is the lossy material.

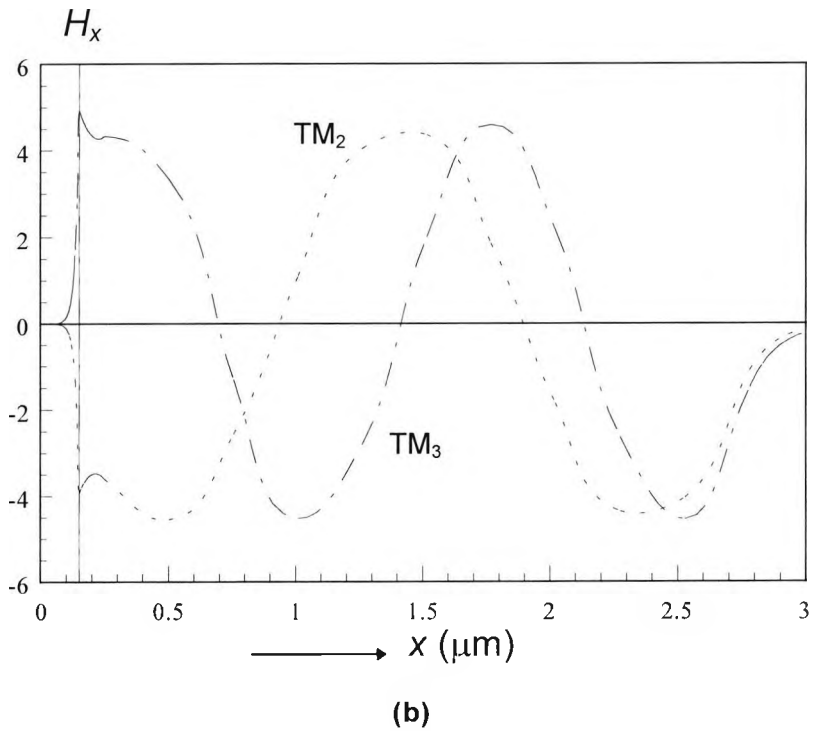
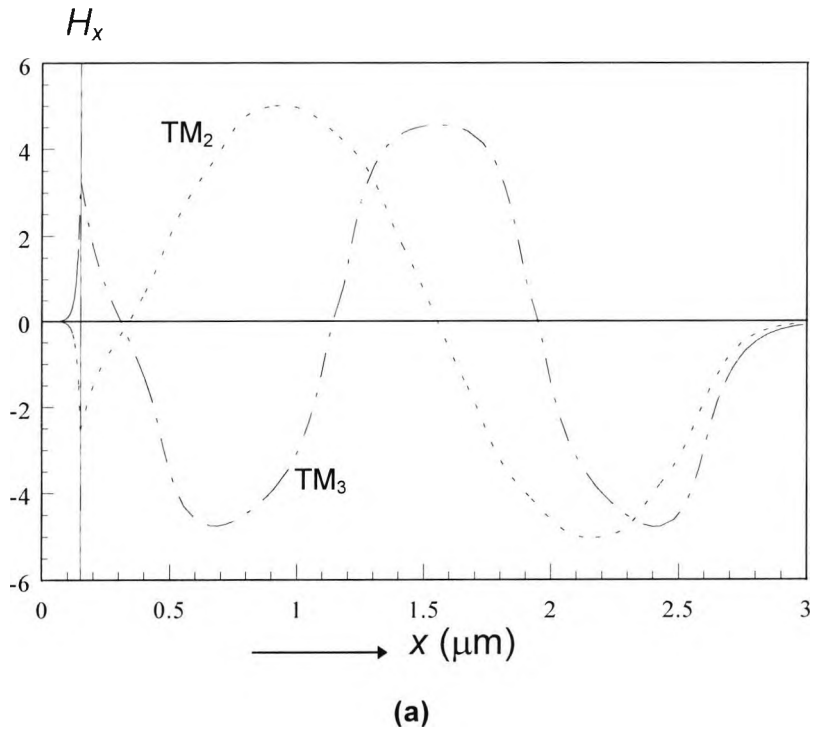


Fig. 4.39 H_x field distribution for the TM_2 and TM_3 modes for a buffer layer thickness: a) $b=0.001\mu\text{m}$, b) $b=0.1\mu\text{m}$.

Figure 4.39, shows the field profiles for the TM_2 and TM_3 , higher order modes for the same values of the buffer layer thickness as in Fig.4.38. As the buffer layer thickness increases, the TM_2 mode is transformed, approximately, to the TM_3 mode and the TM_3 mode into a higher order mode, while in both the modes there is a finite

amount of field intensity in the metal-cladding region, keeping the attenuation constant high.

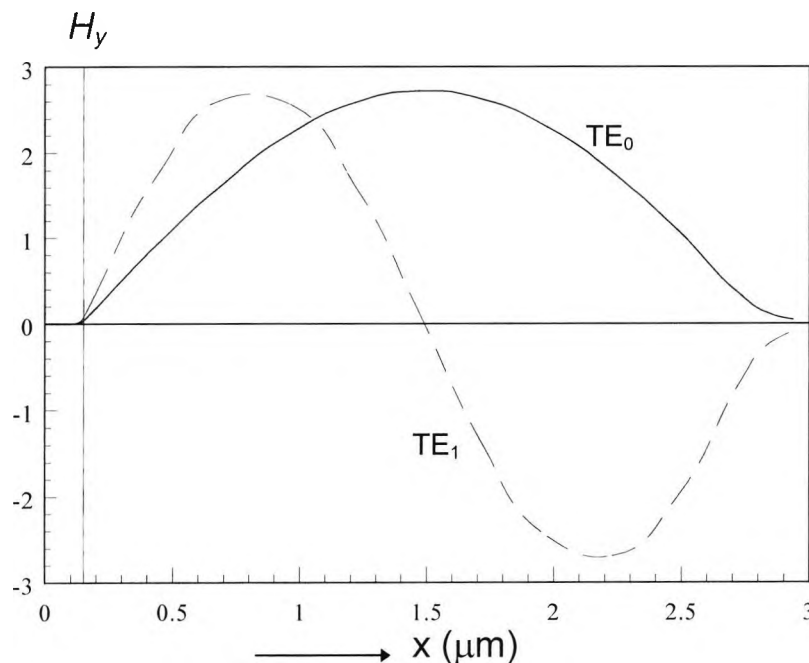


Fig.4.40 H_y field distribution for the TE_0 and TE_1 mode, for a buffer layer thickness, $b=0.053\mu\text{m}$.

By observing the field profiles of the TE_0 and TE_1 modes, for a buffer layer thickness, $b=0.053$, shown in Fig.4.40, it can be seen that the field intensity in the metal-cladding region is negligible, therefore the attenuation constant is very small for all the TE modes, since they are not affected by the metal-cladding and they are purely guided modes.

By considering again the propagation characteristics, shown in Fig.4.36, after the field profiles have been examined, it can be concluded that as the buffer layer thickness increases, every TM mode transforms to the one of next higher order. This was also claimed by Reisinger (1973), but shown only for the TM_0 mode. The above conclusion can be drawn, not only from the propagation characteristics, but from the field profiles as well. The phase constant of the TM_0 mode at large buffer thickness, b , approaches that of the TM_1 mode for small buffer thickness, the corresponding one of the TM_1 , that of TM_2 and so on. This can also be seen from the field profiles, where, in Fig.4.38.b, TM_0 (for $b=0.1\mu\text{m}$) has similar field distribution to that of the TM_1 mode in Fig.4.38.a, (for $b=0.001\mu\text{m}$), except that the field intensity in the metal-cladding has the opposite polarity. Additionally, the TM_1 field profile for $b=0.1\mu\text{m}$, shown in Fig.4.38.b, approaches that of the TM_2 , for $b=0.001\mu\text{m}$, shown in Fig.4.39.a, again with the field intensity in the metal-cladding in reverse polarity, and so on.

Further, from the propagation characteristics, shown in Fig.4.38, it can be seen that as the buffer layer thickness, b , increases, the phase constant of the TM_0 mode approaches that of the TE_0 mode and the phase constant of the TM_1 mode that of the TE_1 mode. This can also be seen from the field profiles of the corresponding TM and TE modes. The TM_0 and TM_1 modes, for $b=0.1\mu\text{m}$, shown in Fig.4.38, have similar profiles to that of the TE_0 and TE_1 modes respectively, shown in Fig.4.40, apart from the field intensity in the metal-cladding interface, which is still appreciable. As the buffer layer thickness increases to beyond $0.1\mu\text{m}$, the field intensity in the metal-cladding weakens and becomes negligible, because the mode gets more confined in the dielectric region, thus leaving the TM modes with an almost identical field profile with their counterpart TE modes. Therefore it can be safely claimed that as the buffer layer increases, the TM modes are transformed to their counterpart TE modes, and propagate with almost the same phase constant, β .

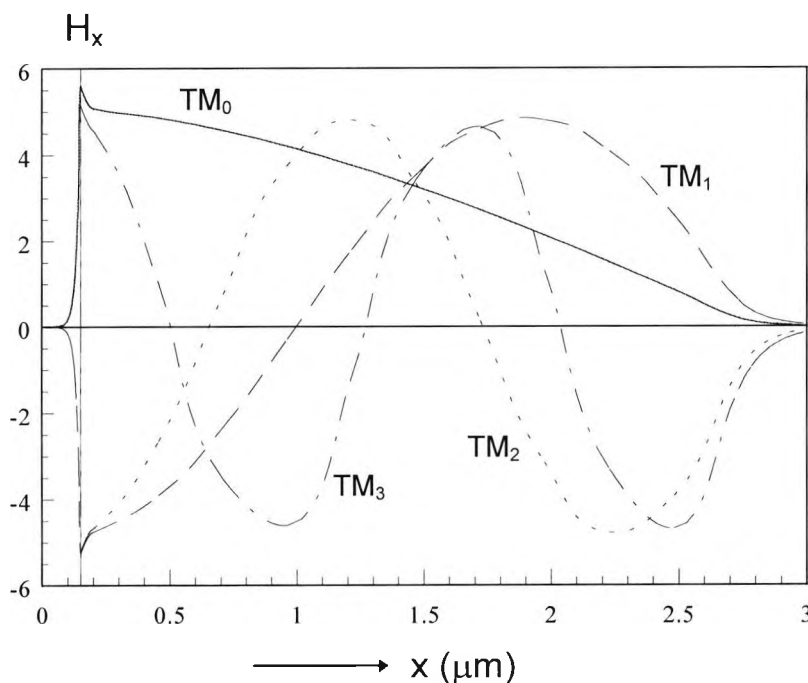


Fig.4.41 H_x field profile for the TM modes for the multilayer metal-clad planar waveguide for buffer layer thickness, $b=0.053\mu\text{m}$.

Additionally, for the propagation characteristics, shown in Fig.4.36, it can be seen that for a buffer layer thickness larger than $b=0.053\mu\text{m}$, the phase constant for all the TM modes reduces in a smooth step-like way to a lower value. For about the same buffer thickness, the attenuation characteristics for the TM modes, shown in Fig.4.37.

intersect just before their absorption peak. For this buffer layer thickness, the TM modes, shown in Fig.4.41, appear to be strongly coupled composite modes, consisting of a surface plasmon mode due to the metal/dielectric interface, and a normal guide mode due to the high refractive index dielectric film. At the above buffer layer thickness, the field intensity is almost equally high, both at the metal/dielectric interface (at $x=1.5\mu\text{m}$) and the dielectric region, for all the TM modes, and therefore the wave attenuation reaches a maximum and an absorption peak is observed. This is the case of a phase-match condition, where a resonant absorption peak is achieved and can be controlled by the buffer layer thickness, which is a very important feature in integrated optics applications.

4.5 Summary

In this Chapter, the complex propagation characteristics of certain types of planar optical waveguides incorporating loss or gain were investigated, by using the scalar **H**-field FEM with perturbation and by solving the complex transcendental equation, and the limit of the perturbation technique was determined by comparing the two approaches. Planar structures incorporating metal films, which exhibit loss and surface plasmon properties, were also analyzed, and finally multilayer structures with metal layers suitable for mode filter applications were also examined.

The analysis of the several planar optical waveguides examined, which are the basic elements of integrated optical circuits, forms the basis for the characterization of more complicated optical waveguide structures, exhibiting similar properties.

5

Two-dimensional modal gain/loss analysis of optical waveguides

5.1 Introduction

In the previous chapter, the analysis of planar waveguides was based on the assumption that the light was confined only in one direction. In most practical applications though, more complicated structures are used, and the modal solution of the optical waveguides confined in both the transverse directions is required. The most common types of optical waveguides used in integrated optics are rectangular strips of dielectric material embedded in other dielectrics, such as the rectangular dielectric and the channel waveguide, or some more complicated structures as the rib waveguide, as shown in Fig.5.1. An analytical solution of such structures is not possible, and therefore, approximate analytical solutions are used, such as are obtained with the Effective index method (Knox and Toullos, 1970), or numerical solutions are obtained such as with the use of the FEM.

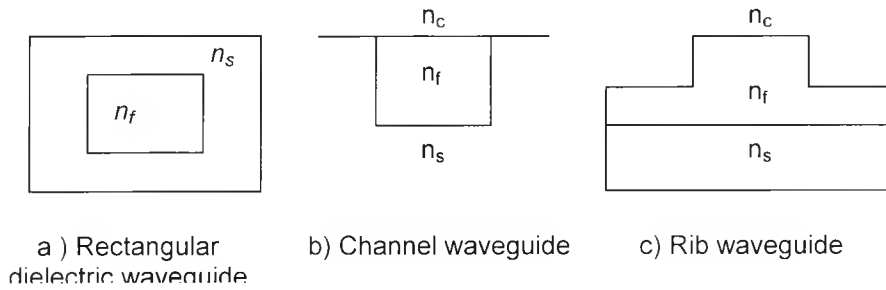


Fig.5.1 Three types of practical optical waveguides

In this chapter, a two-dimensional modal gain/loss analysis was performed for some typical types of optical waveguides, by using the FEM with perturbation and other techniques. Additionally, the gain and attenuation properties of such waveguides were examined in conjunction with some applications in integrated optics and other optical devices.

5.2. The Rectangular dielectric waveguide

The rectangular dielectric waveguide, where a dielectric material is embedded in another dielectric, is one of the most common types of optical waveguides. Depending on the material properties, it can be used in many applications in integrated optic devices and optical communications systems, and because of its simple geometry, it can be analysed by the use of several different approaches.

The shape of the rectangular dielectric waveguide, is such that can be used for the modal analysis of buried heterostructure diode lasers, as proposed by Hayata *et al.* (1986a), which are of great interest, since their emitting wavelength covers the low-loss, low-dispersion region of silica-fused fibers. This type of structure, having active regions, composed of GaInAsP with a stripe geometry, and embedded in InP crystal, have been extensively studied because of their low threshold current.

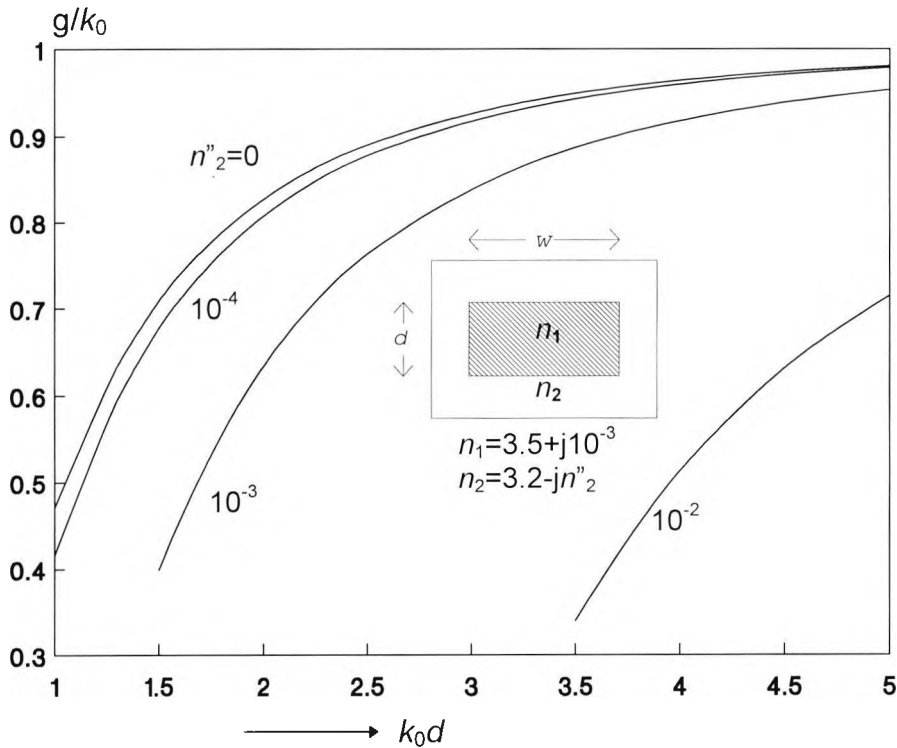


Fig.5.2 Variation of modal gain with the normalized dimension for the TE_{11} mode of an embedded channel waveguide

The modal gain for the simplified representation of a GaInAsP/InP buried heterostructure diode laser structure was calculated, by using the scalar approximation of the FEM with the aid of the perturbation technique. In this type of structure the width of the active region, w , is five times greater than the height of the active layer, d . The imaginary part of the refractive index in the active region is considered to be $+j10^{-3}$ representing the modal gain in this region. Figure 5.2 shows the variation of the modal gain for the E_{11}^x mode with the normalized height, k_0d , for different negative imaginary values (with loss) of the cladding refractive index. As the normalized thickness of the core, k_0d , increases, the normalized gain constant increases, for all the values of the imaginary part of the cladding refractive index. The reason is that as the normalized core thickness, k_0d , increases, the mode becomes more confined in the core region whereas in the cladding there is no appreciable optical power, and therefore the attenuation constant is eventually determined only by the imaginary part of the refractive index of the core. When the imaginary part of the cladding refractive index, n_2 , is equal to zero, indicating a lossless cladding, the normalized gain constant is higher than that for the other cases, where there is finite amount of loss in the cladding. As the imaginary part of the cladding refractive index increases, the

normalized gain constant decreases and when $n''_2=10^{-2}$, there is a larger decrease in the gain than the other cases, because the imaginary part of the cladding index is higher than the imaginary part of the core index. For the above value of the cladding imaginary part, in the range examined, the structure does not become lossy, because the mode is very well confined in the core region which shows gain and there is not much field intensity in the lossy cladding. If the normalized thickness were decreased further than the range shown, there would be a decrease of the core area, and the mode would be more spread into the cladding, which would cause the gain constant to become negative, therefore becoming an attenuation constant.

There is an excellent agreement between results calculated in this work using the FEM and those of Hayata *et al.* (1986) at $k_0=1$, when both the perturbation equations are identical. Results using the perturbation equation are dependent only on the product k_0d , but independent of the values of k_0 and d individually, whereas results using equation (9) in the work of Hayata *et al.* vary with k_0 , even when the product, k_0d , is constant.

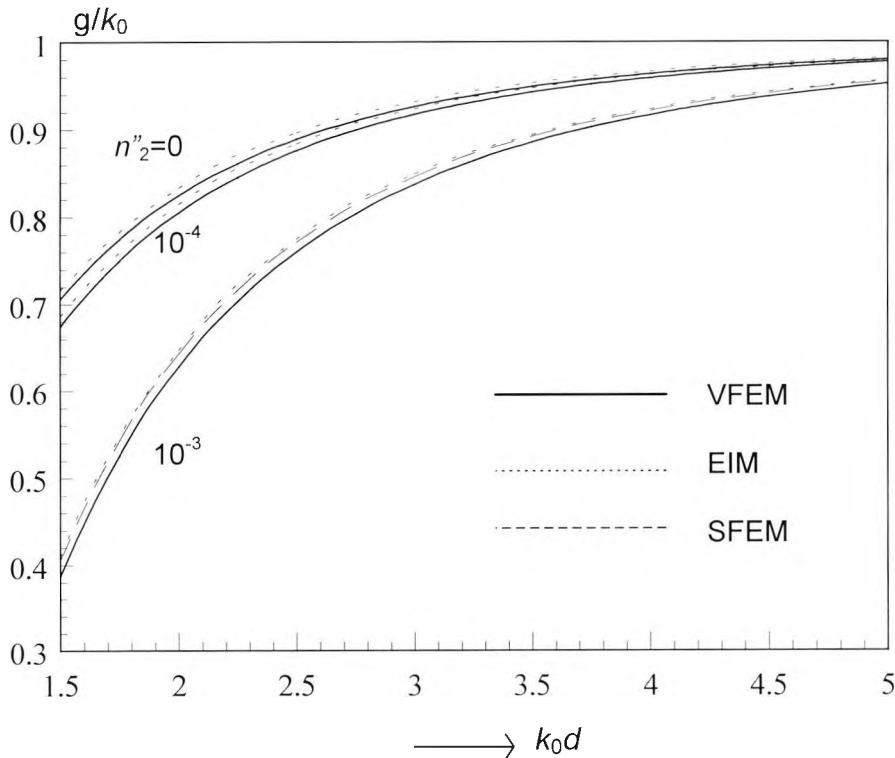


Fig 5.3 Variation of the normalized modal gain (g/k_0) with the normalized dimension for the H_{11}^y mode of an embedded-channel waveguide, using the complex Effective Index Method (EIM) and the scalar and vector Finite Element Method.

Next the complex EIM and scalar and vector FEM approaches are compared for different waveguide dimensions and loss parameters of the above GaInAsP/InP embedded channel waveguide. Variations of the normalized modal gain (g/k_0) with the normalized waveguide dimension (k_0d) are shown in Fig.5.3, for the fundamental H_{11}^y (quasi-TE) mode. Results obtained using the vector finite element method (VFEM) agree very well (with a mean difference of about 2.4%) with those of the complex effective index method (EIM). These results also compare favourably with those using the scalar FEM with perturbation. It can be observed that with the normalized modal gain for $n_2''=10^{-3}$, using the scalar Finite Element Method (SFEM) and the effective index method (EIM), although they agree very well, both of these methods slightly over-estimate the modal gain as compared to the results obtained using the vector Finite Element Method (VFEM). For simplicity only the vector Finite Element Method (VFEM) and the results of the Effective Index Method (EIM) are shown for $n_2''=0$ and 10^{-4} and they also are seen to compare favourably.

The validity of the scalar and vector FEM approaches with respect to the \mathbf{H}_t formulation and the Complex Effective Index Method (EIM), has also been tested for the above GaInAsP/InP embedded rectangular channel waveguide. The variation of the effective indices and modal gain (or loss) for the fundamental quasi TE (H_{11}^y) mode with the total element number is shown in Fig.5.4, for various numerical approaches used in this work. In the \mathbf{H}_t approach, Maxwell's equations are solved in terms of the transverse field components, yielding no spurious solutions, with the use of an efficient complex sparse matrix solver. In the Vector \mathbf{H} -field (H) and the Scalar (S) approaches, the solutions obtained, with the aid of an efficient sparse, real matrix solver, for the lossless case, are used in conjunction with the perturbation technique (P) to calculate the modal gain (or loss) properties. In the Effective Index Method (EIM), the solution of the complex transcendental equation is obtained iteratively, to calculate the complex propagation constant.

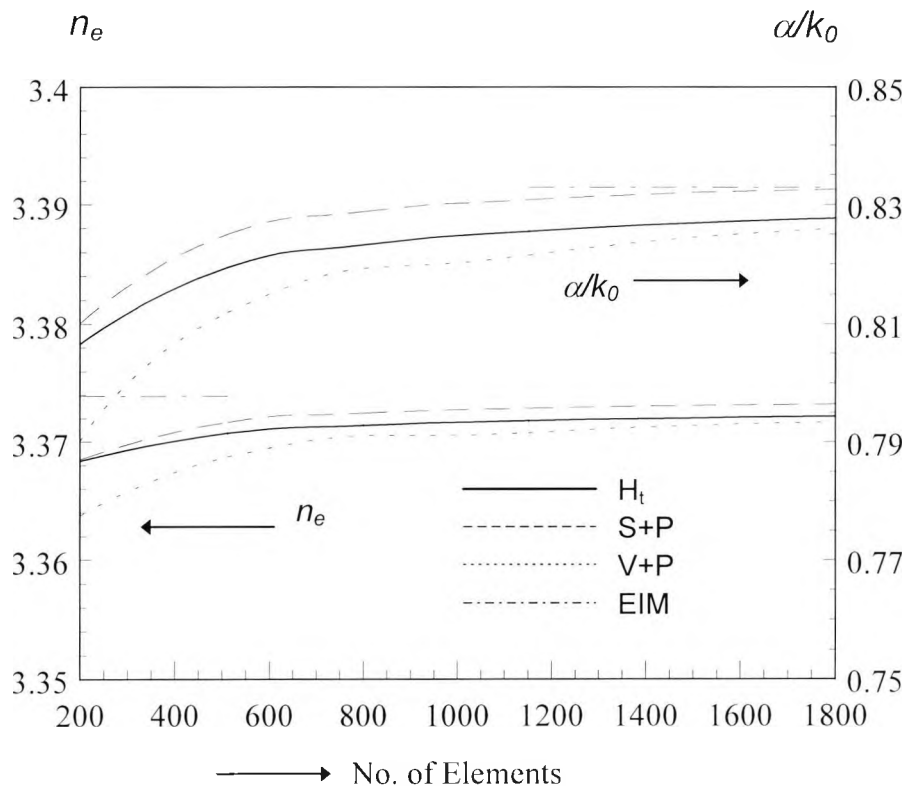


Fig.5.4 Variation of the effective index (n_e) and the normalized attenuation constant (α/k_0) with the mesh division of an embedded channel waveguide, using the H_t , the vector H -field with perturbation (V+P) and the scalar H -field with perturbation (S+P) finite element formulations and the complex effective index method (EIM).

It can be observed that as the number of elements is increased, the modal solution is seen to converge. When the number of elements is 1800, the effective index values (n_e) obtained by the H_t and the vector (V+P) approaches agree well. For the above mesh representation, the Scalar approach (S+P) and the EIM, which is analytical and does not depend on the mesh size, overestimate the effective index, n_e , by about 0.001, compared to the more accurate H_t and the vector (V+P) approaches. The modal gain characteristics, also shown in Fig.5.4, demonstrate similar behaviour for the above methods. In this case, at 1800 elements, the EIM and the scalar (S+P) methods overestimate the factor α/k_0 , by 0.005 (about 434 dB/cm), compared to the use of the H_t and the vector (V+P) approaches.

It can be noted that, for 1800 elements, the cpu time is about 25 seconds on a Sun Classic Sparcstation, for the vector (V+P) solution. The H_t program was executed on a different workstation and appears to require a longer cpu time.

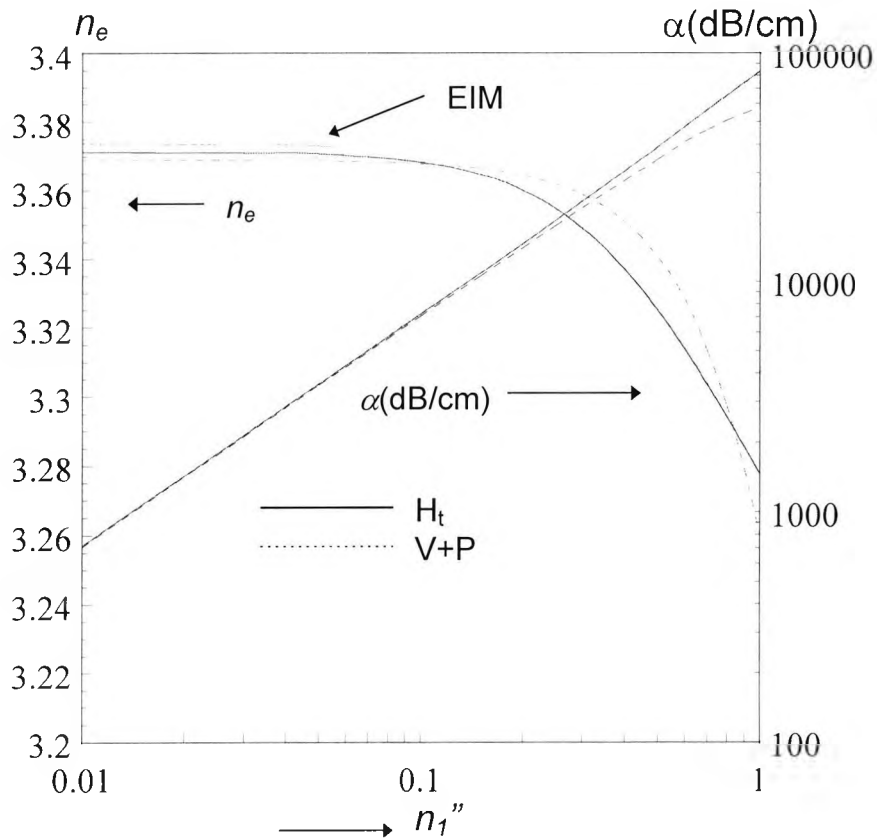


Fig.5.5 Variation of the effective index and the attenuation constant with the imaginary part of the refractive index of the core of an embedded channel optical waveguide (Hayata *et al.*, 1986), using the H_t -formulation, the vector H (V+P) with formulation with perturbation and the Complex Effective index Method (EIM).

In subsequent work, the modal loss is varied by changing the imaginary part of the index to check the limit of the perturbation technique, with $n_2''=0$. Figure 5.5 shows the comparison of the EIM, the vector H method with perturbation (V+P) and the H_t method, for the variation of the imaginary part of the refractive index, n_1'' , as far as the effective index and the modal gain are concerned. In this particular case 1800 first order elements were used to represent the waveguide structure. The attenuation constant, α/k_0 curves, agree well for the V+P and H_t approach and slowly diverge only when the value of α/k_0 is larger than 10000 dB/cm. The EIM fails to converge for values of n_1'' above 0.06 and the numerical procedure becomes unstable. The vector H method and the H_t method begin to diverge, for both the effective index and modal gain, at a value of $n_1''=0.1$.

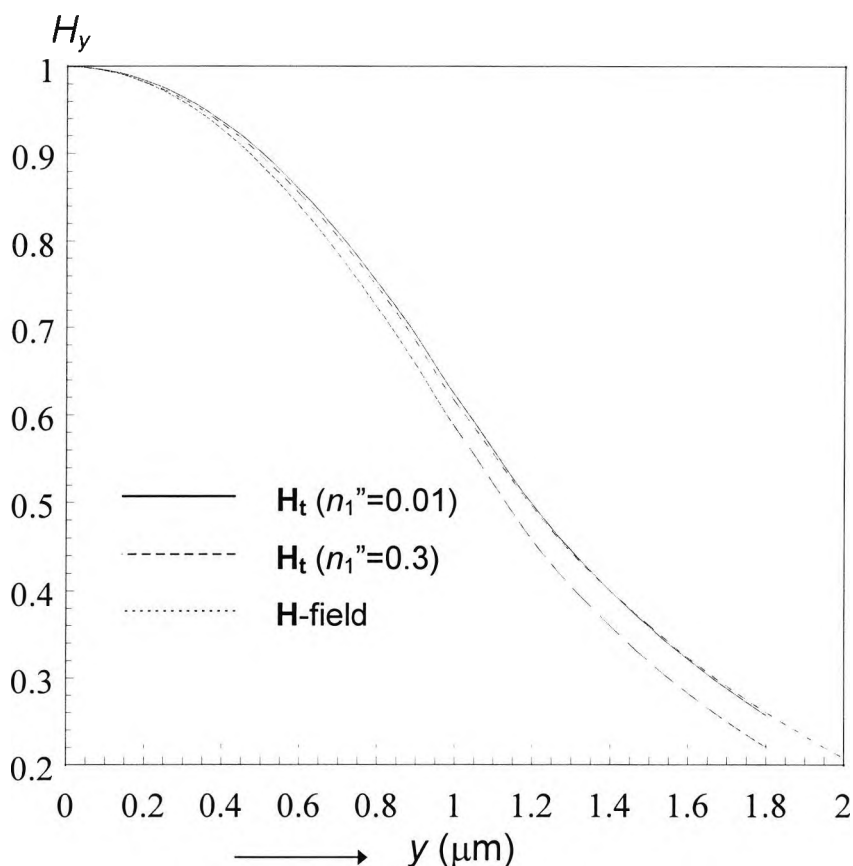


Fig.5.6 H_y , field distribution along the y -axis for different values of the imaginary part of the refractive index of the core (n_1'') of an embedded channel optical waveguide, using the \mathbf{H} vector formulation with perturbation and the \mathbf{H}_t formulation.

Next, the variation of the normalized H_y field profile, along the y -axis, is shown in Fig.5.6 for different values of the imaginary part of the refractive index, n_1'' (0.01 and 0.3), for the \mathbf{H} -field method with perturbation and the \mathbf{H}_t method. As discussed in Section 3.4, in the \mathbf{H} -field formulation, the field profile is calculated without considering the imaginary part of n , and therefore it remains unchanged by definition, since the perturbation is based on this assumption. However in the \mathbf{H}_t formulation, the complex \mathbf{H} -field is calculated, which depends on the complex n values. Here the field profiles and their change due to the change of n_1'' are compared. As the value of n_1'' increases, it can be observed that the mode becomes slightly more confined, but the change is not very significant for lower values of n_1'' . This illustrates the fact that the use of the finite-element approach, incorporating the perturbation technique for such small-to-medium gain/loss values of the refractive index is satisfactory to obtain modal

solutions, both for the complex effective index and the field profile, and this approach is used in the subsequent examples.

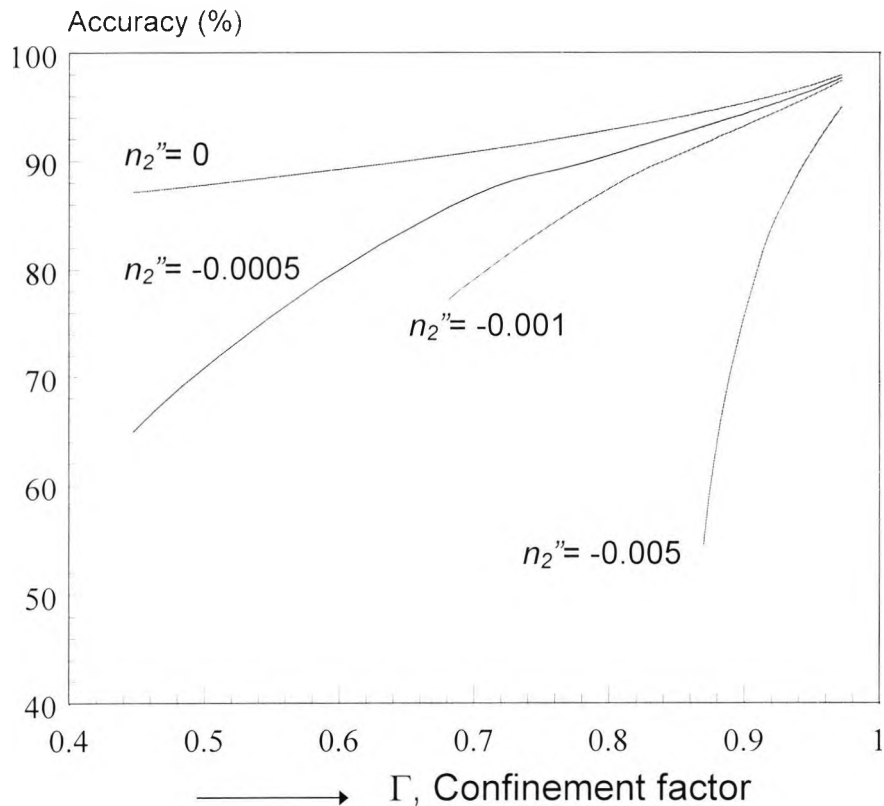


Fig.5.7 Accuracy of the approximate method using the field confinement factor, comparison of the scalar FEM with perturbation with the variation of the confinement factor Γ , for an embedded channel waveguide.

Next, the modal gain of the GaInAsP/InP embedded rectangular channel waveguide was calculated with respect to the field confinement in the guide and the imaginary part of the refractive index, by using the approximate Confinement Factor Method, and the results are compared with those obtained from the FEM with perturbation. The imaginary part of the core refractive index is $n_1'' = 0.001$, representing gain in this region and the imaginary part of the substrate, n_2'' , is taken as negative, indicating a loss in this region, which varies from $n_2'' = 0$ to $n_2'' = -0.005$. The overall modal gain is calculated by using both approaches and the accuracy of the approximate method as compared to the more accurate V+P is shown in Fig.5.7. It can be observed that as the mode confinement in the core increases, the accuracy of the approximate method also improves. When the mode in the core is well confined, all the plots converge towards 100% accuracy, since the field in the substrate is very small and the loss does not much affect the overall modal gain. Additionally, as the

imaginary part of the refractive index in the substrate (n_2'') increases, the overall modal gain will reduce due to the increased loss in the substrate and the results obtained from the approximate method deteriorate further from those calculated using the FEM approach with perturbation. The confinement in the core does not reach 100%, because there is always a small amount of field in the substrate and top cladding regions. It can be noted that when both local gain and loss values are significant (as when $n_2''=-0.005$ and $n_1''=0.001$), the overall modal gain obtained is due to the difference between the local gain and loss values, and the approximate method can yield a large error for the overall modal gain calculation, even when the confinement factor is as large as 90%.

5.3 The Rib Waveguide

The Rib waveguide, shown in Fig.5.1.c, has received considerable attention for several optoelectronics applications, because of the simplicity of its fabrication using semiconductor materials. Advanced growth and etching techniques allow excellent control over the experimental refractive index profiles, and therefore great interest has been shown in the theoretical analysis of such structures (Benson *et al.*, 1992). Various methods have been proposed for the analysis of this type of waveguide, amongst them the Finite Element Method (FEM), the Finite Difference Method (FDM) and the Effective index Method (EIM). The FEM with the aid of the perturbation technique and the complex EIM have been used in order to determine the gain/loss properties of such structures. For more complicated types of the rib waveguide, such as the semiconductor laser rib, where an active region is involved, the FEM with perturbation is used to calculate the modal gain.

5.3.1 The simple Rib waveguide

The simple rib waveguide (shown as insert in Fig.5.8), was proposed by Goel (1973), as an alternative approach to reduce the scattering loss in optical waveguide bends and directional couplers, for integrated optical circuits. The guidance of the energy is achieved if the thickness, D and the refractive indices n_0 , n_1 , n_2 , are chosen so that the slab region of index n_2 , surrounding the rib is beyond the cut-off.

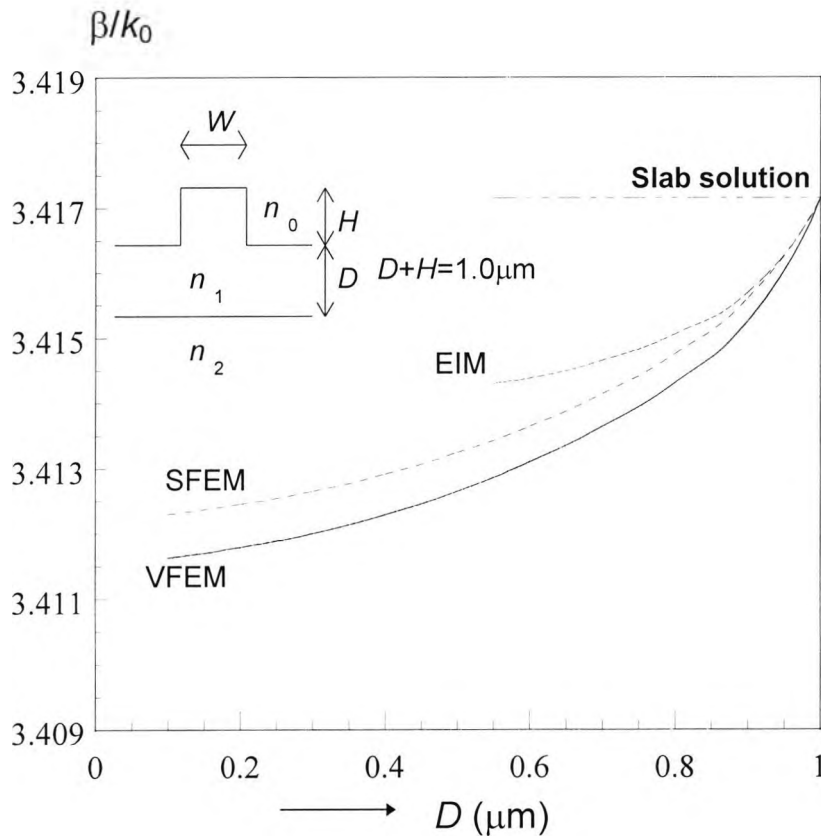


Fig. 5.8 Variation of the normalized propagation constant characteristics for a GaAlAs/GaAs rib waveguide with D , by the Effective index method (EIM) and the scalar (SFEM) and vector (VFEM) Finite Element Method.

Firstly, a loss-less air-clad GaAs/GaAlAs simple rib waveguide is considered with refractive index values $n_0=1.0$, $n_1=3.44$, $n_2=3.4$, a rib width $W=3\mu\text{m}$ and wavelength $\lambda=1.15\mu\text{m}$. The normalized propagation constant, for the H_{11}^y mode is estimated using the Effective Index Method (EIM), the scalar FEM and the vector FEM, as shown in Fig.5.8. In the finite element approach, 7200 first order triangular elements are used to obtain accurate results. For this mesh refinement, the matrix order was 11102 and it required about 4 minutes of computational time on the Sun

Sparcstation 2. The scalar finite element procedure (SFEM) over-estimates the effective index parameter as compared to using the accurate vector finite element (VFEM) solutions. However, it can be observed that when the slab height, D , is below $0.55\mu\text{m}$, the effective index method fails to provide solution, because no solution can be found for the transcendental equation for the outer slab region when $D < 0.55\mu\text{m}$. It can also be observed that, even when the EIM provides a solution, the results are of poor quality considering the small range of the effective index variation that is possible for this structure. All three methods converge when $D=1.0\mu\text{m}$ since in this case, the structure is essentially a three layer planar (as $H=0$) guide where scalar and effective index solutions are also valid and accurate.

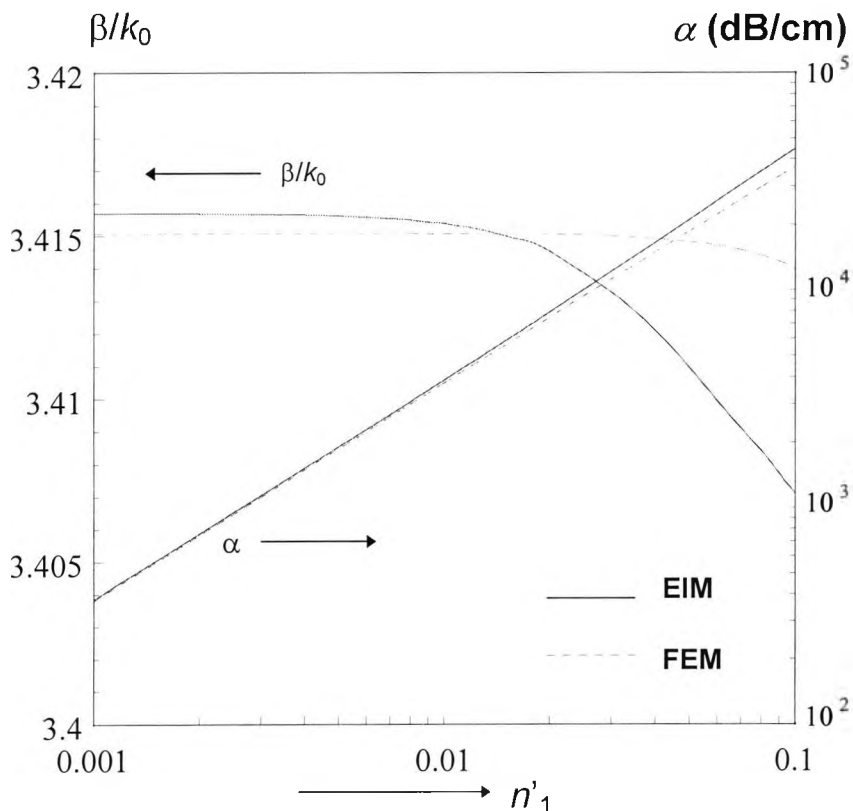


Fig.5.9 Variation of the normalized phase (β/k_0) and the attenuation (α) constants with the imaginary part of the refractive index (n'_1).

Next, the situation where there is a lossy waveguide is considered by introducing an imaginary part to the refractive index, n_1 , and keeping all other parameters the same as for the rib waveguide discussed above is studied. The results for the complex EIM and the vector FEM with perturbation are compared for $D=0.9\mu\text{m}$.

Fig.5.9 shows the variation of the real and imaginary parts of the propagation constant with the imaginary part, n'_1 . In a similar way to the loss-less case, the EIM over-estimates the effective index (β/k_0), for a small value of n'_1 . However, the β/k_0 decrease is very small when n'_1 increases, for the vector FEM solutions, compared to the EIM results. The normalized attenuation constant agrees very well for both of the methods up to 3000 dB/cm, and beyond that value the FEM somewhat underestimates the modal loss value by comparison to the use of the EIM which is probably more accurate for large values of n'_1 .

5.3.2 The Integrated laser Rib Waveguide

Next an integrated laser rib waveguide, as shown in Fig.5.10, is examined. The operating wavelength is $\lambda=1.5\mu\text{m}$ and the active layer thickness, $T=0.15\mu\text{m}$, where $n_0=1.0$, $n_1=3.38+j0.001$ and $n_2=3.17$. The variation of the normalized gain, $(-\alpha/k_0)$, for the H_{11}^y mode is shown here with the thickness of the top confinement layer, H . The modal gain reaches its maximum value when $H\approx 0.55\mu\text{m}$. It can be observed that the vector and scalar finite element results agree very well with the results using the complex H_t formulation (Lu and Fernandez, 1994). However, it can also be observed that the Spectral Index Method (SIM) (Burke *et al.*, 1993) over-estimates the modal gain for this structure, although in the work of Burke *et al.*, a higher rib height was considered to facilitate their simulations. It should also be noted that the results for the other two methods were obtained from a transfer of data from published graphs and may thus be subject to a small degree of error.

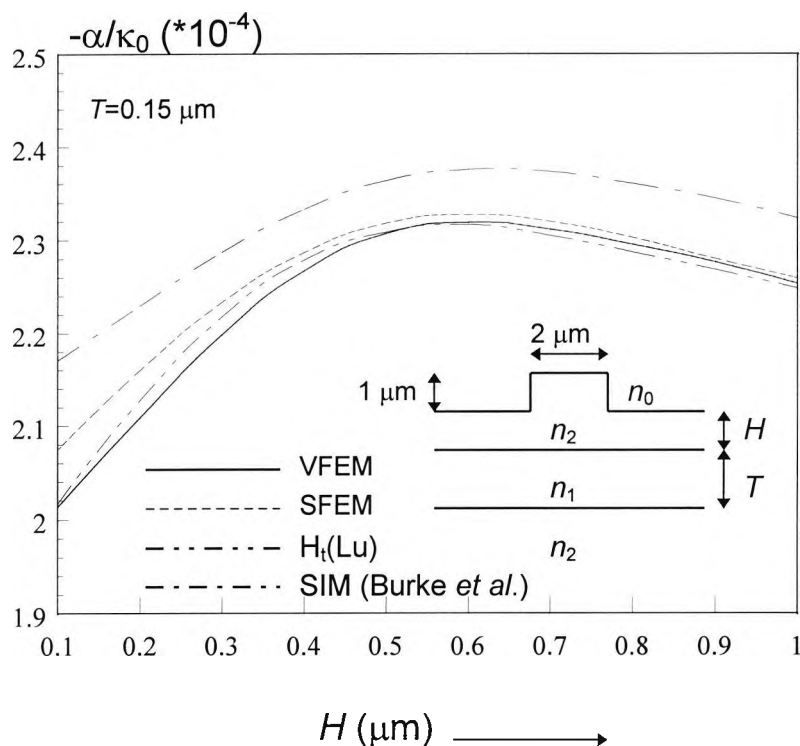


Fig.5.10 Variation of the normalized gain constant with top confinement layer thickness, H , for the H_{11}^y mode of a semiconductor laser rib waveguide, by the vector, scalar and the H_t formulations in the Finite Element Method and the Spectral Index Method.

Further, to compare with another alternative approach, the rib waveguide, shown in Fig.5.10 here is re-examined, but the active layer thickness, T , increased to $0.2 \mu\text{m}$. Figure 5.11 shows the variation of the normalized phase constant, (β/k_0) , for the dominant H_{11}^y mode with the thickness of the top confinement layer, H . In a similar way to that seen in the earlier examples, the Scalar Finite Element results (SFEM) over-estimate the modal effective index consistently, as compared to those of the Vector Finite Element (VFEM). However, the results given by Benson *et al.* (1994) are significantly lower than those obtained using the finite element method. For the limiting value for $H \rightarrow \infty$, which is equivalent to a three layer slab, the accurate normalized propagation constant, (β/k_0) , is 3.20966, which is also shown. It can be clearly identified that finite element solutions will attain this limiting value, whereas the FDM results definitely will not.

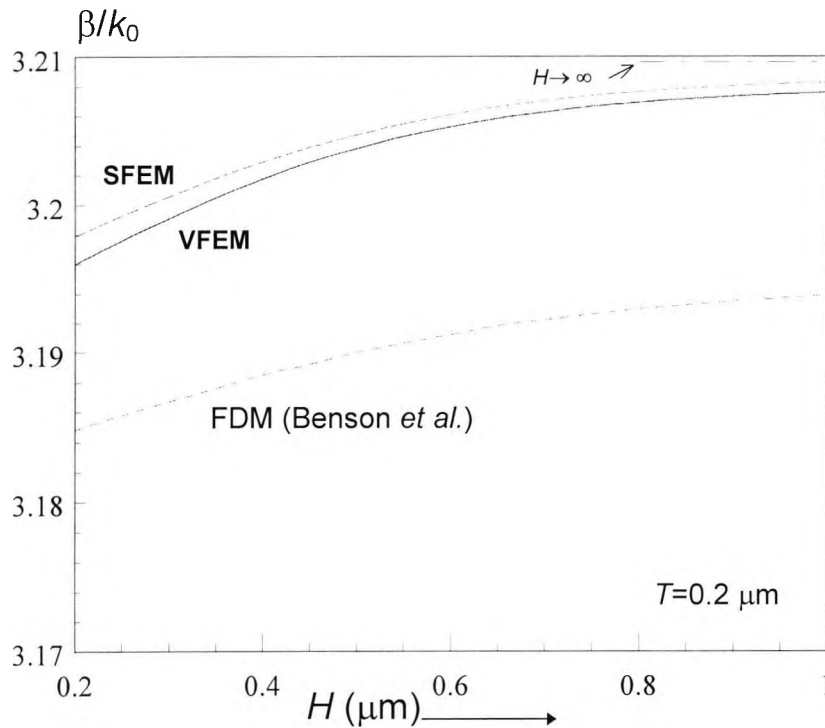


Fig.5.11 Variation of the effective index with the top confinement layer thickness, H , for the H_{11}^y mode, of a semiconductor laser rib waveguide by the scalar and the vector Finite Element Method and the Finite Difference Method (FDM).

Figure 5.12 shows the variation of the normalized modal gain, $(-\alpha/k_0)$, for the dominant H_{11}^y mode with the thickness of the top confinement layer, H . Results obtained using the scalar (SFEM) and vector (VFEM) finite element approaches agree well with each other. Here, the modal gain is not as sensitive to the variation of H , compared to the earlier example with $T=0.15\mu\text{m}$ (shown in Fig.5.10), since the mode is better confined. It can be noted that the modal gain obtained by Benson *et al.* (1994) using the Finite Difference Method (FDM) is significantly lower than the finite element results show. For the limiting case $H \rightarrow \infty$, the accurate normalized modal gain of the three layer equivalent structure has been calculated to be equal to 3.45×10^{-4} . This value again compares favourably with the FEM results and the FDM result would appear to be fairly inaccurate.

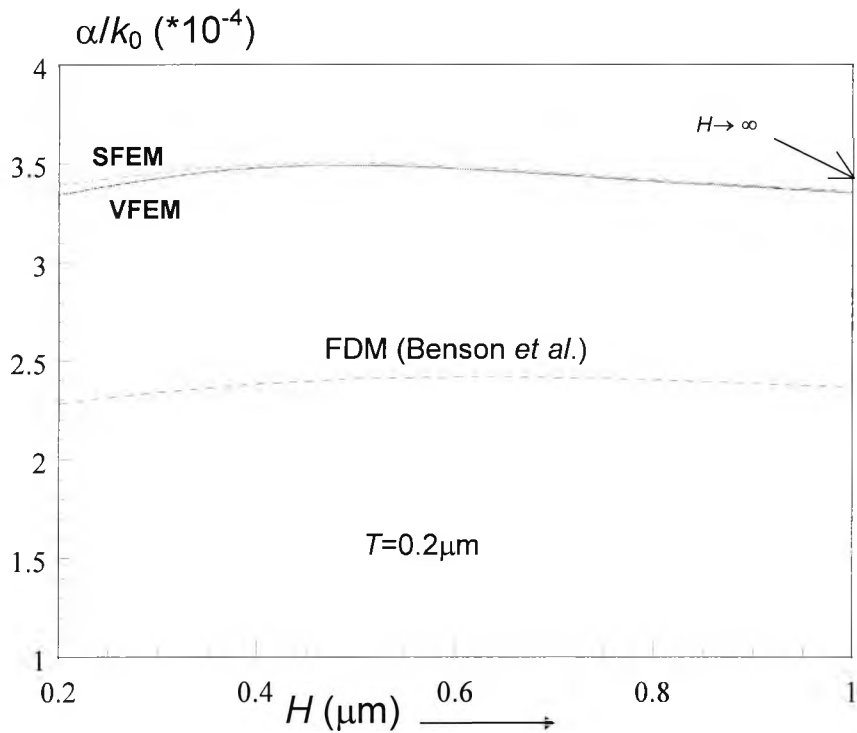


Fig.5.12 Variation of the normalized modal gain with H , for the H_{11}^y mode, of a semiconductor laser rib, by the scalar and the vector FEM with the perturbation technique and the FDM.

Figure 5.13 shows the modal gain/loss characteristics for the same rib waveguide, for $T=0.2\mu\text{m}$, when a negative imaginary part is added to the refractive index, n_2 , to represent loss in the cladding regions. The value of n_1' , responsible for the local gain in the active region, is kept constant at 0.001. When there was no loss in the confinement regions, that is $n_2'=0$, the maximum normalized modal gain, $(-\alpha/k_0)$, was about 3.5×10^{-4} when $H \approx 0.5\mu\text{m}$. However, the maximum normalised modal gain reduces to 2.85×10^{-4} when loss is incurred in both the confinement regions due to the negative value of $n_2' = -10^{-4}$. Furthermore, when the confinement region becomes very lossy ($n_2' = -10^{-3}$) the mode suffers an overall loss and this overall modal loss is minimum when $H \approx 0.5\mu\text{m}$. For a further increase of n_2' , the overall loss is expected to show a greater increase due to local loss in the confinement regions of the rib waveguide.

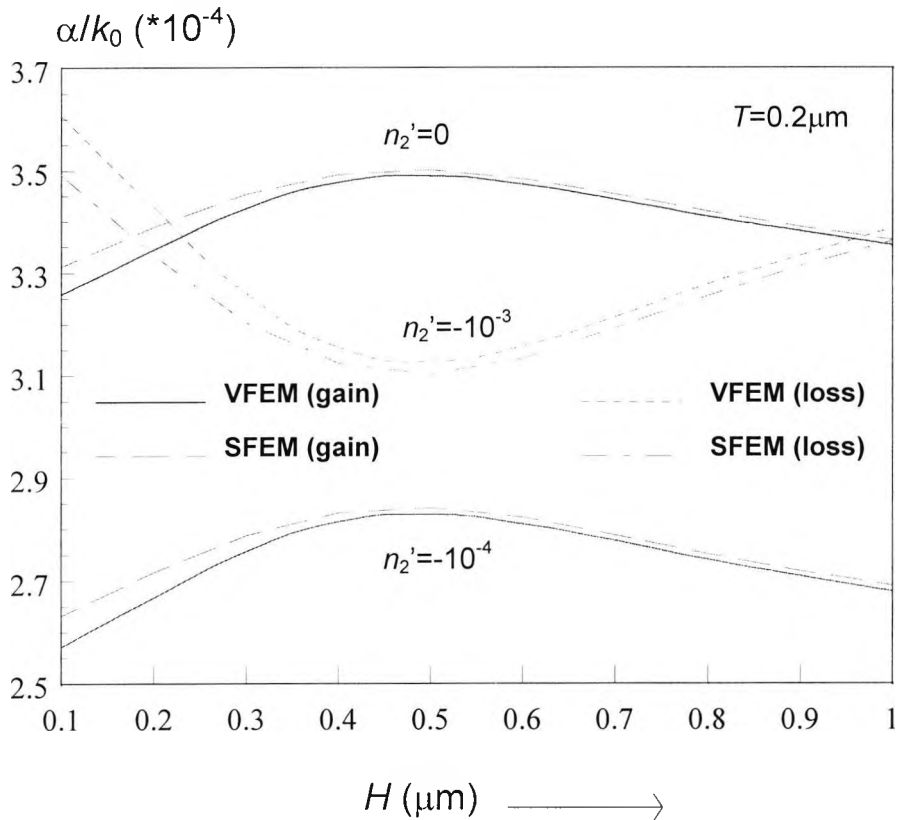


Fig.5.13 Variation of the normalized modal gain with H , for the H_{11}^y mode, by the Vector Finite Element Method

Additionally, the attenuation characteristics of the above laser rib waveguide were calculated, by using Field Confinement method, which was applied earlier to the embedded channel waveguide as shown in Fig.5.7. An amount of loss was introduced in the two cladding regions by adding an imaginary part n_2' in the refractive index n_2 , while the imaginary part of the refractive index of the active layer was considered to be $n_1'=0.001$. The scalar FEM results with perturbation, for different values of the imaginary part of the refractive index of the cladding, n_2' , were compared with the results obtained by the Field Confinement Method, as shown in Fig.5.14. By comparing the results obtained for the laser Rib waveguide with those obtained for the embedded channel, shown in Fig.5.7, it can be seen that the results for the laser Rib structure have similar features, but show a slightly higher accuracy. For example, for $n_1'=0.001$ and $n_2'=0$ for 0.5 confinement factor, Γ , the accuracy obtained is about 88% for the embedded channel waveguide and about 91% for the laser rib waveguide.

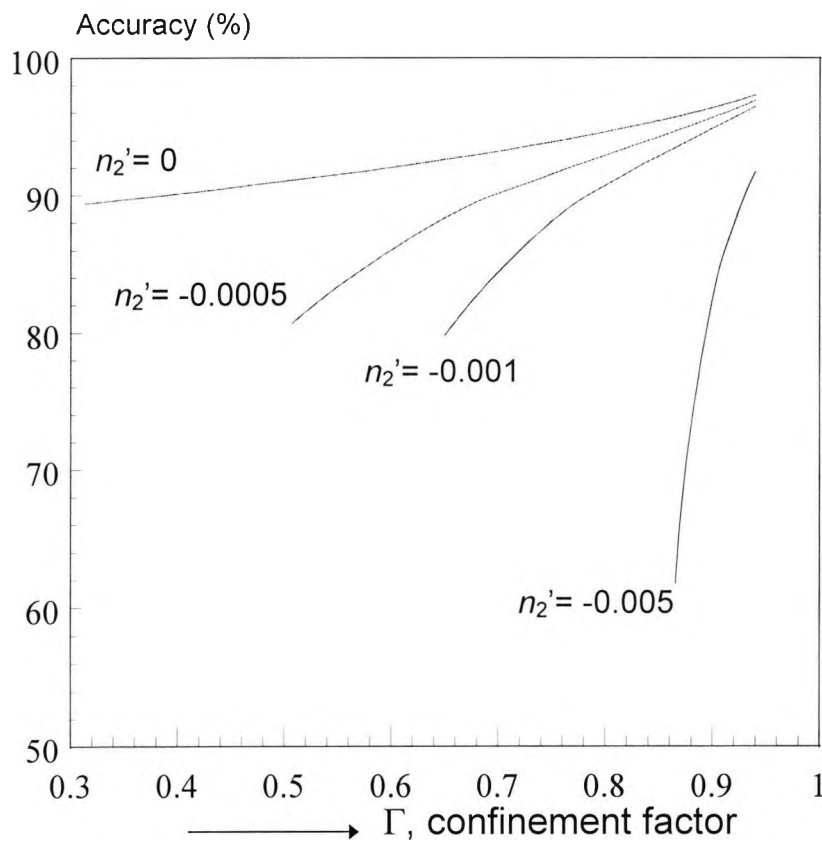


Fig.5.14 Comparison of the scalar FEM with perturbation and the approximate method using the field confinement, with the confinement factor, Γ , for different values of the imaginary part of the refractive index of the substrate of a rib waveguide, n_2' , for constant imaginary part of the refractive index of the active layer $n_1'=0.001$.

5.3.3 Dependence of refractive index, of active layer, on carrier concentration

The device material properties are fundamental to modelling semiconductor optoelectronic components. The measured data for the device material, in semiconductor lasers and laser amplifiers, such as the gain, carrier lifetime and refractive index and their dependence on the injected carrier density, are very important in predicting the laser properties. The carrier concentration profile $N(x,y)$, in a laser material, which is dependent on the injected current, determines the change of the complex refractive index profile, $n(x,y)$.

InGaAsP laser materials exhibit minimum loss in silica-based optical communication systems, at an operating wavelength of $\lambda=1.55\mu\text{m}$. A rib waveguide with an active layer of InGaAsP laser material, at the above operating wavelength, has been examined in order to calculate the gain properties of the structure. Since the small loss condition is examined, the effect of the carrier concentration on the real part of the refractive index has been neglected. The variation of the imaginary part of the refractive index, n'' , along the transverse direction (x) is related to the carrier variation ($N(x)$) and given by:

$$n''(x)=(dn/dN)*N(x) \quad (5.1)$$

where dn/dN is the rate of change of the refractive index with carrier concentration, and $N(x)$ the carrier concentration profile, given by Westbrook (1986):

$$N(x) = \begin{cases} N_0 \left(1 - \frac{\cosh(x/L)}{\exp(s/L)} \right) & x \leq s \\ N_0 \sinh(s/L) \exp(-x/L) & x > s \end{cases} \quad (5.2)$$

where N_0 is the carrier concentration at threshold, s is the half rib width and L the diffusion length.

The average carrier concentration within the active layer, which can be approximated by averaging the carrier profile along the x -axis, can be shown as:

$$N_{av}=(s/w)N_0 \quad (5.3)$$

where w is the half-guide width, which is assumed large compared to the half-rib width, s , as shown in Fig.5.15.

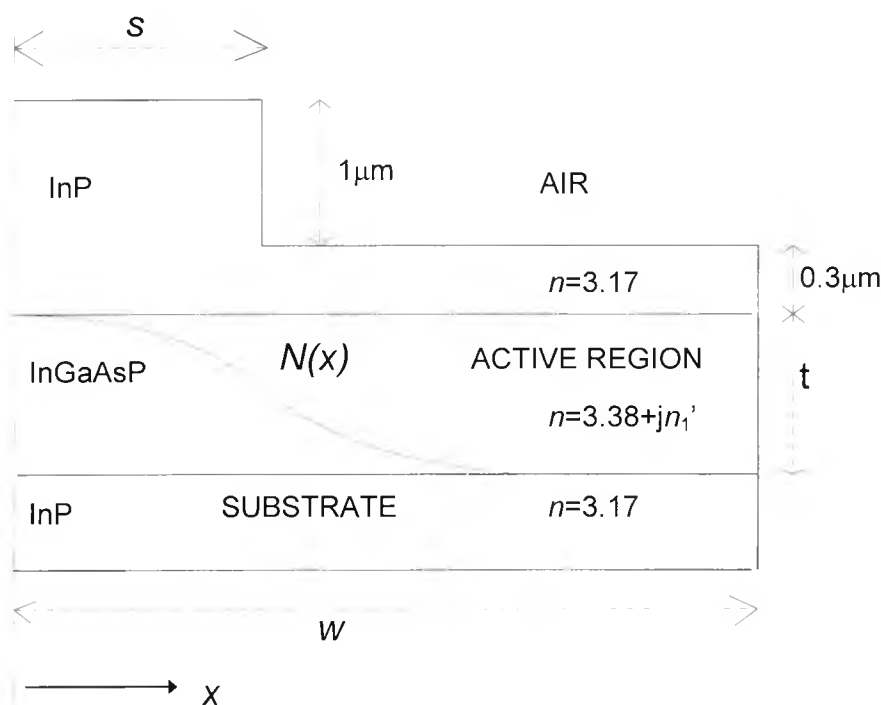


Fig.5.15 Rib waveguide structure where the imaginary part of the refractive index in the active layer varies according to the carrier profile.

An integrated laser rib waveguide, with an InGaAsP active layer, at an operating wavelength of $\lambda=1.5\mu\text{m}$, is examined, as shown in Fig.5.15. The imaginary part of the refractive index in the active region is assumed to vary according to the carrier concentration profile, along the x -axis (Eq.5.2). The carrier concentration at threshold is assumed $N_0=1.0\cdot 10^{18}\text{ cm}^{-3}$, and $dn/dN=-2.8\cdot 10^{-20}\text{ cm}^3$ (Westbrook, 1986). For this example, the rib width is considered to be $5\mu\text{m}$ and the existing one-fold symmetry has been exploited in the numerical simulation. From the above data, the carrier distribution in the active layer is plotted in Fig.5.16, for two different diffusion lengths, $L=1.2\mu\text{m}$ and $L=1.7\mu\text{m}$. For the smaller diffusion length, $L=1.2\mu\text{m}$, the carrier concentration is higher in the centre rib region, and lower outside, and for both distributions the carrier values are identical at the end of the rib. The average carrier distribution, N_{av} , (Eq.5.3) is plotted in the same figure, and it has a value of about 25% of the maximum carrier concentration (10^{18} cm^{-3}). This value corresponds to the ratio of the rib half width ($s=2.5\mu\text{m}$) to the guide half width ($w=20\mu\text{m}$), as defined by (Eq.5.3).

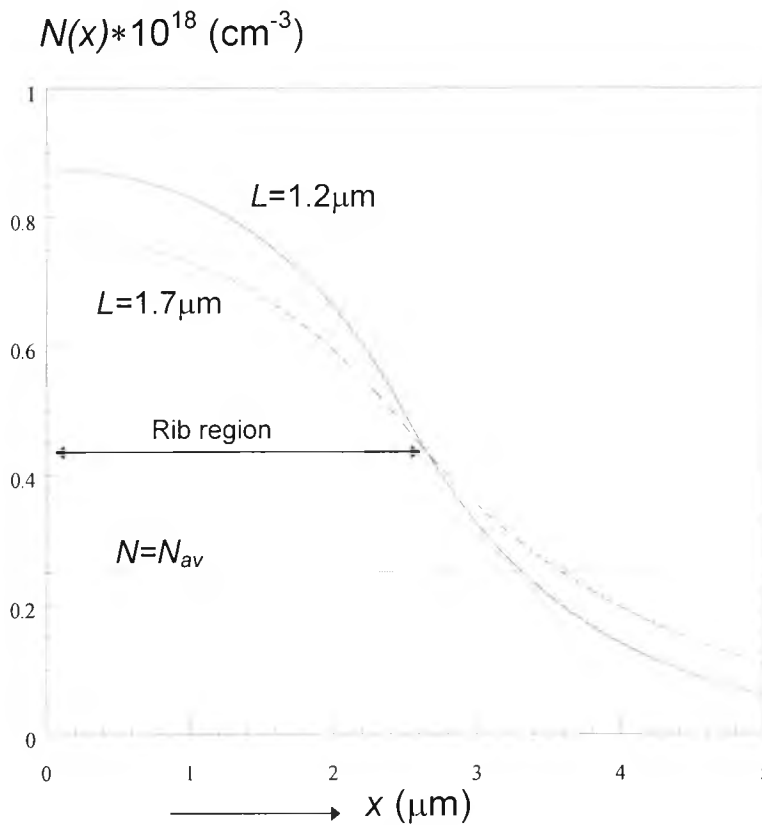


Fig.5.16 Carrier profile along the x -axis in the active layer of the rib semiconductor laser optical waveguide, for different values of the diffusion length L , of the carrier.

In addition, the modal gain for the two diffusion lengths is shown in Fig.5.17, with respect to the threshold carrier concentration, N_0 . As N_0 increases, the modal gain is seen to increase. For a smaller diffusion length the modal gain is higher than that of larger diffusion length, since in the former case, the carrier is more concentrated near the guide centre, where the optical field intensity is also higher. The modal gain for the average carrier concentration is lower, and is independent of the diffusion length.

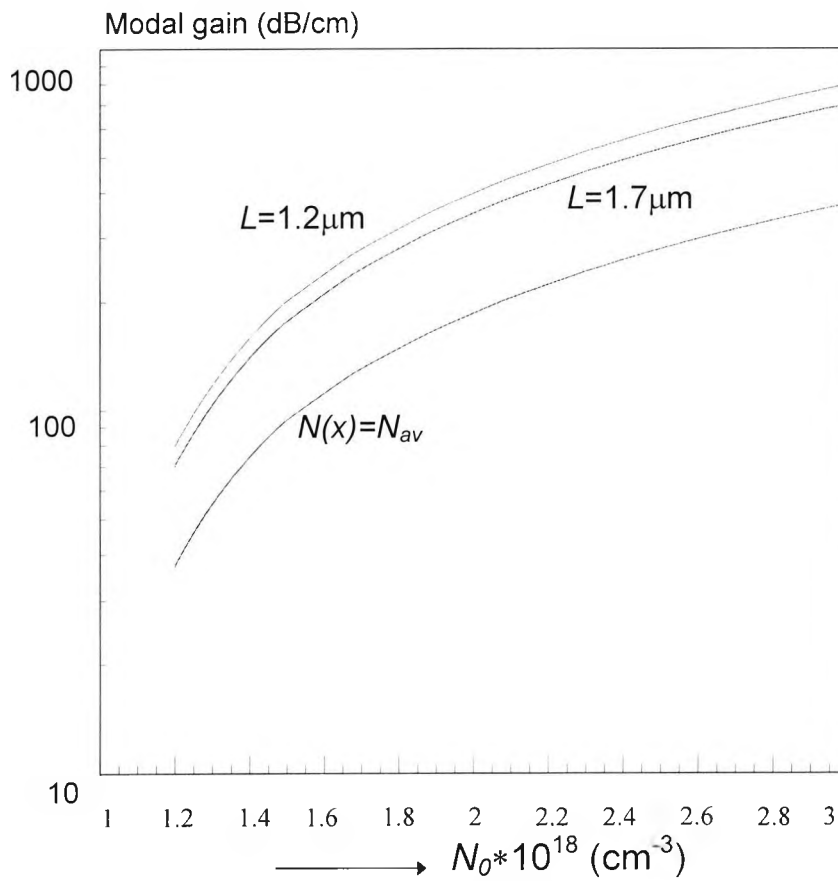


Fig.5.17 Variation of the modal gain constant for the rib semiconductor laser waveguide with the carrier concentration at threshold, N_0 , of the active layer for different values of the diffusion length of the carrier.

5.3.4 Multiple Quantum Well Rib waveguide

Quantum Well (QW) lasers differ from the normal double heterostructure (DH) lasers (Casey and Panish, 1978), like the GaAs/Ga_{1-x}Al_xAs pair, mainly due to the very thin active region they incorporate. By considering the energy level distribution of semiconductor materials, in the conventional semiconductor lasers the electrons in the conduction band are spread over a relatively wide energy range with quite small density at the band edges. By thinning the active region, as in QW structures, the electrons are spread at a smaller energy range with a relatively high densities at the band edge. This makes population inversion easier than in the conventional diode lasers and results in the increase of the modal gain, therefore great reduction of the threshold current. One major drawback of single QW lasers is the poor optical confinement, due to the narrowness of the active region, which leads to the spread of the optical field in the lossy surrounding material and tends to diminish the advantage of the low threshold current. This problem can be overcome by the addition of more QW to form a Multiple Quantum Well structure, which allows a higher optical confinement factor (Wilson and Hawkes, 1989).

Additionally, the modal gain of a single quantum well structure is limited by the step-like density of states, therefore, by increasing the number of quantum wells, to a MQW structure, the modal gain of each quantum well adds up to the total modal gain of the structure (Arakawa and Yariv, 1985). In such devices, the optimum number of quantum wells and their thickness are major parameters, in order to achieve minimum threshold current, therefore higher efficiency. For most practical applications, the thickness of the active layers in MQW structures lie between 0.005-0.01 μm (Yariv, 1989).

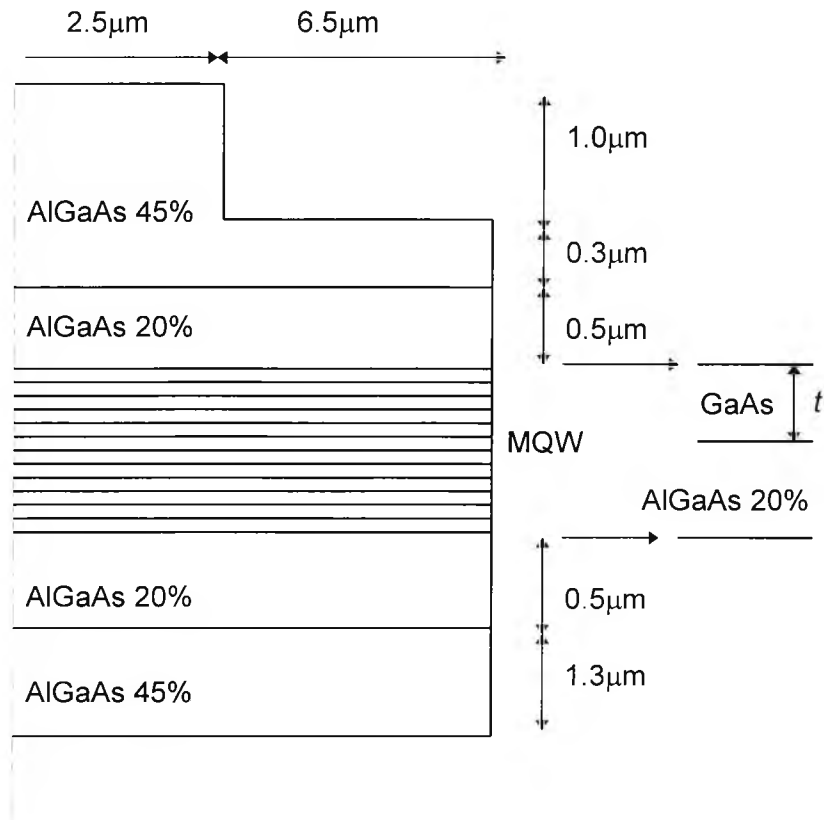


Fig.5.18 Multiple Quantum Well (MQW) Rib waveguide (Al% is given).

A rib waveguide which incorporates a Multiple Quantum Well (MQW) active region, as shown in Fig.5.18, has been examined, where the MQW region consists of GaAs thin active layers with dielectric constant, $\epsilon_1=13.06+j0.1869$ and thickness t , sandwiched by AlGaAs (20% Al) barriers, with dielectric constant $\epsilon_2=11.985$. The substrate of the MQW structure consists of AlGaAs (45%) material, with a dielectric constant $\epsilon_3=11.05$, at an operating wavelength, $\lambda=0.855\mu\text{m}$. Due to the symmetry of the structure, a half symmetry along the y -axis was used in the analysis.

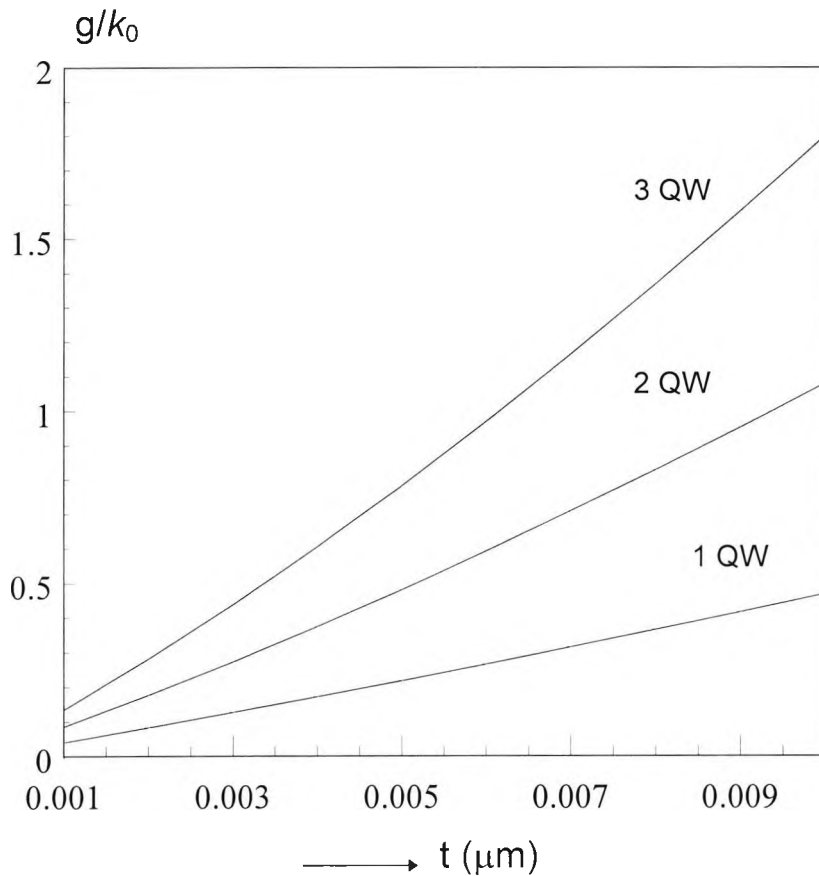


Fig.5.19 Variation of the normalized gain constant with the quantum well thickness for a single, two and three quantum well rib waveguide.

The variation of the normalized gain constant, g/k_0 , with the quantum well thickness, t , for one, two and three Quantum Wells was calculated, by using the scalar FEM with perturbation, as shown in Fig.5.19. For the thickness value, t , up to 100nm, and for all the three values of the QWs, the modal gain of the waveguide increases linearly with the layer thickness, t . For each QW added to the structure, the overall normalized gain constant increases by one above that of the normalised gain constant of the single QW structure, and therefore, by adding N number of QWs the overall modal gain will be N times greater than the modal gain of the single QW structure. In practical applications, the optimum number of QWs required for a particular structure, is determined by the threshold current of the device, in order to achieve optimum efficiency. The normalized gain constant obtained for a thickness of $t=100\text{nm}$, was compared with the value obtained by Cheung *et al.* (1995) and found to be in a very good agreement. Additionally a result for the same thickness, was obtained by using the Field Confinement Method and a comparison shows that this was 93.1% of the previous value, although in this case the field confinement in the active region is much

lower (7.5%) than in other types of structures examined in Sections 5.2 and 5.3.2, for the rectangular dielectric and rib laser waveguides respectively, by using the same approach.

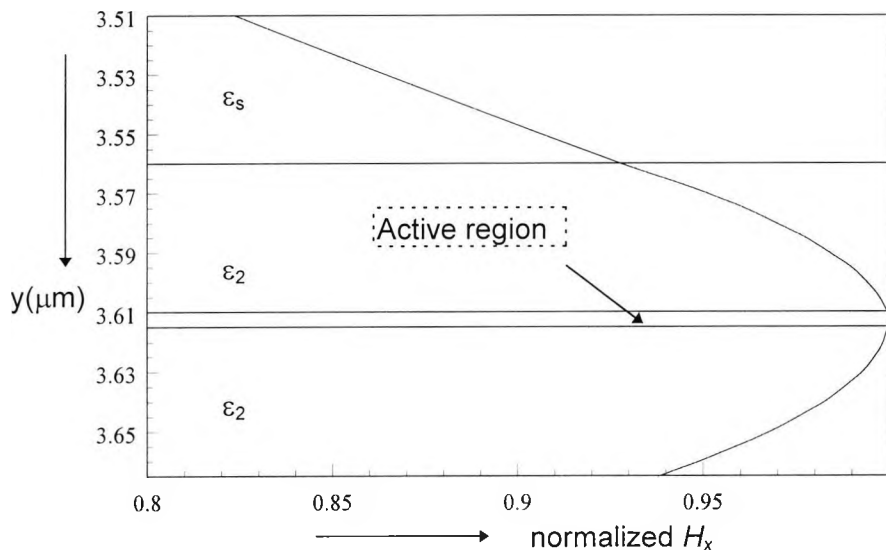


Fig. 5.20 Normalized H_x field profile, along the y -axis of symmetry for a single Quantum Well (QW) structure, for the active layer thickness, $t=0.005\mu\text{m}$

Further, the normalized H_x field profile of the single QW structure for an active layer thickness, $t=0.005\mu\text{m}$, along the symmetry y -axis, has been examined, as shown in Fig.5.20. For this type of structure, the maximum field intensity is located at the middle of the active region and the value at the boundary of the substrate layer, ϵ_2 , is about 94% of the maximum field intensity. This structure, at the above thickness, has a very low confinement factor (about 1%), therefore most of the field is outside the active region, which results in a reduction of the modal gain.

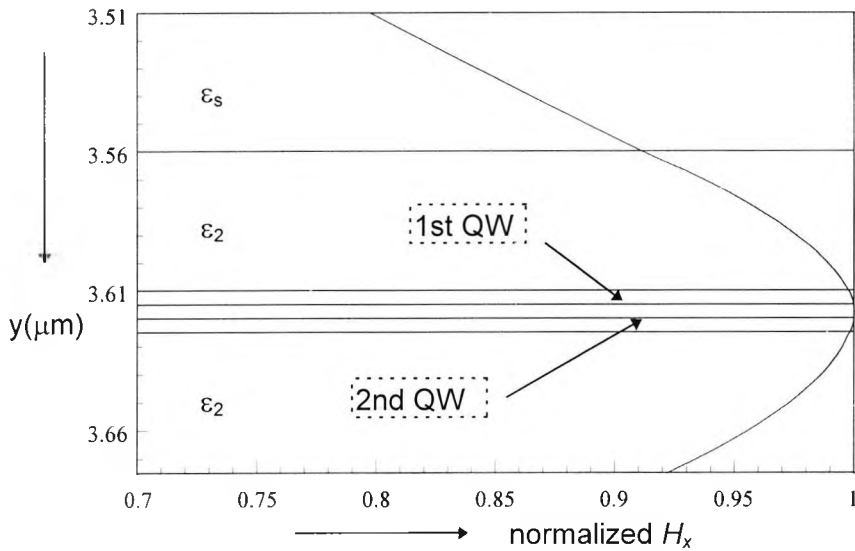
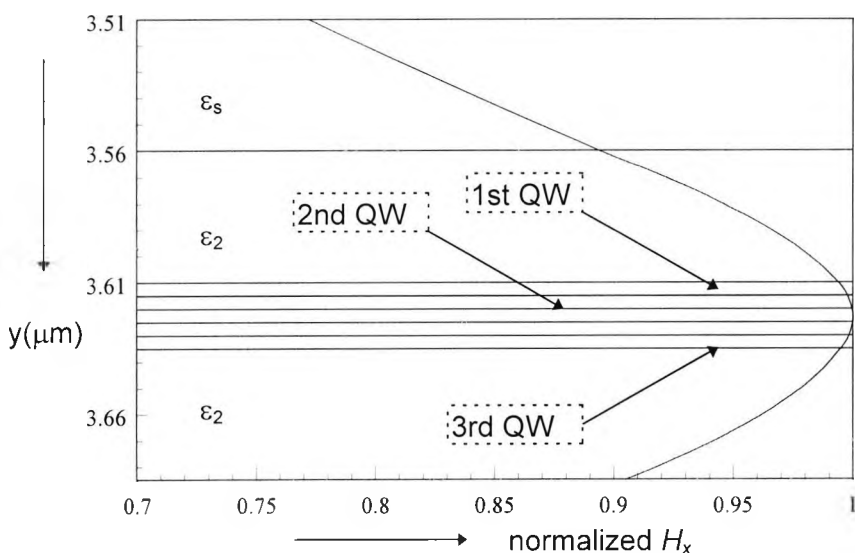


Fig. 5.21 Normalized H_x field profile, along the y -axis of symmetry for a Two Quantum Well (QW) structure, for each QW active layer thickness, $t=0.005\mu\text{m}$

Further, the H_x field profile for a Two QW structure has also been examined for the same active layer thickness, $t=0.005\mu\text{m}$, as shown in Fig.5.21. In this type of structure the maximum field intensity is located at the centre of the separation layer between the two active layers and the mode is more confined than in the single QW structure. The confinement factor for the above thickness was calculated about 2%, which is again, quite low. It can also be noticed field intensity at the boundary of the substrate region has decreased to 92% of the maximum value.



(a)

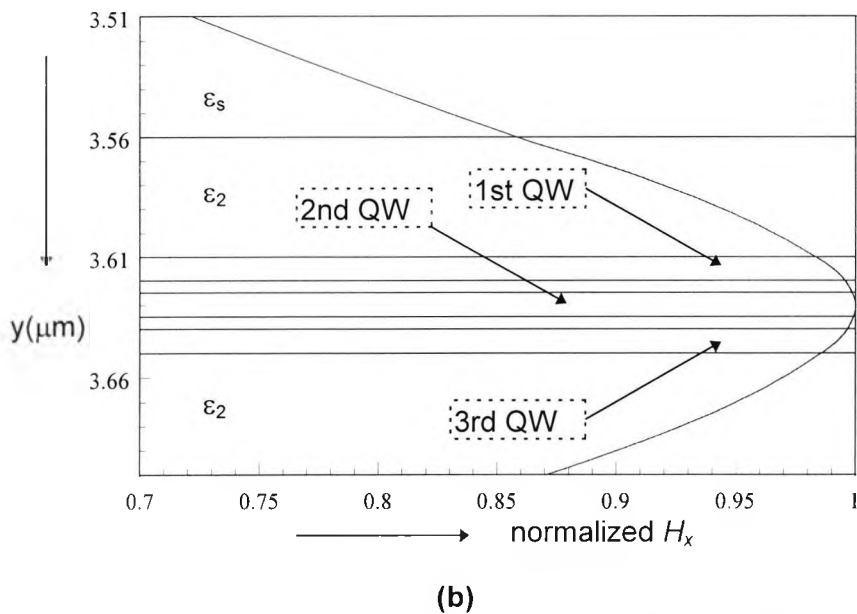


Fig. 5.22 Normalized H_x field profile, along the y -axis of symmetry for a three Quantum Well (QW) structure, for each QW active layer thickness, a) $t=0.005\mu\text{m}$, b) $t=0.01\mu\text{m}$

Next, the H_x field profile of a three Quantum Well Structure has been examined for two different thickness, t , of the active layers, as shown in Fig. 5.22. In this type of waveguide the maximum field intensity is at the centre of the middle active layer and as the thickness, t , of the active layers increases, the optical mode becomes more confined. The confinement factor was calculated at 3.3% and 7.5% for active layer thickness $t=0.005\mu\text{m}$, and $t=0.01\mu\text{m}$ respectively. By considering the confinement factors for the three structures, it can be seen that as the number of quantum wells increases there is an increase by approximately the amount of the field confinement in the active region. This is an analogous situation with the increase of the modal gain observed earlier with the increase of the number of quantum layers. Additionally, in the three quantum well structure, when the thickness of the active layers was doubled, the confinement factor increased by about two times.

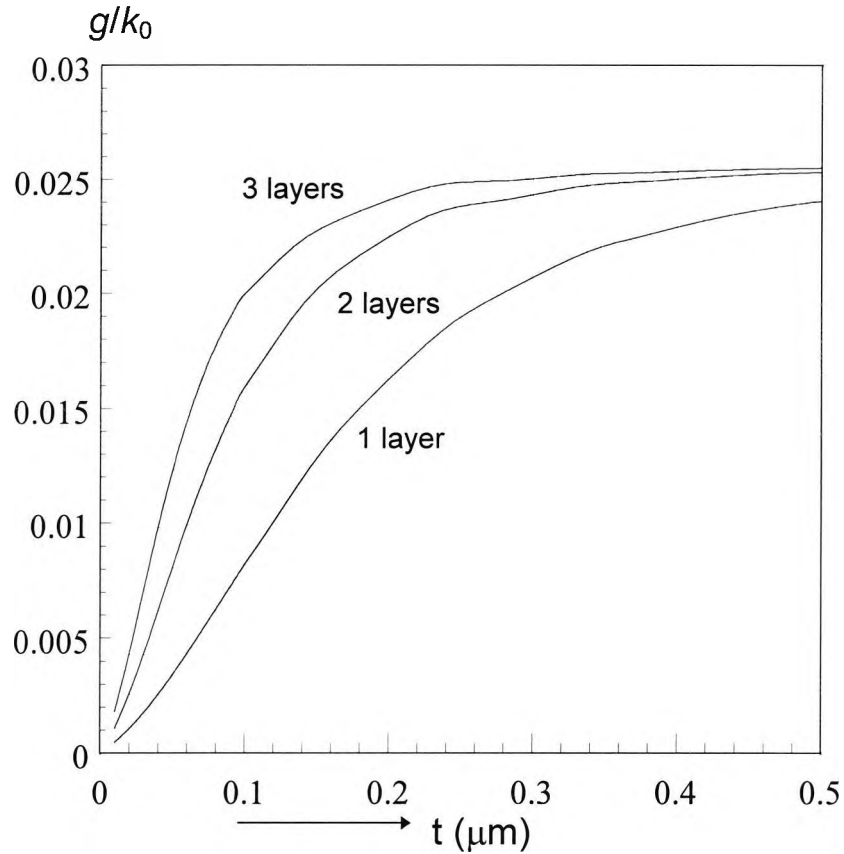


Fig.5.23 Variation of the normalized gain constant with the thickness of the active layer, t , for one, two and three active layers in a rib waveguide structure.

Further, the thickness of the active layers was increased beyond the typical ranges for MQWs, in order to examine the effect of such an increase in the gain properties of the MQW region and the rib waveguide structure as a whole. The variation of the normalized gain constant with the variation of the thickness of the active layers, for the three types of structures is shown in Fig.5.23. As the thickness increases above, $t=0.1\mu\text{m}$, there is a rapid rise of the normalized gain constant, where for the two and three layer structure the rate of increase is higher. At about $t=0.3\mu\text{m}$ all the modal gains begin to saturate and converging to a value of 0.025, with the normalized gain constant of the single layer structure converging more slowly. The increase of the normalized gain constant can be related to the increase of the confinement factor, which at very large thickness is almost 100%, therefore saturation of the gain occurs. Of course, when the thickness of the active layers is increased very much, the waveguide does no longer exhibit the properties of the MQW structure, and mainly the low threshold current, therefore the structure becomes inefficient, since large amount of injection current is required to produce stimulated emission.

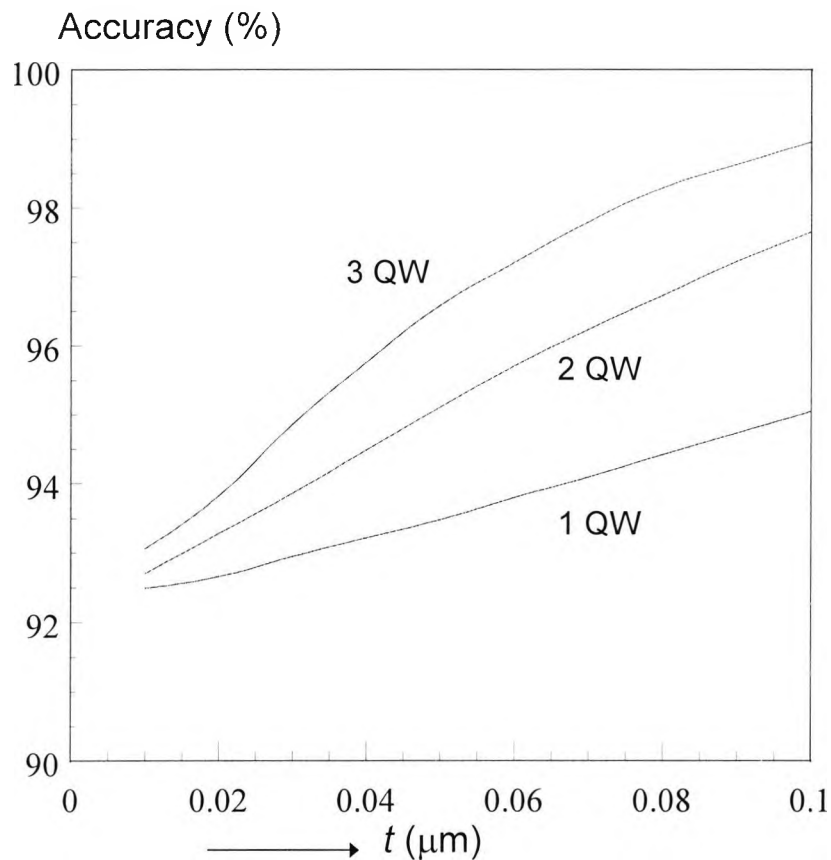


Fig.5.24 Comparison of the scalar FEM with perturbation and the Field Confinement method, with the variation of the active layer thickness for a one, two and three active layer system in a rib waveguide.

Finally, the normalized gain constant for the above structures was calculated by using the approximate Field Confinement approach at a range where the thickness of the active layer had confinement factors higher than in the typical ranges, in order to compare the results with those obtained by using the FEM with perturbation. As it can be seen from the comparison, shown in Fig.5.24, the accuracy of the approximate method, i.e. by using the confinement factor is quite satisfactory. In this type of structure, the confinement in the active layers is small (in the order of 10%) as compared with the previous structure examined. However, as the number of the layers and the modal confinement decreases, the agreement between the two methods seems to deteriorate. Further, in a practical lasing structure, with optical absorption in other regions, the accuracy of the approximate method will deteriorate even further.

5.4 Electro-optic directional coupler modulator

Although dielectric crystal materials, such as lithium niobate (LiNbO_3), cannot be integrated with semiconductors, as there is no possibility of crystal growth on the semiconductor substrate, they can still be used as stand-alone devices in electro-optic waveguides applications, because of their low transmission loss, large electro-optical, piezo-electrical and elasto-optical coefficients (Fouchet *et al.*, 1987), low chirp and high bandwidth. Directional couplers, which are the basis of several guided wave devices, mainly used for optical switching networks, can also be used as intensity modulators. An example of a $\Delta\beta$ coupler modulator is also given in this section, operating on the principle that the applied modulating field changes the refractive index in the two guides, such that the change is antisymmetric, and this then affects the light wave propagation in the two guides (hence the name $\Delta\beta$ modulator), the coupling length and the phase matching between them, which also affects the power coupling efficiency.

The development of an accurate numerical model for optimizing a $\text{Ti}:\text{LiNbO}_3$ directional coupler structure requires the consideration of several fabrication parameters. The effect of the lossy metal electrodes on the optical properties of the above structure, for Aluminum (Al) and Gold (Au) materials, is examined in this section. The metal electrode design is an important issue in order to maximize the overlap between the optical and electric fields, which can be optimized by varying certain parameters, such as the electrode placement and the buffer layer thickness.

A Ti-diffused directional coupler modulator with guide width, w , of $9\mu\text{m}$, where the separation between the guides, s , is $7.5\mu\text{m}$ and the electrode separation, h , is $5\mu\text{m}$, and shown as an insert in Fig.5.25, is considered, where y -axis symmetry is assumed for greater accuracy. The SiO_2 buffer layer has a thickness, d , the extraordinary and ordinary refractive indices for LiNbO_3 are taken to be $n_e=2.14$ and $n_o=2.16$ at an operating wavelength $\lambda=1.56\mu\text{m}$, and the maximum change in the refractive index due to the Ti indiffusion was considered 0.01 and 0.005 for the extraordinary and the ordinary indices respectively.

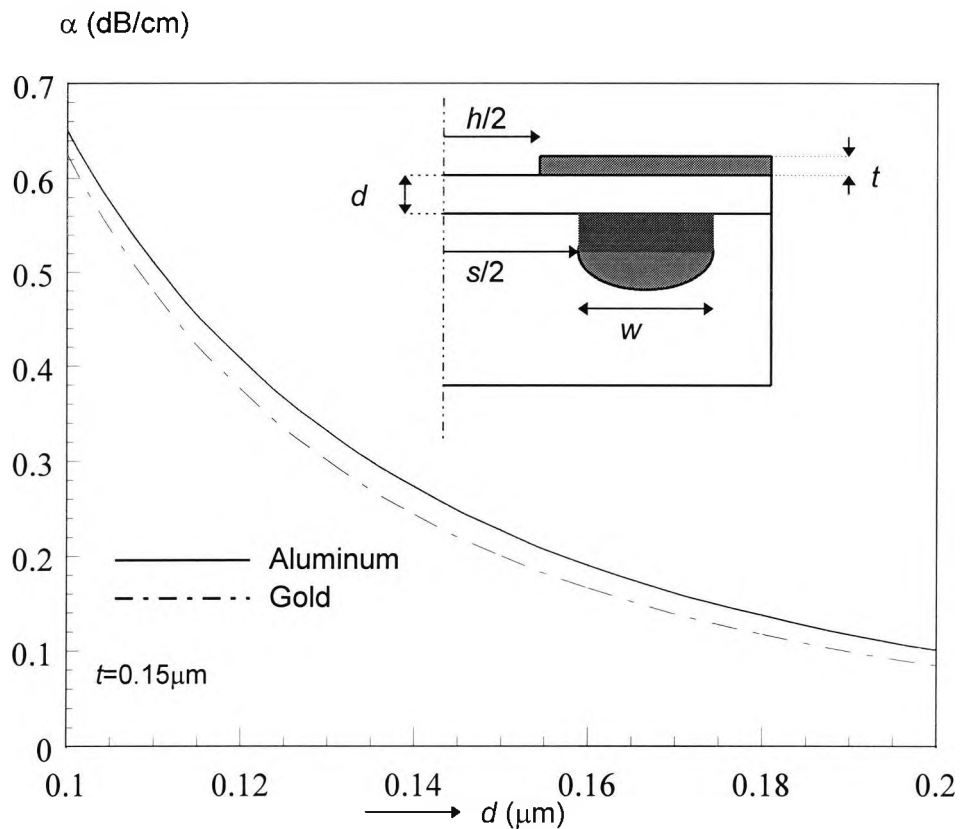


Fig.5.25 Attenuation characteristics for a directional coupler modulator with the variation of the SiO_2 buffer thickness, d , for aluminum and gold metal electrodes.

The modal loss of the TM-polarized mode, for Al and Au metal electrodes of thickness $t=0.15\mu\text{m}$, with complex refractive indices $n_m=1.44-j16$ and $n_m=1.55-j11.5$ respectively, with the variation of the buffer layer thickness, d , has been investigated. From the attenuation curves, shown in Fig.5.25, it can be seen that the modal loss decreases rapidly at first, as the buffer layer thickness (d) increases, but it gradually reaches a steady value at a buffer layer thickness between $0.16\text{-}0.17\mu\text{m}$, which can be considered ideal for the modulator design. The aluminum electrode has always shown a higher attenuation than the gold electrode, for the whole range examined, which is to be expected. The modal loss for the TE-polarized mode, not shown here, is much lower than that of the TM mode, as in all the other structures examined earlier, and therefore, the effect on the optical properties is not considered critical.

5.5 Summary

In this chapter several optical waveguide structures with two-dimensional field mode confinement have been analyzed and the complex propagation characteristics were determined, by using the **H**-field FEM with the perturbation technique, the complex effective index method and the approximate confinement factor method. The normalized gain constant for a simplified representation of a buried heterostructure diode laser structure was calculated, by using the above approaches and the results were in fine agreement, for certain ranges. The accuracy was quite satisfactory, for a low to medium gain level and for a well confined mode by using the FEM with perturbation and the approximate Confinement factor approach respectively. Some of the **H**-field FEM results were also compared with those of the FEM in terms of the H_t variational formulation, and the agreement was found to be sufficiently accurate. Further, the **H**-field FEM with perturbation approach was used for the solution of a simple rib and an integrated laser rib waveguide structure, and the results obtained for the complex propagation constant were compared with some of the approaches mentioned above and found in fine agreement. Next, a multiple quantum well rib structure was analyzed by using the FEM with perturbation and the variation of the field distribution and the normalized attenuation constant with the thickness and the number of the quantum layers, has been examined. Finally, the effect of the lossy metal electrodes on the optical properties a Ti:LiNbO_3 electro-optic directional coupler modulator structure has been studied.

In the next chapter, the FEM with perturbation is used to analyze several other practical device applications with two-dimensional mode confinement, which exhibit surface plasmon properties.

6

Surface plasmon modes in 2-D gain/loss analysis of optical waveguides

6.1 Introduction

As has been demonstrated in Chapter 4, surface plasmon modes can be supported by a single interface between a metal and a dielectric layer. These modes can be coupled to normal dielectric waveguide guided modes, in planar structures, where a thin metal film is attached to a dielectric slab waveguide (as in the multilayer metal-clad waveguide), to form coupled supermodes. Due to the lossy nature of the metal film, a loss analysis of such waveguides is required, to determine the propagation and attenuation characteristics. The Finite Element Method (FEM), in conjunction with the perturbation technique has been applied in several types of planar waveguides, which involved surface plasmon modes and proved to be a very accurate approach, in dealing with low loss devices, for the determination of their gain/loss properties. Surface-plasmon-mode properties are also used in a wide range of device applications, where, 3-D optical waveguide structures are considered, therefore 2-D modal analysis is required, such as in optical polarizers, highly sensitive evanescent optical sensors, or to enhance nonlinear effects in optical devices. In this chapter, the FEM approach with the aid of the perturbation technique is extended to some 3-D

optical waveguides incorporating thin metallic regions, where surface plasmon modes are present, in order to determine their propagation and attenuation characteristics.

6.2 Composite coupled structure

Firstly, the FEM approach with the aid of the perturbation technique was used to determine the complex propagation characteristics of the surface plasmon modes of the structure shown in Fig.6.1.

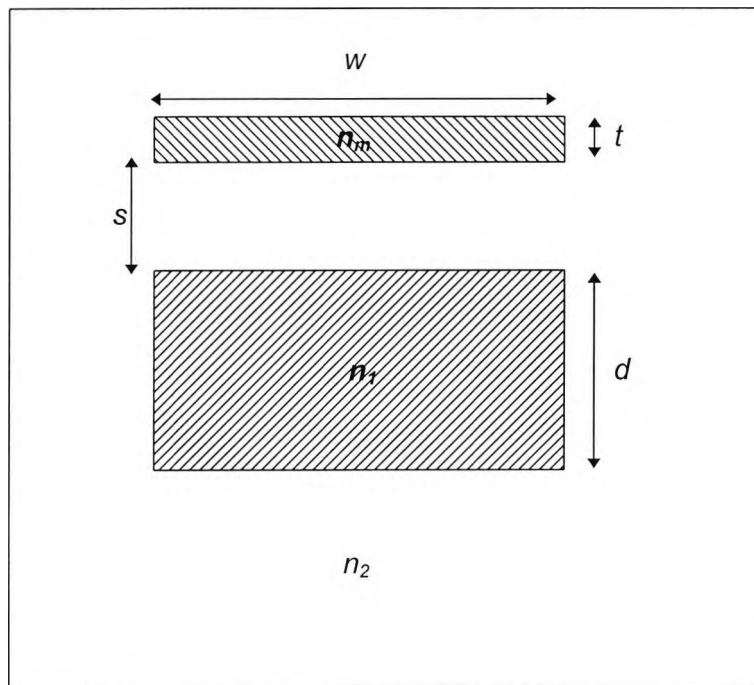


Fig. 6.1 Composite waveguiding structure incorporating a dielectric structure with a metal strip coupled with a dielectric waveguide surrounded by dielectric material

This composite coupled structure consists of an aluminum surface plasmon guide with of finite strip width and an InGaAsP rectangular dielectric waveguide, both surrounded by an InP substrate. In this example, the refractive indices of the lattice matched $\text{In}_{1-x}\text{Ga}_x\text{As}_y\text{P}_{1-y}$ rectangular dielectric waveguide, the InP substrate, and the aluminium strip are $n_1=3.37621$, $n_2=3.20483$ and $n_m=1.2-j12$, respectively, for $y=0.399$, at the operating wavelength, $\lambda=1.3\mu\text{m}$ (Broberg and Lindgren, 1984). The dimensions of the rectangular guide are $d=1.0\mu\text{m}$, where $w=5d$ and the separation from the metal strip, (s), is $1\mu\text{m}$. The effective index, (β/k_0) , the normalized attenuation constant

(α/k_0) , and the field profiles are examined for the first two supermodes, with the variation of the metal strip thickness, t .

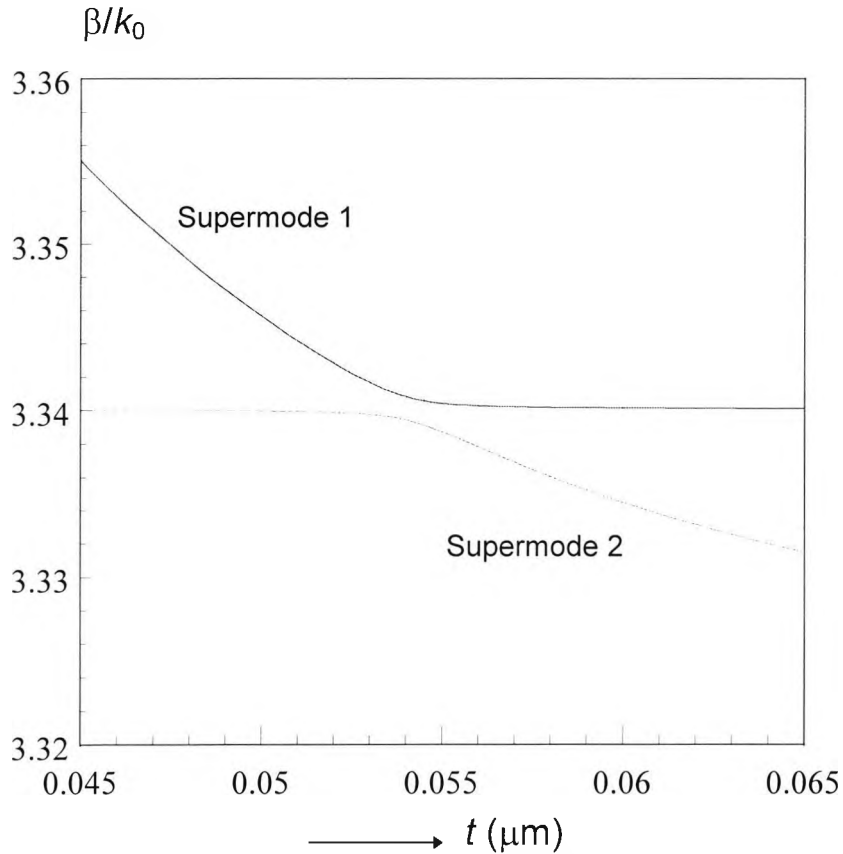
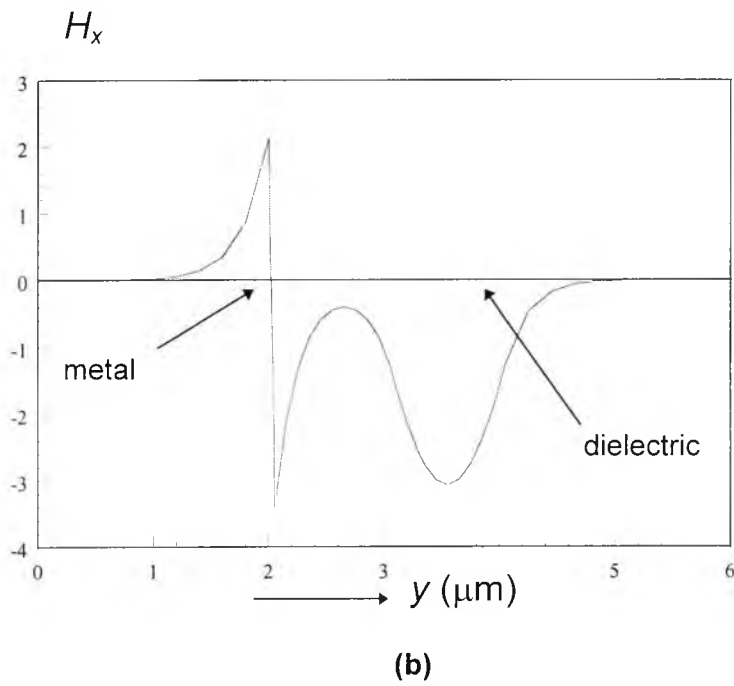
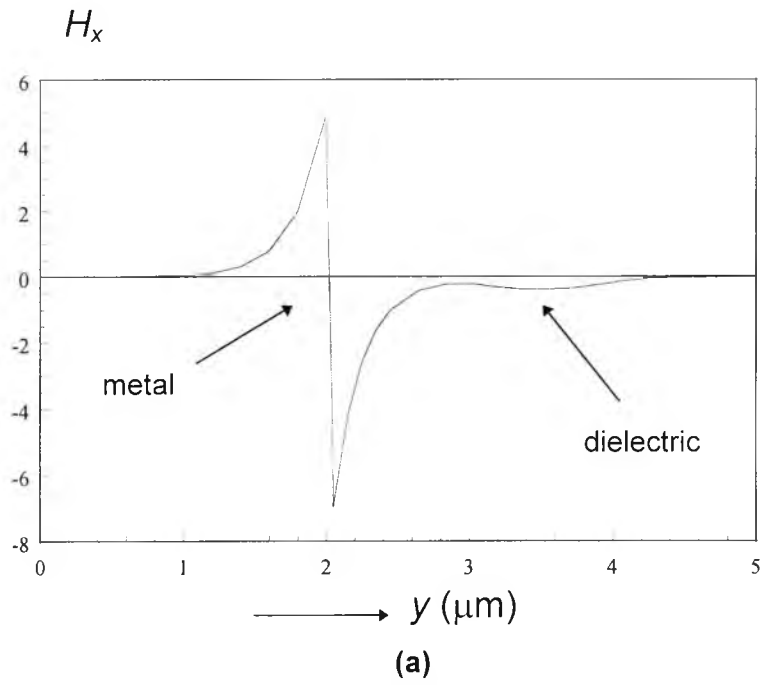


Fig.6.2 Variation of the effective index with metal-strip thickness, t , for the first two supermodes of the coupled structure.

Figure 6.2 shows the variation of the effective indices for the two supermodes with the metal strip thickness, t . The effective index of the first supermode is always higher than that of the second supermode and they never intersect. Near $t \cong 54\text{nm}$, the directional coupler is 'synchronous' as the difference between the propagation constant of the two supermodes is a minimum. The first supermode, for t lower than the synchronous (or phase matched) condition, is similar to the odd-type surface plasmon mode and the field concentrates mostly at the two metal/dielectric interfaces. The modal field profile varies in both the transverse directions, but for simplicity the field profile along the y -axis is presented, as shown in Fig.6.3.a, for $t=0.05 \mu\text{m}$. The effective index of this supermode reduces with t , similar to odd-type surface plasmon mode (as shown in Section 4.3) but for $t > 0.054 \mu\text{m}$ the mode becomes essentially a waveguide mode. In this region most of the power is confined in the dielectric waveguide. For $t=0.06\mu\text{m}$, the modal field profile along the y -axis is shown in Fig.6.3.c.

In this region, the dielectric waveguide mode is hardly affected by the metal strip above, so its effective index is essentially unchanged with the metal strip thickness, t .



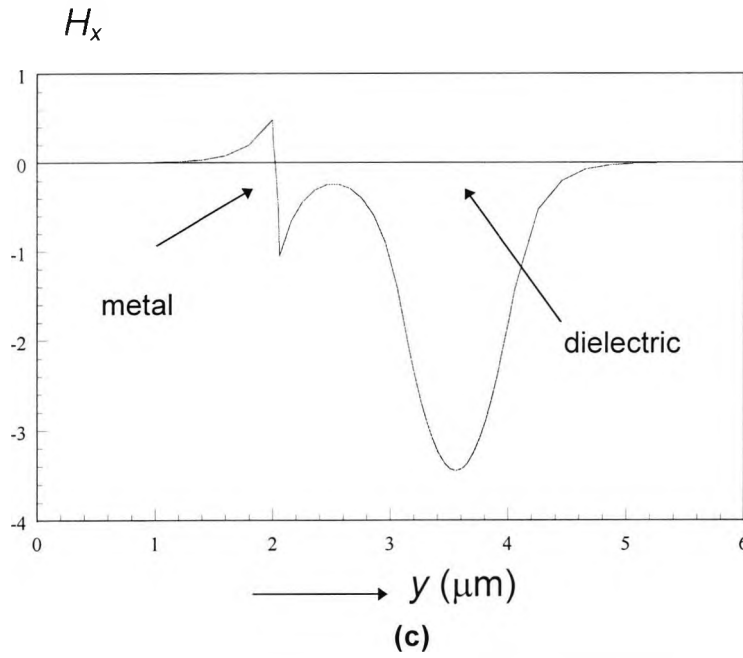
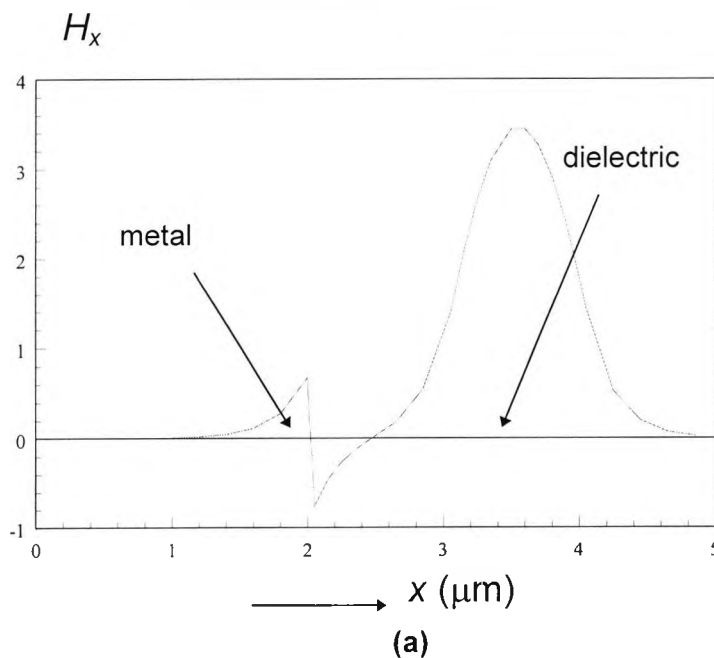
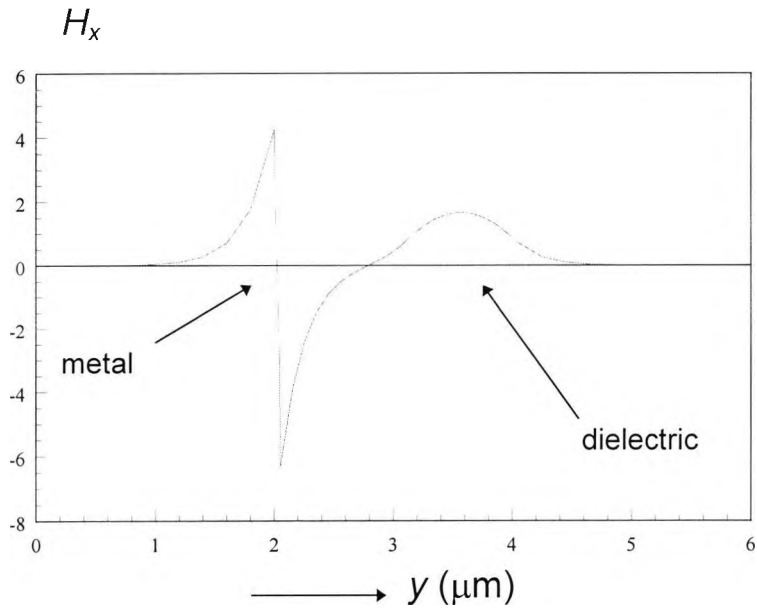


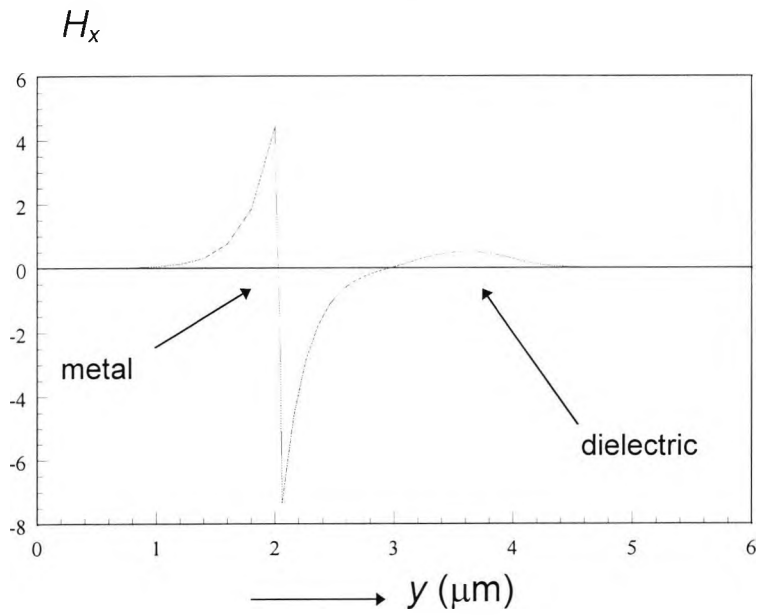
Fig.6.3 H_x field profile along symmetry y -axis for the first supermode, for metal film thickness a) $t=0.05 \mu\text{m}$ b) $t=0.054 \mu\text{m}$, c) $t=0.06 \mu\text{m}$.

For $t < 0.054 \mu\text{m}$, the second mode is again essentially a dielectric waveguide mode and its effective index changes very little with the metal strip thickness, t . The field profile along the y -axis for this mode for $t = 0.05 \mu\text{m}$ is shown in Fig.6.4.a. However, for $t > 0.054 \mu\text{m}$, the second supermode is almost like the odd-type surface plasmon mode and its effective index decreases with the metal thickness. For $t = 0.06 \mu\text{m}$ most of the field is confined at the metal/dielectric interfaces as shown in Fig.6.4.c.





(b)



(c)

Fig.6.4 H_x field profile along symmetry y -axis for the second supermode, for metal film thickness a) $t=0.05 \mu\text{m}$ b) $t=0.054 \mu\text{m}$, c) $t=0.06 \mu\text{m}$.

When the two isolated surface plasmon and dielectric waveguide modes are phase matched, the two supermodes carry equal power in both the waveguiding regions. The field profiles along the y -axis are shown in Fig.6.3.b and Fig.6.4.b, for the first and the second supermodes respectively. The field distribution of the first supermode, for $t=0.054 \mu\text{m}$, can also be seen in Fig.6.5, for half-symmetry along the y -axis. The field is maximum at the centre of the rectangular waveguide and one positive and one negative peak values can also be observed at the two metal/dielectric interfaces. It can also be observed that the field reduces monotonically along the x -direction, for both of the waveguides.

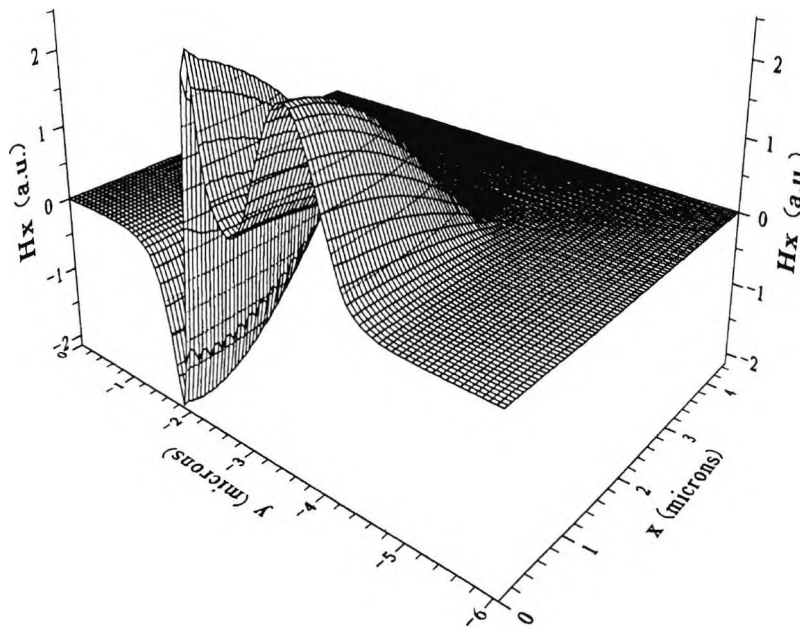


Fig.6.5 H_x field distribution for the first supermode for metal-strip thickness $t=0.054 \mu\text{m}$ (only half the structure is shown because of one-fold symmetry along the y -axis).

The phase matching information is critical in the design of polarizers or sensors as appreciable power transfer between the dielectric waveguide and the surface plasmon modes is only possible when they are phase matched. To our knowledge, this is the first time, that an analysis of surface plasmon modes with two-dimensional confinement has been presented.

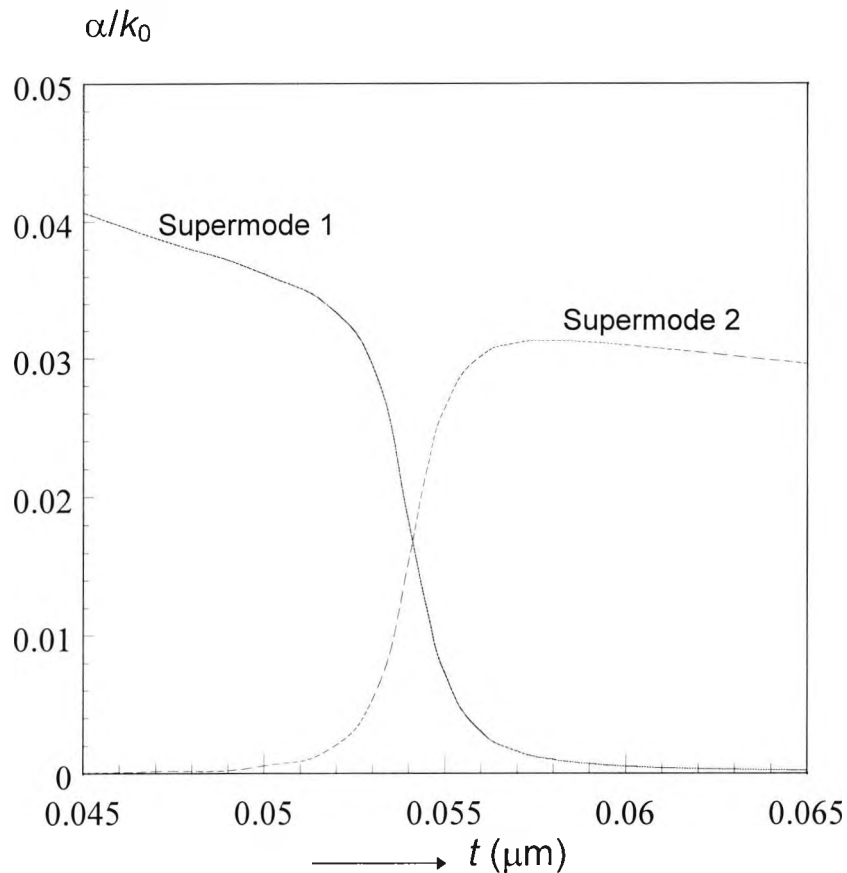


Fig.6.6 Variation of the normalized loss coefficient with metal strip thickness, t , for the coupled structure.

Next, the attenuation characteristics are examined, for the same range of metal strip thickness, as shown in Fig.6.6. For thicknesses below $t=0.054\mu\text{m}$, the loss of the first supermode is high, since the field is concentrated in the lossy metal region (mode profile shown in Fig.6.4.a), while for a metal strip thickness above that value the loss is negligible since most of the field is confined in the loss-less rectangular dielectric guide region (mode profile shown in Fig.6.4.c). The opposite occurs for the second supermode, where the loss is negligible for lower value of t , since the mode is more fibre-like (shown in Fig.6.5.a). However, the loss is high for a higher value of t , since in this case the mode is almost surface-plasmon type (mode profile is shown in Fig.6.5.c). For $t \cong 0.054 \mu\text{m}$, where the two modes are approximately phase matched, both the supermodes suffer appreciable attenuation. This information is useful in designing optical polarizers where TM-like modes from the dielectric waveguide can be coupled to the surface plasmon mode and will be attenuated, whereas the TE-like modes will propagate in the dielectric waveguide since this type of mode does not have its equivalent in the thin metal strip.

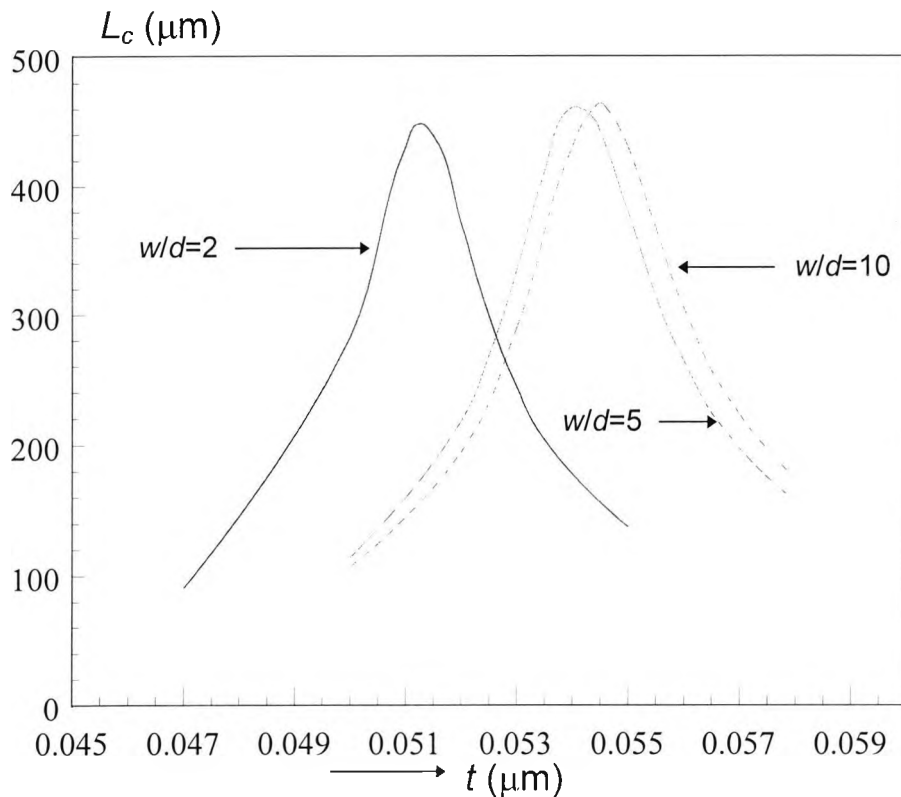


Fig.6.7 Variation of the coupling length with the metal-strip thickness, t , for various aspect ratios (w/d) of the rectangular dielectric waveguide

The effect of varying the width, w , of the guide was then examined in terms of the coupling length, L_c , as shown in Fig.6.7, where L_c is defined by:

$$L_c = \pi / \Delta\beta \quad (6.1)$$

where, $\Delta\beta$, is the phase constant difference between the two supermodes.

It can be observed that the coupling length, L_c , is a maximum when the surface plasmon guide is phase matched with the rectangular dielectric waveguide. The maximum coupling length at phase match depends on the separation between the two guides, s , the metal thickness, t , and the aspect ratio w/d . In the above example the guide separation, s , was kept constant ($s=1\mu\text{m}$) and only the thickness, t , was varied for different values of the aspect ratio.

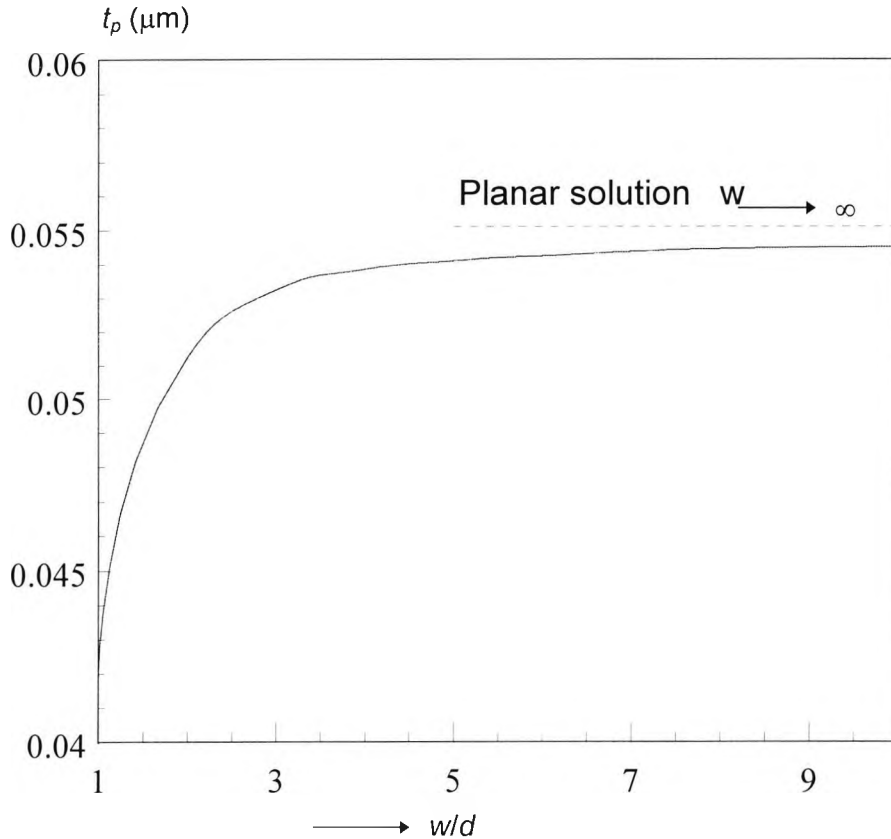


Fig.6.8 Variation of the metal-strip thickness at phase matching, t_p , with the (w/d) aspect ratio. The planar solution for $w/d=\infty$ is shown by the dashed line.

Fig.6.8 shows the variation of the surface plasmon layer thickness, t_p , at phase matching with respect to the aspect ratio (w/d) of the rectangular dielectric waveguide. This value of t_p increases monotonically with (w/d) however, with ever decreasing incremental rates. For very high values of (w/d) , which is equivalent to the slab solution, the planar solution converges towards the two-dimensional solution for any given mesh refinement. In this case only 60 mesh divisions were used, in the y -direction for both the planar and two-dimensional solutions, due to limited computer resources, but the solution accuracy could be increased by using finer mesh divisions if required.

The above numerical approach can be used to optimize optical polarizer design, where the device parameters can be varied to achieve phase matching between the guides. The separation between the guides, s , can also be varied so that the length of the active coupling section can be made equal to the coupling length of the system.

6.3 TE/TM Polarization mode splitters

TE/TM Polarization mode splitters are required in many systems in optical communications in order effectively to separate the TE and TM polarizations of the optical wave. A cross section of a TE/TM mode splitter, based on two parallel rib waveguides, with a metal cladding on one of the ribs, is shown in Fig.6.9. When a composite TE/TM optical wave is launched at the input of the non-metal rib, there is power transfer to the metallized rib, due to the coupling. As was shown in Chapter 4, in planar structures with metal-cladding, the metallic film affects only slightly the propagation characteristics of the TE mode, which propagates almost as in normal dielectric waveguides. Since the two rib regions in the mode splitter structure, apart from the presence of a metal-cladding on one of them, have identical refractive indices, in the case of the TE mode the device can operate as a synchronous directional coupler (Marcuse, 1991), because the isolated mode has approximately the same propagation constant in each guide core region. Therefore, by adjusting the length of the device, the TE mode launched at the non-metal rib can be fully coupled to the metallized rib waveguide. On the other hand, for the TM polarization the two waveguides are not identical due to the presence of gold cladding on one of them. The propagation constants for the TM-polarized light in the two isolated guides are unequal. The TM mode launched in the non-metal rib is not fully coupled to the lossy metallized rib, because of the phase-matching, so it propagates mostly along the non-metal rib, and therefore the two modes are decoupled at the output of the structure. Albrecht *et al.*, (1990) demonstrated that such a structure shown above, can operate in two distinct modes depending on the degree of lateral confinement of optical rib waveguide before metallization. They showed that for strong confinement, metallization generates an asymmetrical coupler, and that for weak confinement, the metallized waveguide is guiding for the TE but non-guiding for the TM polarization.

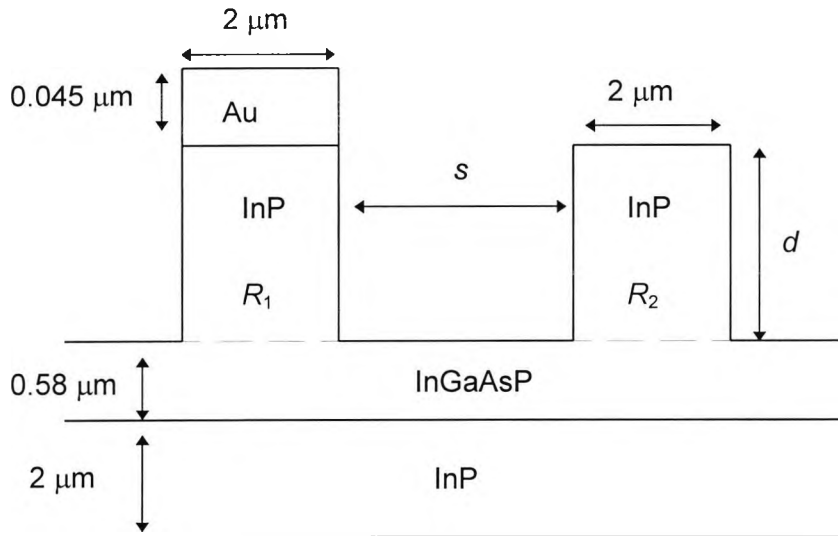


Fig.6.9 Cross section of the TE/TM mode polarization splitter.

The mode polarization splitter (cross-section shown in Fig.6.9), consists of two parallel rib waveguides, with an InGaAsP active region and an InP substrate with refractive indices $n_g=3.38$ and $n_s=3.17$ respectively, and an Au metal-cladding on top of the one with a complex refractive index $n_m=0.18-j10.2$, at an operating wavelength, $\lambda=1.55\mu\text{m}$. A modal analysis of the above cross section, using the scalar FEM with perturbation was performed, in order to calculate the propagation and attenuation characteristics, which can be used in determining the various design parameters of the mode polarization splitter.

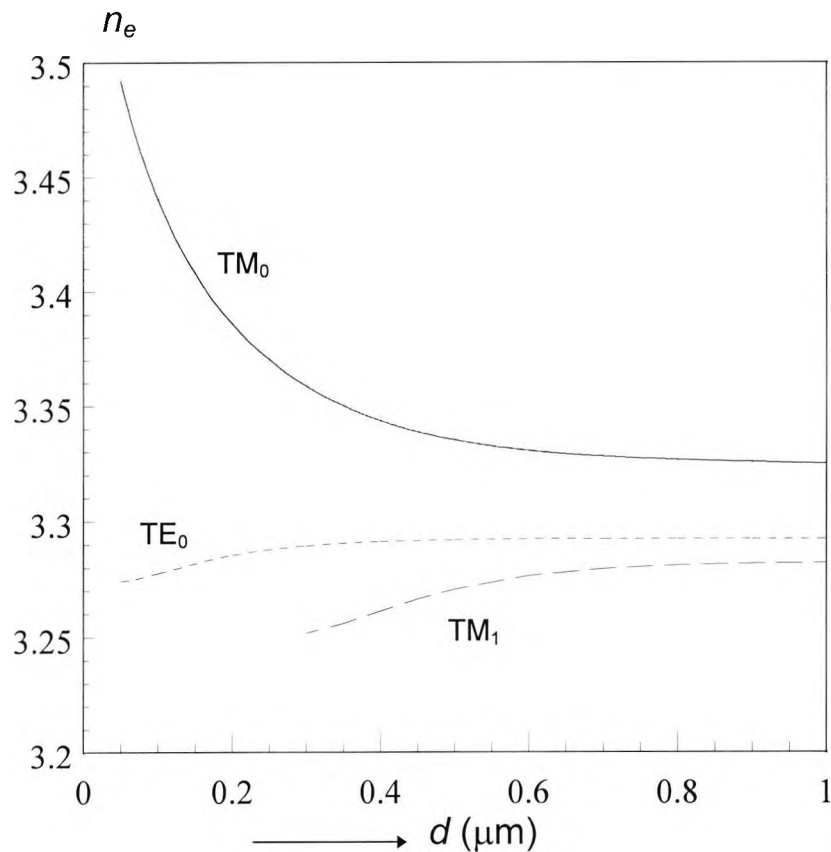
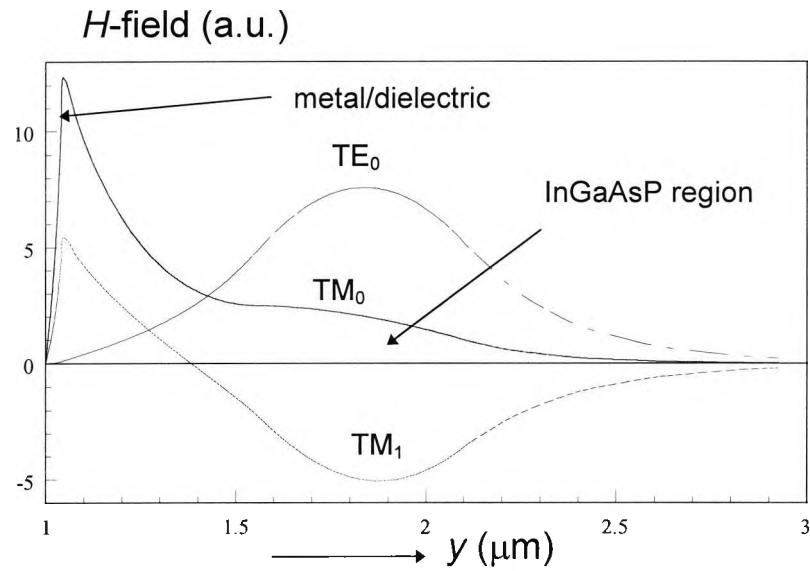
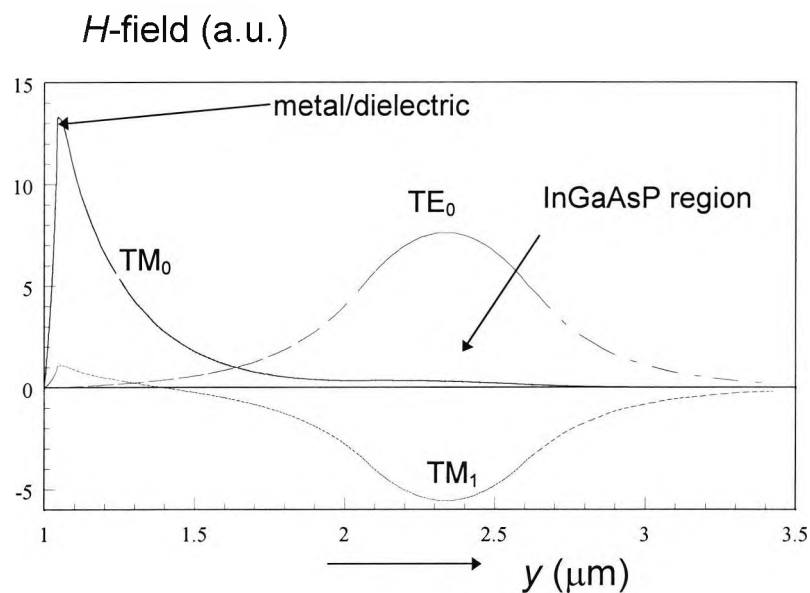


Fig. 6.10 Effective index variation of TE and TM modes, with the variation of the rib height, for a metal-clad rib optical waveguide.

Firstly, the single metal-clad rib waveguide was considered (Left-hand Rib, R_1 , in Fig.6.9), and the variation of the effective index with the increase of the rib height, d was calculated, for the TE_0 , TM_0 and TM_1 modes. From the dispersion curves shown in Fig.6.10, it can be seen that as the rib height, d , increases the effective index of the TM_0 , which is much higher than that of the other modes decreases, while the effective indices of the TM_1 and TE_0 modes, which are predominantly guided by the rib, increase.



(a)



(b)

Fig.6.11 Field profiles along the y -axis of symmetry, for the TE and TM modes of a metal-clad rib waveguide, for rib height a) $d=0.5\mu\text{m}$ and b) $d=1\mu\text{m}$.

The propagation characteristics can be explained in more detail, from the field profiles of the lower order TE and TM modes, for different values of the rib height, shown in Fig.6.11. When the rib height is small, thus when the metal-cladding is close to the guide, the lower order TM_0 mode is mainly a surface plasmon mode coupled to a weak normal guided dielectric mode, therefore it propagates with higher effective index than the normal dielectric guided modes. As the rib height is increased TM_0 mode becomes a pure surface-plasmon mode and propagates only at the metal dielectric

interface. For small rib height, the TM_1 mode has some field intensity at the metal/dielectric interface and more in the InGaAsP region, but as the rib height increases, it becomes almost pure guided dielectric mode, concentrated mostly in the InGaAsP region. The TE mode, which is a dielectric guided mode, is not affected at all by the presence of the metal cladding, therefore it has higher effective index than the TM_1 mode, but that value never exceeds the value of the refractive index of the InGaAsP layer. When the rib height is increased, the TE_0 mode becomes more confined in the rib core region, giving a small increase in the effective index.

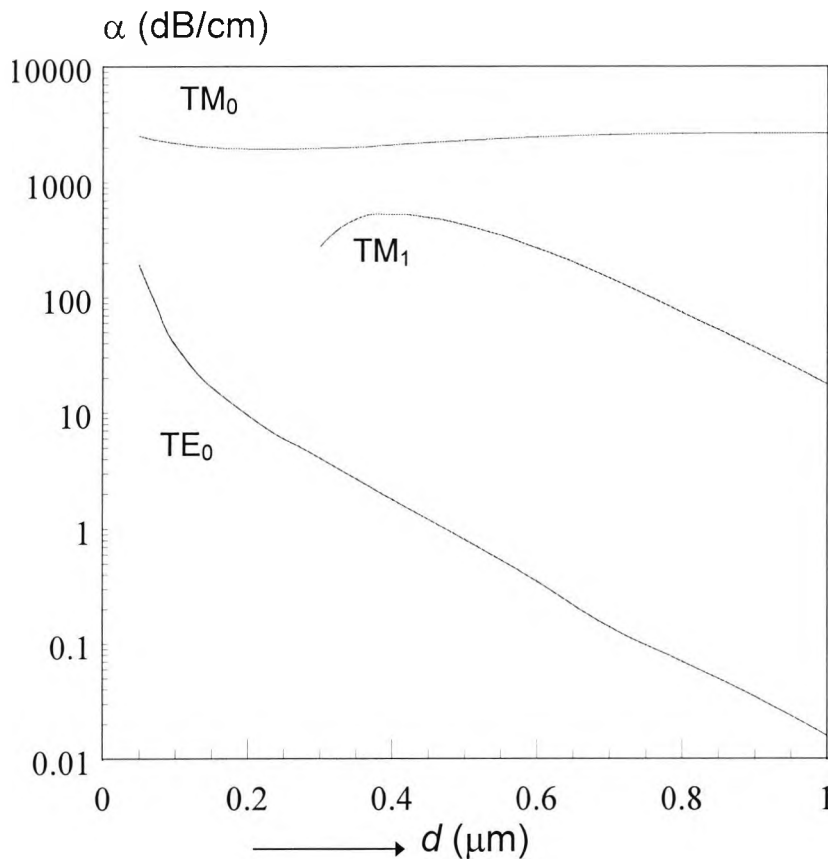


Fig.6.12 Variation of the attenuation constant, with the increase of the rib height, for the TE and TM modes, of the metal-clad rib waveguide.

The attenuation characteristics of the metal-clad rib waveguide, for the TM and TE modes, were also examined and presented in Fig.6.12. As can be seen from the attenuation curves, the TM_0 mode which is a surface plasmon mode, has very high attenuation constant, since it propagates mainly at the metal/dielectric interface, *i.e.*, near the lossy region of the waveguide. The TM_1 mode, which has lower attenuation constant than the TM_0 mode, has some interesting features, at about $d=0.4\mu\text{m}$, where an absorption peak is observed. This situation, which was also demonstrated in section

4.4, and reported by several authors (Polky and Mitchel, 1974; Sun and Yip, 1994), is caused by the strong coupling between the normal guided wave and the surface plasmon wave. The TE_0 has the lowest attenuation characteristics, since there is only a negligible amount of field intensity in the metal region. As the rib height increases the TE_0 mode becomes more confined in the InGaAsP region and the attenuation constant decreases rapidly.

The rib height, in this type of structure is a major parameter in the adjustment of the attenuation level of the waveguide and acts in a similar way as the low-index dielectric buffer, in the multilayer planar structure, in section 4.4.

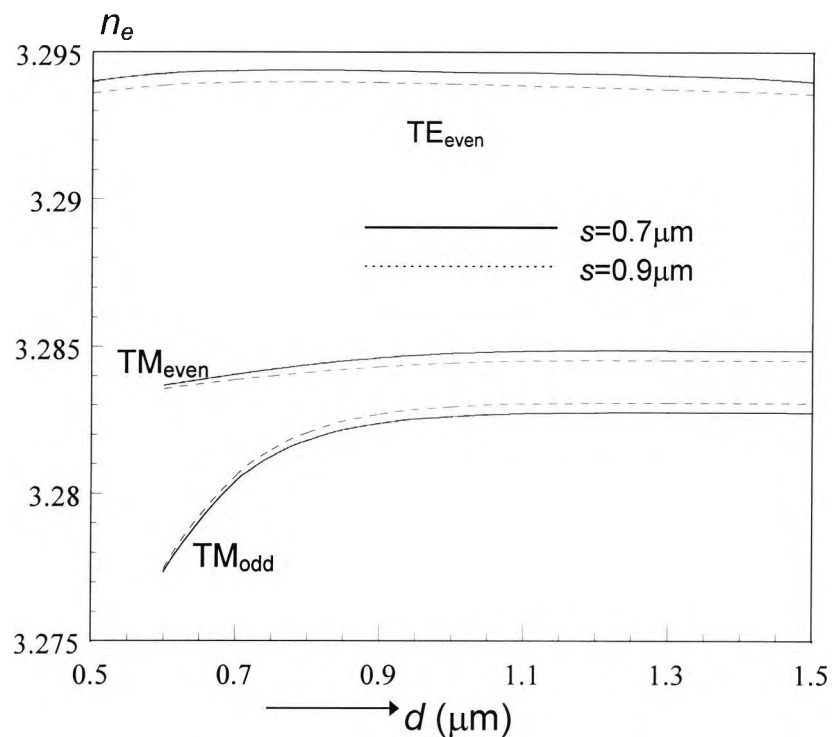


Fig.6.13 Variation of the effective index, with the increase of the rib height, for the TE and TM modes, of the polarization mode splitter, for different separations between the two ribs.

Next, the whole cross-section of the mode splitter, shown in Fig.6.9, was considered, and the properties of the fundamental TE mode and the two low-order TM modes were examined, for different values of separation, s , between the two ribs. From the propagation characteristics, shown in Fig.6.13, it can be seen that the TE_{even} , or TE_{00} mode (where m and n in TE_{mn} , denote the zero crossings along the x and y axes respectively), has the highest effective index which does not change significantly with the increase of the rib height (d), but decreases slightly when the separation is increased. As the separation between the two ribs (s) increases, the effective index of the TM_{even} , decreases while that of the TM_{odd} increases. The effective index of the TM_{even} , or TM_{01} mode is higher than that of the TM_{odd} , or TM_{11} mode, and both indices increase with the increase of the rib height. It should be noted that there exists a TM mode with a higher effective index than those presented, but this was not considered for the coupled structure because it is a pure surface plasmon mode located at the metal/dielectric interface and does not interact with the guided dielectric mode of the active region, and therefore was not suitable in optical polarizing applications.

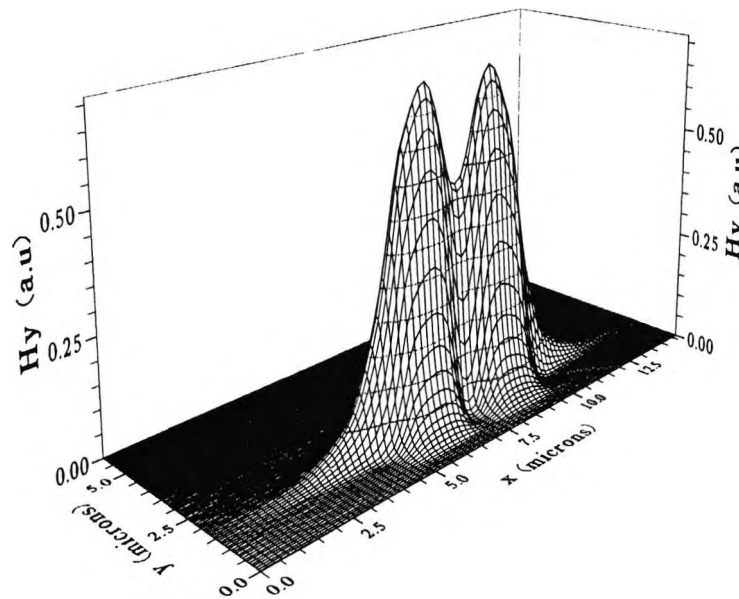


Fig.6.14 H_y field distribution of the TE_{00} mode for $d=0.8\mu\text{m}$ and $s=0.7\mu\text{m}$, of the mode polarization splitter

From the field distribution of the TE_{00} mode, for $s=0.7\mu\text{m}$ and $d=0.8\mu\text{m}$, shown in Fig.6.14, it can be seen that the TE_{00} has high field intensity in the middle of the active region, with peak values below the two ribs, and there is no field variation in the metal region. The TE_{00} mode is a coupled supermode of two guided dielectric modes located at the centre of the active region below each rib.

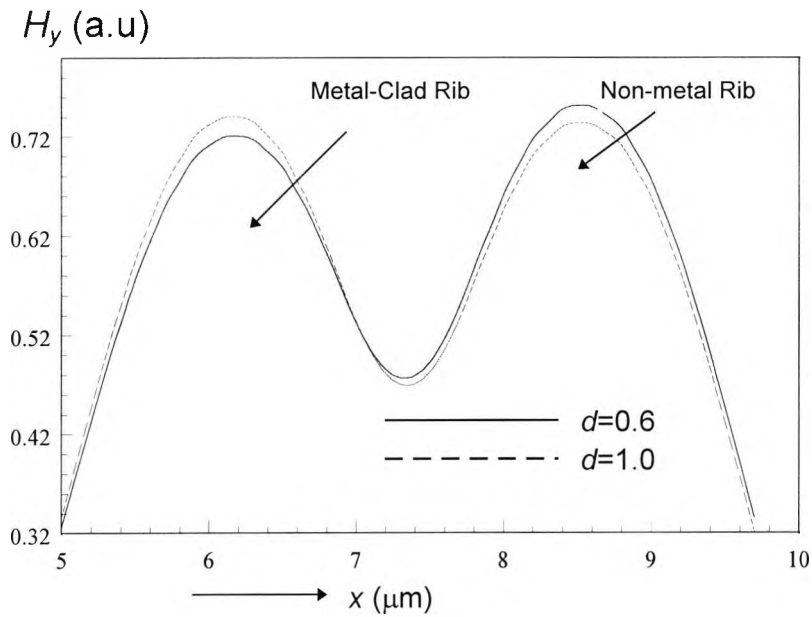


Fig.6.15 H_y field profile, for the TE mode, along the x -axis, in the centre of the InGaAsP dielectric region for different values of the rib height.

The field profile of the TE_{00} mode, along the x -axis at the centre of the InGaAsP dielectric region, shown in Fig.6.15, is more or less symmetrical. Although the TE_{00} mode is not affected much by the metal-cladding, there is still some effect visible. When the rib height is varied from 0.6 to $1\mu\text{m}$, the symmetry of the field intensity at each rib slightly changes. As the rib height is increased, the field intensity at the metal-rib, which is lower than that of the non-metal rib increases, and becomes higher than the other. When the rib height is adjusted at a certain height the two peaks become more balanced. This is the situation, where the two coupled modes have the same propagation constant, and the device operates like a symmetrical directional coupler. By adjusting the length of the device, the power can be fully transferred from the one side to the other, which is a desirable condition in the design of an optical polariser.

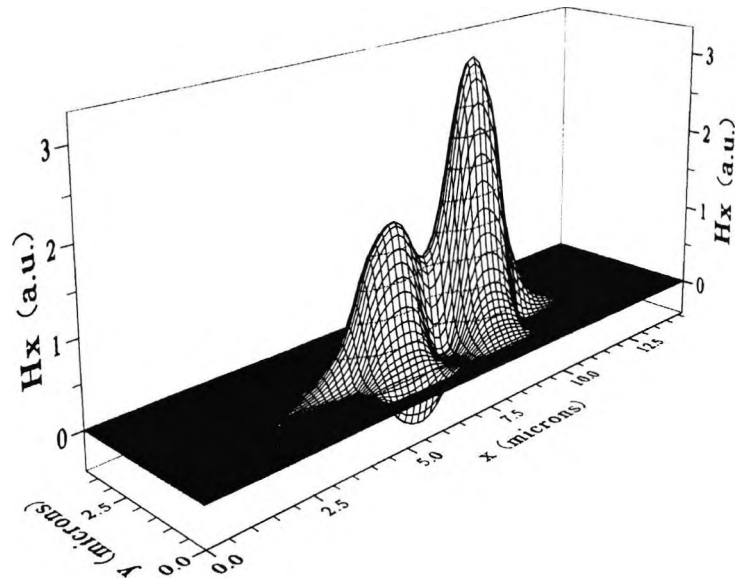


Fig.6.16 H_x field distribution of the TM_{01} mode of the mode polarization splitter, for $d=0.8\mu\text{m}$ and $s=0.7\mu\text{m}$.

From the field distribution of the TM_{01} mode, shown in Fig.6.16, it can be seen that the above mode is asymmetric, with respect to the x -axis variation, and it changes polarity along the y -axis, at the metal-rib side. Although there is a considerable amount of field intensity in the metallic region, the field is stronger in the dielectric region.

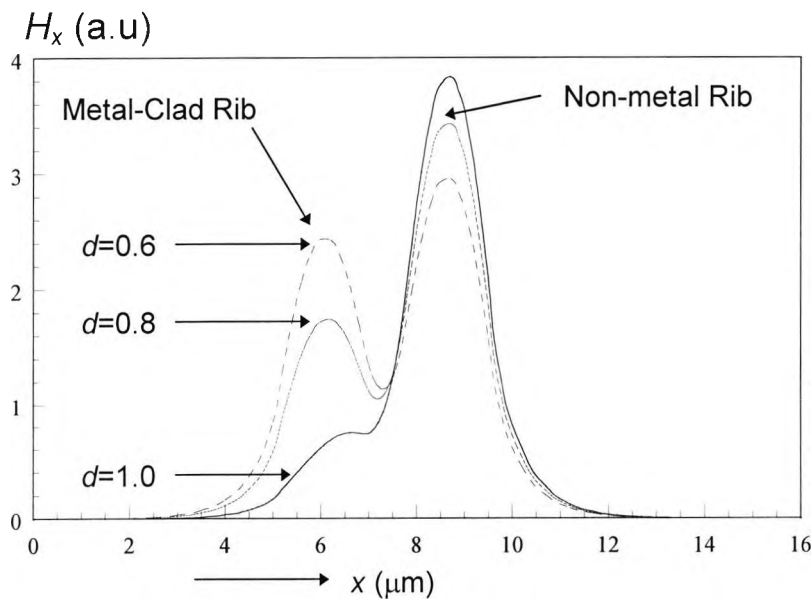


Fig.6.17 H_x field profile, for the TM_{01} mode, along the x -axis, in the centre of the InGaAsP region, for different values of the rib height, at a separation, $s=0.7\mu\text{m}$.

Figure 6.17, shows the H_x field profile along the x-axis, in the centre of the InGaAsP region, for different values of the rib height. As the rib height increases, the field intensity at the side of the metal-rib, which is lower than that of the non-metal, increases, since the metal-cladding is moved away from the dielectric region of the guide. On the other hand, when the rib height is increased, the field intensity at the side of the non-metal rib, decreases, with the tendency to reach the height of the field intensity at the other side. Therefore at large values of rib height, the coupled TM_{01} mode tends to approach the shape of the TE_{00} mode.

In the design of the mode polarization splitter, the optimum device length should be an integer odd or even multiple of the coupling length, for the TE and the TM modes. This can be achieved by finding the optimum separation (s) between the two ribs and the metal-clad rib height (d), but also taking into account the modal loss of the structure, which is an important factor in the overall power transfer performance of the device.

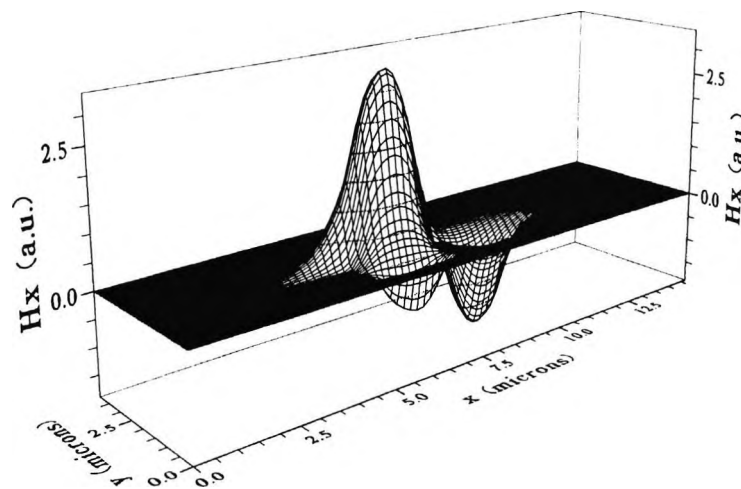


Fig.6.18 H_x field distribution of the TM_{11} mode of the mode polarization splitter, for $d=0.8\mu\text{m}$ and $s=0.7\mu\text{m}$,

The TM_{odd} mode, or TM_{11} , shown in Fig.6.18, has similar behaviour with the TM_{01} mode, with only difference the opposite polarity of the field intensity at the side with the metal-rib and the lower propagation characteristics.

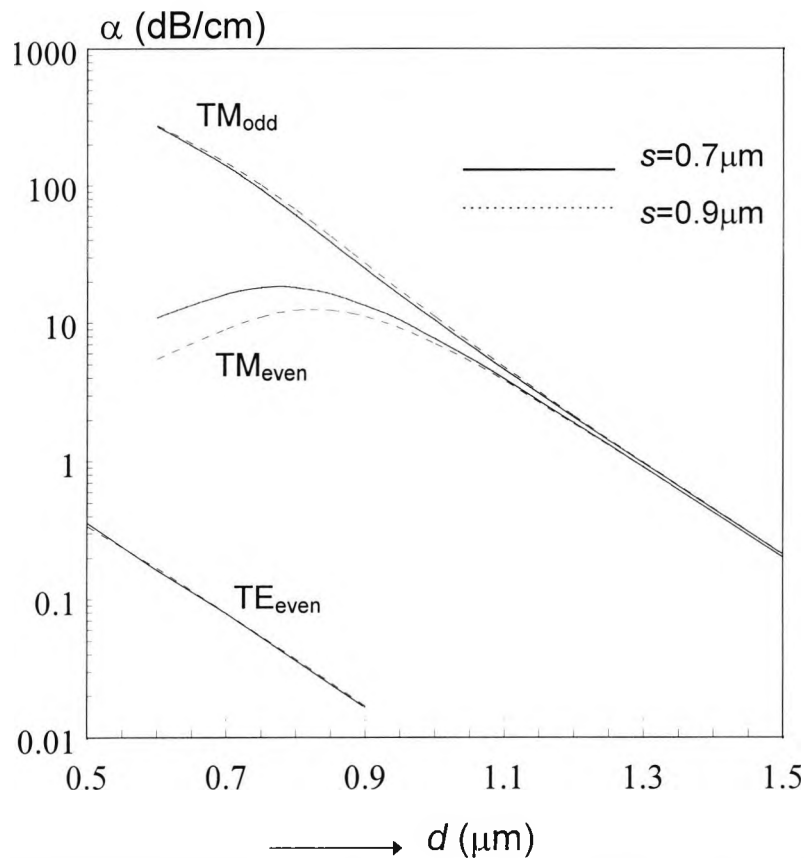


Fig.6.19 Variation of the attenuation constant for the TM modes, of the polarization mode splitter, with the increase of the rib height for different values of the separation, s .

Finally, the variation of the attenuation characteristics of the TE and TM modes, for the polarization mode splitter, with the increase of the rib height, for two different values of the separation, s , was considered and is presented in Fig.6.19. At low rib height, the TM_{even} increases until it reaches an absorption peak, and then it starts decreasing rapidly. For a smaller rib height, where the metal layer is nearer to the guide core, the TM_{odd} mode suffers more attenuation, because the optical power is more confined in the metal-clad rib. The TM_{odd} mode, which is more confined in the metal-clad waveguide side, has a higher attenuation constant than the TM_{even} mode and decreases monotonically as the rib height increases, not showing an attenuation peak over the range examined. For a large rib height (d), the effect of the metal cladding is less, and therefore the modal loss is low, and the two isolated guides are nearly phase matched. The TE mode has the lowest attenuation constant, it being about 1000 times lower than that of the TM_{even} mode, and decreases as the rib height increases in a similar way to that of the TM modes.

6.4 Sub-Micron Metal-Clad Optical Fibers

Metal-clad optical fibers of sub-micron dimensions find an important application in near-field optical scanning microscopy, a technique rapidly developing in the recent years, providing high-resolution imaging in the semiconductor industry and the biological sciences. Single-mode optical fibers are widely used in long-distance telecommunications, and are well developed, providing low loss and very high bandwidth transmission media. However, metal-clad optical fibers with sub-micron diameter are currently being used in near-field scanning optical microscopy (NFSOM) (Durig *et al.*, 1986; Betzig *et al.*, 1987), a technique in which light is transmitted through a metal-coated tapered fiber with a submicron aperture at the end, used as light emitting probe. A subwavelength sized spot is formed on an opaque screen, which is scanned over an object to generate a super-resolution image. The resolution is closer to that of a scanning electron microscope (SEM) than of a conventional microscope, and it has many advantages, since it can operate in air, is not limited to conductive materials and provides information on optical rather than electrical properties.

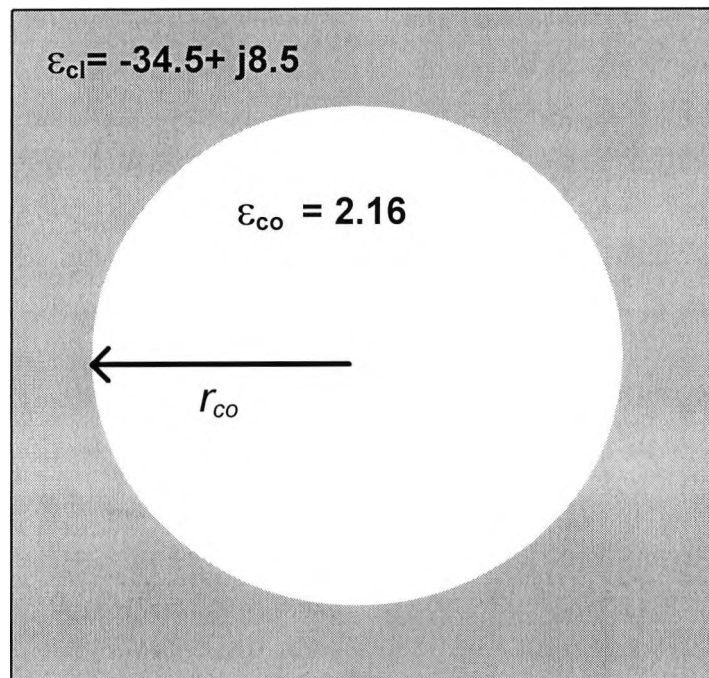


Fig.6.20 Schematic representation of the cross section of a metal-clad optical fiber with core radius r_{co} . The dielectric core medium with dielectric constant $\epsilon_{co}=2.16$ is surrounded by an infinite metal medium (shaded area) with complex dielectric constant $\epsilon_{cl}=-34.5+j8.5$.

Since the optical resolution in NFSOM is determined by the aperture size rather than the wavelength of radiation (Roberts, 1991), a knowledge of the light propagation characteristics in metal-clad optical fibers and near-zone fields produced is required. For optical frequencies, these structures can be represented by a waveguide with a circular dielectric core, normally of glass material, and an infinite metal cladding with a negative dielectric constant, as shown in Fig.6.20. The negative permittivity of the cladding leads to surface plasmon modes (Boardman, 1982), which mainly propagate along the metal-dielectric interface. If the permittivity of the metal coating is purely real (and negative), then surface plasmon modes will not suffer attenuation. However, for the most of the metal, the permittivity value is complex and its imaginary part is responsible for the attenuation of light waves. The degree of attenuation suffered by these modes, can be represented by the imaginary part of the propagation constant of the optical modes, and therefore a complex solution is required.

6.4.1 Classification of propagating modes in metal-clad optical fibers

The classification of the propagating optical modes in metal-clad optical fibers is not an easy task, because in the above structures, as in all optical fibers, apart from the presence of pure TE or TM modes, hybrid modes also exist. These types of modes do not have vanishing longitudinal field components and their classification, which depends on the dominance of either the electric, E_z , or the magnetic, H_z , longitudinal field component, can sometimes be misleading. In the present work, the pure TE and TM modes of metal-clad optical fibers have been analysed, in order to identify the suitable modes for NFSOM applications.

The FEM solution in terms of the vector \mathbf{H} -field formulation for such structures can be cumbersome, due to the presence hybrid modes, where the application of the boundary conditions requires great attention. Additionally, spurious solutions are also present in the above solution, and the application of the penalty coefficient can be tricky, due to the metal-cladding with negative refractive index. Therefore, a scalar approximation of the \mathbf{H} -field formulation has been used in the present analysis, where the hybrid modes and the spurious solutions are eliminated, leaving distinguishable only the pure TE and TM modes. The perturbation technique has also been used in

conjunction with the FEM, for the determination of the attenuation characteristics of the above structures, due to the lossy metal-cladding.

The solution of optical fiber problems with the finite element method, in general, was achieved by the use of ring elements, polar coordinates and Bessel functions in earlier approaches (Koshiya, 1992b). In the approach presented here, the problem is solved in Cartesian coordinates, more commonly used for a wide range of waveguides, and the optical fiber is approximated by a circular dielectric waveguide. Two fold symmetry is exploited to achieve greater accuracy for a given level of computer resources. A combination of electric and magnetic wall boundary conditions are applied to obtain the odd and even type TE and TM polarized waves. Although isoparametric elements can be used to represent the curved edges of the fiber core more effectively: however, in this case a general purpose finite element program has been used where the problem of the triangular elements around the circumference of the core of the fiber is overcome by the use of a very fine mesh which diminishes the effect of those boundary elements. The scalar formulation also enabled the use of finer mesh analysis, with less computational time and memory requirement than a vector formulation, for better representation of the boundary elements.

In order to distinguish the geometry of the various modes, the standard notation TE_{mn} , and TM_{mn} for the optical waveguides was used for the quasi-TE and TM modes respectively. In a guide with circular symmetry, the index m indicates the angular dependence of the mode (counts $2m$ 'zeros' of the mode for a full circle), and the index n denotes the radial dependence (counts the number of 'zeros' along the radial axis).

6.4.2 TM mode analysis

As an illustrative example, in this paper a metal-clad optical fiber, as shown in Fig.6.20 is examined, which has a dielectric core of glass material with dielectric constant $\epsilon_{co}=2.16$ and aluminum coating with complex dielectric constant $\epsilon_{cl}=-34.5+j8.5$, at an operating wavelength $\lambda=0.488\mu\text{m}$.

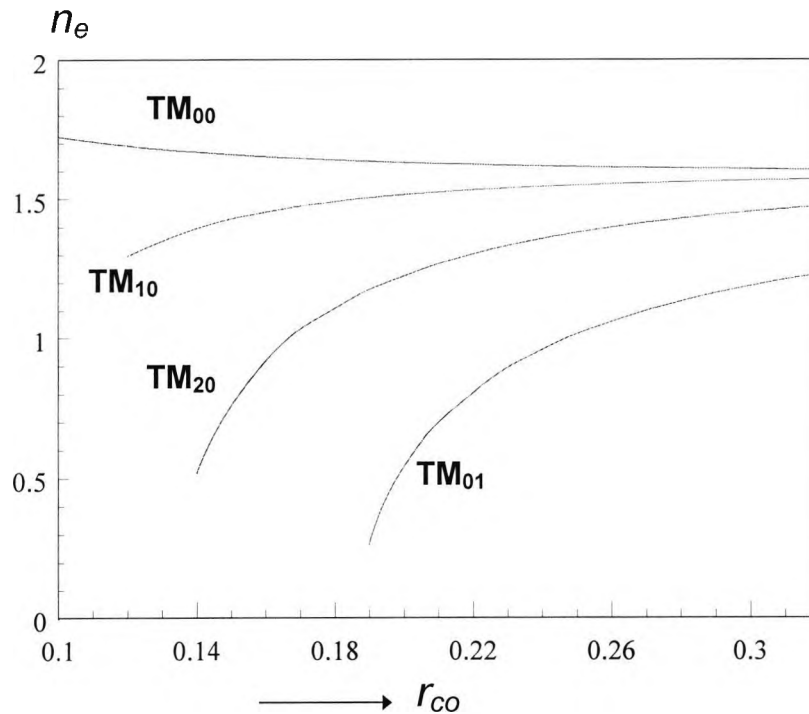


Fig.6.21 Variation of the effective indices with the dielectric core radius of the metal-clad optical fiber for the TM polarized modes.

Figure 6.21 shows the variation of the effective-index, n_e , ($n_e = \beta/k_0$), of the fundamental and the higher order guided optical quasi-TM modes, with the core radius, r_{co} . Here β is the propagation constant and k_0 is the wavenumber. As the core radius is increased, the influence of the metal cladding becomes negligible for the higher order optical modes, and their effective indices tend to reach the refractive index of the core, n_{co} , ($n_{co} = 1.4697$). As the core radius is decreased the effective indices of all the higher order modes decrease and approach the cut-off region, while the effective index of the fundamental TM_{00} mode is increased.

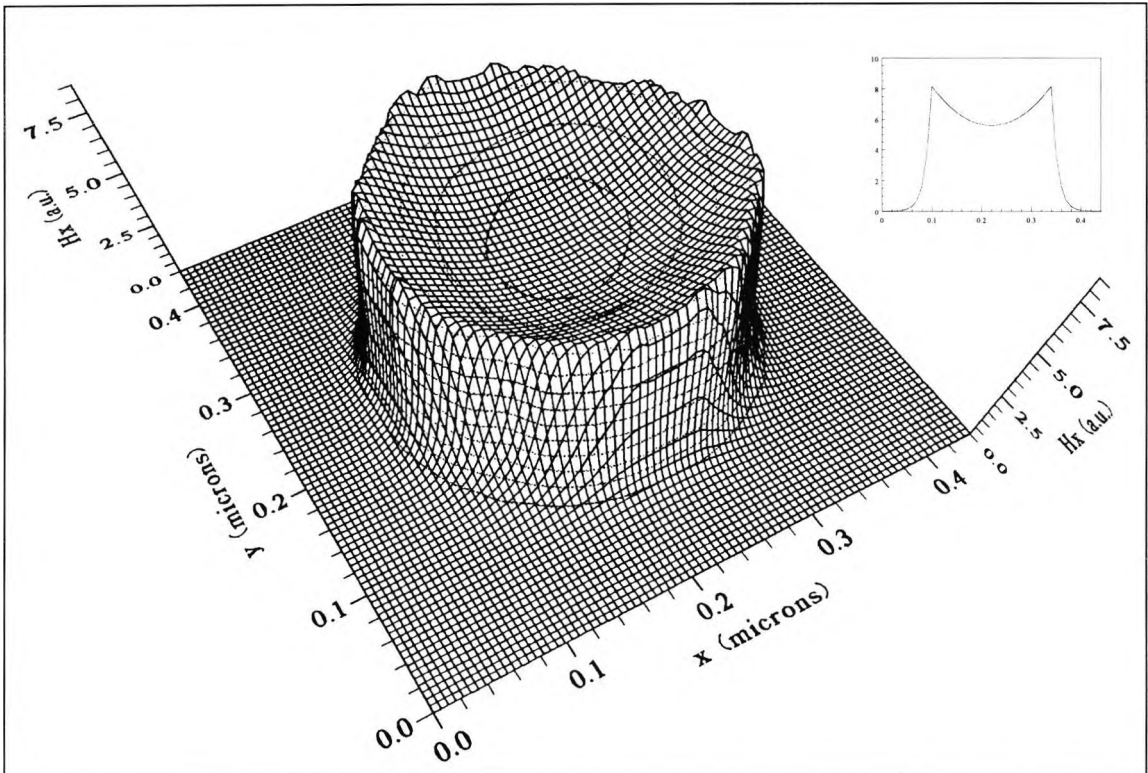


Fig.6.22 Optical field distribution and axial field profile (insert) for the fundamental TM_{00} optical mode of the metal-clad optical fiber, $r_{co}=0.12\mu\text{m}$.

The above behavior of the fundamental TM_{00} optical mode can be explained from its field distribution shown in Fig.6.22 (where the axial field profile is also shown as an insert). The TM_{00} optical mode is a surface plasmon mode, where the field intensity is the highest at the metal/dielectric interface, symmetrically along the circumference of the optical fiber, which reduces to a slightly lower value at the centre region of the dielectric core. As the core radius, r_{co} , increases, the effective index of the TM_{00} mode, decreases, and its limiting value for very large radius, ($r_{co}\rightarrow\infty$), can be approximated with the value of the effective index of a two-layer planar waveguide, n_{pl} , consisting of a single metal/dielectric interface. It is well known that a surface plasmon mode can be supported by a single metal/dielectric interface and its effective index is also higher than the refractive index of the dielectric layer. The effective index of such a planar waveguide, n_{pl} , as described in Section 4.2, with refractive indices of the dielectric-metal layers similar to those of the core/radius regions of the metal-clad fiber respectively, was calculated to be $n_{pl}=1.51853$.

It is also well known that the field is maximum at the metal/dielectric interface and decays exponentially in both the boundary regions. The metal-clad fiber can be considered as a folded-back metal/dielectric interface. The field in the outer metal layer

decays quickly, whereas the slowly decaying field in the dielectric region couples to a similar decaying field at the diametrically opposite side, to form a dip at the centre.

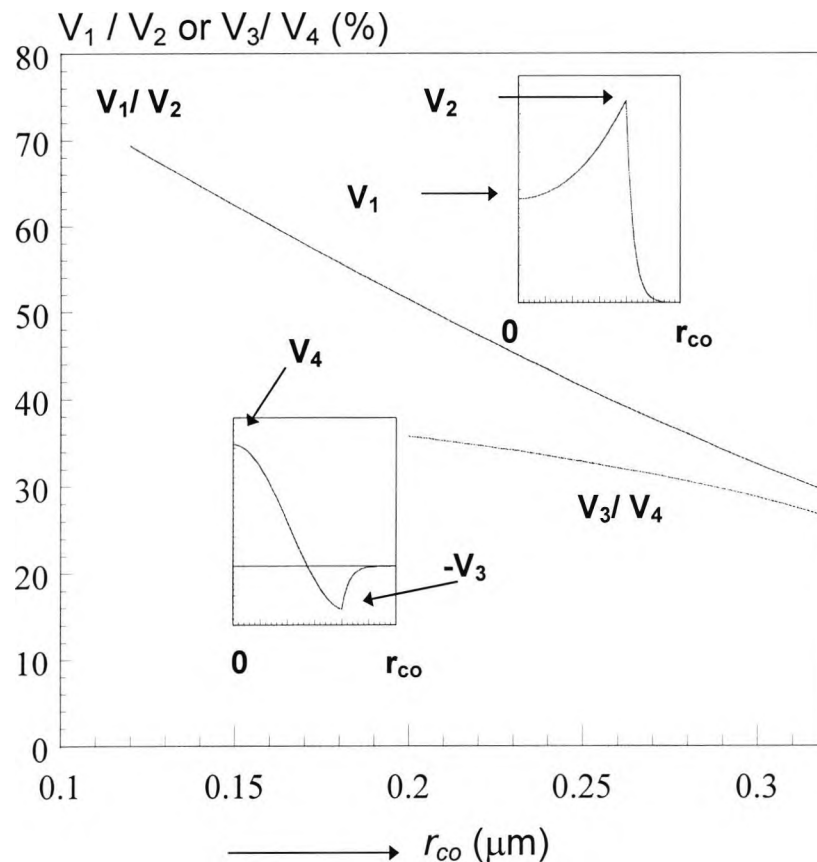


Fig.6.23 Variation of the ratio of the dielectric core to dielectric/metal interface field intensity for the TM_{00} optical mode and the ratio of the dielectric/metal interface to dielectric core field intensity of the TM_{01} optical mode, with the core radius, r_{co} .

The variation of the ratio of the core/interface field intensity, V_1/V_2 , for the TM_{00} optical mode, with the core radius, r_{co} , is shown in Fig.6.23. The field intensity at the metal/dielectric interface along the circumference is always higher than in the centre dielectric core region and as the radius is increased, the ratio decreases, since the field intensity in the core is reduced as this process decouples further two surface plasmon modes at the diametrically opposite ends. When the core radius is decreased, the core field intensity is increased and the optical mode gets flatter at the centre, which is highly desirable for use in NFSOM applications. Since the core region is very small, the effective index of the optical mode is similar in value to the high refractive index experienced with the surface mode at the metal/dielectric interface and its dispersion behaves differently from those of the other higher order optical modes. All the higher order modes are predominantly the fiber modes, perturbed only at the core/cladding dielectric/metal interface.

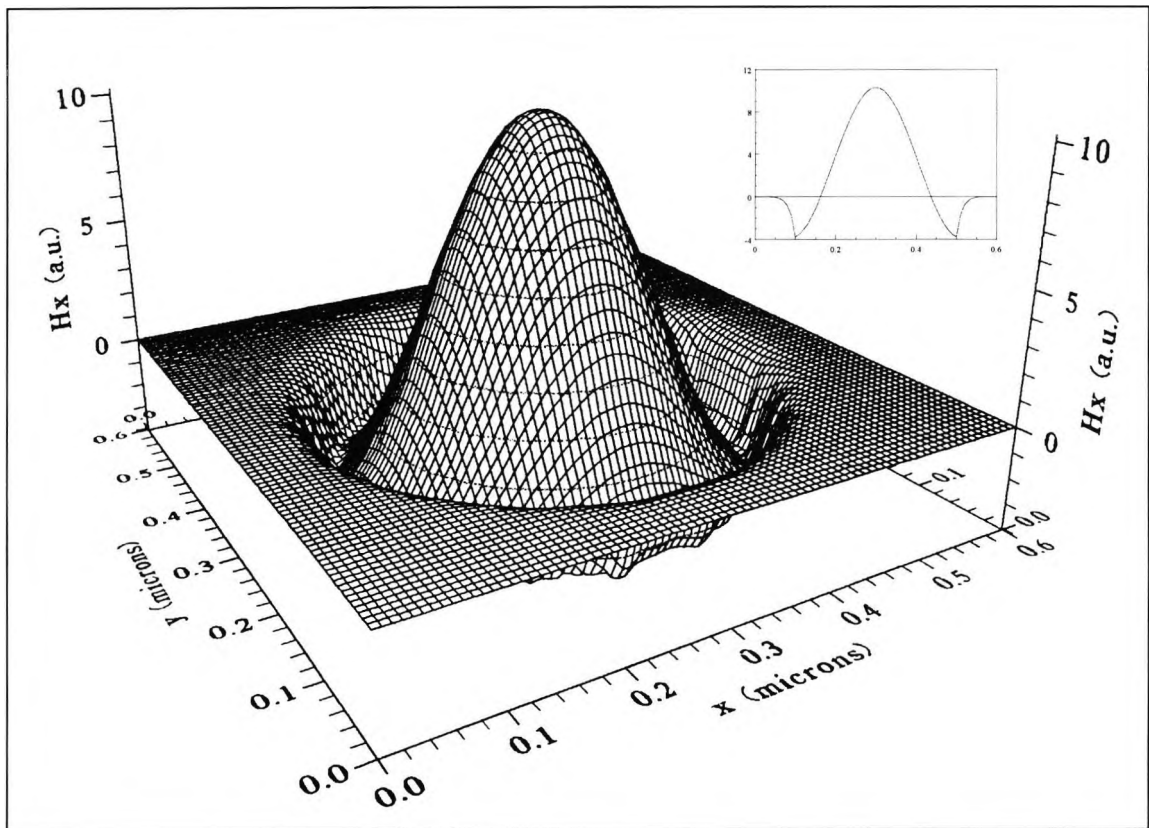


Fig.6.24 Optical field distribution and axial field profile (insert) for the higher order TM_{01} optical mode of the metal-clad optical fiber.

Figure 6.24 shows the field distribution (and the axial field profile in the insert) of the TM_{01} optical mode, which has some desirable features used in NFSOM applications. The field intensity of this optical mode, which is again symmetrical along the circumference, is of higher amplitude in the dielectric core region than at the metal/dielectric interface and it changes sign in the core region near to the metal/dielectric interface. The ratio of the field intensity at interface/core regions, $-V_3/V_4$, shown in Fig.6.23, increases as the radius of the core, r_{co} , is decreased. The ratio curve seems to be flattening for very small values of radius, as it approaches the cut-off, however, never exceeding 40%, indicating no significant change of the ratio at a small radius. Although the field in the dielectric core region reduces as the radius is decreased, it is always higher than the field at the metal/dielectric interface.

The above two optical modes examined, TM_{00} and TM_{01} , which are both symmetric, are used in NFSOM depending on the optical field requirements, whether a strong optical field is required in the centre of the probe, or at the rim of its aperture.

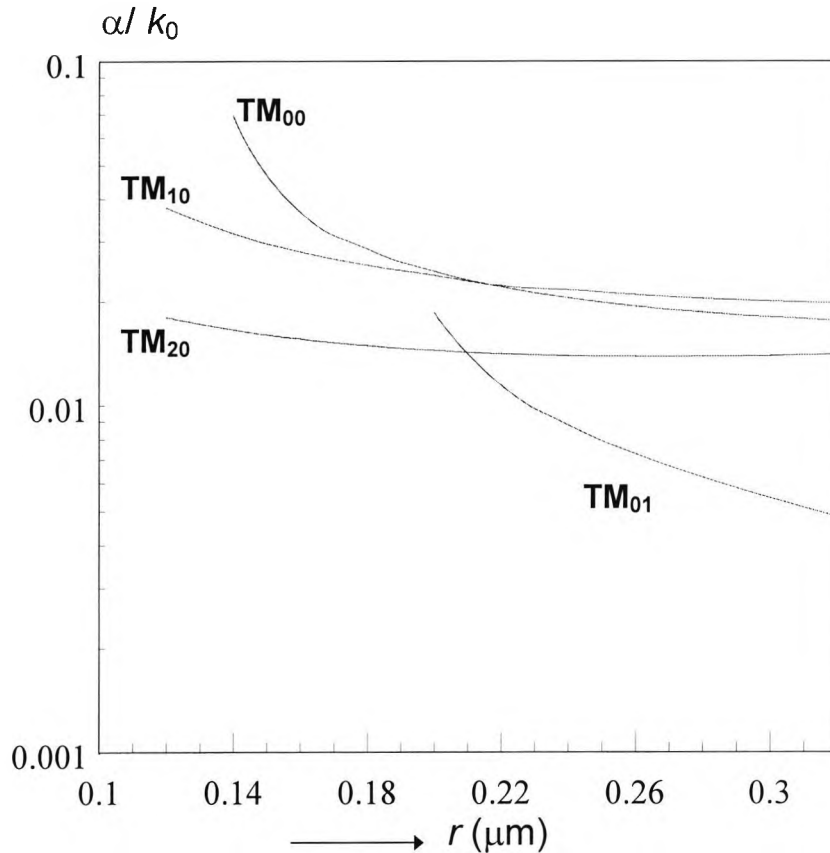
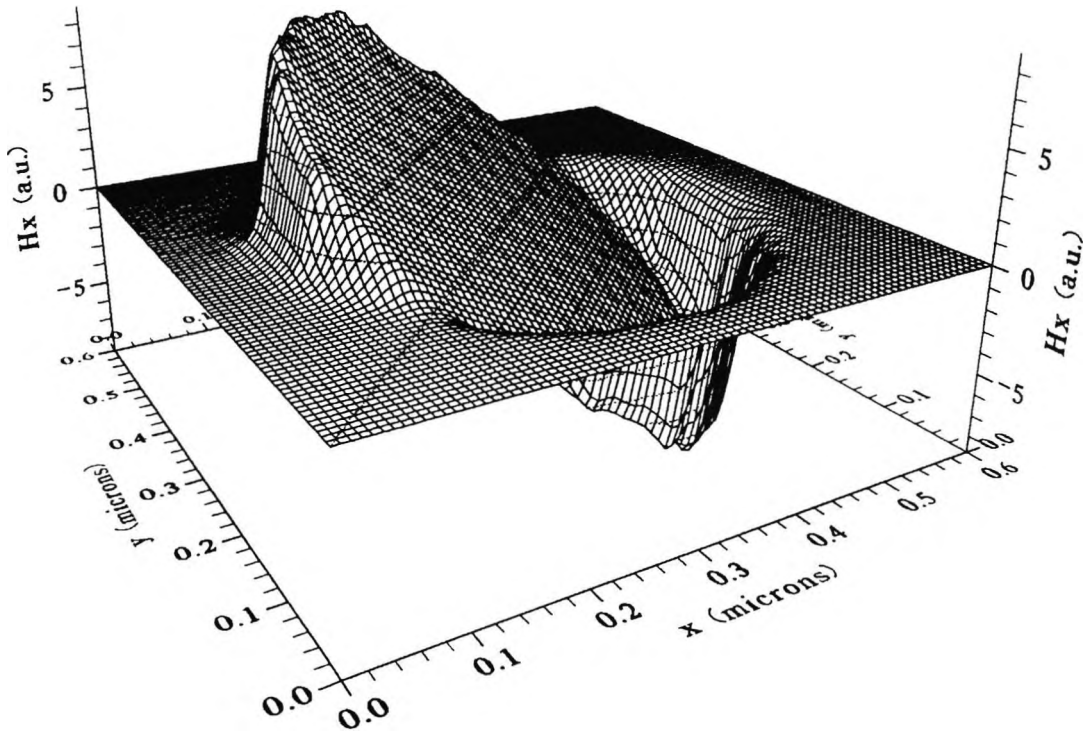


Fig.6.25 Variation of the normalized attenuation constants for the TM polarized modes for the metal-clad optical fiber.

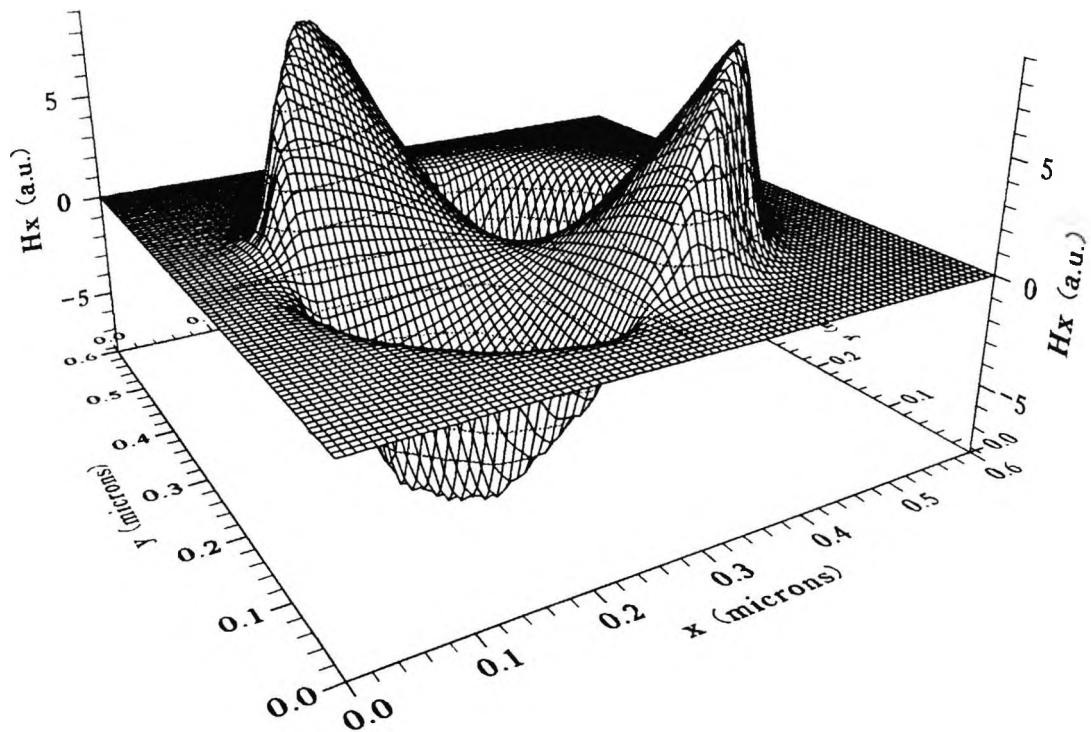
However, these modes also suffer from attenuation, and the normalized attenuation curves for the fundamental and the other higher order TM polarized modes are shown in Fig.6.25. The TM_{00} has the highest normalized attenuation constant for a small radius of the metal-clad optical waveguide, because at this range the optical field is higher at the dielectric/metal interface, and therefore there is more optical field confined in the lossy material, which is the metal-cladding. The total power confinement in the fiber core is also smaller as the core dimension is reduced. All the normalized attenuation curves decrease as the core radius increases since the area of the dielectric core becomes larger than that of the metal-clad area with appreciable field and the optical field in the latter is reducing.

The maximum normalized attenuation constant for the TM modes, in the ranges examined, is that of the TM_{00} , for a core radius $r=0.14\mu\text{m}$, which is about 0.07 ($\approx 78000\text{dB/cm}$). Such a level of attenuation can be considered high, but, according to

Fig.5.9, in Section 5.3.1, where the limit of the perturbation technique is examined, for such attenuation, the accuracy of the approach is not deteriorated by appreciable amount, therefore the results can be considered relatively accurate. On the other hand, the main scope of the analysis of such types of structures, was not the high accuracy of the propagation characteristics, but the classification of the propagating modes and the identification of those modes suitable for NFSOM applications, along with the effect of surface plasmon waves in the above waveguides.



(a)



(b)

Fig.6.26 H_x field distribution for the a) TM_{10} and b) TM_{20} modes for the metal-clad optical fiber.

The TM_{10} and TM_{20} modes, shown in Fig.6.26, have similar characteristics with the normal higher-order fiber modes, with the only difference the sharp field decay, at the exterior of the core circumference, due to the metal/ dielectric boundaries. They have the same field profile along the radial radial direction as the TM_{00} mode: however, they have an azimuthal variation and the variation of their attenuation constant is similar to that of the TM_{01} mode. The TM_{01} optical mode has the lowest attenuation characteristics because, as discussed earlier, the field is more confined in the lossless dielectric core area.

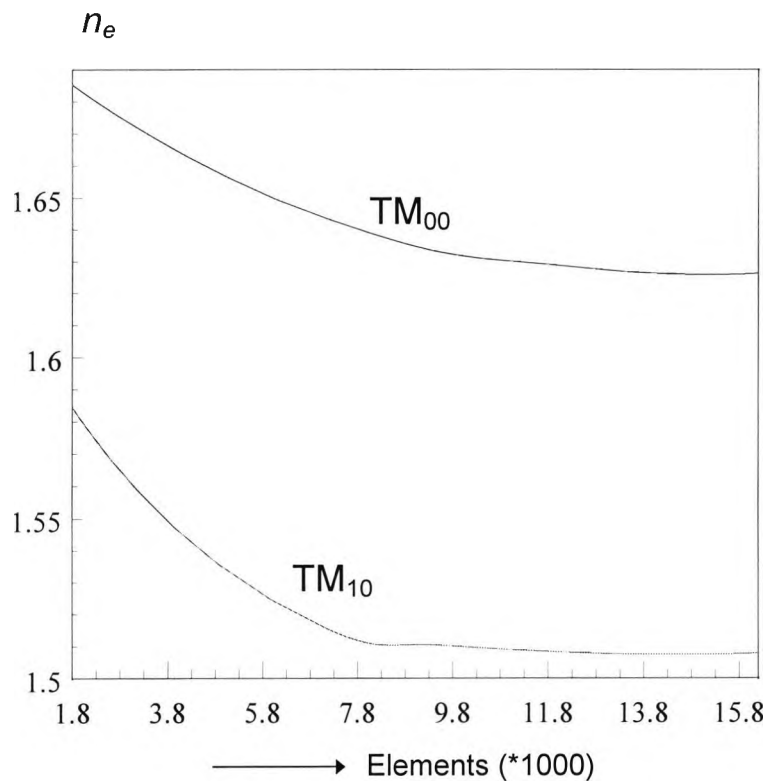


Fig.6.27 Variation of the effective indices of the two TM polarized modes with the mesh refinement for core radius, $r_{co}=0.2\mu\text{m}$.

One of the features of the finite-element method is the potential improvement of the accuracy of the solution by refining the mesh of the cross-sectional area of the waveguide. Mesh refinement tests are always essential in order to investigate the accuracy of the results obtained and to test the convergence of the solution. The variation of the effective index and the normalized attenuation constant, with the increase of the number of finite-elements used, was calculated in this work for the two lower order TM optical modes of the metal-clad optical fiber, at a core radius, r_{co} , of $0.2\mu\text{m}$. From the variation of the effective index of the TM_{00} and TM_{10} optical modes with the mesh refinement, shown in Fig.6.27, it can be seen that both curves tend to converge at the very fine mesh of 16200 finite-elements and the difference from the values obtained for the coarse mesh of 1800 finite-elements is about 3.5% and 5% for the TM_{00} and TM_{10} optical modes respectively. In this work, a mesh of 5000 finite-elements was used for most of the results obtained, which is accurate enough, since the difference from the result obtained with finer mesh, of 16200 finite-elements, is about only about 1%. Solutions obtained with less than 1800 finite-elements are very unstable and the error increases exponentially as the number of finite-elements decreases. On the other hand, as the mesh refinement increases over a certain limit,

the solution may become unstable due to rounding-off errors, but apart from this (which rarely occurs), the only limitations for further mesh refinement are only cpu execution time and the memory capacity of the computer. Typical cpu time required for medium mesh refinement of 5000 elements is about 25 sec, on SUN Classic Workstation.

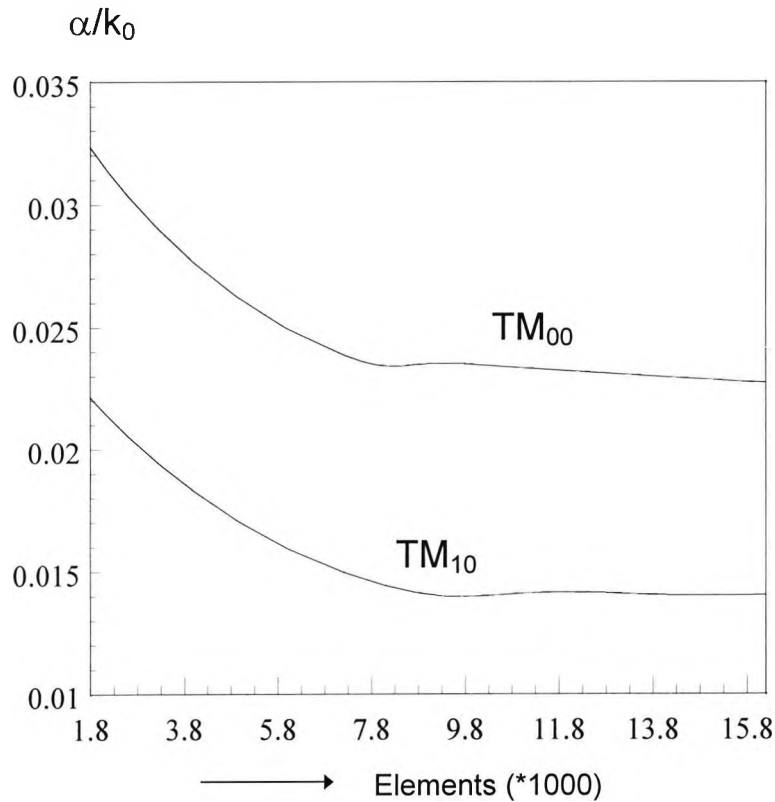


Fig.6.28 Variation of the normalized attenuation constants of the two TM polarized modes with the mesh refinement, for core radius, $r_{co}=0.2\mu\text{m}$.

Additionally, Figure 6.28 shows the variation of the normalized attenuation constants with the mesh refinement for the two lower order TM optical modes. Again, these curves converge at the very fine mesh of 16200 elements and the difference from the solutions calculated with the coarse mesh of 1800 is about 30% and 51% for the TM_{00} and TM_{01} mode. Use of finer mesh division is more important for the loss analysis of such structures than the estimate of the purely real propagation constants.

6.4.3 TE mode analysis

Next, the variation of the effective index with the metal-clad fiber radius, r_{co} , for the fundamental and the higher order TE optical modes is also calculated, and presented in Fig.6.29. It can be seen that the effective indices decrease as the core radius is reduced and all the modes reach a cut-off region after a certain value. It is well known that the TE modes are not much affected by the metal layers and their modal properties are similar to those of other TE modes in dielectric optical waveguides. The fundamental TE_{00} optical mode has a larger effective index and reaches cut-off at a very small core radius, compared to the other higher order TE-polarized modes.

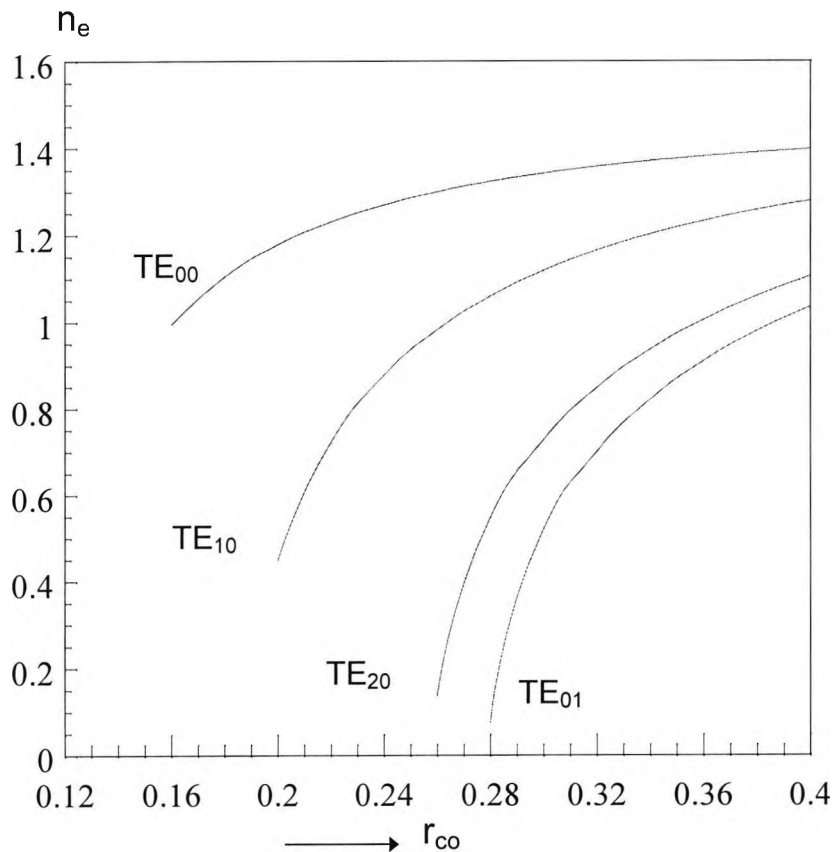


Fig.6.29 Variation of the effective index with the core radius, r_{co} , for the TE polarized modes of the metal-clad optical fiber.

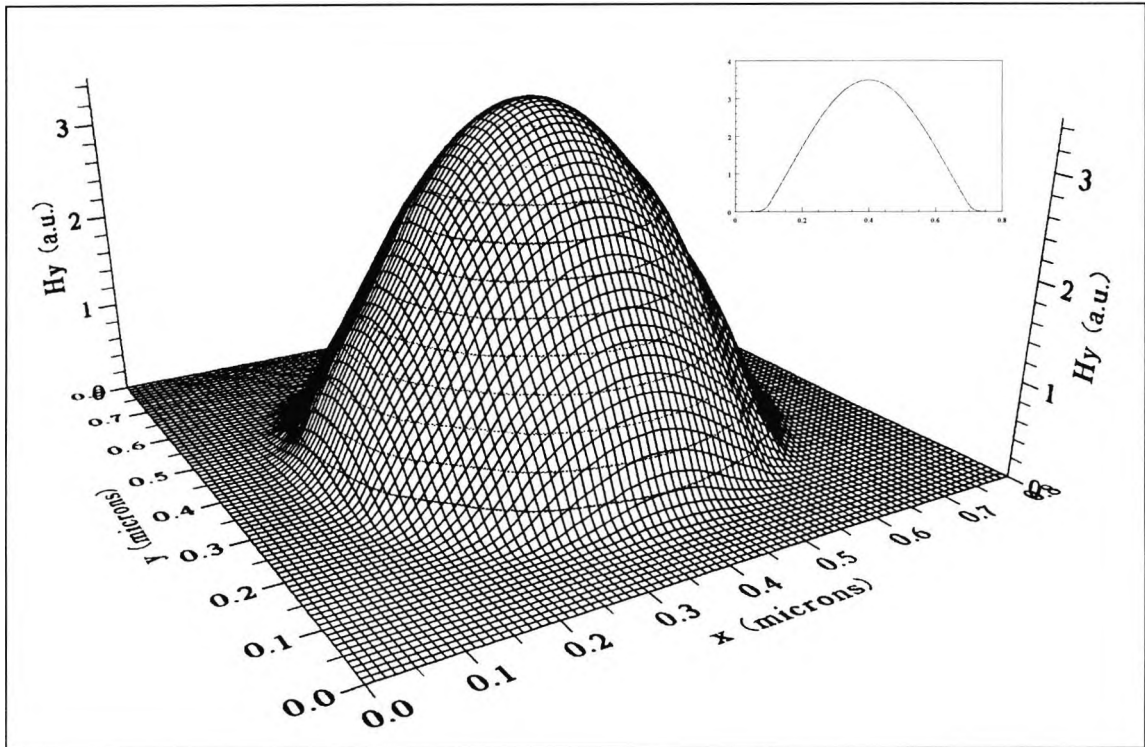


Fig.6.30 Optical field distribution and axial field profile (insert) for the fundamental TE_{00} optical mode of the metal-clad optical fiber.

From the field distribution of the above optical mode, shown in Fig.6.30, and the axial optical field profile (insert), it can be seen that the TE_{00} has characteristics similar to those seen in a standard optical fiber. The field profile is similar to a very well confined fundamental mode in a dielectric waveguide with negligible field in the cladding region. There is a high field intensity at the centre of the dielectric core and the optical field decreases along the radial direction, without any sharp field variations at the metal/dielectric interface. On the other hand, unlike the TM_{00} mode which has a more uniform field profile in the core region with a sharper field decay in the cladding, the TE_{00} does not have a similar feature. The TE_{00} is suitable for use in scanning microscopy, when the scanned object is at the centre of the mode, while the TM_{00} mode is preferable as the object moves at sides, where the field intensity of the above mode is higher.

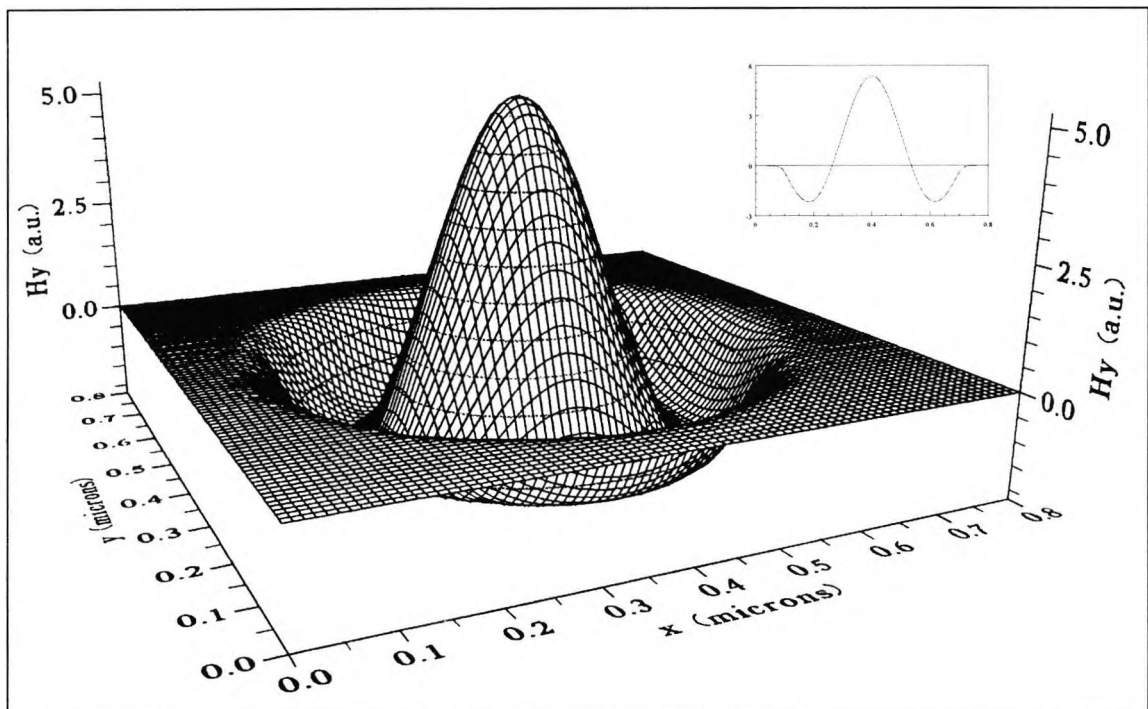


Fig.6.31 Optical field distribution and axial field profile (insert) for the higher order TE_{01} optical mode of the metal-clad optical fiber.

Additionally, the higher order TE_{01} optical mode, which is shown in Fig.6.31 (with the axial optical field profile in the insert), has some interesting features which may be desirable for NFSOM applications, due to their symmetrical shape along the circumference. This mode shows some similarities to the TM_{01} mode illustrated in Fig.6.22, since both the modes have a high field intensity in the centre of the metal-clad optical fiber and an appreciable field at the metal/dielectric boundaries along the circumference. The main difference between them, which can be seen from the axial field profiles in the inserts of the two figures, is the field intensity at the dielectric metal interface. For the TM_{01} mode there is a very sharp change of the field intensity at the interface, while for the TE_{01} optical mode, which is a normal guided fiber mode, since there is no field variation in the metal-cladding, that change is rather smooth.

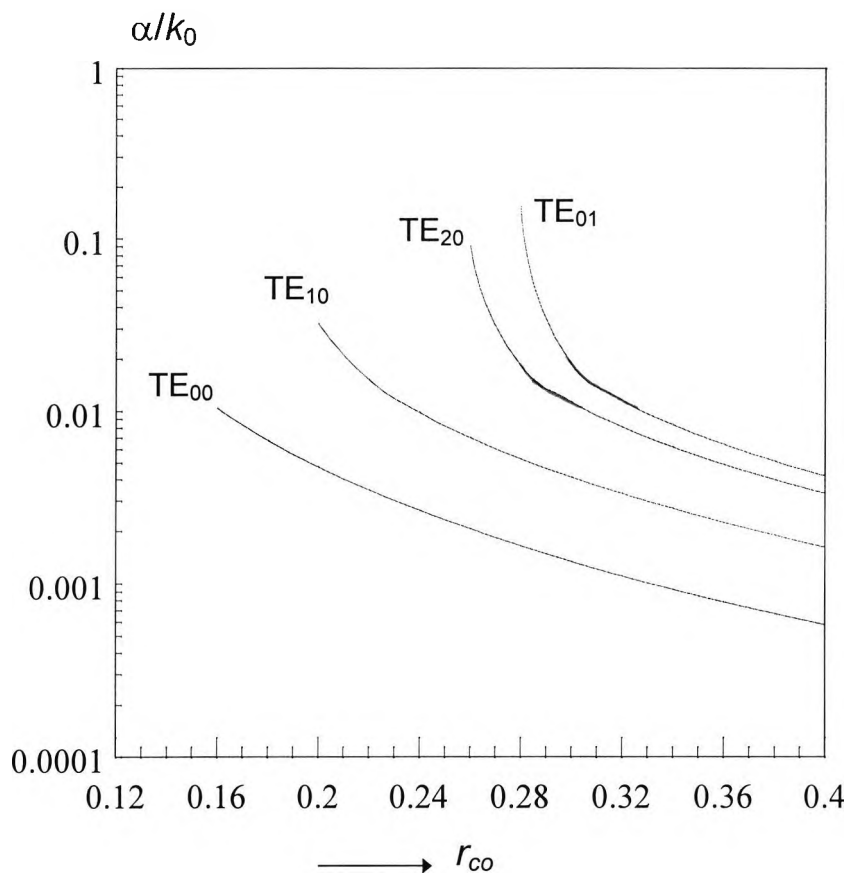
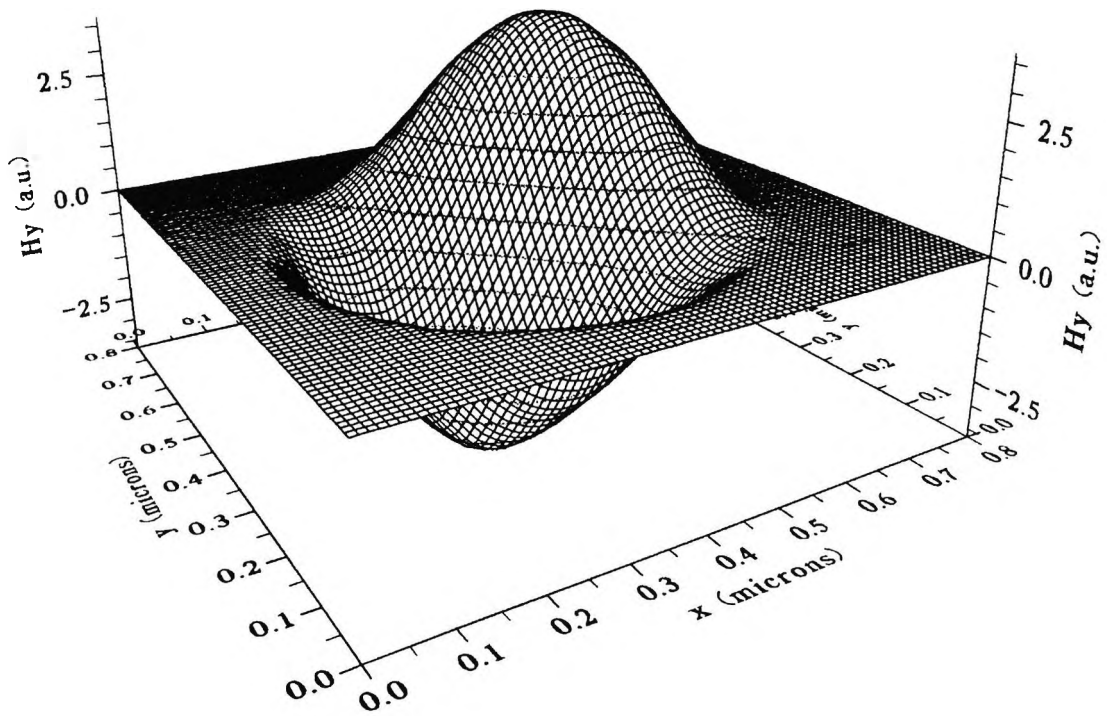
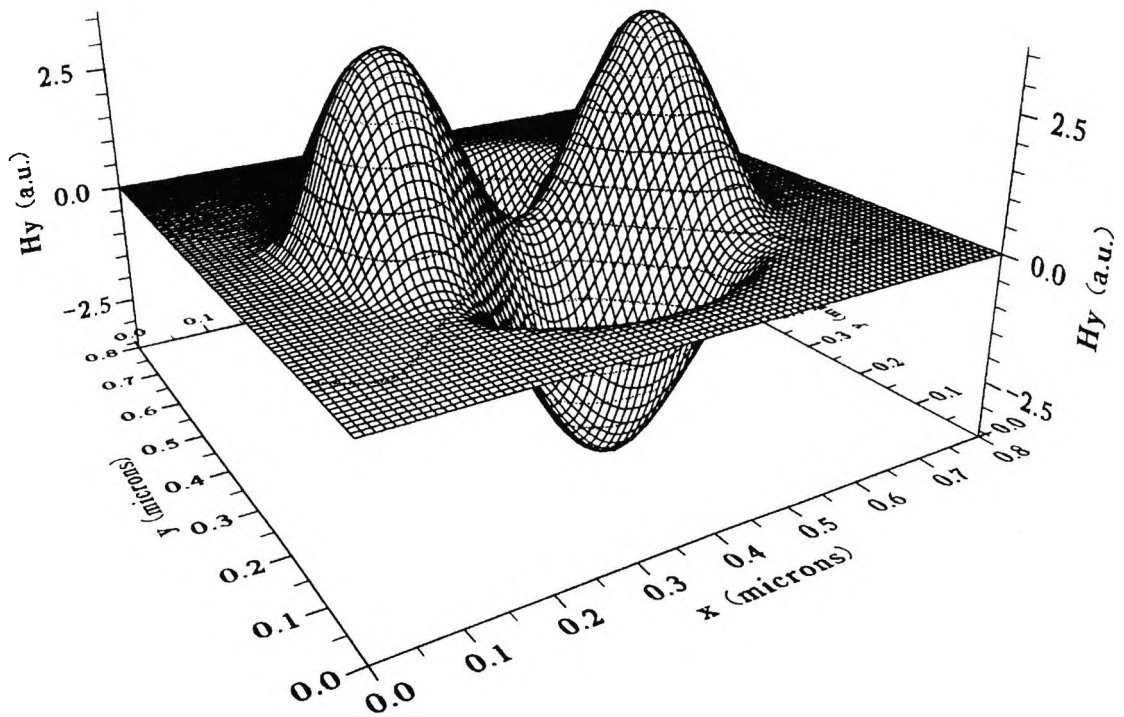


Fig.6.32 Variation of the attenuation constants for the TE polarized modes for the metal-clad optical fiber.

Finally, normalized attenuation curves are plotted for the TE polarized modes, as shown in Fig.6.32. The normalized attenuation constant (α/k_0) decreases for all the TE polarized modes at the similar rate as the core radius increases. The fundamental TE_{00} optical mode has the lowest attenuation characteristics, since there is no appreciable field intensity in the lossy metal-cladding. However the TE_{01} mode has a higher normalized attenuation constant, since there is a finite field intensity at the dielectric/metal interface and inside the metal-cladding.



(a)



(b)

Fig.6.33 H_y optical field distribution for the a) TE_{10} and b) TE_{20} modes for the metal-clad optical fiber.

The TE_{10} and TE_{20} mode profiles, shown in Fig.6.33, are normal higher-order guided fiber modes, since the metal-cladding does not affect their field distributions and they have a similar field profile along the radial direction as the TE_{00} mode. However, their field profiles vary azimuthally and the variation of their attenuation constants are similar to that of the TE_{00} and TE_{01} modes. It can also be noted that the fundamental TE polarized mode, TE_{00} , suffers much lower attenuation than the fundamental TM polarized, TM_{00} , mode, because for the first mode, there is not an appreciable level of field in the lossy metal-cladding.

6.5 Summary

In this chapter the FEM, in conjunction with the perturbation technique, have been used in the analysis of some practical optical waveguides, which exhibit surface plasmon modes due to the metallic elements in their structure. First a composite coupled structure, consisting of an aluminum layer and an InGaAsP rectangular dielectric waveguide, both surrounded by a InP substrate, was studied. The complex propagation characteristics of the first two supermodes of the structures were calculated and the phase matching condition of the above modes has been investigated. Then a TE/TM polarization splitter, based on two parallel rib waveguides, with metal cladding on one of the ribs, was analysed, and the various parameters for the design of an optical polarizer were investigated. Finally, the TM and TE polarized modes of metal-clad optical fiber have been classified and presented and results for propagation and attenuation characteristics have been obtained, by using the finite-element method in conjunction with the perturbation technique. In this approach, the metal-clad optical fibre was solved in Cartesian coordinates with a very fine mesh in order to overcome the problem of representing the curved section along the boundary. With the appropriate boundary conditions, to distinguish the several modes, the problem was solved successfully by using two-fold symmetry in order to achieve a higher accuracy than otherwise. In the above analysis, suitable mode profiles for NFSOM applications were identified and attenuation for the modes was estimated.

7

Discussion and Suggestions for further work

7.1 General conclusions

A general evaluation of the work carried out during the course of this study, in terms of the methodology used and the validity of the results presented, is attempted in the following discussion, which eventually leads to the conclusion that the objectives set out at the beginning of this research were essentially achieved.

An efficient finite element approach, based on the vector and the scalar approximation \mathbf{H} -field variational formulation in conjunction with the perturbation technique, was developed, for the analysis of optical waveguide exhibiting small loss or gain properties. The propagation and attenuation or gain properties of typical optical waveguide structures, incorporating small loss or gain, were investigated by using the above approach and the results presented were compared and found to be in fine agreement with published results for the same structures, obtained by other numerical approaches or experimental work, thus verifying the accuracy of our method. The development of the above numerical algorithm and the establishment of its accuracy, were the prime objective of this work.

An incremental search algorithm was implemented to achieve the solution of the complex transcendental equation, for several types of planar structures, exhibiting loss or gain. The above algorithm was extended to optical waveguides with two-dimensional mode confinement, by developing a complex effective index method (CEIM), where the complex transcendental equation was solved for each transverse direction and polarization respectively. Although the complex effective index method is limited in applications and accuracy when dealing with complicated structures, it can handle any value of loss or gain of optical waveguides with simple geometry. The above feature was utilized to define the limit of the perturbational finite element approach, thus achieving another important objective of this work. The application of the perturbation theory in the solution of optical waveguide problems, is based on the assumption that the propagation constant and the field distribution of a loss-free optical waveguide are perturbed by a *small* amount, in the presence of *small* loss or gain. One of the aims of this study was to investigate the term 'small' in the above assumption, by assigning an upper limit to the perturbation technique, which would determine the maximum overall loss or gain of an optical waveguide, for which the calculations can be considered accurate. This has been achieved by employing the semi-analytical approaches mentioned above, to study the gain and attenuation properties of optical waveguide structures with simple geometry, with the variation of the loss or gain properties of their materials, expressed by the imaginary parts of their refractive indices. The solution of the complex transcendental and the CEIM were used in the analysis of planar optical waveguides and optical waveguides with 2-dimensional confinement, such as rectangular and simple rib waveguides, respectively. The gain and attenuation characteristics of each of the above structures obtained by the semi-analytical method, were plotted and compared with those calculated by the finite element approach with perturbation. The limit of the perturbation technique was then defined as the value of the modal loss or gain at which the two curves diverge. The accuracy of the finite element approach with perturbation for all the structures examined, was shown to deteriorate only when the modal loss or gain was more than 1000 to 10000 dB/cm. Modal loss/gain values below the above range, for which the finite element approach with perturbation has been proved suitable, are typical for the most practical optical waveguide applications.

The gain/attenuation constant for several guided wave devices with elements that exhibit loss or gain in their material properties has also been calculated by an approximate approach developed, which uses the imaginary part of the refractive index

in these regions and the field confinement factor. The results obtained by the above approach were compared with those calculated by using the finite element method with perturbation, for different types of optical waveguide structures. The accuracy of the approximate method was found quite satisfactory in cases where the field is well confined in the area where either gain or loss properties exist, and the gain/attenuation properties can be calculated without applying perturbation or solving directly the complex eigenvalue equation. However, when the confinement factor is smaller or gain and loss exist simultaneously in different regions of the structure, care should be taken in the use of the approximate method.

The accurate modelling of optical waveguides for certain industrial applications, in order to determine the fabrication tolerances in the various dimensions, requires efficient numerical techniques, because analytical approaches are inadequate to deal with the complex geometry and the variation of the dielectric parameters of such structures. The study of the several numerical approaches available for the solution of optical waveguide problems, in order to determine the most suitable approach for such analysis, was one of the objectives of the present work. The earlier work in the field, has shown that the finite element method is a very powerful and accurate numerical approach, capable of handling a wide range of optical waveguide problems, such as the arbitrary cross-section waveguide, including open and odd-shaped boundaries, the arbitrary refractive index profile and the use of anisotropic materials. The vector \mathbf{H} -field variational formulation of the approach, is more preferable than other variational formulations, since the magnetic field \mathbf{H} is naturally continuous across the dielectric interfaces and the associated natural boundary condition is that of an electric wall, which is also convenient to consider in most practical applications. The appearance of non-physical solutions by the application of the \mathbf{H} -field formulation, can be easily treated by the use of the penalty coefficient technique, in which the constraint $\nabla \cdot \mathbf{H} = 0$ is imposed to eliminate effectively the spurious modes.

In the present work, a finite element approach based on the \mathbf{H} -field variational formulation was implemented, for the solution of the several types of loss-free optical waveguides, in order to obtain the propagation constant and nodal field values of the unperturbed guided optical modes. A numerical technique based on the perturbation theory was then implemented, in which the calculated unperturbed parameters of the loss-free waveguides and the perturbed dielectric properties of their materials due to loss or gain were taken into consideration, in order to calculate the overall

attenuation/gain modal characteristics of the above structures, in the presence of loss or gain media. The finite element approach in conjunction with the perturbation technique provides an integrated, accurate and efficient CAD package for the analysis of several types of optical waveguide structures. The above approach combines the ability of the finite element method to analyze accurately optical waveguides with any shape, refractive index profile and anisotropy, and the simplicity and efficiency of the perturbation technique in the determination of the loss and gain characteristics of such structures.

Among the limited methods that can handle optical waveguides exhibiting loss or gain properties, probably one of the most accurate numerical approaches is the finite element approach based on the variational formulation in terms of the transverse components of the magnetic field, also known as the H_t formulation. The above formulation can solve directly the complex eigenvalue problem with reduced number of field components, it is free of spurious modes, since the $\nabla \cdot \mathbf{H} = 0$ constraint is automatically imposed, and can calculate the loss/gain characteristics of optical waveguides with any amount of loss or gain in the dielectric materials. However, the majority of the available complex solvers, which are required for the solution of the complex eigenvalue equation in the above approach, are based on dense matrix algorithms, which are inefficient in terms of computational time and memory requirements. Even with the use of efficient sparse matrix solvers, the presence of complex matrices, requires a great number of iterations to achieve convergence of both the real and imaginary parts, which is time consuming. By contrast, the finite element approach, based on the \mathbf{H} -field formulation, offers a more efficient alternative approach for the solution of optical waveguides with loss/gain characteristics. The two approaches were compared, in terms of accuracy, computational time memory requirements and applicability, for different types of optical waveguides, with two-dimensional field confinement. The results calculated by the \mathbf{H} -field formulation with perturbation, were compared with those obtained by the H_t formulation and found in fine agreement, therefore the accuracy of the \mathbf{H} -field formulation can be considered satisfactory. The efficient sparse real matrix solver required less computational time than the analogous complex matrix solver, for the same number of elements, because the latter needed more iterations to achieve convergence of the solution, which also resulted to more memory space to perform the calculations. The spurious modes observed in the \mathbf{H} -field formulation, can also be eliminated quite easily, by the penalty coefficient technique, and the loss/gain ranges, for which the \mathbf{H} -field formulation with

perturbation is applicable, are the typical loss/gain levels for practical optical waveguide applications.

A finite element approach based on the scalar approximation of the vector **H**-field formulation and the perturbation technique has also been developed in this work. In general, the scalar approximation is a very popular approach, suitable for weakly guiding structures, where the refractive index difference between the guiding region and the substrate or cladding is small, which is the case for the most of the practical optical waveguides. In the present work, the scalar approximation with the perturbation technique has been extensively used for the determination of the gain/attenuation properties of all the types of optical waveguides considered. It has been shown that the above approach was highly accurate in the analysis of simple optical waveguide structures, when compared with the full-vector formulation and other numerical methods. Even in the analysis of structures with complicated geometry, the accuracy of the scalar approach did not deteriorate by a considerable amount. The high efficiency in terms of computational time and memory requirements, and the accuracy, which can be increased further with more mesh refinement without appreciable cost in time and memory space, makes the scalar approximation preferable in certain applications. In some industrial applications, where high accuracy is required in the determination of the fabrication tolerances in the device dimensions, the full vector formulation is certainly more suitable, while in cases where only the characterization of the basic propagation and attenuation/gain properties of the structure is aimed, the scalar formulation is adequate. The choice of the most appropriate approach, depends on the trade off between the high efficiency, in terms of computational time and memory requirements and the high accuracy, and the type of the application.

The knowledge gained from the determination of the fundamental properties of the simple optical waveguide structures, which are the basic elements of the several integrated optics applications, enabled the extension of the analysis to optical waveguides with more complex geometry, whose solutions are of significant practical interest in the optoelectronics industry, thus achieving the final objective of this work. The surface plasmon and attenuation properties of the several planar optical waveguides with metallic elements were thoroughly investigated, and utilized to characterize optical waveguides with two-dimensional confinement which exhibit such properties and have a wide applicability in practical optoelectronic devices. The modal

analysis of certain types of composite coupled structures, where surface plasmon modes and attenuation characteristics take place due to the interaction of metal and dielectric elements, was carried out by using the finite element approach with the perturbation technique. The optimization of certain parameters of such structures that contribute to the phase matching between the guides, is very important in optical polarizer design. The modal and attenuation characteristics, of sub-micron metal-clad fibers were also determined, by using the perturbation approach, and certain optical modes, suitable for near-field scanning microscopy (NFSOM), were identified. NFSOM is one of the recent advances of the lightwave technology, with a wide range of applications in bio-medical science, exhibiting higher efficiency and resolution than other conventional microscopy techniques. Further, the gain and attenuation properties of several semiconductor laser waveguides, which form the basis of integrated optics applications, have been determined. The effect of the variation of the carrier density in the active layers of the above structures, which is very important in the optical properties of semiconductor lasers, has also been investigated. Finally, the effect of the lossy metal electrodes on the optical properties of an electro-optic directional coupler modulator has been examined.

The development, testing and verification of an accurate and efficient numerical algorithm for the modelling of different types of optical waveguides is a very important task and a major part of this work is devoted in achieving that objective, by developing several approaches dealing with the solution of optical waveguides incorporating loss or gain. Apart from the development of a tool for solving certain optical waveguide problems, the application of the approach to practical optical devices is equally important, and therefore a great part of the present work has been focused in utilizing the developed methods for the characterization of several practical optical waveguide structures, like those mentioned above. Such applications, not only enrich the knowledge on practical problems that may arise during the optimization of the several devices, but also boosts up the interest of the optoelectronics industry, in using the package for the determination of the several fabrication tolerances in similar devices.

7.2 Suggestions for future work

It has been shown that the finite element method developed, based on the vector H -field variational formulation, and the perturbation technique, is a highly

efficient and accurate numerical modal analysis approach for the determination of the propagation and attenuation/gain properties of several types of practical optical waveguides. A further application of the present work could be the extension of the approach to the characterization of some more recent advances in integrated optics technology, such as surface-plasmon devices and erbium doped fibers. This work has moved towards that direction, by analyzing certain types of integrated laser structures, optical polarizers, modulators and metal-clad fibers, but apart from the modal analysis, some applications require efficient propagation algorithms, which was not the task of the present research.

A further improvement, in terms of computational method, could be the implementation of an H_t formulation, for the analysis of loss-free structures, which can utilize the existing real symmetric sparse solver, and the application of the perturbation approach to the obtained unperturbed solutions, to extend the approach to optical waveguides with loss or gain. Such an approach could be efficient, and free of spurious solutions, but certain problems could arise in the development of the formulation in terms of compatibility with the existing solver.

Some other modern computer languages and packages, which offer better graphical representation, can also be considered in the future for the modelling of optical waveguides, instead of the FORTRAN language. Of course, that would require additional research in the mathematical field for the development of new solvers to perform the calculations. The development of CAD-type user friendly package would also assist research workers in the area of optoelectronics.

APPENDIX A

Evaluation of the element matrices

The elements of the matrices $[A]_e$ and $[B]_e$ in equations (2.63) and (2.65) can be evaluated by expressing the derivatives of the shape function vectors in terms of the shape function coefficients, as determined in (2.57) and (2.58), and by performing the integration of the shape functions with the aid of equation (2.64).

The 9x9 real symmetric $[A]_e$ element matrix (2.63) can be analyzed into nine, 3x3 sub-matrices, formed by the operations between the shape function vectors and their derivatives as:

$$[A]_e = \frac{1}{\epsilon_0} \begin{bmatrix} \iint_{\Omega_e} \left[\beta^2 \{N\} \{N\}^T + \frac{\partial \{N\}}{\partial y} \frac{\partial \{N\}^T}{\partial y} \right] dx dy & \iint_{\Omega_e} \left[\frac{\partial \{N\}}{\partial y} \frac{\partial \{N\}^T}{\partial x} \right] dx dy & \iint_{\Omega_e} \left[\beta \{N\} \frac{\partial \{N\}^T}{\partial x} \right] dx dy \\ \iint_{\Omega_e} \left[\frac{\partial \{N\}}{\partial y} \frac{\partial \{N\}^T}{\partial x} \right] dx dy & \iint_{\Omega_e} \left[\beta^2 \{N\} \{N\}^T + \frac{\partial \{N\}}{\partial x} \frac{\partial \{N\}^T}{\partial x} \right] dx dy & \iint_{\Omega_e} \left[\beta \{N\} \frac{\partial \{N\}^T}{\partial y} \right] dx dy \\ \iint_{\Omega_e} \left[\beta \{N\} \frac{\partial \{N\}^T}{\partial x} \right] dx dy & \iint_{\Omega_e} \left[\beta \{N\} \frac{\partial \{N\}^T}{\partial y} \right] dx dy & \iint_{\Omega_e} \left[\frac{\partial \{N\}}{\partial y} \frac{\partial \{N\}^T}{\partial y} + \frac{\partial \{N\}}{\partial x} \frac{\partial \{N\}^T}{\partial x} \right] dx dy \end{bmatrix} \quad (\text{A.1})$$

Some typical calculations for the various sub-matrices are shown below

$$\begin{aligned}
& \iint_{\mathcal{E}} \left[\beta^2 \{N\} \{N\}^T + \frac{\partial \{N\}}{\partial y} \frac{\partial \{N\}^T}{\partial y} \right] dx dy = \\
& = \iint_{\mathcal{E}} \left[\beta^2 \begin{Bmatrix} N_1 \\ N_2 \\ N_3 \end{Bmatrix} \{N_1 \ N_2 \ N_3\} + \begin{Bmatrix} a_3 \\ a_6 \\ a_9 \end{Bmatrix} \{a_3 \ a_6 \ a_9\} \right] dx dy = \\
& = \iint_{\mathcal{E}} \left[\beta^2 \begin{bmatrix} N_1^2 & N_1 N_2 & N_1 N_3 \\ N_2 N_1 & N_2^2 & N_2 N_3 \\ N_3 N_1 & N_3 N_2 & N_3^2 \end{bmatrix} + \begin{bmatrix} a_3^2 & a_3 a_6 & a_3 a_9 \\ a_6 a_3 & a_6^2 & a_6 a_9 \\ a_9 a_3 & a_9 a_6 & a_9^2 \end{bmatrix} \right] dx dy = \quad (A.2) \\
& = \begin{bmatrix} (\beta^2 / 6 + a_3^2) & (\beta^2 / 12 + a_3 a_6) & (\beta^2 / 12 + a_3 a_9) \\ (\beta^2 / 12 + a_6 a_3) & (\beta^2 / 6 + a_6^2) & (\beta^2 / 12 + a_6 a_9) \\ (\beta^2 / 12 + a_9 a_3) & (\beta^2 / 12 + a_9 a_6) & (\beta^2 / 6 + a_9^2) \end{bmatrix} \times Area
\end{aligned}$$

$$\iint_{\mathcal{E}} - \frac{\partial \{N\}}{\partial y} \frac{\partial \{N\}^T}{\partial x} = \iint_{\mathcal{E}} - \begin{Bmatrix} a_3 \\ a_6 \\ a_9 \end{Bmatrix} \{a_2 \ a_5 \ a_8\} dx dy = - \begin{bmatrix} a_3 a_2 & a_3 a_5 & a_3 a_8 \\ a_6 a_2 & a_6 a_5 & a_6 a_8 \\ a_9 a_2 & a_9 a_5 & a_9 a_8 \end{bmatrix} \times Area \quad (A.3)$$

$$\iint_{\mathcal{E}} \left[\beta \{N\} \frac{\partial \{N\}^T}{\partial y} \right] dx dy = \iint_{\mathcal{E}} \left[\beta \begin{Bmatrix} N_1 \\ N_2 \\ N_3 \end{Bmatrix} \{a_3 \ a_6 \ a_9\} \right] dx dy = \beta \begin{bmatrix} a_3 & a_6 & a_9 \\ 3 & 6 & 6 \\ a_3 & a_6 & a_9 \\ 6 & 3 & 6 \\ a_3 & a_6 & a_9 \\ 6 & 6 & 3 \end{bmatrix} \times Area \quad (A.4)$$

All the other elements of the matrix $[A]_e$ are determined by different combinations of the above calculations.

There is only one type of non zero 3x3 sub-matrix in the element matrix $[B]_e$ (2.65), which can be evaluated as:

$$[B]_e = \iint_{\mathcal{E}} \left[\{N\} \{N\}^T \right] dx dy = \iint_{\mathcal{E}} \begin{bmatrix} N_1^2 & N_1 N_2 & N_1 N_3 \\ N_2 N_1 & N_2^2 & N_2 N_3 \\ N_3 N_1 & N_3 N_2 & N_3^2 \end{bmatrix} dx dy = \begin{bmatrix} 1/6 & 1/12 & 1/12 \\ 1/12 & 1/6 & 1/12 \\ 1/12 & 1/12 & 1/6 \end{bmatrix} \times Area \quad (A.5)$$

The shape function coefficients in all of the above calculations are determined in terms of the coordinates of the triangular elements, by cyclic exchange of the subscripts in (2.43).

APPENDIX B

Calculations for a four-layer planar optical waveguide

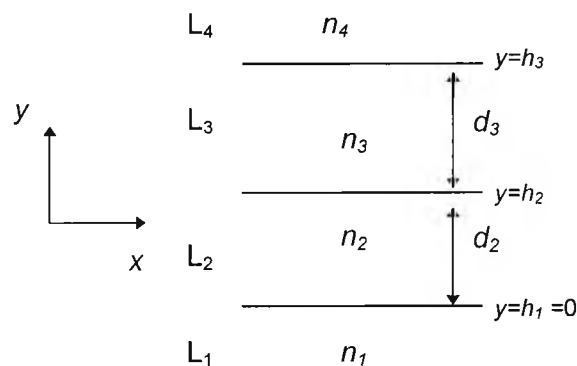


Fig.B.1 Four-layer planar waveguide

A four-layer planar optical waveguide, as shown in Fig.B.1, is being considered, where n_1 to n_4 , h_1 to h_4 and d_1 to d_2 , are the refractive indices the heights and the thickness of the various layers respectively. By considering TE analysis, where the non-vanishing fields are E_x , H_y and H_z , and by applying boundary conditions (3.22) and (3.23) for the transverse components, E_x and H_z , the following expressions are derived:

a) For $y = h_1 = 0$,

$$A_1 + B_1 - A_2 - B_2 = 0 \quad (\text{B.1})$$

$$A_1 p_1 + B_1 p_1 - A_2 p_2 + B_2 p_2 = 0 \quad (\text{B.2})$$

b) For $y=h_2$,

$$A_2 \exp(p_2 d_2) + B_2 \exp(-p_2 d_2) - A_3 - B_3 = 0 \quad (\text{B.3})$$

$$A_2 p_2 \exp(p_2 d_2) - B_2 p_2 \exp(-p_2 d_2) - A_3 p_3 + B_3 p_3 = 0 \quad (\text{B.4})$$

c) For $y=h_3$,

$$A_3 \exp(p_3 d_3) + B_3 \exp(-p_3 d_3) - A_4 - B_4 = 0 \quad (\text{B.5})$$

$$A_3 p_3 \exp(p_3 d_3) - B_3 p_3 \exp(-p_3 d_3) - A_4 p_4 + B_4 p_4 = 0 \quad (\text{B.6})$$

The above equations can be expressed in matrix form as:

$$[D][A_1 \ B_1 \ A_2 \ B_2 \ A_3 \ B_3 \ A_4 \ B_4]^T = [0] \quad (\text{B.7})$$

where $[D]$ is the matrix containing the coefficients of the constants (A_1 to A_4 and B_1 to B_4) and can be evaluated as:

$$[D] = \begin{bmatrix} 1 & 1 & -1 & -1 & 0 & 0 & 0 & 0 \\ p_1 & -p_1 & -p_2 & p_2 & 0 & 0 & 0 & 0 \\ 0 & 0 & \exp(p_2 d_2) & \exp(-p_2 d_2) & -1 & -1 & 0 & 0 \\ 0 & 0 & p_2 \exp(p_2 d_2) & -p_2 \exp(-p_2 d_2) & -p_3 & p_3 & 0 & 0 \\ 0 & 0 & 0 & 0 & \exp(p_3 d_3) & \exp(-p_3 d_3) & -1 & -1 \\ 0 & 0 & 0 & 0 & p_3 \exp(p_3 d_3) & -p_3 \exp(-p_3 d_3) & -p_4 & p_4 \end{bmatrix} \quad (\text{B.8})$$

APPENDIX C

Calculations for the scalar FEM with perturbation

By discretizing the cross section of an arbitrarily shaped optical waveguide into first order triangular elements, and expressing the field vectors \mathbf{H}_0 and \mathbf{E}_0 in terms of their components along each direction, the perturbation formula (3.32) can be written as:

$$\alpha = \frac{\omega \sum_e \varepsilon'_e \iint_{\Delta} (E_x^2 + E_y^2 + E_z^2) dx dy}{2 \sum_e \iint_{\Delta} (E_x H_y + E_y H_x) dx dy} \quad (\text{C.1})$$

For the TE modes, $E_y = E_z = H_x = 0$, therefore, by using Maxwell's equations for the planar optical waveguide (3.1-3.2) to express the magnetic field components, the perturbation formula can be written in terms of E_x , which is the dominant field component as:

$$\alpha = \frac{k_0^2 \sum_e \varepsilon'_e \iint_{\Delta} (E_x^2) dx dy}{2\beta \sum_e \iint_{\Delta} (E_x^2) dx dy} \quad (\text{C.2})$$

E_x can be expressed, in terms of the shape function vector, $\{N\}$ (2.52), for each triangular element as:

$$E_x = \{N\}^T \{E_x\}_e \quad (C.3)$$

By re-arranging the matrices, the perturbation formula can then be written as:

$$\begin{aligned} \alpha &= \frac{k_0^2 \sum_e \varepsilon'_e \iint_{\Delta} (\{E_x\}_e^T \{N\} \{N\}^T \{E_x\}_e) dx dy}{2\beta \sum_e \iint_{\Delta} (\{E_x\}_e^T \{N\} \{N\}^T \{E_x\}_e) dx dy} = \\ &= \frac{1}{2\beta} \frac{\{E_x\}^T \left[\sum_e k_0^2 \varepsilon'_e \iint_{\Delta} \{N\} \{N\}^T dx dy \right] \{E_x\}}{\{E_x\}^T \left[\sum_e \iint_{\Delta} \{N\} \{N\}^T dx dy \right] \{E_x\}} \end{aligned} \quad (C.4)$$

where $\{E_x\}$ is the nodal field vector for E_x .

Equation (C.4) can then be expressed in matrix form as:

$$\alpha = \frac{1}{2\beta} \frac{\{E_x\}^T [K'] \{E_x\}}{\{E_x\}^T [B] \{E_x\}} \quad (C.5)$$

By using (2.64), matrices $[B]$ and $[K']$ can be defined as:

$$[B] = \sum_e \iint_{\Delta} \begin{bmatrix} N_1^2 & N_1 N_2 & N_1 N_3 \\ N_2 N_1 & N_2^2 & N_2 N_3 \\ N_3 N_1 & N_3 N_2 & N_3^2 \end{bmatrix} dx dy = \sum_e \begin{bmatrix} 1/6 & 1/12 & 1/12 \\ 1/12 & 1/6 & 1/12 \\ 1/12 & 1/12 & 1/6 \end{bmatrix} \times Area_e \quad (C.6)$$

$$[K'] = \sum_e \iint_{\Delta} k_0^2 \varepsilon'_e \begin{bmatrix} N_1^2 & N_1 N_2 & N_1 N_3 \\ N_2 N_1 & N_2^2 & N_2 N_3 \\ N_3 N_1 & N_3 N_2 & N_3^2 \end{bmatrix} dx dy = \sum_e k_0^2 \varepsilon'_e \begin{bmatrix} 1/6 & 1/12 & 1/12 \\ 1/12 & 1/6 & 1/12 \\ 1/12 & 1/12 & 1/6 \end{bmatrix} \times Area_e \quad (C.7)$$

For the TM modes, $H_y = H_z = E_x = 0$, therefore, by using Maxwell's equations (3.4 and 3.5) to express the electric field components, the perturbation formula can be written in terms of the H_x dominant field component as:

$$\alpha = \frac{\sum_e \frac{\epsilon'_e}{\epsilon_e^2} \iint_{\Delta} \beta H_x^2 + \left(\frac{\partial H_x}{\partial y} \right)^2 dx dy}{2\beta \sum_e \iint_{\Delta} \frac{1}{\epsilon_e} H_x^2 dx dy} \quad (\text{C.8})$$

The H_x field component, for a triangular element, can be expressed in terms of the shape function vector $\{N\}$ as:

$$H_x = \{N\}^T \{H_x\}_e \quad (\text{C.9})$$

By using the above transformation, the perturbation formula can be expressed as:

$$\alpha = \frac{\sum_e \frac{\epsilon'_e}{\epsilon_e} \iint_{\Delta} \left(\beta \{N\}^T \{H_x\}_e \{N\}^T \{H_x\}_e + \frac{\partial \{N\}^T}{\partial y} \{H_x\}_e \frac{\partial \{N\}^T}{\partial y} \{H_x\}_e \right) dx dy}{2\beta \sum_e \frac{1}{\epsilon_e} \iint_{\Delta} (\{N\}^T \{H_x\}_e \{N\}^T \{H_x\}_e) dx dy} \quad (\text{C.10})$$

By re-arranging the matrices, (C.10) can be written as:

$$\alpha = \frac{\sum_e \frac{\epsilon'_e}{\epsilon_e} \iint_{\Delta} \left(\{H_x\}_e^T \left[\beta \{N\} \{N\}^T + \frac{\partial \{N\}}{\partial y} \frac{\partial \{N\}^T}{\partial y} \right] \{H_x\}_e \right) dx dy}{2\beta \sum_e \frac{1}{\epsilon_e} \iint_{\Delta} (\{H_x\}_e^T \{N\} \{N\}^T \{H_x\}_e) dx dy} \quad (\text{C.11})$$

Then, the perturbation formula can be formulated in matrix notation as:

$$\alpha = - \frac{1}{2} \frac{\{H_x\}^T [L] \{H_x\}}{\{H_x\}^T [B'] \{H_x\}} \quad (\text{C.12})$$

$$[L] = (\beta[M] + \frac{1}{\beta}[Q]) \quad (\text{C.13})$$

$$[M] = \sum_e \iint_{\Delta} \frac{\epsilon'_e}{\epsilon_e^2} \{N\} \{N\}^T dx dy \quad (\text{C.14})$$

$$[Q] = \sum_e \iint_{\Delta} \frac{\epsilon_e'}{\epsilon_e^2} \{N_y\} \{N_y\}^T dx dy \quad (C.15)$$

$$\{N_y\} = \frac{\partial \{N\}}{\partial y} \quad (C.16)$$

where $\{H_x\}$ is the nodal field vector for H_x .

By using (2.64) for the estimation of the surface integrals and, (2.57) and (2.58) for the coefficients of the derivatives of the shape function vectors, matrices $[L]$ and $[B]$ in the perturbation formula (C.12) can be evaluated as:

$$[L] = \sum_e \left(\frac{\epsilon_e'}{\epsilon_e} \begin{bmatrix} \frac{\beta}{6} + \frac{1}{\beta} a_3^2 & \frac{\beta}{12} + \frac{1}{\beta} a_3 a_6 & \frac{\beta}{12} + \frac{1}{\beta} a_3 a_9 \\ \frac{\beta}{12} + \frac{1}{\beta} a_6 a_3 & \frac{\beta}{6} + \frac{1}{\beta} a_6^2 & \frac{\beta}{12} + \frac{1}{\beta} a_6 a_9 \\ \frac{\beta}{12} + \frac{1}{\beta} a_9 a_3 & \frac{\beta}{12} + \frac{1}{\beta} a_9 a_6 & \frac{\beta}{6} + \frac{1}{\beta} a_9^2 \end{bmatrix} \times Area_e \right) \quad (C.17)$$

$$[B'] = \sum_e \frac{1}{\epsilon_e} \begin{bmatrix} a_3^2 & a_3 a_6 & a_3 a_9 \\ a_6 a_3 & a_6^2 & a_6 a_9 \\ a_9 a_3 & a_9 a_6 & a_9^2 \end{bmatrix} \times Area_e \quad (C.18)$$

APPENDIX D

Calculations for the full H-field vector FEM with perturbation

In the perturbation formula (3.32), the Electric field, \mathbf{E}_0 can be analyzed in terms of its components along each direction as:

$$\mathbf{E}_0 = \hat{x}E_x + \hat{y}E_y - j\hat{z}E_z \quad (\text{D.1})$$

where E_x , E_y , and E_z are the Electric field components, and \hat{x} , \hat{y} and \hat{z} , the normal unit vectors in each direction respectively.

Then, the square of the magnitude of the electric field, $|\mathbf{E}_0|^2$, is defined by:

$$|\mathbf{E}_0|^2 = E_x^2 + E_y^2 + E_z^2 \quad (\text{D.2})$$

By using the Maxwell's equations, the Electric field components can be expressed in terms of the magnetic field components in the perturbation formula, as it has been shown in equation (3.53). By expressing the magnetic field in terms of the shape function vectors, by using (3.54), and expanding the square terms, the numerator of the perturbation formula (3.53) can then be expressed as:

$$\frac{1}{\omega} \sum_e \frac{\epsilon'}{\epsilon^2} \iint_{\Delta} \left[\begin{aligned} & \{H_y\}_e^T \beta^2 \{N\} \{N\}^T \{H_y\}_e + \{H_z\}_e^T \{N_y\} \{N_y\}^T \{H_z\}_e - \{H_y\}_e^T 2\beta \{N\} \{N_y\}^T \{H_z\}_e + \\ & + \{H_z\}_e^T \{N_x\} \{N_x\}^T \{H_z\}_e + \{H_x\}_e^T \beta^2 \{N\} \{N\}^T \{H_x\}_e - \{H_x\}_e^T 2\beta \{N\} \{N_x\}^T \{H_z\}_e + \\ & - \{H_x\}_e^T \{N_y\} \{N_y\}^T \{H_x\}_e - \{H_y\}_e^T \{N_x\} \{N_x\}^T \{H_y\}_e + \{H_x\}_e^T 2\{N_y\} \{N_x\}^T \{H_y\}_e \end{aligned} \right] dx dy \quad (D.3)$$

where $\{N\}$, is the shape function vector (2.52), and $\{N_x\}$ and $\{N_y\}$ are defined by:

$$\{N_x\} = \frac{\partial \{N\}}{\partial x}, \quad \{N_y\} = \frac{\partial \{N\}}{\partial y} \quad (D.4)$$

By considering common terms and re-arranging, (D.3) can be written as:

$$\frac{1}{\omega} \sum_e \frac{\epsilon'}{\epsilon^2} \iint_{\Delta} \left[\begin{aligned} & \{H_x\}_e^T [\beta^2 \{N\} \{N\}^T - \{N_y\} \{N_y\}^T] \{H_x\}_e + \{H_y\}_e^T [\beta^2 \{N\} \{N\}^T - \{N_x\} \{N_x\}^T] \{H_y\}_e + \\ & + \{H_z\}_e^T [\{N_y\} \{N_y\}^T + \{N_x\} \{N_x\}^T] \{H_z\}_e - \{H_x\}_e^T 2\beta \{N\} \{N_x\}^T \{H_z\}_e \\ & - \{H_y\}_e^T 2\beta \{N\} \{N_y\}^T \{H_z\}_e + \{H_x\}_e^T 2\{N_y\} \{N_x\}^T \{H_y\}_e \end{aligned} \right] dx dy \quad (D.5)$$

Alternatively, the square of the magnitude of the electric field, $|\mathbf{E}_0|^2$, in the perturbation formula (3.32), can be expressed as:

$$|\mathbf{E}_0|^2 = \mathbf{E}_0 \mathbf{E}_0 \quad (D.6)$$

where \mathbf{E}_0 can be written in matrix notation as:

$$|\mathbf{E}_0| = \begin{bmatrix} E_x \\ E_y \\ -jE_z \end{bmatrix} = \frac{1}{\omega\epsilon} \begin{bmatrix} 0 & \beta & -j\frac{\partial}{\partial y} \\ -\beta & 0 & j\frac{\partial}{\partial x} \\ j\frac{\partial}{\partial y} & -j\frac{\partial}{\partial x} & 0 \end{bmatrix} \begin{bmatrix} H_x \\ H_y \\ -jH_z \end{bmatrix} \quad (D.7)$$

By discretising the waveguide cross-section into triangular and expressing the magnetic field components for each element in terms of the shape function vector $\{N\}$, equation (D.7) can be written as:

$$|E_0| = \frac{1}{\omega \epsilon} \begin{bmatrix} \{0\}^T & \beta\{N\}^T & -\{N_y\}^T \\ -\beta\{N\}^T & \{0\}^T & \{N_x\}^T \\ j\{N_y\}^T & -j\{N_x\}^T & \{0\}^T \end{bmatrix} \begin{Bmatrix} \{H_x\} \\ \{H_y\} \\ \{H_z\} \end{Bmatrix} \quad (D.8)$$

By using the above equation (D.8), the numerator of the perturbation formula (3.32) can be expressed as:

$$\begin{aligned} & \frac{1}{\omega} \sum_e \frac{\epsilon_e'}{\epsilon_e^2} \iint_{\Delta} \{E_0\}_e \{E_0\}_e = \\ & = \frac{1}{\omega} \sum_e \frac{\epsilon_e'}{\epsilon_e^2} \iint_{\Delta} \begin{Bmatrix} \{H_x\}_e \\ \{H_y\}_e \\ \{H_z\}_e \end{Bmatrix}^T \begin{bmatrix} \{0\} & -\beta\{N\} & j\{N_y\} \\ \beta\{N\} & \{0\} & -j\{N_x\} \\ -\{N_y\} & \{N_x\} & \{0\} \end{bmatrix} \begin{bmatrix} \{0\}^T & \beta\{N\}^T & -\{N_y\}^T \\ -\beta\{N\}^T & \{0\}^T & \{N_x\}^T \\ j\{N_y\}^T & -j\{N_x\}^T & \{0\}^T \end{bmatrix} \begin{Bmatrix} \{H_x\}_e \\ \{H_y\}_e \\ \{H_z\}_e \end{Bmatrix} = \\ & = \frac{1}{\omega} \sum_e \frac{\epsilon_e'}{\epsilon_e^2} \iint_{\Delta} \begin{Bmatrix} \{H_x\}_e \\ \{H_y\}_e \\ \{H_z\}_e \end{Bmatrix}^T \begin{bmatrix} [GFX] & [DYDX] & [GNDX] \\ [DXDY] & [GFY] & [GNDY] \\ [GDXN] & [GDYN] & [GFZ] \end{bmatrix} \begin{Bmatrix} \{H_x\}_e \\ \{H_y\}_e \\ \{H_z\}_e \end{Bmatrix} = \\ & \frac{1}{\omega} \sum_e \frac{\epsilon_e'}{\epsilon_e^2} \iint_{\Delta} \{H\}_e^T [C] \{H\}_e \end{aligned} \quad (D.9)$$

where,

$$[GFX] = [\beta^2 \{N\}^T \{N\} - \{N_y\}^T \{N_y\}] \quad (D.10)$$

$$[GFY] = [\beta^2 \{N\}^T \{N\} - \{N_x\}^T \{N_x\}] \quad (D.11)$$

$$[GFZ] = [\{N_y\}^T \{N_y\} + \{N_x\}^T \{N_x\}] \quad (D.12)$$

$$[GNDX] = [-\beta\{N\}^T \{N_x\}] \quad (D.13)$$

$$[GNDY] = [-\beta\{N\}^T \{N_y\}] \quad (D.14)$$

$$[DYDX] = [\{N_y\}^T \{N_x\}] \quad (D.15)$$

$$[GDXN] = [GNDX]^T \quad (D.16)$$

$$[GDYN] = [GNDY]^T \quad (D.17)$$

$$[DXDY] = [DYDX]^T \quad (D.18)$$

The denominator of the perturbation formula (3.32) can be expressed as:

$$2 \sum_e \iint_b \begin{bmatrix} \hat{x} & \hat{y} & \hat{z} \\ E_x & E_y & E_z \\ H_x & H_y & H_z \end{bmatrix} \cdot \hat{Z} d\Omega = \quad (D.15)$$

$$= 2 \sum_e \iint_b [E_x H_y - E_y H_x] d\Omega$$

By expressing the Electric field in terms of the Magnetic field, via Maxwell's equations the denominator of the perturbation formula (3.53) can be expressed in a discretized form, in terms of the shape function vector $\{N\}$, as:

$$\frac{2}{\omega} \sum_e \frac{1}{\epsilon_e} \iint_{\Delta} \left\{ \begin{aligned} & \{H_y\}_e^T \beta \{N\} \{N\}^T \{H_y\}_e - \{H_z\}_e^T \{N\} \{N_y\}^T \{H_y\}_e + \\ & - \{H_z\}_e^T \{N\} \{N_x\}^T \{H_x\}_e + \{H_x\}_e^T \beta \{N\} \{N\}^T \{H_x\}_e \end{aligned} \right\} dx dy \quad (D.16)$$

By formulating into matrix notation, the numerator of the perturbation formula (3.54) can be then written as:

$$2 \sum_e \frac{1}{\epsilon_e} \{H\}^T [D] \{H\} \quad (D.17)$$

where, the element matrix $[D]$ is given by:

$$[D] = \iint_{\Delta} \begin{vmatrix} \beta[G] & [0] \\ [0] & \beta[G] \\ -[X] & -[Y] \end{vmatrix} dx dy \quad (D.18)$$

where

$$[G] = \{N\} \{N\}^T \quad (D.19)$$

$$[X] = \{N_x\} \{N\}^T \quad (D.20)$$

$$[Y] = \{N_y\} \{M\}^T \quad (\text{D.21})$$

The surface integrals in both the numerator and the denominator, involving shape function vectors can be evaluated by using (2.64), (2.57) and (2.58) in a similar way as it has been done in Appendix C, for the scalar case.

APPENDIX E

List of Publications by the Author Relevant to the Thesis

1. C. Themistos, B.M.A. Rahman and K.T.V. Grattan (1994). Finite Element Analysis for Lossy Optical Waveguides by Using Perturbation Techniques. IEEE Photonics Technology Letters 6 (4): 537-539.
2. C. Themistos, B.M.A. Rahman and K.T.V. Grattan (1995). Finite element characterization of optical waveguides with modal loss/gain. Invited Paper, Progress in electromagnetics Symposium, p.393, Seattle, USA.
3. C. Themistos, B.M.A. Rahman, A. Hadjicharalambous and K.T.V. Grattan (1995). Loss/Gain Characterization of Optical Waveguides. Journal of Lightwave Technology 13 (8): 1760-1765.
4. C. Themistos, B.M.A. Rahman and K.T.V. Grattan (1995). Finite-element analysis of surface-plasmon modes for lossy optical waveguides by the use of perturbation techniques. Applied Optics 34 (33): 7695-7701.

5. C. Themistos, B.M.A. Rahman and K.T.V. Grattan (1997). Accurate Solutions of Sub-micron Metal Clad Optical Fibers for Optical Scanning. *Institute of Physics Congress '97*, Leeds, p.134, 24-27, March.
6. C. Themistos, A. Hadjicharalambous, B.M.A Rahman, K.T.V. Grattan, and F.A. Fernandez. Gain/Loss Characterisation of Optical Waveguide and Semiconductor Laser Structures. IEE Proceedings -Optoelectronics, in press.
7. C. Themistos, B.M.A. Rahman, K.T.V. Grattan. Accurate solutions for sub-micron metal-clad optical fibers for optical scanning microscopes. J. Nondestructive testing and evaluation, in press.
8. M. Rajarajan, C. Themistos, B.M.A. Rahman, K.T.V. Grattan (1997). Characterization of metal clad TE/TM mode splitters using the finite element method. Journal of Lightwave Technology 15 (12): 2264-2269.
9. N. Anwar, C. Themistos, B.M.A. Rahman, K.T.V. Grattan, "Design considerations for an electro-Optic directional coupler modulator", submitted to Journal of Lightwave Technology.
10. C.Themistos, B.M.A. Rahman and K.T.V. Grattan, "TM/TE solutions for sub-micron lossy metal-clad optical fibres using the finite element method," submitted to IEE Proceedings-Optoelectronics.
11. C.Themistos, B.M.A. Rahman and K.T.V. Grattan. Analysis of lossy TE/TM modes in metal-clad optical waveguides", submitted to Applied Optics.

REFERENCES

- Abid Z.E., Johnson K.L. and Gopinath A. (1993). Analysis of dielectric guides by vector transverse magnetic field finite elements. Journal of Lightwave Technology 11 (10): 1545-1548.
- Adams M.J. (1981). An introduction to optical waveguides. (New York: John Wiley & Sons).
- Al-Bader S.J., and Imtaar M. (1992). TM-polarized surface-plasma modes on metal-coated dielectric cylinders. Journal of Lightwave Technology 10 (7): 865-872.
- Albrecht P., Hamacher M., Heidrich H., Hoffman D., Nolting H.-P. and Weinert C.M. (1990). TE/TM mode splitters on InGaAsP/InP. IEEE Photonics Technology Letters 2 (2): 114-115.
- Alexander F.B., Bird V.R., Carpenter D.R., Manley G.W., McDermott P.S., Peloke J.R., Quinn H.F., Riley R.J. and Yetter L.R. (1964). Spontaneous and stimulated infra-red emission from Indium Phosphide Arsenide diodes. Applied Physics Letters 4 (1): 13-15.
- Alferov Zh.I., Andreev V.M., Portnoi E.L. and Trukkan M.K. (1970). AlAs-GaAs heterojunction injection lasers with a low-room temperature threshold. Soviet Physics Semiconductors 3: 1107-1110.
- Arakawa Y. and Yariv A. (1985). Theory of gain, modulation response, and spectral linewidth in AlGaAs Well Lasers. IEEE Journal of Quantum Electronics QE-21 (10): 1666-1674.
- Aubourg M., Villotte J.P., Godon F. and Garault Y. (1983). Finite element analysis of lossy waveguides - Application to microstrip lines on semiconductor substrate. IEEE Transactions on Microwave Theory and Techniques MTT-31 (4): 326-331.
- Austin M.W. (1984). Theoretical and experimental investigation of GaAs/GaAlAs and n/n⁺ GaAs Rib waveguides. Journal of Lightwave Technology LT-2 (5): 688-694.
- Bandyopadhyay A. and Basu P.K. (1994). A new variational method of incorporating loss in the analysis of coupled multiple-quantum-well three-

- dimensional waveguides. IEEE Journal of Quantum Electronics 30 (9): 2026-2033.
- Barcelos S., Zervas M.N. and Russell P.St.J. (1995). Selective excitation of fiber-modes using surface plasmons. IEEE Photonics Technology Letters 7 (9): 1051-1053.
 - Batchman T.E. and McMillan K.A. (1977). Measurement on positive-permittivity metal-clad waveguides. IEEE Journal of Quantum Electronics QE-13 (4):187-192.
 - Bates R.H.T., James J.R., Gallett I.N.L. and Millar R.F. (1973). An overview of point matching. Radio Electronics Engineer 43 (3): 193-200.
 - Benson T.M., Bozeat R.J. and Kendall P.C. (1992). Rigorous effective index method for semiconductor rib waveguides. IEE Proceedings-J 139 (1): 67-70.
 - Benson T.M., Bozeat R.J. and Kendall P.C. (1994). Complex finite difference method applied to the analysis of semiconductor lasers. IEE Proceedings-Optoelectronics 141 (2): 97-101.
 - Benson T.M., Kendall P.C., Martin M.A. and Stern M.S. (1992). Polarisation correction applied to scalar analysis of semiconductor rib waveguides. IEE Proceedings-J 139 (1): 39-41.
 - Berini P. and Wu K. (1996). Modelling lossy anisotropic dielectric waveguides with the method of lines. IEEE Transactions on Microwave Theory and Techniques 44 (5): 749-759.
 - Berk A.D. (1956). Variational principles for electromagnetic resonators and waveguides. IRE Transactions on Antennas Propagation AP-4: 104-111.
 - Betzig E., Isaacson M. and Lewis A. (1987). Collection mode near-field scanning optical microscopy. Applied Physics Letters 51 (25): 2088-2090.
 - Bierwirth K. Schulz N. and Arndt F. (1986). Finite-difference analysis of rectangular dielectric waveguide structures. IEEE Transactions on Microwave Theory and Techniques MTT-34 (11): 1104-1114.
 - Boardman A.D. (1982). Electromagnetic surface modes. (New York: John Willey & Sons).
 - Bond W.L., Cohen B.G., Leite R.C.C. and Yariv A. (1963) Observation of the dielectric waveguide mode of light propagation in p-n junctions. Applied Physics Letters 2 (3):57-59.
 - Borchert B. and Stegmuller B. (1990). Yield analysis of distributed feedback metal-clad ridge-waveguide laserdiodes for coherent system applications. IEE Proceedings-J 137 (4): 265-272.

- Brauer J.R. (1988). What every engineer should know about finite element analysis. (New York: Marcel Dekker.).
- Brodberg B. and Lindgren S. (1984). Refractive index of $\text{In}_{1-x}\text{Ga}_x\text{As}_y\text{P}_{1-y}$ layers and InP in the transparent wavelength region. Journal of Applied Physics 55 (9): 3376-3381.
- Buah P.A., Rahman B.M.A. and Grattan K.T.V. (1997). Numerical study of soliton switching in active three-core non-linear fiber couplers. Journal of Quantum Electronics 33 (5): 874-878.
- Burke S.V. (1990). Spectral index method applied to rib and strip-loaded directional couplers. IEE Proceedings-J 137 (1): 7-10.
- Burke S.V., Benson T.M., Bozeat R.J. and Martin M.A. (1993). Comparison of finite difference and spectral index methods for analyzing semiconductor waveguides incorporating regions of optical loss or gain. In: Proceedings IEEE IPR Conference, Palm Springs CA, pp.35-38.
- Butler J.F., Calawa A.R., Phelan R.J., Harman T.C., Strauss A.J. and Rediker R.H. (1964). PbTe diode laser. Applied Physics Letters 5 (4): 75-77.
- Buus J. (1984). Application of the effective index method to nonplanar structures. IEEE Journal of Quantum Electronics QE-20 (10): 1106-1109.
- Casey H.C. and Panish M.B. (1978). Heterostructure lasers, Part A: Fundamental principles. (New York: Academic Press).
- Cheung P., Silveira M. and Gopinath A. (1995). Analysis of lossy dielectric guides by transverse magnetic field finite elements method. Journal of Lightwave Technology 13 (9): 1873-1875.
- Chiang K.S. (1994). Review of numerical and approximate methods for the modal analysis of general optical dielectric waveguides. Bell Systems Technical Journal 26: S113-S134.
- Chiang K.S. (1996). Analysis of the effective-index method for the vector modes of rectangular-core dielectric waveguides. IEEE Transactions on Microwave Theory and Techniques 44 (5):692-700.
- Chiang K.S., Lo K.M., Kwok K.S. (1996). Effective-index method with built-in perturbation correction for integrated optical waveguides. Journal of Lightwave Technology 14 (2): 223-228.
- Clarricoats P.J.B. and Slinn K.R. (1965). Complex modes of propagation in dielectric loaded circular waveguide. Electronics Letters 1 (5): 145-146.
- Clough R.W. (1960). The finite element method in plane stress analysis. Proceedings of the Second Conference on Electronic Computation, ASCE.

- Coalson R.D., Pant D.K., Ali A. and Langer D.W. (1994). Computing the eigenmodes of lossy field-induced optical waveguides. Journal of Lightwave Technology 12 (6): 1015-1022.
- Courant R. (1943). Variational method for the solution of problems of equilibrium and vibrations. Bulletin of the American Mathematical Society 49.
- Csendes Z.J. and Silvester P. (1970). Numerical solution of dielectric loaded waveguides.: I-finite element analysis. IEEE Transactions on Microwave Theory and Techniques MTT-18: 1124-1131.
- Cullen A.L., Ozkan O. and Jackson L.A. (1971). Point-matching technique for rectangular-cross-section dielectric rod. Electronics Letters 7 (17): 497-499.
- Cvetkovic S.R., Fernandez F.A., Zhao A.P., Ettinger R.D., Sewell G. and Davies J.B. (1994). Comparison of two interactive finite-element programs for analysis of optical and microwave waveguides. Journal of Lightwave Technology 12 (7): 1112-1120.
- Dagli N. and Fonstad C.G. (1987). A new method of analyzing and modelling integrated optoelectronic components. In: IEEE Microwave and Millimeter-wave monolithic Circuits Symposium: 39-41.
- Daly P. (1984). Finite element approach to propagation in elliptical and parabolic waveguides. International Journal of Numerical Methods 20 (4): 681-688.
- Davies J.B. (1972). Review of methods for numerical solution of the hollow-waveguide problem. IEE Proceedings 119 (1): 33-37.
- Davies J.B. (1989). The finite element method. In: Numerical techniques for microwave and millimeter-wave passive structures, ed. by T. Itoh. (New York: Wiley), pp. 33-132.
- Davies J.B. (1993). Finite element analysis of waveguides and cavities - a review. IEEE Transactions on Magnetics 29 (2): 1578-1583.
- Deri R.J. and Kapon E. (1991). Low-Loss III-V Semiconductor optical waveguides. IEEE Journal of Quantum Electronics QE-27 (3): 626-640.
- Di Pasquale F. and Zoboli M. (1993). Analysis of erbium-doped waveguide amplifiers by a full-vectorial finite-element method. Journal of Lightwave Technology 11 (10): 1565-1573.
- Dillon B.M., Webb J.P. (1994). A comparison of formulations for the vector finite element analysis of waveguides. IEEE Transactions on Microwave Theory and Techniques MTT-42 (2): 308-316.
- Durig U., Pohl D.W. and Rohner F. (1986). Near-field optical-scanning microscopy. Journal of Applied Physics 59 (10): 3318-3327.

- Eliseev P.G., Drakin A.E. and Pittroff W. (1994). A study of laser emission wavelength variations in 1.5 μm InGaAsP/InP BRS laser diodes: theoretical model and experiment. IEEE Journal of Quantum Electronics 30 (10): 2271-2276.
- Elsasser W.M. (1947). Attenuation in a dielectric circular rod. Journal of Applied Physics 20:1193-1196.
- English W.J. Young F.J. (1971). An E vector variational formulation of the Maxwell's equations for cylindrical waveguide problems. IEEE Transactions on Microwave Theory and Techniques MTT-19: 40-46.
- Erteza I.A. and Goodman J.W. (1995). A scalar variational analysis of rectangular dielectric waveguides using Hermite-Gaussian modal approximations. Journal of Lightwave Technology 13 (3): 493-506.
- Ettinger R.D., Fernandez F.A., B.M.A. Rahman and J.B. Davies (1991). Vector finite element solution of saturable nonlinear strip-loaded optical waveguides. IEEE Photonics Technology Letters 3 (2): 147-149.
- Feit M.D. and Fleck J.A. (1980) Computation of mode properties in optical fiber waveguides by a propagating beam method. Applied Optics 19 (7): 1154-1164.
- Fernandez F.A., Davies J.B., Zhu S. and Lu Y. (1991). Sparse matrix eigenvalue solver for finite element solution of dielectric waveguides. Electronic Letters 27 (20): 1824-1826.
- Fouchet S., Carencio A., Dauguet C., Guglielmi R. and Riviere L. (1987). Wavelength dispersion of Ti induced refractive index in LiNbO₃ as a function of diffusion parameters. Journal of Lightwave Technology 5 (5): 700-708,
- Gerdes J., Helf K.H. and Pregla R. (1991). Full-wave analysis of travelling wave Electrodes with finite thickness for electro-optic modulators by the method of lines. Journal of Lightwave Technology 9 (4): 461-467.
- Giles C.R and Desurvire E. (1991). Modelling erbium doped fiber amplifiers. Journal of Lightwave Technology 9 (2): 271-283.
- Goano M., Maio I. and Montrosset I. (1992) Design of high power low noise polarization insensitive ridge waveguide laser amplifiers. Journal of Lightwave Technology 10 (12): 1879-1889.
- Goell J.E. (1969). A circular-harmonic computer analysis of rectangular dielectric waveguides. Bell Systems Technical Journal 48: 2133-2160.
- Goell J.E. (1973). Rib waveguide for integrated optical circuits. Applied Optics 12 (12): 2797-2798.

- Goyal I.C., Gallawa R.L. and Ghatak A.K. (1993). Improved variational analysis of inhomogeneous optical waveguides. Journal of Lightwave Technology 11 (10): 1575-1578.
- Gupta V.L. and Sharma E.K. (1992). Metal-clad and absorptive multilayer waveguides: an accurate perturbation analysis. Journal of Optical Society of America 9 (6): 953-956.
- Hakki B.W. (1973). Carrier and gain profiles in GaAs stripe geometry lasers. Journal of Applied Physics 44 (11):5021-5028.
- Halevi P. (1982). Polaritons at the surface of two dielectric media. In: Electromagnetic surface modes, ed. by A.D. Boardman (New York: John Willey & Sons).
- Hall R.N. (1976). Injection Lasers. IEEE Transactions on Electron Devices ED-23 (7): 700-704.
- Hall R.N., Fenner G.E., Kingsley J.D., Soltys T.J. and Carison R.O. (1962). Coherent light emission from GaAs junctions. Physical Review Letters 9 (9): 366-368.
- Hano M. (1984) Finite-element analysis of dielectric loaded waveguides. IEEE Transactions on Microwave Theory and Techniques MTT-32 (10): 1275-1279.
- Hayashi I., Panish M.B. and Foy P.W. (1969). A low-threshold room-temperature injection laser. IEEE Journal of Quantum Electronics QE-5: 211-212.
- Hayashi I., Panish M.B. and Reinhart F.K. (1971). GaAs-Al_xGa_{1-x}As double heterostructure injection lasers. Journal of Applied Physics 42 (5): 1929-1941.
- Hayashi I., Panish M.B., Foy P.W. and Sumski S. (1970). Junction lasers which operate continuously at room temperature. Applied Physics Letters 17 (3): 109-111.
- Hayata K., Koshiba M. and Suzuki M. (1986a). Lateral mode analysis of buried heterostructure lasers by the finite-element method. IEEE Journal of Quantum Electronics QE-22 (6): 781-788.
- Hayata K., Koshiba M., Eguchi M. and Suzuki M. (1986b). Vectorial finite-element method without any spurious solutions for dielectric waveguiding problems using transverse magnetic-field component. IEEE Transactions on Microwave Theory and Techniques MTT-34 (11): 1120-1124.
- Hayata K., Miura K. and Koshiba M. (1988). Finite-element formulation for lossy waveguides. IEEE Transactions on Microwave Theory and Techniques 36 (2): 268-276.

- Henry C.H., Logan R.A. and Bertness K.A. (1981). Spectral dependence of the change in refractive index due to carrier injection. Journal of Applied Physics 52 (7): 4457-4461.
- Hocker G.B. and Burns W.K. (1977). Mode dispersion in diffused channel waveguides by the effective index method. Applied Optics 16 (1): 113-118.
- Holonyak N. and Bevacqua S.F. (1962). Coherent (visible) light emission from Ga(As_{1-x}P_x) junctions. Applied Physics Letters 1 (4): 82-83.
- Hondros D. and Debye P. (1910). Elektromagnetische wellen on dielectrischen Drahten. Ann. Physik 32: 465-476.
- Hornsby J.S. and Gopinath A. (1969). Numerical analysis of a dielectric-loaded waveguide with a microstrip line - Finite difference methods. IEEE Transactions in Microwave Theory and Techniques MTT-17 (9): 684-690.
- Hornsby J.S. and Gopinath A. (1969). Numerical analysis of a dielectric-loaded waveguide with a microstrip line - finite-difference methods. IEEE Transactions on Microwave Theory and Techniques MTT-17 (9):684-690.
- Hulse C.A. Knoesen A. (1992). Iterative calculation of complex propagation constants of modes in multilayer planar waveguides. IEEE Journal of Quantum Electronics 28 (12): 2682-2684.
- Hunziker G., Knop W. and Harder C. (1994). Gain measurements on one, two, and three strained GaInP quantum well laser diodes. IEEE Transactions on Quantum Electronics 30 (10): 2235-2238.
- Jin J. (1993). The finite element method in electromagnetics. (Canada: John Wiley & Sons).
- Johnstone W., Steward G., Culshaw B. and Hart T. (1988). Fibre-optic polarisers and polarising couplers. Electronics Letters 24 (14): 866-868.
- Jung C., Yee S. and Kuhn K. (1994). Integrated optics waveguide modulator based on surface plasmon resonance. Journal of Lightwave Technology 12 (10): 1802-1806.
- Kaminow I.P., Mammel W.L., Weber H.P. (1974). Metal-clad optical waveguides: analytical and experimental study. Applied Optics 13 (2): 396-405.
- Kao K.C. and Hockham G.A. (1966). Dielectric-fibre surface waveguides for optical frequencies. Proceedings IEE 113: 1151-1158.
- Kapany N.S. (1967). Fiber Optics: Principles and applications. (New York: Academic Press).
- Kapany N.S. and Burke J.J. (1961). Fiber optics. IX. Waveguide effects. Journal of the Optical Society of America 51 (10): 1067-1078.

- Kendall P.C., McIlroy P.W.A. and Stern M.S. (1989). Spectral index method for rib waveguide analysis. Electronics Letters 25 (2): 107-108.
- Kendall P.C., Robertson M.J., McIlroy P.W.A., Ritchie S. and Adams M.J. (1990). Advances in rib waveguide analysis using the weighted index method or the method of moments. IEE Proceedings-J 137 (1): 27-29.
- Knox R.M. and Toullos P.P. (1970). In: Proceedings of MRI Symposium on submillimeter waves, ed. by Fox. J. (Brooklyn: Polytechnic Press), pp. 497-516.
- Kogelnik H. (1990). Theory of optical waveguides. In: Guided-wave optoelectronics, ed. by Tamir T.(Heidelberg: Springer-Verlag), pp. 7-87.
- Kogelnik H. and Shank C.V. (1972). Coupled-wave theory of distributed feedback lasers. Journal of Applied Physics 43 (5): 2327-2335.
- Koshiba M. (1990). The finite-element method. In: Analysis methods for electromagnetic wave problems, ed. by Yamashita E. (London: Artech House), pp. 1-31.
- Koshiba M. (1992a). Optical waveguide analysis. (New York: McGraw-Hill).
- Koshiba M. (1992b). Optical waveguide theory by the finite element method. (Tokyo: KTK Scientific Publishers).
- Koshiba M. and Suzuki M. (1985). Vectorial wave analysis of optical waveguides with rectangular cross-section using equivalent network approach. Electronics Letters 21 (22): 1026-1027.
- Koshiba M., Hayata K. and Suzuki M. (1984). Approximate scalar finite-element analysis of anisotropic optical waveguides with off-diagonal elements in a permittivity tensor. IEEE Transactions on Microwave Theory and Techniques MTT-32 (6): 587-593.
- Koshiba M., Hayata K. and Suzuki M. (1985a). Improved finite-element formulation in terms of the magnetic field vector for dielectric waveguides. IEEE Transactions on Microwave Theory and Techniques MTT-33 (3): 227-233.
- Koshiba M., Hayata K., Suzuki M. (1985b). Finite-element formulation in terms of the electric-field vector for electromagnetic waveguide problems. IEEE Transactions on Microwave Theory and Techniques MTT-33 (10): 900-905.
- Koshiba M., Ishii H. and Suzuki M. (1982). Simple equivalent network for a rectangular dielectric image guide. Electronics Letters 18 (11): 473-474.
- Koshiba M., Maruyama S. and Hirayama K. (1993). A vector finite element method with the high-order-mixed-interpolation-type triangular elements for optical waveguiding problems. IEEE Journal of Lightwave Technology 12 (3): 495-502.

- Kovacs G. (1982). Optical excitation of surface plasmon-polaritons in layered media. In: Electromagnetic surface modes, ed. by A.D. Boardman (New York: John Willey & Sons).
- Kuhn L., Heidrich P.F. and Lean E.G. (1971). Optical guided wave mode conversion by an acoustic surface wave. Applied Physics Letters 19: 428-430.
- Kumar A., Thyangarajan K. and Ghatak A.K. (1983). Analysis of rectangular-core waveguides: An accurate perturbation approach. Optics Letters 8 (1): 63-65.
- Lee J.F. (1994). Finite element analysis of lossy dielectric waveguides. IEEE Transactions on Microwave Theory and Techniques 42 (6): 1025-1031.
- Lee W. and Wang S. (1995). Guided-wave characteristics of optical graded-index planar waveguides with metal-cladding: A simple analysis method. Journal of Lightwave Technology 13 (3): 416-421.
- Lu Y. and Fernandez F.A. (1993a). An efficient finite element method of inhomogeneous anisotropic and lossy dielectric waveguides. IEEE Transactions on Microwave Theory and Techniques MTT-41 (6-7):1215-1223.
- Lu Y. and Fernandez F.A. (1993b). Finite element analysis of lossy dielectric waveguides. IEEE Transactions on Magnetics 29 (2): 1609-1612.
- Lu Y. and Fernandez F.A. (1994). Vector finite element analysis of integrated optical waveguides. IEEE Transactions on Magnetics 30 (5): 3116-3119.
- Lusse P., Stuwe P., Schule J. and Unger H.G. (1994). Analysis of vectorial mode fields in optical waveguides by a new finite difference method. Journal of Lightwave Technology 12 (3): 487-494.
- Ma C. and Liu S. (1988) Optical characteristics analysis and TE₀ mode selection for asymmetric metal-clad waveguides. Optical and Quantum Electronics 20 (2): 323-328.
- Mabaya N., Lagasse P.E. and Vandenbulcke P. (1981). Finite Element Analysis of optical waveguides. IEEE Transactions on Microwave Theory and Techiques MTT-29 (6): 600-605.
- Manning J., Olshansky R. and Su C.B. (1993). The carrier-induced change in AlGaAs and 1.3 μ m InGaAsP diode lasers. IEEE Journal of Quantum Electronics QE-19 (10): 1525-1530.
- Mao Z. and Huang W.P. (1992). Analysis of optical rib waveguides and couplers with buried guiding layer. IEEE Journal of Quantum Electronics 28 (1):176-183.
- Marcatili E.A.J. (1969). Dielectric rectangular waveguide and directional coupler for integrated optics. Bell Systems Technical Journal 48: 2071-2102.

- Marcuse D. (1991). Theory of dielectric optical waveguides. 2nd Ed. (San Diego: Academic Press).
- Martin W.E. (1973). Waveguide electro-optic modulation in II-V compounds. Journal of Applied Physics 44 (8): 3703-3707.
- Marz R. (1994). Integrated optics: Design and modelling (Boston: Artech House).
- McAulay A.D. (1977). The Finite element solution of dissipative electromagnetic surface waveguides. International Journal for Numerical Methods in Engineering 11: 11-25.
- Miller S.E. (1969). Integrated Optics: An introduction. The Bell System Technical Journal 48 (7): 2059-2069.
- Miller S.E., Marcatilli E.A.J. and Li T. (1973). Research toward optical-fiber transmission system. Proceedings of the IEEE 61 (12): 1703-1726.
- Mirshekar-Syahkal D. and Davies J.B. (1982). Accurate analysis of coupled strip-finline structure for phase constant, characteristic impedance, dielectric losses and conductor losses. IEEE Transactions on Microwave Theory and Techniques MTT-30: 906-910.
- Miya T., Terunuma Y., Hosaka T. and Miyashita T. (1979). Ultimate low-loss single-mode fiber at 1.55 μ m. Electronics Letters 15 (4): 106-108.
- Morita N. (1990), The boundary element method. In: Analysis methods for electromagnetic wave problems, ed. by Yamashita E. (London: Artech House), pp. 33-77.
- Nallo C.D., Frezza F. and Galli A. (1995). Full-wave modal analysis of arbitrarily-shaped dielectric waveguides through an efficient boundary-element-method formulation. IEEE Transactions on Microwave Theory and Techniques 43 (12): 2982-2990.
- Nathan M.I., Dumke W.P., Burns G., Dill F.H. Jr. and Lasher G. (1962) Stimulated emission of radiation from GaAs p-n junctions. Applied Physics Letters 1 (3): 62-64.
- Ng F.L. (1974) Tabulation of methods for the numerical solution of the hollow waveguide problem. . IEEE Transactions on Microwave Theory and Techniques MTT-22: 322-329.
- Novotny L. and Hafner C. (1994). Light propagation in a cylindrical waveguide with a complex, metallic, dielectric function. Physical Review E 50 (5): 4094-4106.

- Novotny L., Pohl D.W. and Regli P. (1994). Light propagation through nanometer-sized structures: the two-dimensional-aperture scanning near-field optical microscope. Journal of Optical Society of America 11 (6): 1768-1779.
- Okoshi T. and Kitazawa S. (1990). In: Analysis methods for electromagnetic wave problems, ed. by Yamashita E. (London: Artech House), pp.341-369.
- Osterberg H. and Smith L.W. (1964). Transmission of optical energy along surface: Parts I and II. Journal of Optical Society of America 54: 1073-1084.
- Panish M.B., Hayashi I. and Sumski S. (1969). A technique for the preparation of low-threshold room-temperature GaAs Laser diode structures. IEEE Journal of Quantum Electronics QE-5: 210-211.
- Pantic Z. and Mittra R. (1986). Quasi-TEM Analysis of Microwave Transmission Lines by the finite-element method. IEEE Transactions on Microwave Theory and Techniques MTT-34 (11): 1096-1103.
- Paulsen K.D., Lynch D.R. and Strohben J.W. (1988). Three-dimensional finite, boundary, and hybrid element solutions of the Maxwell equations for lossy dielectric media. IEEE Transactions on Microwave Theory and Techniques MTT-36 (4):682-693.
- Pen S.T. and Oliner A.A. (1981). Guidance and leakage properties of a class of open dielectric waveguides: Part I-Mathematical formulations. IEEE Transactions on Microwave Theory and Techniques MTT-29 (9): 843-855.
- Pohl D.W., Denk W. and Lanz M. (1984). Optical Stethoscopy: Image recording with resolution $\lambda/20$. Applied Physics Letters 44 (7): 651-653.
- Pola J.R.P., Biehlig W. and Lederer F. (1996). A generalization of the spectral index method toward multiple rib waveguides. Journal of Lightwave Technology 14 (3): 454-461.
- Polky J.N. and Mitchel G.L. (1974). Metal-clad planar dielectric waveguide for integrated optics. Journal of the Optical Society of America 64 (3): 274-279.
- Prade B. and Vinet J.Y. (1994). Guided optical waves in fibers with negative dielectric constant. Journal of Lightwave Technology 12 (1): 6-18.
- Prade B., Vinet J.Y. and Mysyrowicz A. (1991). Guided optical waves in planar heterostructures with negative dielectric constant. Physical Review B 44 (24): 13556-13572.
- Pregla R. (1993). Method of lines for the analysis of multilayered gyrotropic waveguide structures. IEE Proceedings-J 140 (3): 183-192.

- Qiao L. and Wang J. (1992). A modified Ray-Optic method for arbitrary dielectric waveguides. IEEE Journal of Quantum Electronics 28 (12): 2721-2727.
- Qing D.K., Chen X.M., Itoh K. and Murabayashi M. (1996). A theoretical evaluation of the absorption coefficient of the optical waveguide chemical or biological sensors by group index method. Journal of Lightwave Technology 14 (8): 1907-1917.
- Quist T.M., Rediker R.H., Keyes R.J., Krag W.E., Lax B., McWhorter A.L. and Zeigler H.J. (1962). Semiconductor maser of GaAs. Applied Physics Letters 1 (4): 91-92.
- Raether H. (1977). Surface plasma oscillations and their applications. Physics Thin Films 9: p.145.
- Rahman B.M.A. and Davies J.B. (1984a). Finite-element analysis of optical and microwave waveguide problems. IEEE Transactions on Microwave Theory and Techniques MTT-32 (1): 20-28.
- Rahman B.M.A. and Davies J.B. (1984b). Penalty function improvement of waveguide solution by finite elements. IEEE Transactions on Microwave Theory and Techniques MTT-32 (8): 922-928.
- Rahman B.M.A. and Davies J.B. (1985). Vector-H finite element solution of GaAs/GaAlAs rib waveguides. IEE Proceedings-J Optoelectronics 132 (6): 349-353.
- Rahman B.M.A. and Davies J.B. (1984c). Finite-element solution of integrated optical waveguides. Journal of Lightwave Technology LT-2 (5): 682-688.
- Rahman B.M.A. and Davies J.B. (1988). Analysis of optical waveguide discontinuities. Journal of Lightwave Technology 6 (1): 52-57.
- Rahman B.M.A., Fernandez F.A. and Davies J.B. (1990). Review of Finite Element Methods for Microwave and Optical Waveguides. Proceedings of the IEEE 79 (10): 1442-1448.
- Rahman B.M.A., Liu Y., Grattan K.T.V. (1993). Finite-element modeling of one- and two-dimensional MQW semiconductor optical waveguides. IEEE Photonics Technology Letters 5 (8): 928-931.
- Rahman B.M.A., Souza J.R. and Davies J.B. (1990) Numerical analysis of nonlinear bistable optical waveguides. IEEE Photonics Technology Letters 2 (4): 265-267.
- Reisinger A. (1973). Characteristics of optical guided modes in lossy waveguides. Applied Optics 12 (5): 1015-1025.

- Rickman A.G., Reed G.T. and Namavar F. (1994). Silicon-on-insulator optical rib waveguide loss and mode characteristics. Journal of Lightwave Technology 12 (10): 1771-1776.
- Roberts A. (1991). Small-hole coupling of radiation into a near-field probe. Journal of Applied Physics 70 (8): 4045-4049.
- Rogge. U. and Pregla R. (1991). Method of lines for the analysis of strip-loaded optical waveguides. Journal of Optical Society of America-B 8 (2): 459-463.
- Saad M.S. (1985). Review of numerical methods for the analysis of arbitrarily-shaped microwave and optical dielectric waveguides. IEEE Transactions on Microwave Theory and Techniques MTT-33 (10): 894-899.
- Saini M., Sharma E.K. and Singh M.P. (1995). Strong effect of output coupling on the performance of metal-clad waveguide polarizers. Optics Letters 20 (4): 365-367.
- Schlereth K.-H and Tacke M. (1990). The complex propagation constant of multilayer waveguides: An Algorithm for a personal computer. IEEE Journal of Quantum Electronics 26 (4): 627-630.
- Schulz U. and Pregla R. (1981). A new technique for the analysis of the dispersion characteristics of planar waveguides and its application to microstrips with tuning septums. Radio Science 16 (6): 1173-1178.
- Schweig E. and Bridges W.B. (1984). Computer analysis of dielectric waveguides: A finite-difference method. IEEE Transactions on Microwave Theory and Techniques MTT-32 (5): 531-541.
- Sharma E.K., Ghatak A.K. and Goyal I.C. (1983). Matrix method for determining propagation characteristics of optical waveguides. IEEE Journal of Quantum Electronics QE-19 (8): 1231-1233.
- She S.X. (1994). Metal-clad optical polarizers; perturbation analysis. Optics Communications 105 (3,4): 175-177.
- Sherrill B.M. and Alexopoulos N. (1987). The method of lines applied to a finline/strip configuration on an anisotropic substrate. IEEE Transactions on Microwave Theory and Techniques MTT-35 (6): 568-575.
- Shubert R. and Harris H. (1968). Optical surface waves on thin films and their application to integrated data processors. IEEE Transactions on Microwave Theory and Techniques MTT-16 (12): 1048-1054.
- Silveira M. and Gopinath A. (1995). Analysis of dielectric guides by transverse magnetic field finite element penalty method. Journal of Lightwave Technology 13 (3): 442-446.

- Silvester P.P. and Ferrari R.L. (1991). Finite elements for electrical engineers. 2nd Ed. (Cambridge: Cambridge University Press).
- Snitzer E. and Osterberg H. (1961). Observed dielectric modes in the visible spectrum. Journal of the Optical Society of America 51 (5): 499-505.
- Snyder A.W. and Love J.D. (1991). Optical waveguide theory. 2nd Ed. (London: Chapman and Hall).
- Soldano L.B., Vreede A.H., Smit M.K., Verbeek B.H., Metaal E.G. and Groen F.H. (1994). Mach-Zehnder Interferometer Polarization Splitter in InGaAsP/InP. IEEE Photonics Technology Letters 6 (3): 402-405.
- Srivastava R., Kao C.K. and Ramasway R.V. (1987). WKB analysis of surface waveguides with truncated index profiles. Journal of Lightwave Technology LT-5 (11): 1605-1609.
- Stegeman G.I. and Burke J.J. and Hall D.G. (1983). Surface polariton waves guided by thin, lossy metal films. Optics Letters 8 (7): 383-385.
- Stegman G.I. and Burke J.J. (1983). Long-range surface plasmons in electrode structures. Applied Physics Letters 43 (3): 221-223.
- Stern M.S., Kendall P.C. and McIlroy P.W.A. (1990). Analysis of the spectral index method for vector modes of rib waveguides. IEE Proceedings-J 137 (1): 21-26.
- Strube J. and Arndt F. (1985) Rigorous hybrid-mode analysis of the transition from rectangular waveguide to shielded dielectric image guide. IEEE Transactions on Microwave Theory and Techniques MTT-33 (5): 391-401.
- Sudbo A.S. (1992). Why are accurate computations of mode fields in rectangular dielectric waveguides difficult. Journal of Lightwave Technology 10 (4): 418-419.
- Suematsu Y., Hakuta M., Furuya K., Chiba K., Hasumi R. (1972). Fundamental transverse electric field (TE_0) mode selection for thin-film asymmetric light guides. Applied Physics Letters 21 (6): 291-293.
- Sun L. and Yip G.L. (1994). Analysis of metal-clad optical waveguide polarizers by the vector beam propagation method. Applied Optics 33 (6): 1047-1050.
- Tamir T. (1979). Integrated Optics. 2nd Ed. (New York: Springer-Verlag).
- Tamir T. (1990). Guided wave optoelectronics. 2nd Ed. (Berlin: Springer-Verlag).
- Tien P.K. (1971). Light waves in thin films and integrated optics. Applied Optics 10 (11): 2395-2413.

- Tien P.K., Martin R.J., Blank S.L., Wemple S.H. and Varnerin L.J. (1972). Optical waveguides of single crystal garnet films. Applied Physics Letters 21 (5): 207-209.
- Tien P.K., Ulrich R. and Martin R.J. (1969). Modes of propagating light waves in thin deposited semiconductor films. Applied Physics Letters 14 (9): 291-294.
- Tomas M.S. and Lenac Z. (1985). Coupled surface polariton with guided wave polariton modes in asymmetric metal clad dielectric waveguides. Optics Communications 55 (4): 267-270.
- Torres P. and Guzman A.M. (1997). Complex finite-element method applied to the analysis of optical waveguide amplifiers. Journal of Lightwave Technology 15 (3): 546-550.
- Turner, M.J., Clough R.W., Martin H.C. and Topp L.J. (1956). Stiffness and Deflection analysis of complex structures. Journal of the Aeronautical Sciences 23 (9): 805-823.
- Westbrook L.D. (1986). Measurements of dg/dn and dn/dN and their dependence on photon energy in $\lambda=1.5\mu\text{m}$ InGaAsP laser diodes. IEE Proceedings-J 133 (2): 135-142.
- Wexler A. (1969) Computation of electromagnetic fields. IEEE Transactions on Microwave Theory and Techniques MTT-17 (8): 416-439.
- Willsch R. (1994). High performance metal-clad fibre-optic parameter. Electronics Letters 26 (15): 1113-1114.
- Wilson J. and Hawkes J.F.B. (1989). Optoelectronics: An Introduction. (Prentice Hall)
- Wolf H.F. (1979). Handbook of fiber optics: Theory and applications. (New York: Garland STPM Press).
- Wolf T., Westermeier H. and Amann M.C. (1990). Continuously tunable metal-clad ridge waveguide distributed feedback laser diode. Electronic Letters 26 (22): 1845-1846.
- Working Group I, COST 216. (1989). Comparison of different modelling techniques for longitudinally invariant integrated optical waveguides. IEE Proceedings-J 136 (5): 273-280.
- Wu R.B. and Chen C.H. (1986). A scalar variational conformal mapping technique for weakly guiding dielectric waveguides. IEEE Journal of Quantum Electronics QE-22 (5): 603-609.

- Yamamoto T. and Koshiba M. (1993). Numerical analysis of curvature loss in optical waveguides by the finite-element method. Journal of Lightwave Technology 11 (10): 1579-1583.
- Yamamoto Y., Kamiya T. and Yanai H.(1975). Characteristics of optical guided modes in multilayer metal-clad planar optical guide with low-index dielectric buffer layer. IEEE Journal of Quantum Electronics QE-11 (9): 729-736.
- Yamashita E. and Atsuki K. (1990). The point-matching method. In: Analysis methods for electromagnetic wave problems, ed. by Yamashita E. (London: Artech House), pp. 79-106.
- Yariv A. (1989). Quantum Electronics. 3rd Ed. (New York: John Wiley & Sons).
- Yariv A. and Leite R.C.C. (1963). Dielectric waveguide mode of light propagation in p-n junctions. Applied Physics Letters 2 (3): 55-57.
- Yariv A. and Yeh P. (1984). Optical waves in crystals. (New York: John Willey & Sons).
- Yeh C., Ha K. Dong S.B. and Brown W.P. (1979). Single-mode optical waveguides. Applied Optics 18 (10): 1490-1504.
- Yeh C., Ha K., Dong S.B. and Brown W.P. (1975). Arbitrarily shaped inhomogeneous optical optical fiber or integrated optical waveguides. Journal of Applied Physics 46 (5): 2125-2129.
- Yevick D. and Hermansson B. (1989). New formulations of the matrix beam propagation method: Application to rib waveguides. IEEE Journal of Quantum Electronics 25 (2): 221-229.
- Yevick D. and Hermansson B. (1990). Efficient beam propagation techniques. Journal of Quantum Electronics 26 (1): 109-112.
- Young T. (1992). Finite element modeling of a polarization optical amplifier. Journal of Lightwave Technology 10 (5): 626-633.
- Zervas M. (1991). Surface plasmon-polariton waves guided by thin metal films. Optics Letters 16 (10): 720-722.
- Zhou W.B. and Itoh T. (1982). Analysis of trapped image guides using effective dielectric constant and surface impedances. IEEE Transactions on Microwave Theory and Techniques MTT-30 (12):2163-2166.
- Zhu L. and Zhang W.X. (1988). The eigen-weighted BIEM for solving arbitrary cross-section waveguide. IEE AP-S International Symposium: Antennas and Propagation 1-3, ch.342, pp.589-591.
- Zienkiewicz O.C. and Taylor R.L. (1989). The finite element method. 4th ed.(London: Mc Graw-Hill).